Galactic Chemical Evolution Signatures in Stellar Atmospheres and Their Possible Planetary Connection

Thesis

The Open University

A THESIS SUBMITTED FOR THE DEGREE OF DOCTOR OF PHILOSOPHY

ELENA NICKSON

GALACTIC CHEMICAL EVOLUTION SIGNATURES IN STELLAR ATMOSPHERES AND THEIR POSSIBLE PLANETARY CONNECTION

THE OPEN UNIVERSITY

DEPARTMENT OF PHYSICAL SCIENCES

July 8, 2016

DATE OF SUBMISSION: 14 SEPTEMBER 2015
DATE OF AWARD: 4 JULY 2016

ProQuest LLC.
789 East Eisenhower Parkway
P.O. Box 1346
Ann Arbor, MI 48106 – 1346

Abstract

In recent years there have been many studies to determine whether there is a chemical signature in stellar atmospheres that can be linked to the presence of planets. Most of these studies have involved bulk analysis of stars to identify whether planet-hosting stars have a higher metallicity than non planet-hosting stars. These studies led to the work of Meléndez et al. [49], which identified a signature in the solar photosphere which was likely caused by the presence of planets.

To further explore this theory, I obtained high-quality spectra from the ESPaDOnS spectropolarimeter at the CFHT for 10 stars with similar stellar parameters (effective temperature, surface gravity, microturbulence velocity and metallicity). I performed a differential abundance analysis on the planet-hosting star 61 Vir against 9 comparison stars. This analysis indicated that there is no planetary signature present in 61 Vir but instead, that there is a signature observed when performing the same analysis on an individual star basis, which is observable with age. I determined the relative ages of the stars and then perform a differential abundance analysis of 9 stars using a younger tenth star as reference. From this I found likely evidence of galactic chemical evolution in the stellar atmospheres.

Acknowledgements

Firstly, I would like to thank my supervisors: Dr Carole Haswell, Dr Luca Fossati and Dr Ulrich Kolb. Without them this project wouldn't have existed and I wouldn't have had the incredible opportunities I have experienced throughout my PhD. I will be forever indebted to them for the time and dedication they put in to help me succeed. I am particularly thankful to Dr Luca Fossati who spent many long hours helping me to understand the topic at the start, and continued to help me whenever needed.

Secondly, I would like to thank my Mum and my Dad. They both went above and beyond the call of duty to help me in any way that I needed throughout the 1738 days of my PhD. Their support helped me through the painful times as well as the brilliant times.

Finally, I would like to thank my three loves: E.T., Dr Ellie Arroway, and my husband. E.T. and Dr Ellie Arroway always inspired me to keep going and find the answers whilst my husband put up with everything, including marrying me, whilst I undertook and completed this thesis. To him especially, I will be eternally grateful.

Contents

List of Figures

List of Tables

Chapter 1

Introduction

The discovery of the first exoplanet orbiting a solar-type star by Mayor and Queloz [48] signalled the beginning of a revitalisation of planet formation studies. The ability to study not only our Solar System but other planetary systems has opened up further opportunities for understanding mechanisms involved in planet formation and evolution. However, the discovery of exoplanets hasn't just revitalised the field of planet formation but has also opened up studies into how typical a star the Sun is and whether its properties are linked to it being a planet host.

This thesis is intended to study a planet-hosting star to understand whether there are possible planetary signatures present in stars outside of the Solar System. Up to now there have been some studies (Meléndez et al. [51], Mack et al. [47], Teske et al. [73]) looking at the signatures present in stars other than the Sun but the number of lines has always been small and the uncertainty on the abundances too large in many cases. The selection of few spectral lines leads to differences between results, as will be seen in Section 4.2. It was therefore important to undertake a study with a large number of lines to see the overall effect from reducing the number of spectral lines selected.

The introduction of this thesis discusses the formation and chemical patterns present in our Solar System (Section 1.1) before detailing the background for measuring and understanding spectral lines (Section 1.2). The chemistry of the Sun and possible sig-

natures of giant exoplanets and their effect on their host star is discussed in Section 1.3 before an overview of the publication which first suggested the volatile and refractory signature, Meléndez et al. [49], is presented Section 1.4. The introduction is concluded with a summary of the impact of Meléndez et al. [49].

1.1 The Solar System

The Solar System formed in a gravitationally unstable giant molecular cloud. Once formed, a gaseous protoplanetary disk remained around the star consisting predominantly of Hydrogen and Helium with some heavier elements. Planetesimals were slowly formed in this disk from clumps of dust and gas which, over time, became the planetary objects we know today. At the time of planet formation, the temperature of the inner Solar System, where the terrestrial planets formed, was not cold enough for volatile materials to condense, resulting in the inner planets being formed mostly from rocky silicates and refractory material. The outer Solar System, where the gas giants formed, was cool enough for volatile materials to condense, resulting in planets primarily formed of volatile ices and little refractory material, which was accreting onto the cores of the giant planets and their satellites.

The chemical composition of the Solar System was determined by measuring elemental abundances of the solar photosphere and chondritic meteorites. Chondritic meteorites formed 4.6 billion years ago [1] at the same time as the planets and asteroids. Carbonaceous chondrites escaped the fractionation process [2] remaining relatively unaltered from the time of formation. They provide a unique archaeological insight into the early Solar System. As can be seen in Figure 1.1, when Hydrogen and some of the other lighter elements such as Nitrogen and Oxygen are excluded, there is a very close correspondence in the composition of the elements in the Sun and the meteorites.

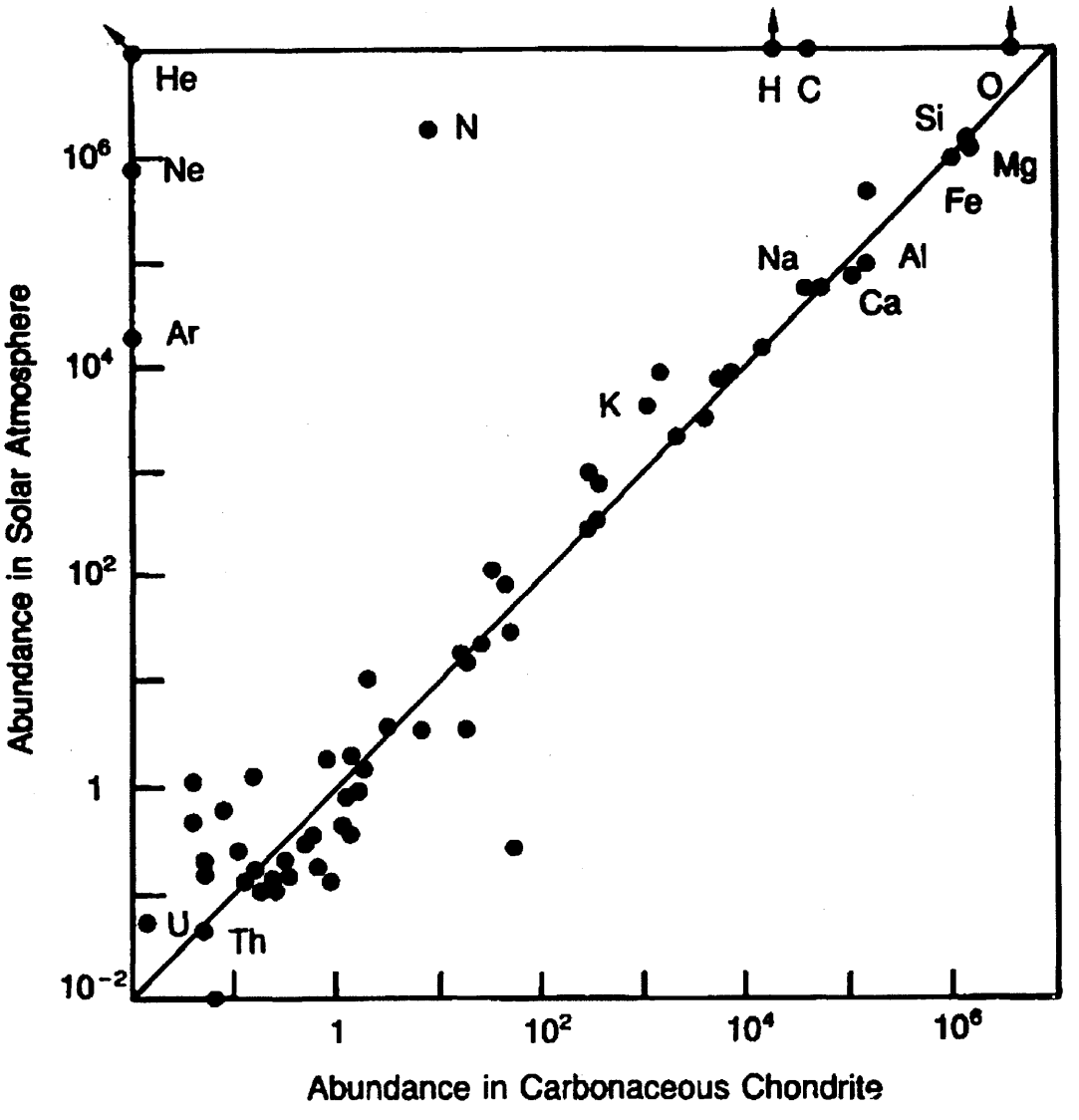

Figure 1.1: A comparison between the logarithms of the abundances in the Sun with carbonaceous chondritic meteorites. Figure from `http://geophysics.ou.edu`

The solar composition used in this analysis is taken from Grevesse and Sauval [31], listed in Table 1.1.

Table 1.1: Element abundances in the present day Solar photosphere and C1 chondrite meteorites, whose chemical composition resembles the composition of the Solar photosphere [31]. The abundances are listed in the usual logarithmic (dex) scale relative to Hydrogen $[A_{El} = \log(N_{El}/N_H) + 12]$.

Element	Photosphere (dex)	Meteorites (dex)
C	8.55 ± 0.05	-
N	7.97 ± 0.07	-
O	8.87 ± 0.07	-
Na	6.33 ± 0.03	6.32 ± 0.02
Mg	7.58 ± 0.05	7.58 ± 0.01
Al	6.47 ± 0.07	6.49 ± 0.01
Si	7.55 ± 0.05	7.56 ± 0.01
S	7.33 ± 0.11	7.20 ± 0.04
K	5.12 ± 0.13	5.13 ± 0.02
Ca	6.36 ± 0.02	6.35 ± 0.01
Sc	3.17 ± 0.10	3.10 ± 0.01
Ti	5.02 ± 0.06	4.94 ± 0.02
V	4.00 ± 0.02	4.02 ± 0.02
Cr	5.67 ± 0.03	5.69 ± 0.01
Mn	5.39 ± 0.03	5.53 ± 0.01
Fe	7.50 ± 0.04	7.50 ± 0.01
Co	4.92 ± 0.04	4.91 ± 0.01
Ni	6.25 ± 0.01	6.25 ± 0.01
Zn	4.60 ± 0.08	4.67 ± 0.04
Rb	$2.60 \pm (0.15)$	2.41 ± 0.02
Sr	2.97 ± 0.07	2.92 ± 0.02
Y	2.24 ± 0.03	2.23 ± 0.02
Zr	2.60 ± 0.02	2.61 ± 0.02
Nb	1.42 ± 0.06	1.40 ± 0.02
Ba	2.13 ± 0.05	2.22 ± 0.02
La	1.17 ± 0.07	1.22 ± 0.02
Ce	1.58 ± 0.09	1.63 ± 0.02
Nd	1.50 ± 0.06	1.49 ± 0.02
Sm	1.01 ± 0.06	0.98 ± 0.02
Eu	0.51 ± 0.08	0.55 ± 0.02

1.2 Spectral Lines

A spectral line results from the emission or absorption of light in a narrow frequency range from a uniform and continuous spectrum. The appearance of a spectral line is dependent on intrinsic and non-intrinsic astrophysical processes occurring in the stellar

atmosphere.

1.2.1 Broadening

Every line will be subject to natural broadening, an effect due to Heisenberg's Uncertainty Principle whereby the energy cannot be perfectly defined, resulting in a Lorentzian line profile. There are three other main types of broadening: pressure broadening, Doppler broadening and rotational broadening. Pressure broadening is very common in main sequence stars because of the frequency of particle interactions due to the high density. In collisions, the energy of the atomic transitions is disturbed such that it is increased or decreased depending on the distance to the perturber (Figure 1.2, [30]). This variation in energy leads to the line becoming broadened resulting in, as with the natural broadening, a Lorentzian line profile.

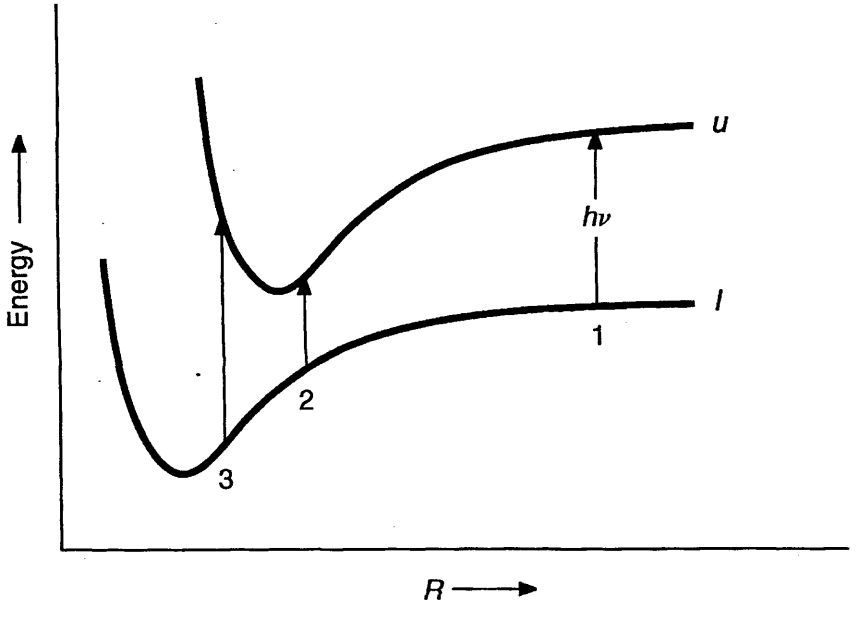

Figure 1.2: The upper u and lower l atomic levels of a transition have energies dependent on the distance R to the perturber. The unperturbed transition energy (1) can be decreased (2) or increased (3) depending on the distance. Figure from Gray [30].

There are two other main forms of pressure broadening: Stark broadening and van der Waals broadening. An atom, when approached by an electron or ion, will be in an electric field temporarily, causing the lines to become broadened through the Stark

effect. Neutral-neutral reactions will give rise to temporarily induced dipole moment interactions causing lines to become broadened through the van der Waals forces. The Stark broadening is more prevalent in hot stars due to larger quantities of ions whilst the van der Waals broadening is more prevalent in cool stars.

In stellar atmospheres, atoms have random velocities due to their thermal energy. Consequently, some atoms travel towards the observer whilst others travel away producing a Doppler shift in the spectral line known as Doppler broadening. The velocities take a Maxwell-Boltzmann distribution resulting in a Gaussian line profile. Stellar rotation and pulsation also result in Doppler broadening on a macroscopic scale due to coherent mass motions. The amount of broadening is dependent on the rotation rate and angle of inclination of the axis of rotation to the line of sight. The effects cannot be combined with the Doppler broadening as they do not follow the same distribution and there is no single simple distribution that can express the combined effect. An additional broadening mechanism to consider is macroturbulence which is due to large scale turbulence motions in the photosphere. The macroturbulence broadening is seen as a broadening of the spectral lines without altering their total absorption.

A spectral line which is broadened by both Doppler and pressure broadening will take the form of a Voigt profile due to convolution (Figure 1.3). The Doppler broadening dominates in the core of the line whilst the pressure and natural broadening become increasingly more significant in the wings of the line.

Hyperfine Structure

The spectral lines which will be analysed in this thesis could be subject to an effect other than broadening: hyperfine structure.

Hyperfine structure is the splitting of spectral lines into two or more closely spaced components. It is caused by orbital interactions between the intrinsic spin of the electrons and the intrinsic spin of the atomic nuclei. High resolution spectra are required to observe this phenomenon. It leads to the broadening and shifting of spectral lines, typically altering the line profile so that it is very shallow and wide or asymmetrical.

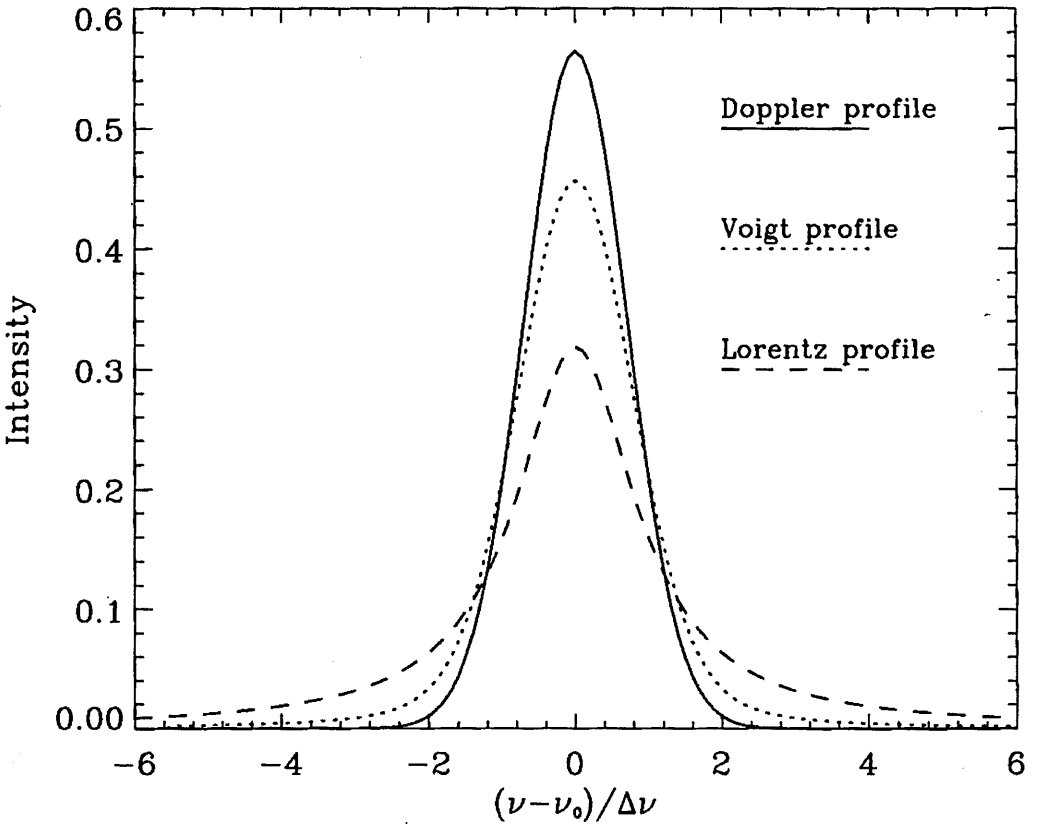

Figure 1.3: Illustration of the different broadening profiles: Doppler which is due to thermal energy; Voigt which is due to the convolution of Doppler and pressure broadening; and Lorentz due to the natural broadening.

Hyperfine structure also affects line strengths, the effect of which is seen in equivalent width measurements. Consequently, hyperfine structure can lead to abundances being overestimated [58].

1.2.2 Equivalent Width

The strength of a spectral line is measured as its equivalent width W which is defined as the area of a box reaching to the continuum with the same area as the spectral line (Figure 1.4). The continuum is produced by the thermal energy of the observed star and is visualised as a region of the spectrum with no distinguishable spectral lines. For stars, which are in thermal equilibrium, the continuum emission can be approximated as a blackbody spectrum with a peak emission determined by the effective temperature of the star (see Section 3.5.1 for further discussion about effective temperature). The

continuum is normalised to unity after the spectrum has been flat-fielded to remove any remaining curvature in the spectrum. This is necessary so that the measurement of the spectral lines is calculated between 0 and 1 for every line, ensuring uniformity. The equivalent width is calculated as

$$W_\lambda = \int \frac{F_c - F_\lambda}{F_c} d\lambda \tag{1.1}$$

where F_λ is the flux of the line, F_c is the flux from the continuum and the integral is taken over the whole spectral line. W_λ is dependent on the number of atoms in the energy state of the transition forming the line.

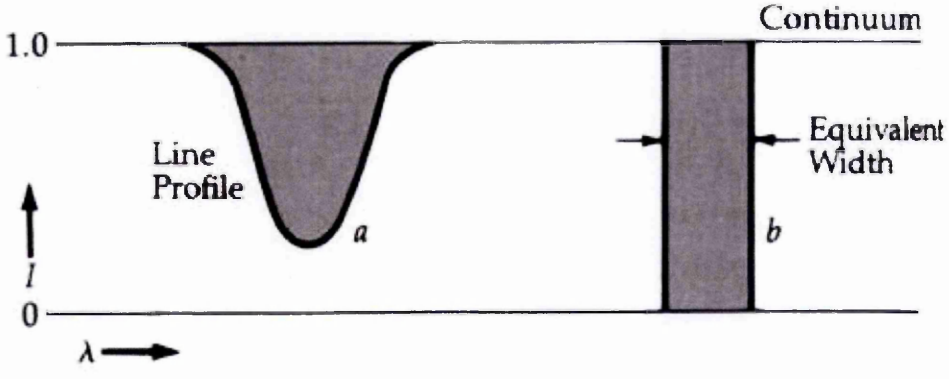

Figure 1.4: Depiction of how a line profile is measured as an equivalent width taken from Gray [30].

1.2.3 Abundances

This section is based on Gray [30]. The "curve of growth" can be used to describe the dependence of abundance on equivalent width. The "curve of growth" is computed from many aspects including the atomic constants for the line, surface gravity ($\log g$), temperature distribution and type and strength of the damping. Assuming a simple cool stellar model, the surface flux F_ν in a line is

$$F_\nu = F_c e^{-\tau_\nu}, \tag{1.2}$$

where τ_ν is the optical depth and F_c is the continuum flux. Assigning L to be the geometrical thickness of the photosphere, the optical depth is simply calculated using

$$\begin{aligned}\tau_\nu &= \int_0^L l_\nu \rho \, dx \\ &= \int_0^L N \alpha \, dx \\ &= A \int_0^L \left(\frac{N}{N_E}\right) N_H \alpha \, dx \end{aligned} \tag{1.3}$$

where α is the atomic absorption coefficient per hydrogen atom. l_ν is the line absorption coefficient, ρ is the mass density, and N/N_E is the ratio of line absorbers to total number of elements per cubic centimetre. The abundance $A = N_E/N_H$ is proportional to τ_ν and therefore is exponentially proportional to F_ν.

In weak lines, the Doppler core dominates the width and the lines are formed at $\tau_\nu \ll 1$ so Eq. 1.2 can be expanded to give

$$\tau_\nu \approx \frac{F_c - F_\nu}{F_c}. \tag{1.4}$$

The line depth is therefore proportional to both τ_ν and A for the weak lines. Consequently, the equivalent width W is proportional to A.

Wings, which follow a delta-function, dominate the profile in strong lines so that $\alpha \approx (\pi e^2/mc)(\gamma/4\pi^2) f/\Delta\nu^2$, where f is the oscillator strength. By substituting α

into Equation 1.3, it can be seen that

$$\tau_\nu = \frac{\pi e^2}{mc}\frac{Af}{\Delta\nu^2}\int_0^L \left(\frac{N}{N_E}\right) N_H \frac{\gamma}{a\pi^2}\,dx$$
$$\approx \frac{\langle\gamma\rangle Afh}{\Delta\nu^2} \tag{1.5}$$

where $\langle\gamma\rangle$ denotes the depth-average damping constant and h is substituted for the integral and remaining constants for simplification. In the strong line regime, the line depth varies as

$$1 - e^{\tau_\nu} = \frac{F_c - F_\nu}{F_c}, \tag{1.6}$$

resulting in an equivalent width of

$$W = \int_0^\infty (1 - e^{\tau_\nu})\,d\nu$$
$$= \int_0^\infty (1 - e^{\langle\gamma\rangle Afh/\Delta\nu^2})\,d\nu$$
$$= \left(\langle\gamma\rangle Afh\right)^{\frac{1}{2}} \int_0^\infty (1 - e^{\frac{1}{u^2}})\,du, \tag{1.7}$$

where $u^2 = \Delta\nu^2/\langle\gamma\rangle Afh$. The equivalent width of a strong line is therefore proportional to the square root of the abundance.

1.3 Exoplanet signatures

There have been many previous studies to determine whether the Sun has an unusual chemical composition [34, 35, 60], all of which concluded that the Sun is a typical star, albeit depleted in lithium [3].

This solar lithium depletion generated interest in whether stars with planets have a peculiar lithium abundance. Chen and Zhao [11], Gonzalez [26], Israelian et al. [38] among others suggested that lithium is depleted in stars with planets compared to those

without, due to the star-planet interaction causing an increased rate of lithium burning in the stellar interior. However, the connection between lithium abundance and the presence of planets is inconclusive due to potential observational biases in stellar age and metallicity affecting the results [46, 50, 6].

Gonzalez [25] first indicated that on average, planet host stars were metal-rich compared to stars without known planets. Further chemical composition studies by various groups (e.g. Gonzalez et al. [27], Santos et al. [65], Ecuvillon et al. [15], Udry and Santos [77]) have confirmed this hypothesis. A bias in the selection of stars analysed might also be the cause of finding that planets orbit preferentially around metal-rich stars.

There are two primary planetary formation processes which could lead to an alteration in the stellar chemistry. The first, proposed by Gonzalez [25] and further developed in Schuler et al. [66], suggested that stars could have accreted refractory-rich planetary material but not to the extent that the overall stellar metallicity would be enchanced. However, a reduction in the uncertainties and developments with differential abundance analyses could show that the metallicity is enhanced. The second is discussed in Section 1.4.

1.4 Meléndez 2009

The terrestrial planets and meteorites of the inner Solar System are enhanced in refractory elements compared to volatiles [56]. Meléndez et al. [49] found an interesting counterpoint to this abundance pattern: the Sun exhibits a corresponding depletion in these refractory elements.

Figure 1.5 shows the main result from Meléndez et al. [49]: the solar photospheric abundances display a decrease of refractory elements (e.g. Fe-peak elements and Al) of $\sim$20% compared to volatiles (e.g. C, N, O). This analysis is performed relative to solar twins and analogs without known planets. The solar twins were defined as stars with [Fe/H] within 0.07 dex and $T_{\rm eff}$ within 75 K of the Sun whilst the parameters

for analogs were defined to [Fe/H] within 0.25 dex and $T_{\rm eff}$ within 250 K. There is a strong correlation between the abundance differences and condensation temperature ($T_{\rm cond}$). The condensation temperature of an element is the temperature at which 50% of the element will be in a solid state at a pressure of 10^{-4} bar. The probability of this correlation occurring in a random sample is of the order 10^{-9}.

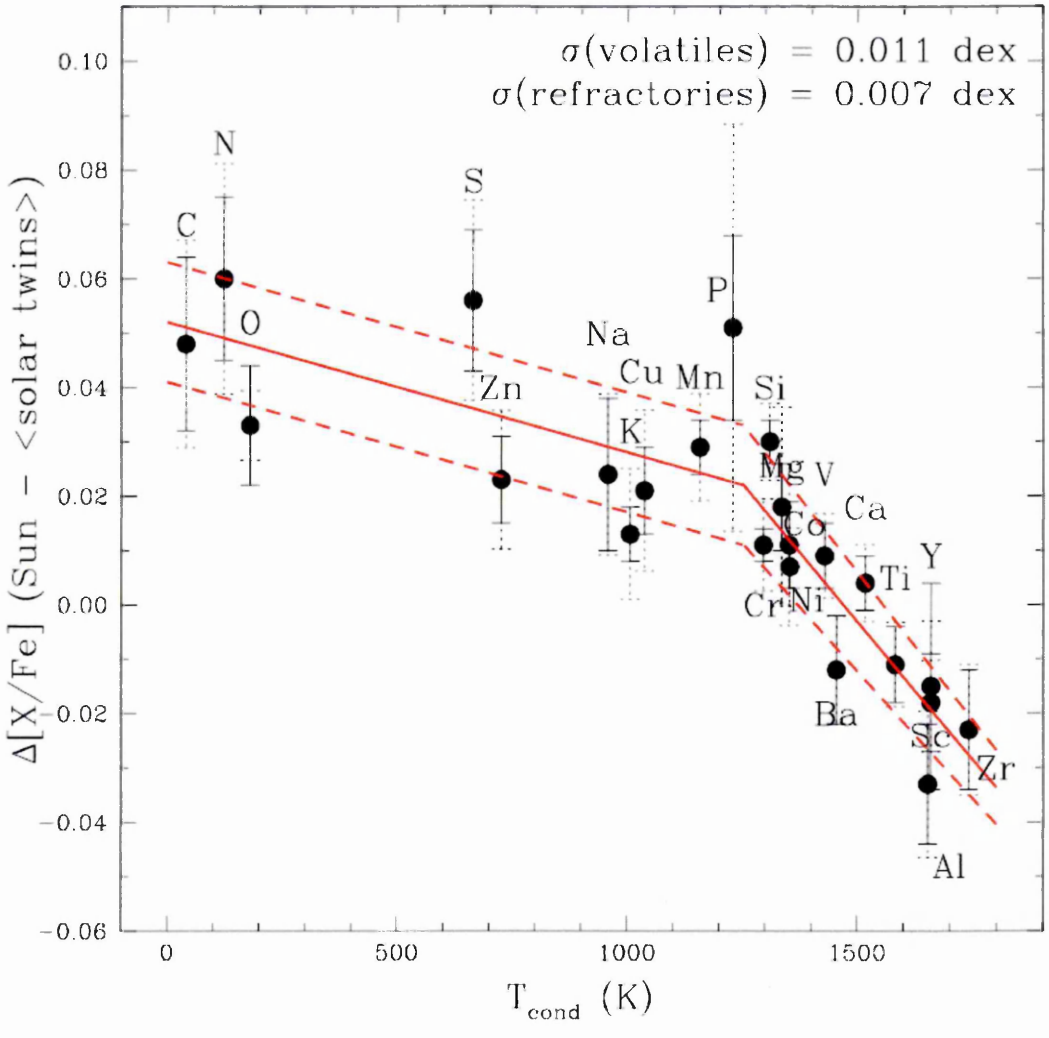

Figure 1.5: Differences between [X/Fe] of the Sun and the mean values in the solar twins as a function of $T_{\rm cond}$. The solid lines are fits to the abundance pattern, dashed lines represent the standard deviation from the best fits. The solid error bars represent 1σ uncertainties in the mean abundance of the solar twins, dashed error bars are the 1σ uncertainties when the Sun is included. Figure taken from Meléndez et al. [49] for clarity.

Many scenarios were considered and dismissed as the cause of the trend. One possibility was that the comparison stars were younger and therefore metal-rich compared

to the Sun. This was tested by calculating the stellar ages which gave a median age similar to solar thereby eliminating this possibility. An alternative theory is that the Sun formed from a nebula in which dust containing refractory elements was blown away prior to the Sun's formation. This was dismissed as there is no explanation as to why only the Sun and not the comparison stars, which were selected to be from the solar neighbourhood, was affected. The most likely scenario suggested was that the presence of terrestrial planets is the cause of the trend. The mass of refractory elements missing in the Sun's photosphere is approximately equal to that locked up in the Solar System's terrestrial planets. If the planets locked up the refractory material in the proto-solar disk, it would have been unable to accrete onto the solar photosphere therefore causing the Sun to be depleted of refractory materials.

Proto-planetary disks have typical lifetimes of $<$10 Myr [8, 67] which is smaller than the expected duration (30 Myr) for the solar convective zone to reach its current size, according to the D'Antona and Mazzitelli [13] model starting with a fully convective Sun. It is assumed that the signature was imprinted once the convective zone reached its present size [49], resulting in timescale problems. Nordlund [53] discussed the viability of this scenario for models of the Sun by Wuchterl and Klessen [85] and Wuchterl and Tscharnuter [86] which assume the Sun was never fully convective. This assumption allows for the imprinting of the abundance pattern with no timescale problems.

The majority of the comparison stars used in Meléndez et al. [49] had not been searched for planets. If we assume that these stars did not undergo the planet formation process, refractory material in the proto-stellar disk would have accreted onto the proto-star, enriching the star in the refractory elements that the Sun is depleted in. This leads to the abundance pattern seen in Fig. 1.5. If the comparison stars had been depleted in refractory elements too, there would be no significant abundance trend.

1.4.1 Impact of Meléndez 2009

This discovery could have very important implications. If it is found that the solar abundance trend is related to the presence of terrestrial planets, it could be the start of developing a method for identifying stars which host terrestrial planets by utilising the chemical composition of the star. Current methods of planet detection are very efficient in the detection of giant planets but the number of terrestrial planets detected is minimal with current technology, although Kepler is rapidly improving this number. The transit and radial velocity methods for detecting planets require long observational periods whereas single observations of a star are required to obtain the spectra for abundance analysis providing a greater number of opportunities for planet detection. This method would specifically flag up likely terrestrial planet host stars when other methods are not always able to.

The results from Meléndez et al. [49] showed that the abundance difference between the low and high $T_{\rm cond}$ elements is about 0.1 dex[1]. This is of the same order of magnitude or below the smallest error bars on the abundances obtainable with the most advanced abundance analysis techniques on a single star (e.g. LTE analysis: [62, 22]; non-LTE analysis: [59]). These uncertainties increase when one takes into account all the systematic errors that might be present when comparing abundance patterns of different stars. To reduce these systematic errors, it is important to perform a differential rather than absolute abundance analysis.

[1]The unit "dex" refers to a unit of magnitude in logarithm.

Chapter 2

Observations and Data Reduction

This thesis is based on observations obtained with the ESPaDOnS spectropolarimeter at the Canada-France-Hawaii Telescope (CFHT). In this Chapter I outline the instrument together with the adopted target selection, data reduction and normalisation techniques.

This work is based on the determination of abundances of a planet-hosting reference star relative to other stars with similar stellar parameters (further discussed in Section 2.2) but which have no known planetary companions. By selecting stars which are similar, the star-to-star abundance differences are minimised due to their physical characteristics. One of the main systematic errors on the abundances is caused by the assumption of Local Thermodynamic Equilibrium (LTE) in line formation. Other systematic errors could be caused by inaccuracies in the line transition probabilities ($\log gf$ which will be discussed in Section 3.3) and assumptions with model atmospheres (discussed in Section 3.1).

2.1 ESPaDOnS

The data were collected in service mode using the Echelle SpectroPolarimetric Device for ObservatioNs of Stars (ESPaDOnS) spectropolarimeter at the 3.6 metre optical/infrared Canada-France-Hawaii Telescope (CFHT) at Mauna Kea, between February and

July 2011 (see Table 2.1 for exact dates). ESPaDOnS is fibre-fed from a Cassegrain module which contains the guiding and calibration facilities and an optional polarisation analyser. The instrument has three modes: "object only", "object+sky" and "polarimetric". The observations were performed in object-only spectroscopic mode to obtain the highest nominal available resolution of 80 000. This involves the flux being collected through a single fibre over a spectral region of 3700 to 10 500 Å. The full spectrum spans 40 grating orders with a 79 groves/mm grating. The nature of the echelle orders causes three small gaps in the spectra at 9224 – 9234Å, 9608 – 9636Å and 10026 – 10074Å with all other regions fully covered. The CCD is an 2kx4.5k EEV and provides four different readout speeds. The exposure times varied from 173 seconds for the brightest targets to 2163 seconds for the faintest (Table 2.1).

Table 2.1: Table showing the observation date, exposure time and SNR per pixel for the target stars using the Libre-ESpRIT package. The SNR is taken at a wavelength of 5520 Å. The stars marked with † and ‡ are the stars which have had 2 or 4 exposures respectively added to increase the SNR.

Target Name	Observation Date	Exposure Time (s)	SNR pp
61 Vir	15.03.2011	185	747
HD 18144	09.07.2011	2163	839
HD 18803	16.03.2011	1045	833
HD 47127	21.02.2011	1280	816
HD 51219	21.02.2011	2163	781
HD 58781	21.02.2011	1850	831
HD 111395	15.03.2011	771	803
HD 140538	15.03.2011	491	735
HD 201219†	09.07.2011	3760	781
HD 223498‡	09.07.2011	5096	871

To perform data reduction, exposures of the Thorium-Argon (ThAr) lamp wavelength calibration spectrum, a single bias spectrum and a series of flat-field exposures were collected at the beginning and end of each night as is the standard routine. ESPaDOnS spectra are reduced automatically using the Libre-ESpRIT reduction pipeline available at the CFHT which proceeds in two general steps. It first requires the wavelength calibration which is done by taking comparison exposures with Thorium/Argon or Thorium/Neon lamps. This spectrum is then recorded in 2D before being extracted

into a 1D spectrum. The spectrum from each of the orders is curved so Libre-ESpRIT performs a geometrical analysis using calibration exposures to determine the position and shape of each order and the wavelength-to-pixel relationship.

Geometrical information, obtained from the flat field, bias exposure and stellar frames, is used alongside the CCD characteristics to perform an optimal extraction, leaving fully reduced spectra. For a full description of Libre-ESpRIT see Donati et al. [14].

2.2 Target selection

To study whether the presence of rocky planets affects the chemical composition, the data for a star known to host a potentially rocky exoplanet, a Super-Earth, was collected. A Super-Earth is a planet considered to be more massive than Earth but significantly less massive than Uranus and Neptune. Currently, the upper mass bound is considered to be 10 M_{Earth} [78] but there is no guarantee that a Super-Earth is actually rocky without knowing its radius [61]. They are harder to detect using conventional exoplanet detection methods due to their small mass and radius. Using the terrestrial planets in the Solar System as a guide, it is expected that rocky planets are overabundant in refractory (high $T_{\rm cond}$) compared to volatile (low $T_{\rm cond}$) elements (as discussed in Section 1.4).

61 Virginis, hereafter called 61 Vir was chosen as the planet-hosting star. The 61 Vir system is the first known system with a Super-Earth orbiting around a G-type Sun-like star. 61 Vir is a solar type, solar metallicity star [$T_{\rm eff} = 5571$ K, $\log g = 4.47$; 79] hosting 3 planets: two Uranus-like planets and a potential Super-Earth, the latter with a projected mass of $5.1 M_{Earth}$ [see Table 2.2; 82]. This planetary system has not been detected using the transit method so the radii of the planets have not been determined, preventing us from definitely concluding that there is a Super-Earth. These three planets are believed to contain a substantial mass of heavy elements and therefore a signature even more pronounced than in Meléndez et al. [49] might be observed.

Table 2.2: 61 Vir planetary system basic parameters [82] truncated at the second digit. Error bars are less than $10^{-2} - 10^{-3}$.

Planet	Period days	e	$m\sin i$ M_{jup}	a AU
61 Vir b	4.21	0.12	0.02	0.05
61 Vir c	38.02	0.14	0.06	0.22
61 Vir d	123.01	0.35	0.07	0.48

Meléndez et al. [49] performed a differential abundance analysis as they had stars which shared similar parameters to the Sun. This allowed for the same lines to be measured in all the stars because they would undergo similar effects due to having the comparable effective temperatures, surface gravities and metallicities.

To ensure a differential abundance analysis could be performed in this study, twins and analogs of 61 Vir were chosen as comparison stars. As with Meléndez et al. [49], the twins were defined as stars with [Fe/H] within 0.07 dex and $T_{\rm eff}$ within 75 K whilst the parameters for analogs were defined to [Fe/H] within 0.25 dex and $T_{\rm eff}$ within 250 K. The parameters for 61 Vir and the comparison stars were taken from Valenti and Fischer [79] ensuring a consistency in the basic data used to select the comparison stars. Stars with similar ages were favoured but there is an age uncertainty of at least 2 – 3 Gyr. All targets are within 50 pc and belong to the thin disk population[1]. 61 Vir is a thin disk star so only thin disk stars have been selected as comparison stars so that they should show similar metallicity traits to 61 Vir.

Accounting for all of these limitations on the comparison star selection, 4 twins and 5 analogs of 61 Vir were found in the Valenti and Fischer [79] catalog. The Valenti and Fischer [79] catalog contains stellar properties for 1040 nearby F, G, and K stars. The properties were obtained by fitting the observed spectrum to a synthetic spectrum directly and include, but are not limited to, the effective temperature, surface gravity, metallicity, projected rotational velocity, and certain abundances. Of these stars, one is known to be in a double or multiple star system (HD 140538) and one is a BY

[1]The Galactic disk can be split into thick and thin disk populations. In the thick disk, stars are older and more metal poor. The thin disk hosts young, metal-rich stars.

Draconis variable star (HD 111395). BY Draconis stars exhibit quasi-periodic light changes caused by the presence of surface spots and stellar rotation [18]. The remaining stars are high proper motion stars and none are known to have rocky companions. Appendix A contains information on radial velocity searches for these stars using the primary radial velocity search spectrographs. The full target list is shown in Table 2.3.

Table 2.3: Basic parameters for the stars to be analysed. The stellar twins, as identified using the constraints from Meléndez et al. [49] on the Valenti and Fischer [79] data, are marked with a dagger. Data are taken from Valenti and Fischer [79].

Target	Vmag	$T_{\rm eff}$ K	Age Gyr	[M/H] dex
61 Vir	4.74	5571	6.3	0.09
HD 18144†	7.41	5511	7.9	0.05
HD 18803†	6.62	5638	5.4	0.09
HD 47127†	6.84	5605	7.8	0.07
HD 51219	7.41	5642	7.3	0.00
HD 58781†	7.24	5604	6.9	0.06
HD 111395	6.29	5654	4.4	0.06
HD 140538	5.80	5653	5.4	0.06
HD 201219	8.01	5653	5.5	0.09
HD 223498	8.34	5628	6.6	0.14

2.3 Solar data

Data from the National Solar Observatory (NSO) were used to measure the solar spectrum and determine any $\log gf$ corrections[2]. In a differential abundance analysis, correcting the $\log gf$ does not change the differential results but it does allow for more precise relative abundances and parameters.

2.4 Normalisation

An IDL tool, developed and maintained by Dr. O. Kochukhov, Uppsala University, was used to perform continuum normalisation. As mentioned in Section 1.2, continuum

[2]more information on $\log gf$ can be found in Section 3.3

normalisation requires setting the continuum regions in the spectrum to a fixed value, 1.00 in this case, throughout the observed wavelength range. Unlike the iraf *continuum* task, it allows one to preview the spectra, cut it to look at smaller sections, and provides a much better visualisation of the spectrum (see Fig. 2.1) whilst having all the same computational capabilities. This leads to a more precise continuum setting.

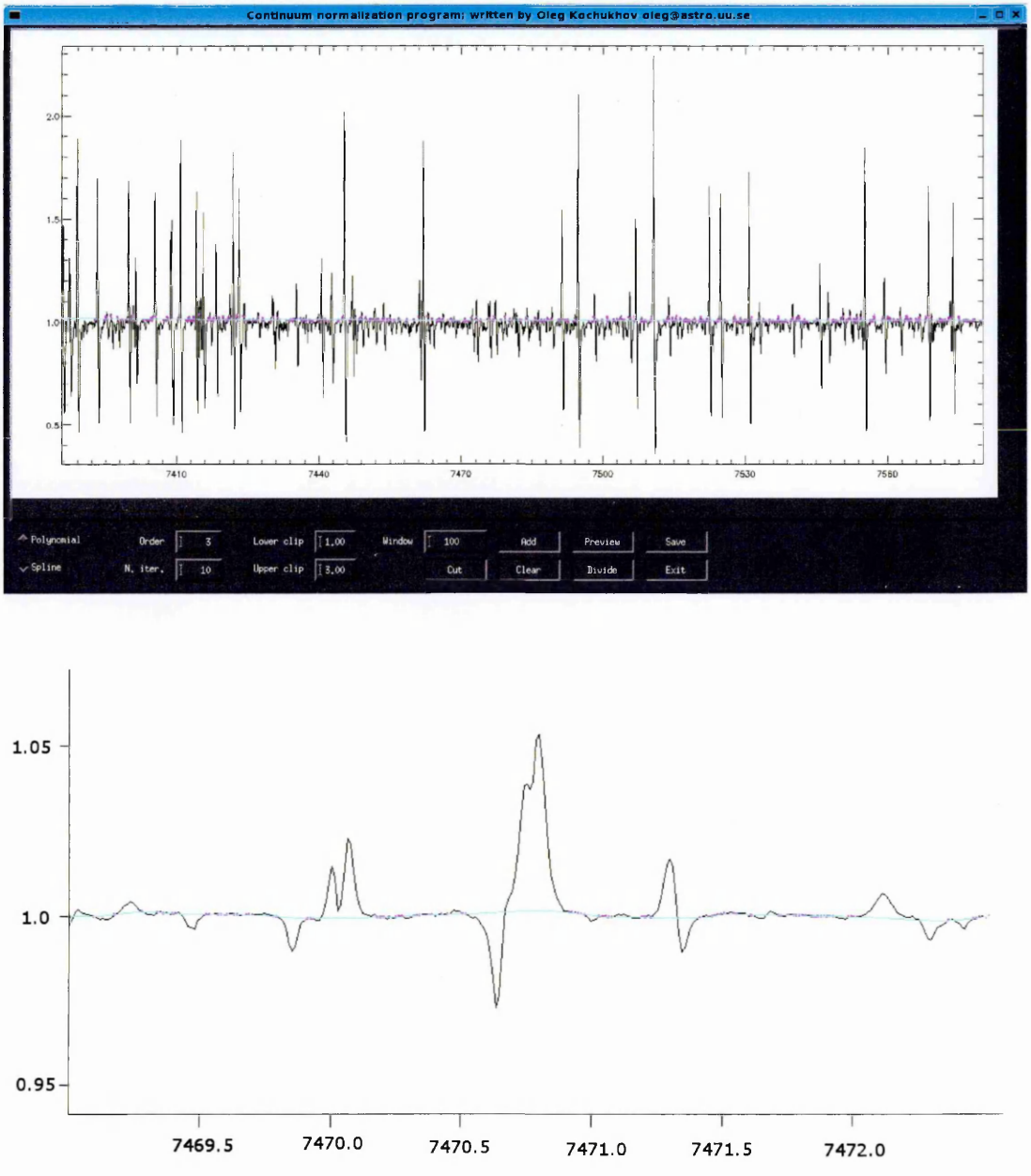

Figure 2.1: Layout of the normalisation tool showing the ratio of the wavelength shifted spectra (top panel) and zoomed in section of the normalisation tool (bottom panel). The blue line corresponds to the normalisation fitting line, the purple points correspond to the fitted spectral points and the black line is the spectrum. Colours have been inverted for clarity.

The continuum can be described using a polynomial or spline in this tool. The polynomial and spline continuum fitting make the following sequence of operations:

- fit through the spectrum of a smooth line (polynomial of a given degree or spline for a given smoothing parameter);
- compute the standard deviation of the fit;
- reject the points above and below the clipping threshold which moves the normalisation up or down.

In both cases, the number of iterations used can also be modified, varying the fit as seen in Figure 2.2. When the number of iterations is small (≈5) (Figure 2.2a) there are more fitted spectral points compared to when the number of iterations is large (≈20) (Figure 2.2b). The continuum fit will usually be in the form of a low order polynomial or a high smoothing parameter line.

The normalisation of the planet host star, 61 Vir was performed with the aid of a synthetic spectrum.

To normalise 61 Vir, the observed spectrum (R_o) is divided by the synthetic spectrum (R_s) to produce a ratio spectrum (R_r), as seen in Fig 2.1. The observed spectrum is then divided by the normalisation line of the ratio spectrum (N_R), shown in blue in Fig. 2.1 to produce the normalised spectrum ($\hat{R}$). The normalisation of the comparison stars is then performed using the normalised spectrum for 61 Vir and an identical technique. To emphasise the position of the spectral lines, a small velocity shift (1 km/s) was introduced between the normalised planet host star ($\hat{R}$) and the observed comparison star (C_o) so that the real spectral lines are enhanced and anything which is not present in both spectra remains at the noise level. This provides the benefit of more defined spectral lines and less enhancement of noise which could be mistaken for spectral lines. Normalising each spectrum using the same spectrum also ensures that the same features are present across the spectra. The equations describing the normalisation are expressed in Eq. 2.1. The adopted notation is my own as there is no standard notation.

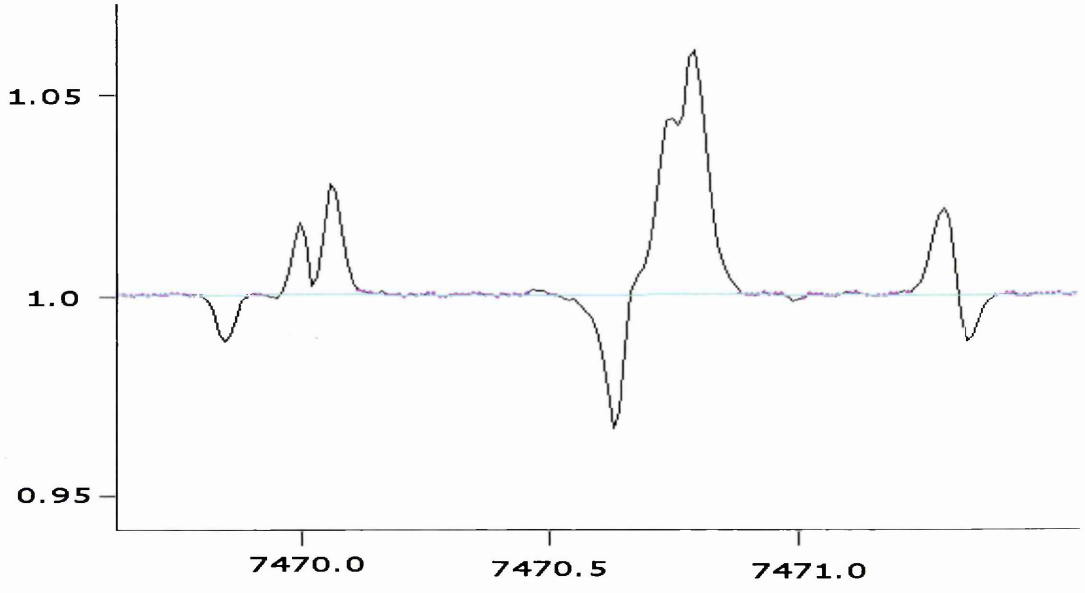

(a) 5 iterations

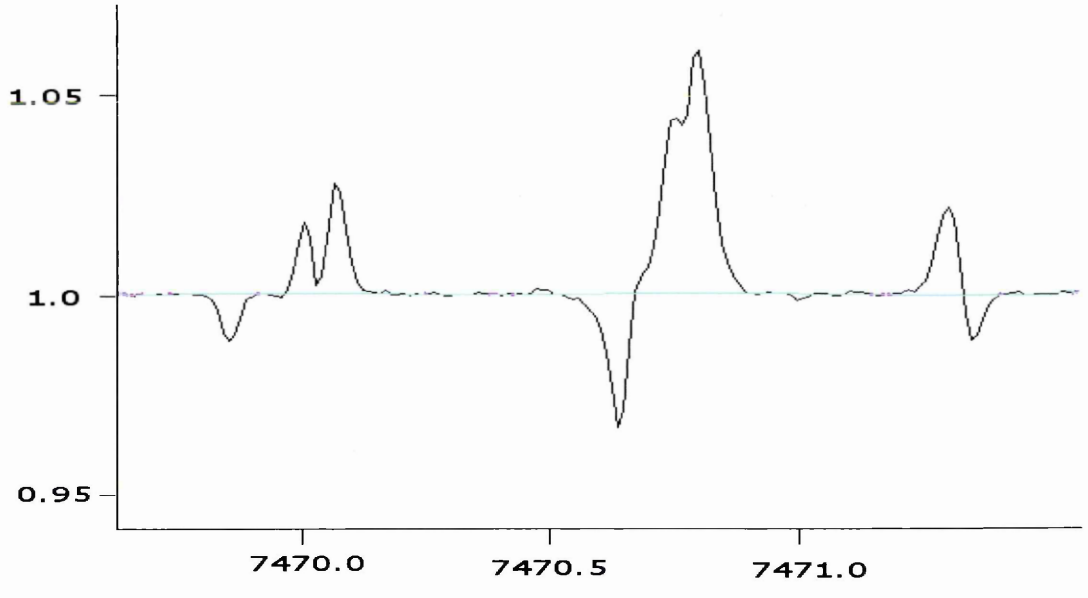

(b) 20 iterations

Figure 2.2: Examples of the difference in the number of spectral points fitted with number of iterations. The colours are as in Figure 2.1 with the purple points representing the number of fitted spectral points.

$$\begin{aligned} \frac{R_o}{R_s} &= R_r \\ \frac{R_o}{N_R} &= \hat{R} \\ \frac{C_o}{\hat{R}} &= C_r \\ \frac{C_o}{N_C} &= \hat{C} \end{aligned} \tag{2.1}$$

Normalisation is more effective in smaller sections and so the spectra were split into the individual echelle orders using a program in C. For stars with multiple spectra, these were interpolated and averaged using an IDL code so that the normalisation was performed in each order individually. The synthetic spectra used for the planet host star were made in these same echelle orders with 10 Å overlaps between each order. On completion of the normalisation, the orders were concatenated using an IDL code which, for regions where the spectra overlap, interpolates the flux onto the wavelength of the previously normalised order.

Chapter 3

Differential abundance analysis

In this Chapter I briefly describe the background for model atmospheres and spectral synthesis before discussing the method by which the spectral lines to be measured were selected. I then describe the adopted method of parameter and abundance determination for the differential abundance analysis.

3.1 Model atmospheres

Spectral lines are formed in the atmosphere of a star, defined by the boundary where photons decouple from matter, which is assumed to not have its own energy source. The mathematical models used to create model atmospheres have to contain information about the distribution as a function of depth of the main physical stellar quantities, such as pressure and temperature at geometric depth intervals in the atmosphere. These models must be self-consistent so that a unique solution is created for each set of parameters: effective temperature ($T_{\rm eff}$), surface gravity ($\log g$), microturbulence velocity ($\upsilon_{\rm mic}$), and metallicity. Further explanations of these parameters can be found in Section 3.5.1.

In most 1-D plane-parallel model atmospheres, the following assumptions are made:

- local thermodynamical equilibrium (LTE) - the thermal distribution of electrons and ions follows a Boltzmann distribution;

- energy conservation - $\nabla F_{rad} = 0$ where F_{rad} is the stellar flux;
- plane-parallel geometry - the atmosphere is composed of plane-parallel layers with $r_{atm} << R_{star}$;
- homogeneous abundances throughout the atmosphere;
- hydrostatic equilibrium - no large scale motions;
- time independent atmospheres - statistical equilibrium;
- energy is transported by radiation and convection only;
- free electrons obey a Maxwellian distribution.

The model atmospheres used in this work were MARCS model atmospheres [36]. The MARCS model atmospheres were chosen because they treat molecules as well as other opacity sources which are important for cool stars (spectral type K to M) like the ones being analysed in this work. The MARCS team[1] provide a grid of one-dimensional, hydrostatic, plane-parallel and spherical LTE model atmospheres for stars up to spectral type M. For the grid used in this thesis, the parameters range in $T_{\rm eff}$ from 2500 to 8000 K with steps of 100 K between 2500 and 4000 K and steps of 250 K between 4000 and 8000 K. In cgs units, $\log g$ ranges from -1.0 to +5.5 in steps of 0.5. The logarithmic metallicity relative to solar is between -5.0 and +1.0 in variable steps using the solar abundance from Grevesse et al. [33]. The model format used is the ".krz" format[2] which is more compact than some of the other formats available while still providing the information needed.

This thesis uses the solar [Fe/H] grid with abundances from Grevesse et al. [32]. However, for precise stellar parameter determination, particularly for a differential analysis, the parameter intervals available with the standard MARCS grid are not small enough. To overcome this I developed a code to linearly interpolate the parameters within the interval range (see Appendix D for more information. As such, given a

[1] http://marcs.astro.uu.se/

[2] http://marcs.astro.uu.se/krz_format.html

grid of 8 model atmospheres with every combination of minimum and maximum $T_{\rm eff}$, $\log g$ and metallicity, any model atmosphere with parameters between can be linearly interpolated.

3.2 Spectral synthesis

Solving the radiative transfer equation (RTE) is the basis of all spectral synthesis codes. The differential form of the RTE is presented as

$$I_\nu - S_\nu = \mu \frac{dI_\nu}{d\tau_\nu}, \tag{3.1}$$

where $\mu = \cos\theta$ and $S_\nu = \eta_\nu/\kappa_\nu$ is the source function. η_ν and κ_ν are the emission and absorption coefficients per volume element as a function of frequency ν while $\tau_\nu = -\kappa_\nu \rho\, ds$ denotes the optical depth. The dominant energy transport mechanism is radiation and as such, the modelling of a stellar atmosphere requires solving the RTE. Formally, the solution is

$$I_\nu(\mu) = e^{-\frac{\tau_\nu}{\mu}} \int_c^{\tau_\nu} \frac{S_\nu}{\mu} e^{-\frac{t}{\mu}}\, dt \tag{3.2}$$

where $I_\nu(\mu)$ is the intensity of the radiation emitted outwards from depth c, the lower limit of the integral. The RTE can only be solved when the form of the source function is known.

The continuum and spectral lines provide different contributions to the source function due to the different processes that produce them. It is therefore necessary to separate the source functions when understanding the characteristics of spectral lines. The source function contribution of the continuum can be represented as $\eta_{\nu,C}$ whilst the contribution from the spectral lines is $\eta_{\nu,L}$ where C and L represent the continuum and line respectively. Assuming that the components can be added together, it can be written that

$$\eta_\nu = \eta_{\nu,C} + \eta_{\nu,L} \tag{3.3}$$

and

$$\kappa_\nu = \kappa_{\nu,C} + \kappa_{\nu,L}. \tag{3.4}$$

When scattering is accounted for, the source function is assumed to take the form

$$S_\nu = \frac{\kappa_\nu B_\nu(T) + \sigma_\nu J_\nu}{\kappa_\nu + \sigma_\nu} \tag{3.5}$$

where $B_\nu(T)$ is a Planck function, σ_ν denotes the scattering and J_ν is the mean intensity. J_ν is the total energy emitted by unit of surface area summed over all directions

$$J_\nu = \frac{1}{4\pi}\int I_\nu d\omega. \tag{3.6}$$

Substituting the Planck function (B_ν) for the continuum source function, $\eta_{\nu,C}$, the total source function can now be written as

$$\begin{aligned} S_\nu &= \frac{\eta_{\nu,C} + \eta_{\nu,L}}{\kappa_{\nu,C} + \kappa_{\nu,L}} \\ &= \frac{\kappa_{\nu,C} B_\nu + \kappa_{\nu,L} S_{\nu,L}}{\kappa_{\nu,C} + \kappa_{\nu,L}} \\ &= \frac{\kappa_{\nu,C}}{\kappa_\nu} B_\nu + \frac{\kappa_{\nu,L}}{\kappa_\nu} S_{\nu,L} \end{aligned} \tag{3.7}$$

This can all be rewritten using Einstein coefficients. The Einstein A coefficient, A_{ji} is the probability per unit time of an electron decaying radiatively from an upper state j to a lower state i. To calculate the rate of spontaneous downward transitions per second, per volume, this is multiplied by the number density in the upper state giving $n_j A_{ji}$.

Similarly, there is an Einstein coefficient for absorption B_{ij} which is the probability per unit time of an atom absorbing a photon and radiatively exciting an electron from the lower state to the upper state. For this to occur, there must be a radiation field of intensity J_ν present which is evaluated at ν corresponding to the transition. The rate of upwards transitions is then $n_i B_{ij} J_\nu$ where n_i is the number density in the lower state.

There will also be stimulated downward transitions in the presence of a radiation field which must be accounted for and can be represented as $n_j B_{ji} J_\nu$.

The downward and upward transitions will balance so that

$$n_i B_{ij} J_\nu = n_j A_{ji} + n_j B_{ji} J_\nu \tag{3.8}$$

which, when rearranged to solve for the intensity becomes

$$J_\nu = \frac{A_{ji}/B_{ji}}{(n_i/n_j)(B_{ij}/B_{ji}) - 1}. \tag{3.9}$$

In thermal equilibrium, $J_\nu = B_\nu(T)$, meaning that the Einstein coefficients must be related in a way that Eq. 3.9 takes the form of a Planck spectrum.
Assuming a Boltzmann occupation of the upper and lower levels we have

$$\frac{n_i}{n_j} = \frac{g_i}{g_j} e^{h\nu/kT} \tag{3.10}$$

where $g_{i,j}$ is the statistical weight of energy level i, j. This gives

$$J_\nu = \frac{A_{ji}/B_{ji}}{(g_i B_{ij}/g_j B_{ji}) e^{h\nu/kT} - 1} \tag{3.11}$$

To ensure $J_\nu = B_\nu(T)$ for any T and ν

$$\frac{A_{ji}}{B_{ji}} = \frac{2h\nu^3}{c^2} \tag{3.12}$$

and

$$\frac{g_i B_{ij}}{g_j B_{ji}} = 1 \tag{3.13}$$

It can be seen from Eq. 3.12 and 3.13 that the three Einstein coefficients are not only related but are independent of T and therefore will not be affected out of thermal equilibrium.

Defining the line absorption profile, Φ_ν and the line emission profile, Ψ_ν which are

both normalised to 1 and using the Einstein coefficients, the source function describing the spectral lines can now be written as

$$S_\nu = \frac{\eta_\nu}{\kappa_\nu} = \frac{h\nu n_j A_{ji} \Psi_\nu}{h\nu(n_i B_{ij} - n_j B_{ji})\Phi_\nu} \tag{3.14}$$

It is possible to describe the absorption line profiles classically but the quantum mechanics of atomic transitions is necessary for a full understanding of the spectral lines. To account for the quantum mechanics, an oscillator strength f_{ij} was introduced which is different for each line and is defined as

$$f_{ij} = \frac{m_n h\nu}{\pi e^2} B_{ij}. \tag{3.15}$$

The transition probability, $\log gf$, of a line is then the logarithm of the statistical weight g multiplied by the oscillator strength f of the energy level.

In this work, synthetic spectra were calculated with SYNTH3 [41], a tool that calculates the synthetic spectra based on models at any effective temperature. Spectral line information from the Vienna Atomic Line Database (VALD)[3] [42] is listed in the input file for SYNTH3. The input file contains information on the central wavelength, atomic species, transition probability ($\log gf$), excitation energies and damping constants.

3.3 Line selection and measurement

The normalised spectra were visualised and measured using an IDL tool called BINMAG[4], the layout of which can be seen in Fig. 3.1 when a synthetic and observed spectrum are plotted. The code permits the display of up to six synthetic and six observed spectra simultaneously. Various parameters can be fitted automatically including projected rotational velocity ($\upsilon \sin i$) and radial velocity (υ_r). It provides two methods for the measurement of equivalent widths: direct integration and the fitting of a Gaussian

[3] http://www.astro.uu.se/~vald/php/vald.php
[4] http://www.astro.uu.se/ oleg/

line profile. Of these, direct integration is used preferentially in cases where the lines are unblended whereas line profile fitting is required to solve simple blends that would be otherwise unmeasurable.

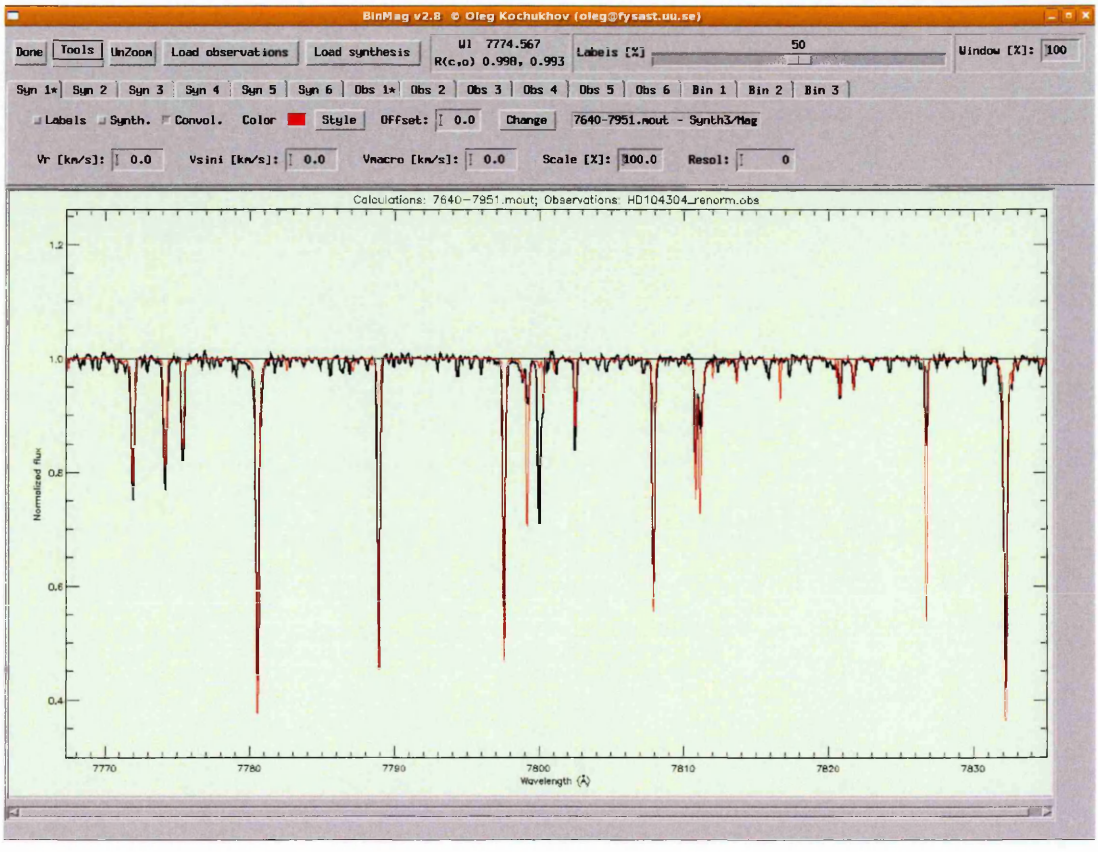

Figure 3.1: Layout of the BINMAG visualisation and fitting tool. The red line corresponds to the synthetic spectrum whilst the black line corresponds to the observed spectrum. There are cases where the synthetic and observed spectral lines do not match due to incorrect broadening parameters, $\log gf$ values or wavelengths, or missing spectral lines in the line list.

The spectra were inspected to select spectral lines which were unblended, close to continuum regions and were strong enough to be measurable. I defined a measurable line as one having an equivalent width W_λ greater than 2mÅ. This was the smallest line that could be seen and measured. A weaker line could be due to noise. The value of 2mÅ was derived using the spectrum SNR and the star's $\upsilon \sin i$. The error, or measurable line limit, is then derived by assuming a triangle with depth equal to $1/(2\times\text{SNR})$ and a width equal to $2\times\upsilon\sin i$.

Figure 3.2 shows the process by which I selected the lines to be measured. The

final adopted line list with equivalent widths for all the stars in this analysis can be found in Appendix B.

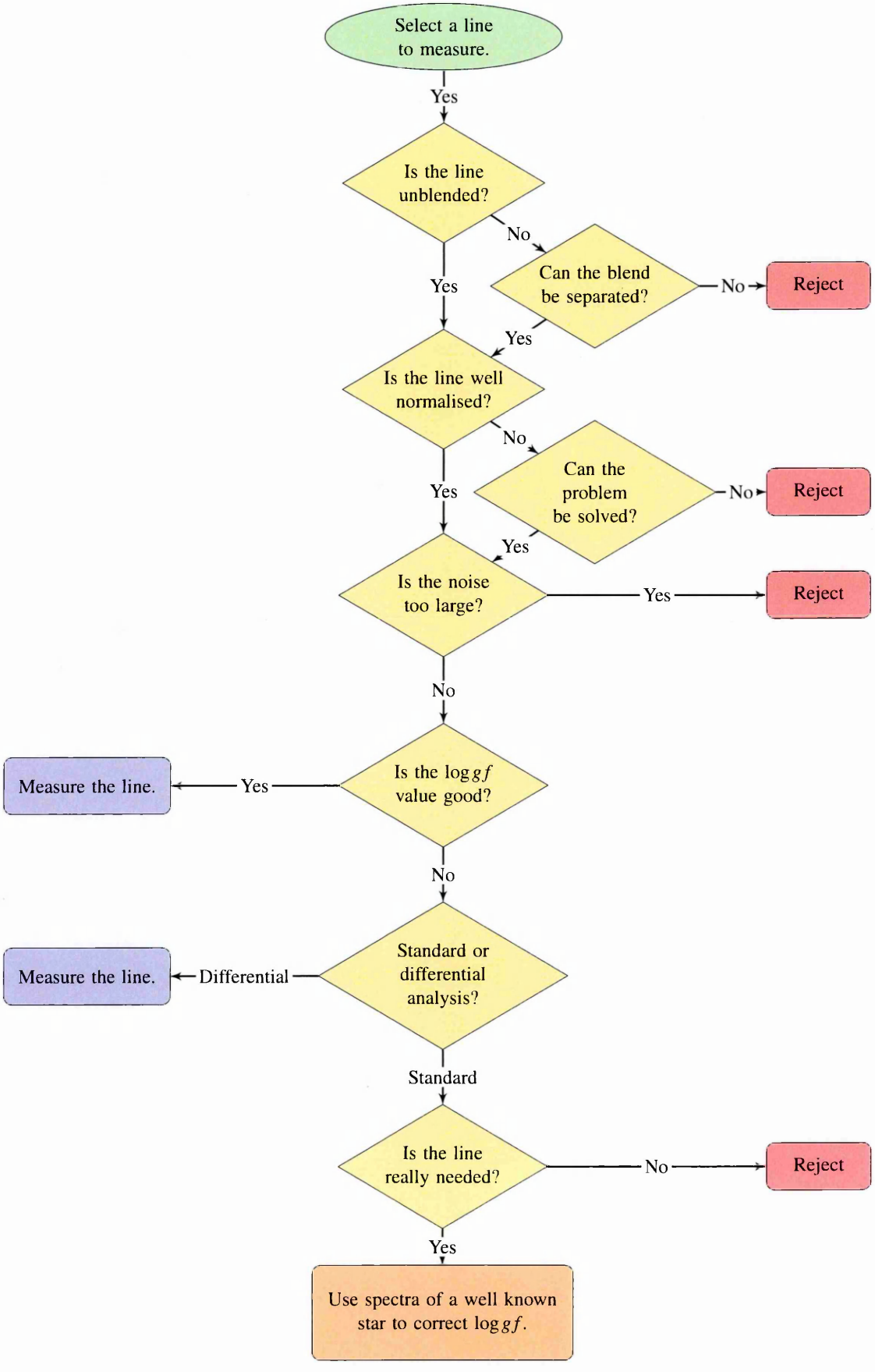

Figure 3.2: Line Selection Flowchart

The first thing to consider is whether the line might be blended. I needed to determine if the blend is due to the proximity of the central wavelengths of the absorption lines to each other or due to broadening effects. If the line is blended due to certain macroscopic broadening mechanisms i.e., resolution, projected rotational velocity ($\upsilon \sin i$) and macroturbulence velocity (υ_{macro}), and can be separated using a line profile fitting, then it can still be measured. This can be determined visually using the BINMAG visualisation tool. If not, then the line must be rejected.

The normalisation of the continuum is the next item to consider. If the line is well normalised then it can be measured but if you are unsure of the normalisation, there are two options that must be considered. The first option is to see if the line can be renormalised so that the line can be measured. If this is not possible then the line must be rejected. The second option is to decide if the line is of importance for example, a line of carbon, nitrogen or oxygen, and if it is, to measure it anyway, taking care to ensure the best normalisation region is being used.

Noise can be a problem in the measurement of the spectral lines, especially in lines found towards the blue end of the spectrum or near telluric regions. In the blue end of the spectrum, the signal is not as high and blending is more of a problem so it is harder to determine the continuum level around the spectral line. If the noise level is comparable to the depth of the spectral line, then it must be rejected.

The transition probability $\log gf$ of a spectral line provides information on the statistical weight of the energy level g and its associated oscillator strength f. This provides us with a transition probability for the line which is determined through empirical laboratory measurements and/or quantum-mechanical calculations. To determine if the $\log gf$ value is good we can compare two lines with the same line parameters, particularly excitation energy, against the synthetic spectrum. In most cases, if the line profile matches the synthetic spectrum for one line but there is little or no synthetic profile for the other observed line, then the $\log gf$ value is bad for the second line. If the value of $\log gf$ is good then the spectral line can be measured with no more problems. If the $\log gf$ value is bad, it may need to be corrected depending on the type of analysis.

In a differential abundance analysis, the same lines are measured in each star so the $\log gf$ value will be the same in each star. Any changes in the derived differential abundance will not occur because there is no difference in the $\log gf$ value. If a standard analysis is being performed, a bad $\log gf$ value will affect the derived abundance of that line so a decision must be made on how important the line is. If the line is one of hundreds of Fe I lines, then it can be rejected. If it is necessary to the analysis then it will need to be corrected.

For a large number of lines, the simplest way of determining if $\log gf$ value for any lines is bad is to plot the abundance against wavelength for each measured line of a particular ion and see if there are any lines with vastly different abundances to the average. These are then confirmed as having a bad $\log gf$ value, as determined by the method described previously, and corrected.

To correct the $\log gf$ values the equivalent width of the same line is measured in the solar spectrum. In this case, the solar spectrum was obtained from the NSO [44]. The abundance of the line is then derived using a model atmosphere with the solar parameters (as described in Section 3.6). The Grevesse et al. [32] solar abundances were adopted for this analysis because I used a 1-dimensional model in LTE as was done in Grevesse et al. [32]. This is to be consistent with using 1-dimensional models for the analysis. The Asplund et al. [5] solar abundances were obtained with a hybrid 3-dimensional NLTE model atmosphere and spectral synthesis, hence by using the Asplund et al. [5] abundances, a systematic uncertainty would be introduced via the $\log gf$ values. The solar abundance for the same ion is then subtracted from the measured abundance as

$$A_{measured} - A_{Grevesse} = \delta. \tag{3.16}$$

If there is a difference in abundance, δ, this is then added to the $\log gf$ value for the line being corrected as

$$\delta + \log gf_{initial} = \log gf_{corrected}. \tag{3.17}$$

Once corrected, both observed profiles should match both synthetic profiles.

Where possible, elements were only measured if multiple line profiles could be measured for the element but in some cases, single lines were measured. There were many refractory elements for which only a single line could be measured and, as the behaviour of refractory material is of significance, these elements were included. There was also only a single line measurable for nitrogen but the behaviour of carbon, nitrogen and oxygen together is also of importance so this was included.

3.3.1 Hyperfine structure lines

If a spectral line looks asymmetric, has a flat-bottom line profile, or appears to have extra broadening but there are no other lines near it, there could be a spectral line located there which has not yet been identified (i.e. not present in the line list) or it could be displaying hyperfine structure.

The presence of hyperfine structure is determined by the nuclear spin of an atom. If an atom has an integer nuclear spin, it will not present hyperfine structure. However, if an atom has a non-integer nuclear spin (e.g. 1/2, 3/2, 5/2 etc), it will present hyperfine structure. Each atom will present hyperfine structure to a different extent and in many cases it does not need to be considered. The elements which can be observed in the stars in this sample which are known to present hyperfine structure are Sodium, Aluminium, Scandium, Titanium, Vanadium, Chromium, Manganese, Cobalt, Nickel, Rubidium, Strontium, Yttrium, Niobium, Barium, and various rare earth elements.

Of the elements measured in this analysis, the lines of 11 elements are potentially subject to relevant hyperfine structure. All the measured lines for these elements - Vanadium, Manganese, Cobalt, Copper, Zinc, Rubidium, Niobium, Barium, Lanthanum, Samarium and Europium - were examined for evidence of hyperfine structure in the line profiles. Figure 3.3 depicts a selection of line profiles for varying elements showing evidence of hyperfine structure. Lines with hyperfine structure should not be a problem in a differential abundance analysis due to the lines behaving the same way

in the similar stars. However, if the abundance of the stars being compared differs significantly, the hyperfine structure becomes a significant problem, especially in saturated lines. The importance of hyperfine structure for a certain line of a certain element strongly depends on the abundance of the element. For example, if Vanadium was very abundant in one star but not so much in another star, the effect of the hyperfine structure would differ.

In total, 32 lines had to be removed from the line list due to strong evidence of hyperfine structure components. In principle, all lines of an element affected by hyperfine structure exhibit it but unless it was clearly observed in any of the stars, the element was kept. One line, Lanthanum 4804.04, seen in Figure 3.4, displays a distorted line profile for reasons potentially due to hyperfine structure or, more likely a blend, and as such was removed from the line list to ensure only the most accurately measurable lines were included.

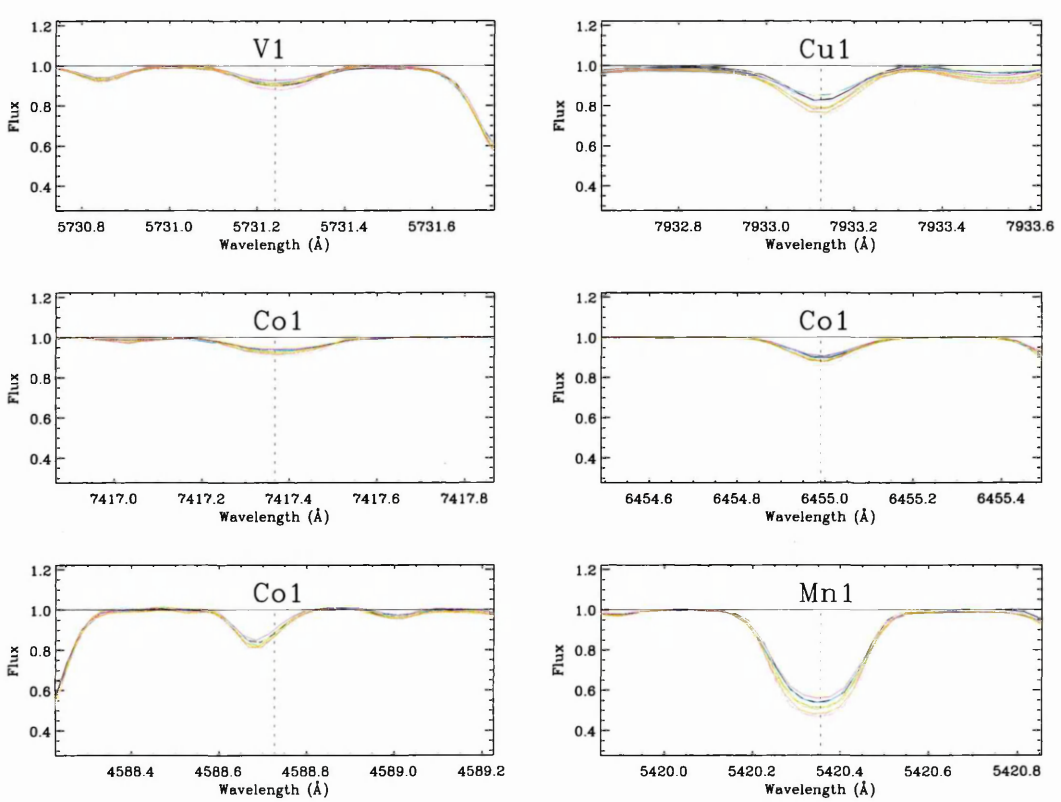

Figure 3.3: Examples of lines displaying unresolved hyperfine structure. The different lines visualised represent each of the stars in the sample.

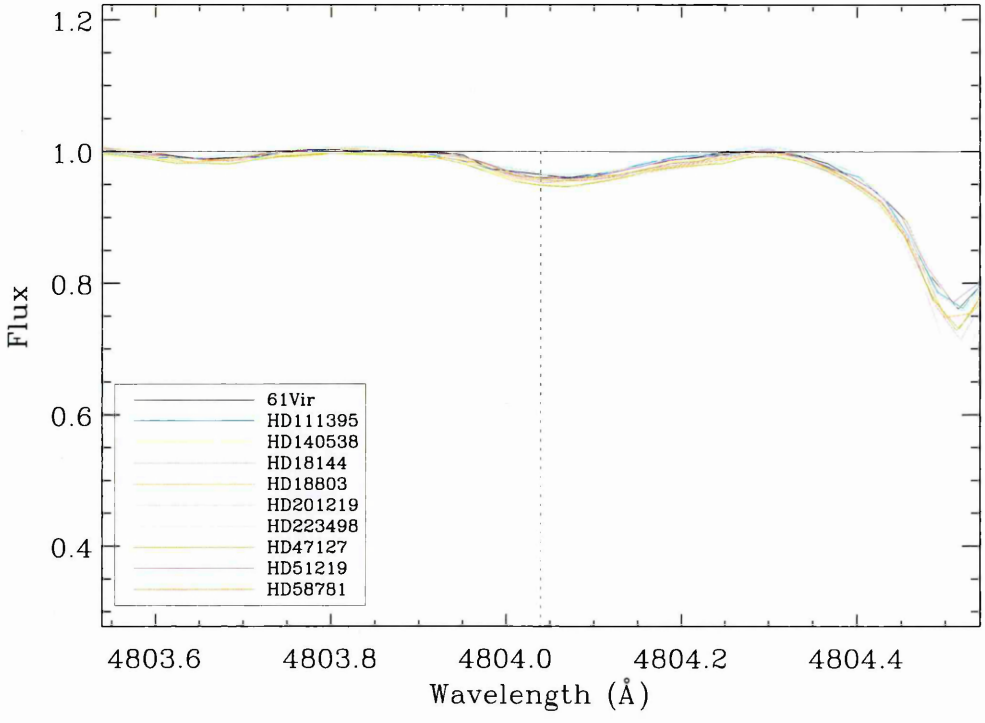

Figure 3.4: The La 4804.04 line for all stars. It can be clearly seen that the line is distorted which could either be due to an unknown blend or hyperfine structure.

3.3.2 Meléndez line list

To determine whether the signature observed in Meléndez et al. [49] was due to the line selection, the complete line list used in both Meléndez et al. [49] and Meléndez et al. [51], hereafter known as the Meléndez line list, was obtained. I attempted to measure all the lines used in this list but some of them could not be measured. The spectral range of the spectra under analysis differed slightly and some lines were excluded due to blends or lack of continuum. One example of this is the scandium 2 line at 6279.75 Å which cannot be resolved in all the stars due to additional lines within the same region that cannot be resolved, as seen in Figure 3.5. Where the excluded line is one of only two or three lines for the element, it is likely to have an impact on the results. For elements where many lines are measured, e.g. iron, the effect is likely to be negligible. Of the 350 lines in the Meléndez line list, 299 were measured as listed in Appendix C. All analysis done from this point is with both the line list selected by

me and the Meléndez line list.

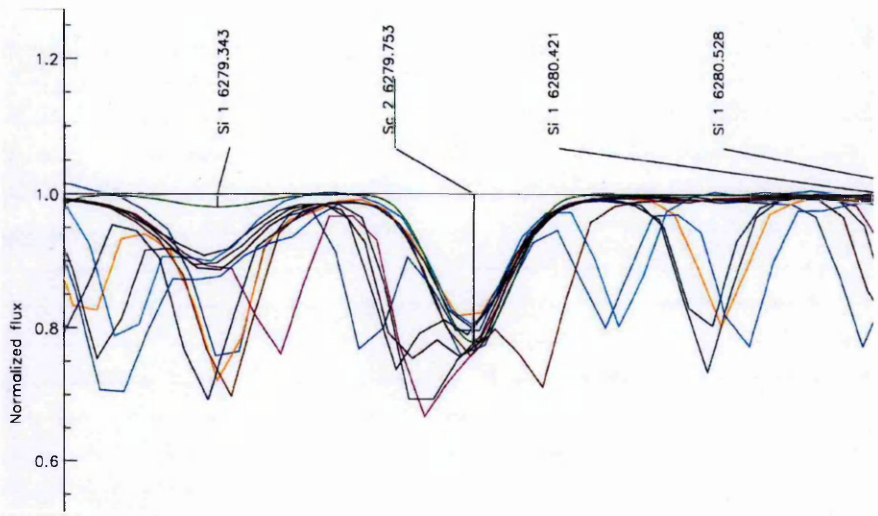

Figure 3.5: The region around Scandium 6279.75. This line was included in the Meléndez line list but could not be included in this work as the stars have other features in the same region.

3.4 Molecular lines

Molecular lines are produced by the emission or absorption from molecules which form in cool stars. All the stars in this analysis are considered cool stars and so the effect of molecular lines on the spectra has to be considered. Molecular lines can cause blends with other lines, leading to the abundance for the line being incorrect. The synthetic spectra used in this work does not include molecular lines.

To identify whether molecular lines were present in the stellar spectra I used the graphical software package SpectroWeb[45]. SpectroWeb contains digital spectra for a series of bright stars including the Sun, covering a wavelength region from 3300 Å to 6800 Å. It enables the identification of both atomic lines and molecular lines using a synthetic spectrum. Using the software, I eliminated any lines which were blended by molecules as it would not have been possible to separate the blend without further molecular information within the library used for identification. This resulted in the removal of no more than 20 lines.

3.5 Parameter determination

The most important step in an abundance analysis is deriving the fundamental parameters: $T_{\rm eff}$, $\log g$ and $\upsilon_{\rm mic}$. This must be done before the abundances can be determined as changes to the parameters during an analysis will change the abundances of each element. There are many methods of deriving stellar parameters utilising photometry, spectroscopy and spectrophotometry. In this thesis the stellar parameters were determined using the spectroscopic method of removing the dependence of the three equilibria - excitation, ionisation and "microturbulence". This is done by using a series of recursive steps starting from a set of initial parameters and arriving at a final set of atmospheric parameters which simultaneously fulfil the three equilibria and a stable metallicity.

At the core of these equilibria lies the Saha equation which gives the fraction of an element in ionisation state compared to neutral state for a gas in local thermodynamic equilibrium with low density.

The parameters and abundances were performed using the WIDTH9 code rather than the SYNTH3 code. This was due to the familiarity with WIDTH9 and due to its method of treating blends.

3.5.1 Absolute parameters

The absolute parameters (Table 3.1) for all of the stars were determined to provide zero-point stellar abundances for each line i, $A_i^\star$, for a given model atmosphere, where

$$A(X) = log\left(\frac{N_X}{N_{TOT}}\right) \tag{3.18}$$

N_X is the number density of element X and N_{TOT} is the total number density of all elements. This introduces a systematic uncertainty due to the unknown Helium abundance since

$$N_{TOT} \sim N_H + N_{He} \tag{3.19}$$

where N_H is the number of hydrogen particles per unit volume and N_{He} is the number of helium particles per unit volume. For hydrogen, this is well understood but there is a lot of uncertainty surrounding the amount of helium. It is often assumed that $N_{He}/N_{TOT} \sim 0.04$ [63] which is not a problem for a standard analysis but can become a problem for a differential analysis. The reason for this is that changes in the stellar abundances are more sensitive in a differential abundance so if N_{He} changes from star to star it might affect the analysis.

The effect of the systematic uncertainty has been considered greatly in this analysis. If one star had a different helium abundance to another star, a rigid shift in the abundances of all elements being compared with the other star would be observable and element-to-element trends would not be introduced.

Effective Temperature

The effective temperature of a star, $T_{\rm eff}$, is defined by the equation,

$$\int_0^\infty F_\nu d\nu = \sigma T_{\rm eff}^4 \tag{3.20}$$

where the integral shows the total power radiated by the star per unit area and σ is the Stefan-Boltzmann constant. This takes the form of a Stefan-Boltzmann equation which demonstrates that the effective temperature is the temperature of a black body with the same luminosity L and radius R as the star, as seen in Equation 3.21.

$$L = 4\pi R^2 \sigma T_{\rm eff}^4 \tag{3.21}$$

The location within the stellar photosphere of line formation is dependent on the excitation energy χ associated with the spectral line. Lines from low excitation energies will be formed higher in the photosphere where the pressure and temperature are lower whilst lines with high excitation energies are formed deeper in the photosphere, in regions of higher pressure and temperature. In the absence of vertical chemical inhomogeneities, all lines of the same ion, regardless of all other parameters, must have

the same derived abundance. The derived abundance is dependent on the excitation energy, which in turn is related to $T_{\rm eff}$. To obtain the same abundance, $T_{\rm eff}$ must be adjusted until the abundance is independent of the excitation energy. This is known as the excitation equilibrium.

In this work, the effective temperature of each star was determined by extracting the abundance and excitation potential of each Fe I line at different effective temperatures until there was no correlation between the two quantities (Figure 3.6). The uncertainty on the effective temperature was determined by modifying the temperature of the star until the mean of the slope for excitation potential against abundance ($\mu_{FeI-\chi}$) was equal to the standard deviation on the slope $\sigma_{FeI-\chi}$ (Equation 3.22). The difference between the temperature at which Equation 3.22 is satisfied and the effective temperature of the star provides the uncertainty (Equation 3.23).

$$\mu_{FeI-\chi} = \sigma_{FeI-\chi} \tag{3.22}$$

$$\sigma_{T_{\rm eff}} = T_{\rm eff} - T(\mu_{FeI-\chi} = \sigma_{FeI-\chi}) \tag{3.23}$$

Surface Gravity

The surface gravity, $g = GM/R^2$, is usually expressed as a logarithm $\log g$ because it has large variations. The Saha equation for ionisation states i and $i+1$ is written as

$$\frac{n_{i+1}}{n_i} P_e = 2\frac{U_{i+1}}{U_i}\frac{(2\pi m_e)^{3/2}}{h^3}(kT)^{5/2} e^{-\chi/kT} \tag{3.24}$$

where U_i and U_{i+1} are the partition functions and n_i and n_{i+1} are the number of atoms in their respective states. The ionisation energy χ is dependent on the electron pressure P_e and thus indirectly on $\log g$. The relationship between pressure and surface gravity can be expressed as $P \propto g^{1/3}$ for cool stars [30]. To obtain the same abundance for the element in both ionisation stages, the electron pressure and surface gravity must

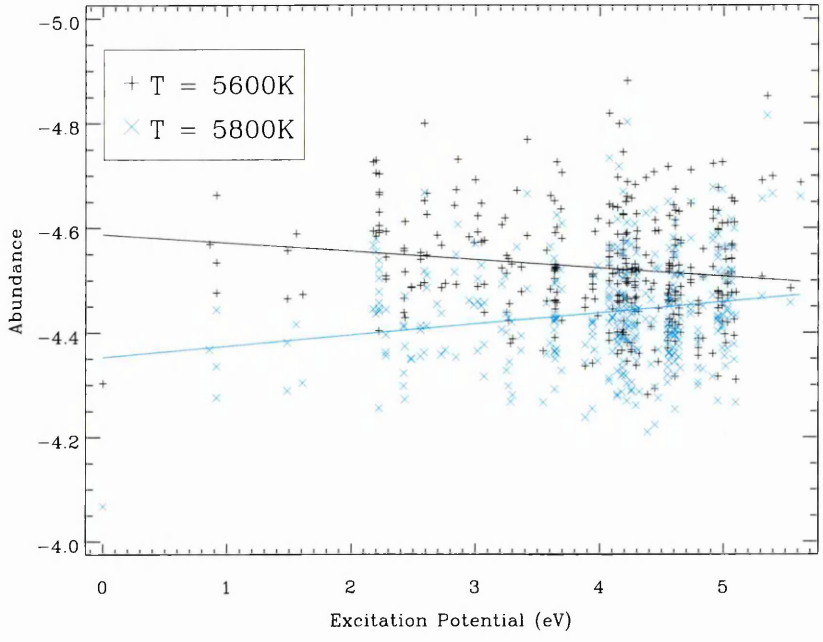

Figure 3.6: The Fe 1 abundances for each line were determined using two temperatures, 5600 K (black) and 5800 K (blue), for 61 Vir. As can be seen by the positive trend in the higher temperature and the negative trend in the lower temperature, the temperature at which there is no trend falls somewhere in the middle of these values. When there is no correlation between the abundance and excitation potential the approximate stellar effective temperature has been found for this star.

be independent. This is achieved by adjusting the value of $\log g$ until two stages of ionisation for the same element produce the same elemental abundance. This is known as the ionisation equilibrium.

In this work, the surface gravity of each star was determined by achieving independence between Fe I and Fe II. This is done by finding the surface gravity at which the average abundance of the Fe I lines is equal to the average abundance of the Fe II lines, illustrated in Figure 3.7. The uncertainty on the surface gravity, $\sigma_{\log g}$, is then calculated using the square root of the sum of squares (Equation 3.25) where σ_{FeI} and σ_{FeII} are the uncertainties on the average abundance of Fe I and Fe II respectively.

$$\sigma_{\log g} = \sqrt{\sigma_{FeI}{}^2 + \sigma_{FeII}{}^2} \tag{3.25}$$

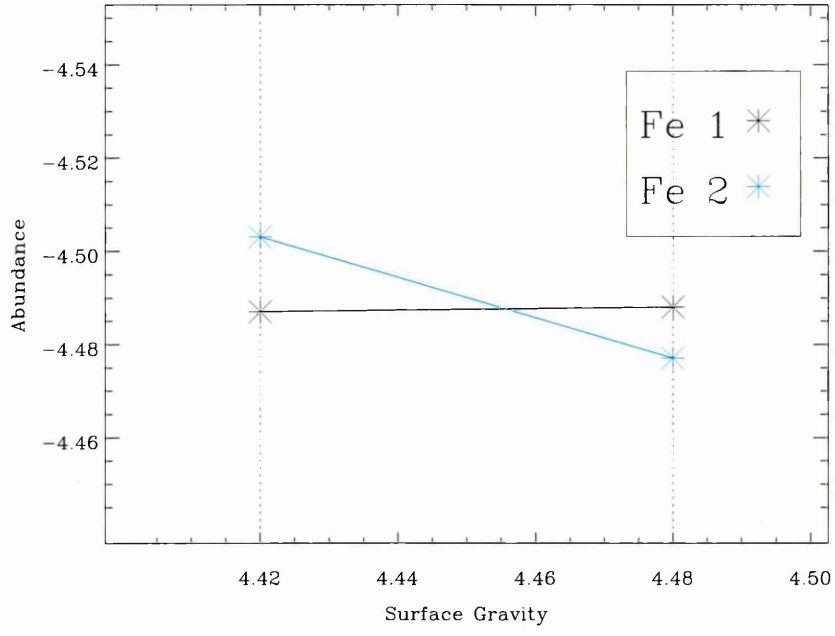

Figure 3.7: The average abundance at two surface gravities, 4.42 and 4.48 cms^{-2}, has been calculated for both Fe 1 (black) and Fe 2 (blue) to show illustrate the dependence on abundance. The point of intersection between the two lines is the point of independence between Fe 1 and Fe 2 and the approximate value of $\log g$ for this star.

Microturbulence velocity

The third equilibrium is used to derive microturbulence velocity, υ_{mic}, which is postulated as small-scale turbulent motions within the atmosphere [30]. In this sense, small scale refers to motions of the same size, or smaller, than the line forming region. Strong lines are mostly affected by microturbulence which causes them to exhibit greater equivalent widths than broadening predicts. This can be seen in Figure 3.8 where lines in the saturation region appear to have larger equivalent widths with stronger microturbulence than when there is little microturbulence. Although saturated lines change with microturbulence, it can be seen that weak lines are independent of microturbulence. Any correlation between the line abundance and equivalent width has to be eliminated to determine υ_{mic}.

To find the correct value of υ_{mic}, the abundance of Fe I (see Section 3.5.3 for explanation regarding Fe) is plotted against the equivalent width EW of the lines until the abundance is independent of the line strength. This was performed using a large num-

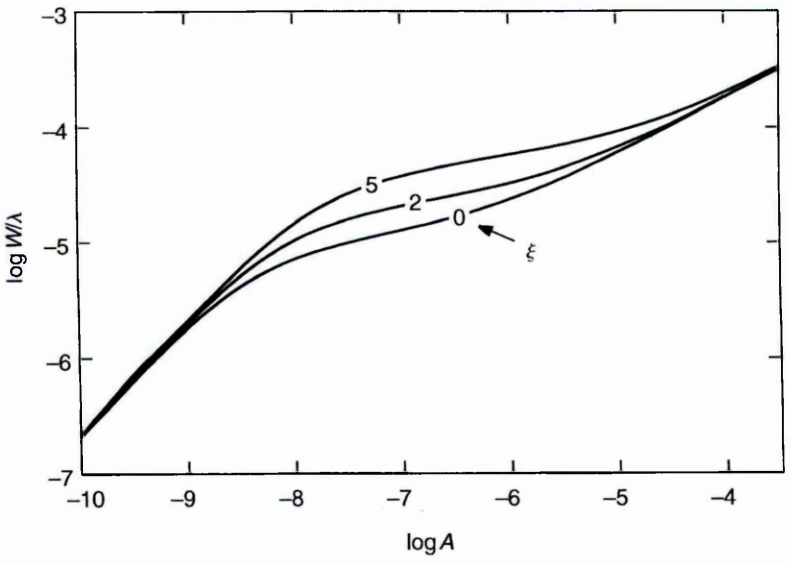

Figure 3.8: Abundance against equivalent width curve of growth showing the effect of different microturbulence velocities ξ for an assumed Gaussian distribution (in kms^{-1}) on saturation. Figure from Gray [30].

ber of both strong and weak lines so that the effect of microturbulence on the strong lines could be seen and then eliminated. This also allowed for a large baseline (3 – 170 mÅ) through which the correlation and independence could be determined.

The uncertainty on the microturbulence velocity was determined by modifying the microturbulence velocity of the star until the mean of the slope for equivalent width against abundance (μ_{FeI-EW}) was equal to the standard deviation on the slope σ_{FeI-EW} (Equation 3.26). The difference between the microturbulence velocity at which Equation 3.26 is satisfied and the microturbulence velocity of the star provides the uncertainty (Equation 3.27).

$$\mu_{FeI-\chi} = \sigma_{FeI-\chi} \tag{3.26}$$

$$\sigma_{\upsilon_{\mathrm{mic}}} = \upsilon_{\mathrm{mic}} - \upsilon_{\mathrm{mic}}(\mu_{FeI-\chi} = \sigma_{FeI-\chi}) \tag{3.27}$$

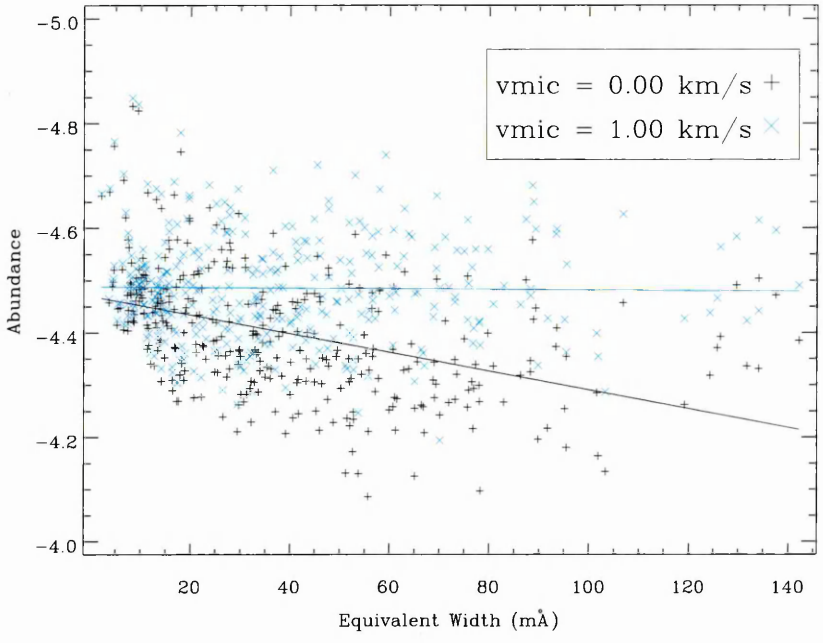

Figure 3.9: The Fe 1 abundances for each line were determined using two equivalent widths, $0.00 kms^{-1}$ (black) and $1.00 kms^{-1}$ (blue), for 61 Vir. A clear trend can be seen in the lower velocity whereas the higher velocity almost has no correlation, indicating that the microturbulence velocity of the star is close to the higher value. When there is no correlation between the abundance and equivalent width the approximate stellar microturbulence velocity has been found for this star.

Metallicity

The stellar metallicity also needs to be calculated when using the MARCS models. This is calculated by finding the difference between the iron abundance in the Sun, given by Grevesse et al. [32] as -4.54 dex, and each star. The iron abundance used for each star is calculated using Fe I and Fe II together, calculating the abundance as though all the Fe lines belonged to the same ion. This can be done because the ionisation equilibrium is being imposed, requiring Fe I and Fe II have the same abundance.

Table 3.1: Table showing the absolute parameters - $T_{\rm eff}$ (K), $\upsilon_{\rm mic}$ (kms^{-1}), log$g$ (ms^{-2}), [Fe/H](dex) - with errors in brackets for the sample of stars using my line list and the Meléndez line list.

		My line selection	Meléndez line selection
61 Vir	$T_{\rm eff}$	5684 (35)	5708 (46)
	$\upsilon_{\rm mic}$	1.02 (0.06)	0.87 (0.13)
	log$g$	4.45 (0.138)	4.55 (0.135)
	[Fe/H]	0.053 (0.159)	0.076 (0.234)
Sun	$T_{\rm eff}$	5908 (50)	5914 (52)
	$\upsilon_{\rm mic}$	1.06 (0.07)	0.97 (0.09)
	log$g$	4.58 (0.139)	4.59 (0.150)
	[Fe/H]	0.048 (0.160)	0.040 (0.320)
HD 111395	$T_{\rm eff}$	5764 (42)	5776 (46)
	$\upsilon_{\rm mic}$	1.13 (0.06)	0.89 (0.14)
	log$g$	4.56 (0.134)	4.68 (0.120)
	[Fe/H]	0.137 (0.165)	0.162 (0.237)
HD 140538	$T_{\rm eff}$	5794 (34)	5816 (46)
	$\upsilon_{\rm mic}$	1.07 (0.07)	0.92 (0.13)
	log$g$	4.52 (0.137)	4.67 (0.124)
	[Fe/H]	0.095 (0.173)	0.108 (0.257)
HD 18144	$T_{\rm eff}$	5672 (43)	5678 (46)
	$\upsilon_{\rm mic}$	1.05 (0.07)	0.75 (0.16)
	log$g$	4.58 (0.146)	4.62 (0.141)
	[Fe/H]	0.144 (0.151)	0.182 (0.209)
HD 18803	$T_{\rm eff}$	5772 (36)	5792 (48)
	$\upsilon_{\rm mic}$	1.07 (0.06)	0.88 (0.14)
	log$g$	4.52 (0.140)	4.62 (0.130)
	[Fe/H]	0.146 (0.168)	0.168 (0.250)
HD 201219	$T_{\rm eff}$	5758 (46)	5786 (50)
	$\upsilon_{\rm mic}$	1.11 (0.07)	1.02 (0.12)
	log$g$	4.58 (0.142)	4.64 (0.142)
	[Fe/H]	0.160 (0.163)	0.131 (0.250)
HD 223498	$T_{\rm eff}$	5670 (43)	5676 (46)
	$\upsilon_{\rm mic}$	1.04 (0.06)	0.79 (0.16)
	log$g$	4.44 (0.146)	4.47 (0.127)
	[Fe/H]	0.225 (0.154)	0.269 (0.217)
HD 47127	$T_{\rm eff}$	5724 (37)	5742 (44)
	$\upsilon_{\rm mic}$	1.08 (0.06)	0.85 (0.12)
	log$g$	4.37 (0.139)	4.45 (0.130)
	[Fe/H]	0.147 (0.170)	0.187 (0.247)
HD 51219	$T_{\rm eff}$	5728 (39)	5758 (44)
	$\upsilon_{\rm mic}$	1.07 (0.06)	0.90 (0.12)
	log$g$	4.41 (0.138)	4.49 (0.131)
	[Fe/H]	0.047 (0.172)	0.072 (0.257)
HD 58781	$T_{\rm eff}$	5726 (39)	5740 (46)
	$\upsilon_{\rm mic}$	1.07 (0.06)	0.83 (0.14)
	log$g$	4.44 (0.144)	4.50 (0.144)
	[Fe/H]	0.150 (0.165)	0.190 (0.242)

3.5.2 Differential parameters

An initial set of parameters for the stellar sample (seen in Table 3.1) was determined as a baseline for the differential parameters which can be seen in Table 3.2. The relative spectroscopic equilibrium was achieved using differential abundances δA_i for each line

i,

$$\delta A_i = A_i^{refstar} - A_i^{\star}. \tag{3.28}$$

The effective temperature is found by imposing the relative excitation equilibrium χ_{exc} of δA_i for Fe I lines:

$$d(\delta A_i^{FeI})/d(\chi_{exc}) = 0, \tag{3.29}$$

while the surface gravity ($\log g$) is obtained using the relative ionisation equilibrium of Fe I and Fe II:

$$\Delta^{FeII-FeI} \equiv \langle \delta A_i^{FeII} \rangle - \langle \delta A_i^{FeI} \rangle. \tag{3.30}$$

The microturbulence velocity $\upsilon_{\rm mic}$was obtained when the differential abundances δA_i^{FeI} showed no dependence with the equivalent width EW:

$$d(\delta A_i^{FeI})/d(EW) = 0. \tag{3.31}$$

The spectroscopic solution is found when the three conditions (Eqs. 3.29-3.31) are satisfied simultaneously, and when the metallicity obtained from the iron lines is the same as that of the input model atmosphere, calculated in the same way as in Section 3.5.1.

Table 3.2: Table showing the differential parameters - $T_{\rm eff}$ (K), $\upsilon_{\rm mic}$ (kms^{-1}), log$g$ (ms^{-2}), [Fe/H](dex) - with errors in brackets for the sample of stars using my line list and the Meléndez line list when compared against 61 Vir.

		My line selection	Meléndez line selection
HD 111395	$T_{\rm eff}$	5760 (4)	5779 (3)
	$\upsilon_{\rm mic}$	1.15 (0.05)	0.90 (0.13)
	log$g$	4.54 (0.048)	4.69 (0.060)
	[Fe/H]	0.134 (0.084)	0.162 (0.112)
HD 140538	$T_{\rm eff}$	5795 (4)	5819 (1)
	$\upsilon_{\rm mic}$	1.06 (0.06)	0.93 (0.06)
	log$g$	4.53 (0.050)	4.69 (0.058)
	[Fe/H]	0.096 (0.088)	0.108 (0.121)
HD 18144	$T_{\rm eff}$	5674 (15)	5676 (3)
	$\upsilon_{\rm mic}$	1.05 (0.01)	0.76 (0.23)
	log$g$	4.58 (0.056)	4.62 (0.058)
	[Fe/H]	0.144 (0.091)	0.181 (0.122)
HD 18803	$T_{\rm eff}$	5773 (1)	5792 (3)
	$\upsilon_{\rm mic}$	1.07 (0.04)	0.89 (0.16)
	log$g$	4.52 (0.049)	4.63 (0.060)
	[Fe/H]	0.146 (0.088)	0.168 (0.115)
HD 201219	$T_{\rm eff}$	5751 (9)	5782 (1)
	$\upsilon_{\rm mic}$	1.14 (0.07)	1.01 (0.12)
	log$g$	4.55 (0.051)	4.63 (0.073)
	[Fe/H]	0.154 (0.088)	0.132 (0.131)
HD 223498	$T_{\rm eff}$	5665 (1)	5676 (1)
	$\upsilon_{\rm mic}$	1.05 (0.06)	0.79 (0.24)
	log$g$	4.42 (0.045)	4.47 (0.053)
	[Fe/H]	0.222 (0.089)	0.269 (0.119)
HD 47127	$T_{\rm eff}$	5723 (1)	5743 (3)
	$\upsilon_{\rm mic}$	1.08 (0.06)	0.86 (0.22)
	log$g$	4.36 (0.058)	4.45 (0.063)
	[Fe/H]	0.146 (0.093)	0.185 (0.119)
HD 51219	$T_{\rm eff}$	5728 (4)	5757 (3)
	$\upsilon_{\rm mic}$	1.07 (0.07)	0.91 (0.21)
	log$g$	4.41 (0.042)	4.50 (0.059)
	[Fe/H]	0.047 (0.089)	0.070 (0.124)
HD 58781	$T_{\rm eff}$	5726 (4)	5738 (3)
	$\upsilon_{\rm mic}$	1.07 (0.06)	0.83 (0.24)
	log$g$	4.44 (0.061)	4.50 (0.063)
	[Fe/H]	0.150 (0.090)	0.190 (0.116)

The differential parameters were determined relative to 61 Vir, for which the abundances were determined using the absolute parameters calculated as in Section 3.5.1. A series of four semi-automated codes were developed for the other stars (see Appendix E for explanation of the codes).

3.5.3 Remarks on the method

The derived temperature value is almost always dependent on the choice of element and ion. Fe I and Ti I for example, will probably give two different values for the temperature. This difference in temperature could be as little as 20 K but also as much

as 300 K [23].

As the derived $T_{\rm eff}$ depends on the choice of ions, there are different ways of proceeding with the determination. The method of choosing one element to be analysed for all stars, is the one implemented in this study. The only elements that can be used in this temperature regime are iron and titanium as they are the ones with the most lines in the neutral and singly ionised states. It is logical to use Fe I and Fe II as they have the greatest number of lines in these stars. Alternatively, the temperature can be derived for lots of elements and then averaged to give a final temperature. When line profile fitting is used rather than direct integration, large values of macroturbulence velocity ($\upsilon_{\rm macro}$) might lead to the temperature derived from Fe I being generally higher than when measuring using a combination of all the other elements [23].

In this work, there is a difference between the temperature derivations for the different line lists. When the uncertainties are accounted for, this difference is of the order 20 K. The difference in the number of iron lines in the two analyses (more than twice the number of Fe I lines were included in my line list than the Meléndez line list) is likely to be the cause of this difference.

3.6 Abundance determination

As previously mentioned, equivalent widths were used to measure abundances because they don't require lots of computational time and are independent of $\upsilon \sin i$, $\upsilon_{\rm macro}$ and resolution. The abundance is determined from the equivalent width using the "curve of growth" as described in Section 1.2.3.

The output equivalent width file, an example of which is given in Appendix B, includes information on the ion measured, the excitation energy of the spectral line and $\log gf$, as well as the equivalent width. This contains the information required for the modified version [76] of the WIDTH9 code [43] to derive the abundances of each line.

The absolute abundances for 61 Vir were calculated using the model atmosphere

derived from the absolute parameters determined. The abundances of the comparison stars were calculated using the model atmospheres created using their differential parameters. As the stars are very similar and therefore exhibit the same spectral lines, the only synthetic spectrum created was for 61 Vir, which was used for calculating the abundances. The WIDTH9 code derives both the abundance for each line and the average abundance for each ion.

The differential abundances were calculated in two ways, both of which used a line-by line basis as the same lines were measured in all stars. The first method required the calculation of the average of all the comparison star abundances

$$\langle A_i \rangle = \frac{\sum_{j=1}^{n} A_i^j}{n} \tag{3.32}$$

where n denotes the number of comparison stars and as before, A_i is the abundance for a single line. This average abundance was then subtracted from the abundance of the same line in 61 Vir. Once this was performed for each line of the ion, the average for that ion was calculated to present the differential abundance of 61 Vir relative to the average of the comparison stars

$$\delta A_e = \frac{\sum_{i=1}^{n_e} (A_i^{61\,Vir} - \langle A_i \rangle)}{n_e} \tag{3.33}$$

where n_e denotes the number of lines of ion e and δA_e denotes the differential abundance of the ion.

The second method, adopted in the later stages of this analysis, required the calculation of the differential abundance for each star relative to 61 Vir. This is done using a similar method as previously described but instead of averaging all the stars, the abundance of each line in the comparison star is subtracted from the abundance of each line in 61 Vir. This is once again averaged for each ion to present the differential abundances and then repeated for each of the stars. This can alternately be done with the abundance of each line in 61 Vir being subtracted from the abundance of each line in the comparison stars.

To be consistent with the Meléndez et al. [49] analysis, the abundances had to then be normalised to iron. This is done to ensure any systematic differences in stellar metallicities are removed. For each ion, the differential abundance of Fe I, δA_{FeI}, was subtracted as

$$\delta A_{\hat{e}} = \delta A_e - \delta A_{FeI} \tag{3.34}$$

where $\delta A_{\hat{e}}$ denotes the differential abundance relative to Fe I of the ion.

An attempt to recreate the Meléndez et al. [49] results was not attempted due to the data not being readily available for the sample used in that analysis.

3.6.1 Uncertainties

The uncertainties on the differential abundances for ions with multiple lines were calculated using the standard deviation of the differential abundances for each ion. In the cases where there was a single line measured for the ion, the uncertainties had to be determined through an alternative method. This was done by plotting the standard deviation of each ion with multiple lines against the number of lines measured (Figure 3.10) and visually determining the convergent standard deviation [22]. The convergent plots for the Meléndez line list can be seen in Figure 3.11.

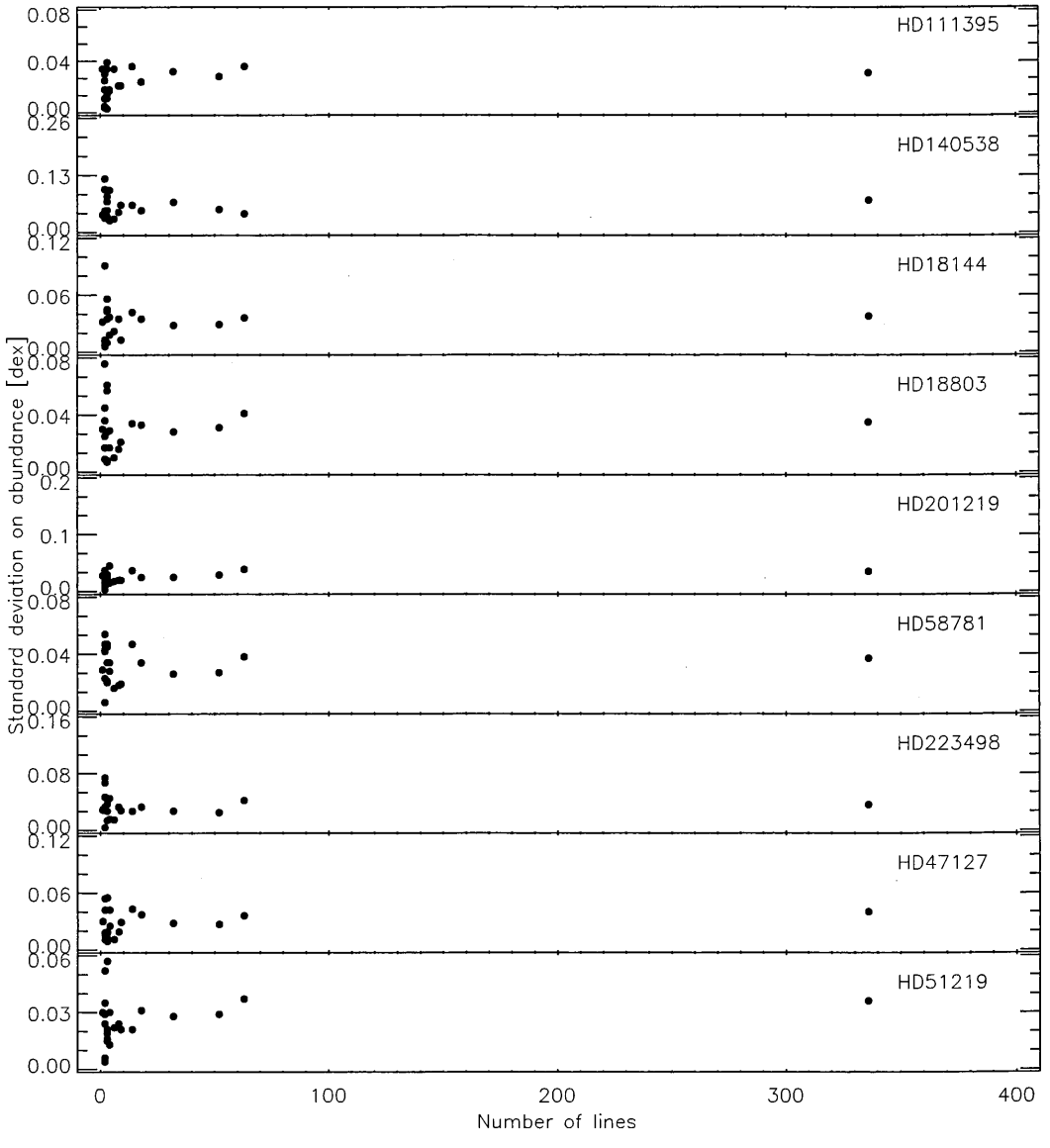

Figure 3.10: The standard deviation of the abundance for each element for which more than 1 line was measured as a function of number of lines. The abundances were obtained using my line list.

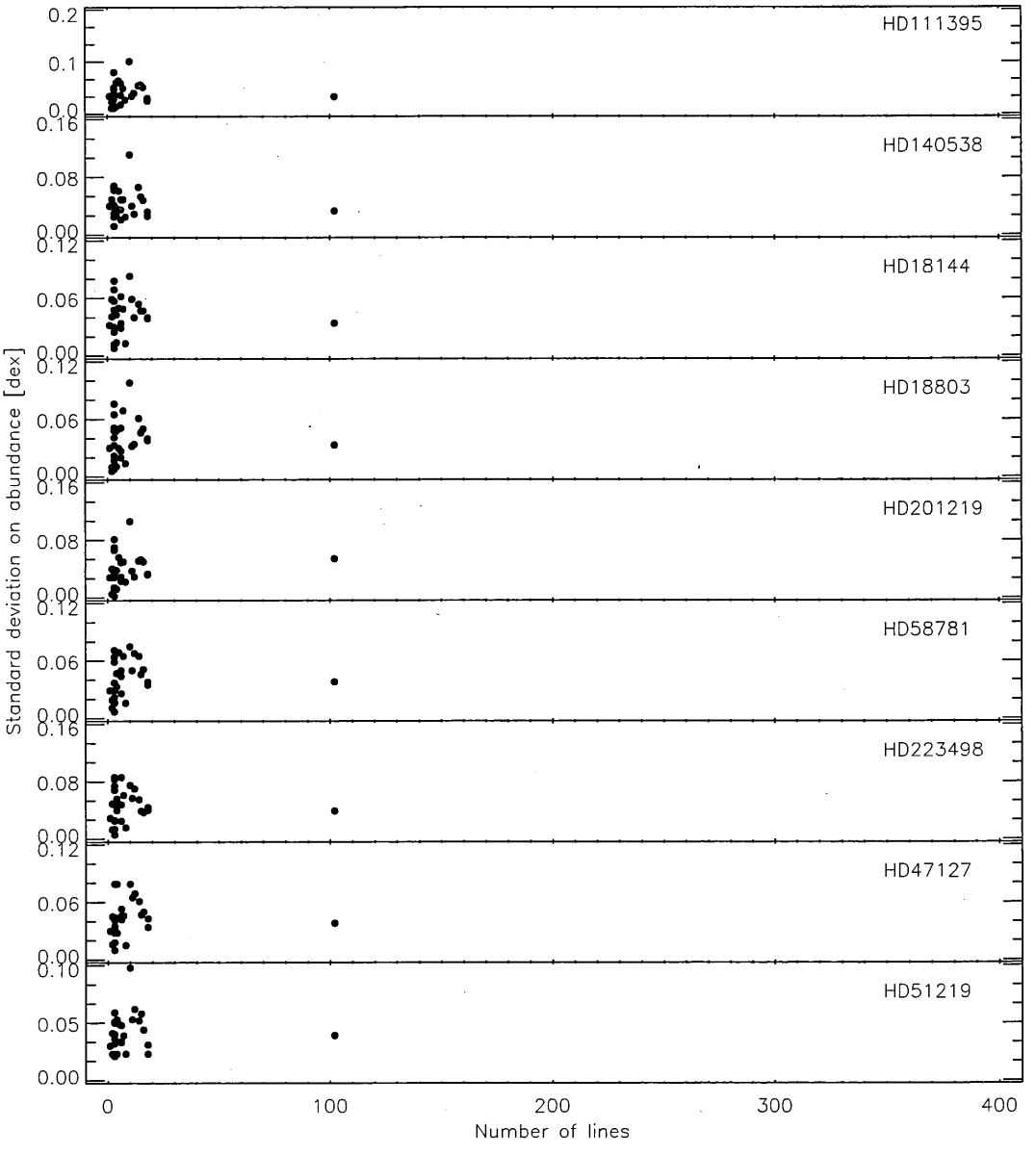

Figure 3.11: The standard deviation of the abundance for each element for which more than 1 line was measured as a function of number of lines. The abundances were obtained using the Meléndez line list.

Chapter 4

Attempting the detection of a planetary signature in the chemical composition of 61 Virginis

In this Chapter I aim to describe the results obtained when performing a differential abundance analysis of 61 Vir against a series of comparison stars. I have performed this analysis with two line lists: the lines I selected and the line list used by Meléndez et al. [51] to show how the line list affects the abundance pattern. The first half of this Chapter describes the analysis and results obtained using my line list whilst the second half of the Chapter focuses on the analysis using the line list used by Meléndez et al. [51]. The analysis using both line lists enables clarification of whether results observed are due to the line list or due to the stars in the sample.

4.1 Signatures

The fundamental parameters and abundances for all stars in the sample were obtained as outlined in Chapter 3.

4.1.1 Comparison to the average of the sample

A differential abundance analysis was performed, comparing 61 Vir with the average of the comparison stars. The differential abundance of each element was then normalised to iron and, as in Meléndez et al. [49], plotted against condensation temperature (see Section 1.4 for explanation of condensation temperature).

My results, depicted in Fig. 4.1 reveal that the 61 Vir abundances relative to Fe depart from the mean abundance ratios in the comparison stars. In Meléndez et al. [49], the solar abundances departed from the mean abundance ratios of the twins but they showed a clear signature comprising of two linear trends. There is no such clearly observable signature in my results. The volatile elements, except rubidium, are either enhanced or of a similar abundance in 61 Vir but the refractory elements vary significantly compared to the comparison stars.

The scale of the abundance differences is larger in my results than in Meléndez et al. [49]. For example, the element which is most differently abundant in both my sample and Meléndez et al. [49] is Nitrogen which is enhanced by 0.06 $\pm$ 0.017 dex (3σ) in Meléndez et al. [49] and 0.17 $\pm$ 0.030 dex (6σ) in my analysis. The element which is the least abundant differs because my analysis includes more elements with higher $T_{\rm cond}$ which tend to be more depleted, a signature traditionally associated with planets. The most depleted element in Meléndez et al. [49] is Aluminium which is depleted by -0.04 $\pm$ 0.012 dex (3σ) whilst the most depleted in my analysis is Europium by -0.25 $\pm$ 0.030 (8σ) dex. The difference between the most depleted and most enhanced element in Meléndez et al. [49] is 0.1 $\pm$ 0.021 dex whilst it is 0.42 $\pm$ 0.042 dex in my analysis.

There is a potential negative linear slope between the abundance and $T_{\rm cond}$ of the elements. To check the significance of the results, I used the IDL LINFIT routine to first generate a linear fit with the uncertainties. This was done for two separate samples: the first with all elements included, and the second with elements for which only one line had been measured excluded. These elements were excluded as they are

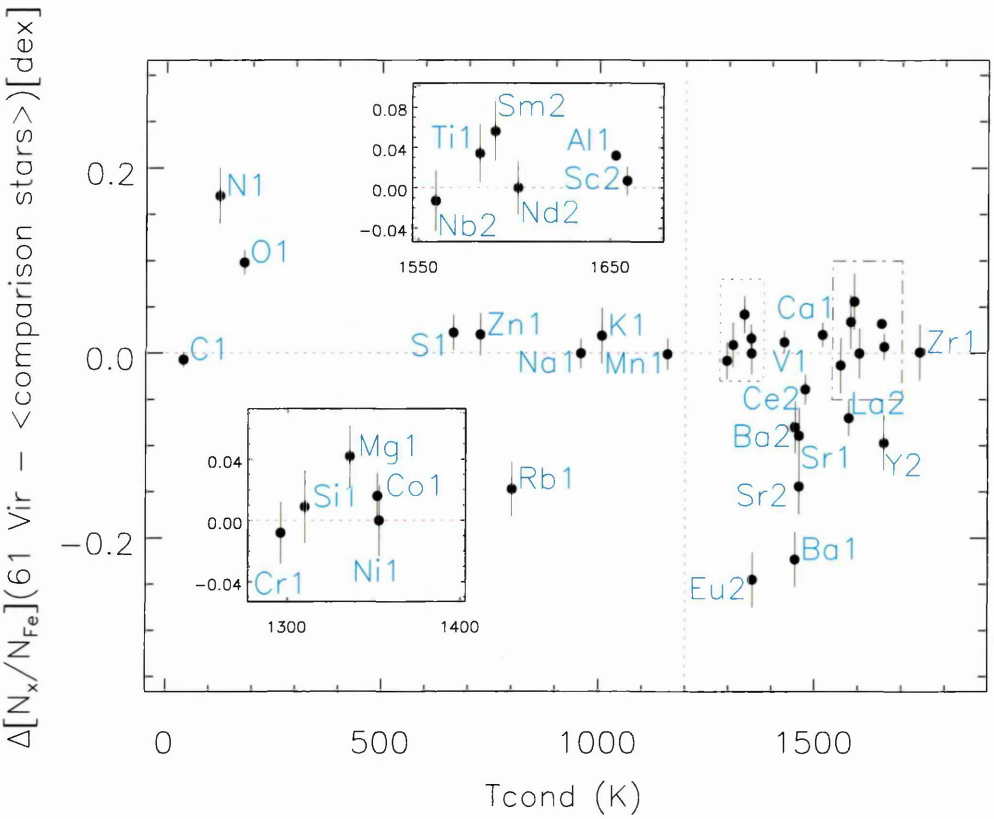

Figure 4.1: Differential abundance ratios of 61 Vir relative to the average of the comparison stars vs. dust condensation temperature. The figure displays two inset panels covering the two sections marked in dashed lines for clarity. Plotted abundances are relative to Fe. The red dotted line at 1200 K represents the break assumed between volatile and refractory elements in Meléndez et al. [49].

primarily the elements with the higher condensation temperatures and I wanted to see if they were affecting the trend in any way.

As can be seen in Fig. 4.2, the two fits differ slightly. I performed the Spearman's ρ and Kendalls' τ rank correlations[1] on both samples, as was done in Meléndez et al. [49], with the results shown in Table 4.2. Both correlations measure the association between two variables or vectors: the linear fit and the real data. The significance is a value in the interval [0.0, 1.0]; a small value (less than 0.1) indicates a significant correlation. The values of the significance show that there is not a significant correlation. The differences in the values when the single line elements are excluded and the

[1]These were calculated using the R_CORRELATE IDL function *http://www.astro.washington.edu/docs/idl/cgi-bin/getpro/library07.html?*$R_{CORRELATE}$

Table 4.1: Table showing the condensation temperature, number of lines measured, differential abundance of 61 Vir relative to the average of the comparison stars and standard deviation for all the elements measured in this sample. The abundance is relative to iron.

Element	$T_{cond}(K)$	Nlines	$\Delta[X/Fe]$ (dex)	σ (dex)
C1	40	4	-0.007	0.008
N1	123	1	0.170	0.030
O1	180	3	0.098	0.013
Na1	958	2	0.000	0.016
Mg1	1336	3	0.042	0.020
Al1	1653	2	0.032	0.005
Si1	1310	18	0.009	0.024
S1	664	3	0.022	0.019
K1	1006	1	0.019	0.030
Ca1	1517	9	0.020	0.013
Sc2	1659	4	0.007	0.014
Ti1	1582	63	0.034	0.029
V1	1429	6	0.012	0.012
Cr1	1296	32	-0.008	0.020
Mn1	1158	2	-0.001	0.017
Fe1	1334	336	0.000	0.029
Fe2	1334	14	0.003	0.028
Co1	1352	8	0.016	0.015
Ni1	1353	52	0.000	0.023
Zn1	726	2	0.020	0.023
Rb1	800	1	-0.147	0.030
Sr1	1464	1	-0.089	0.030
Sr2	1464	1	-0.144	0.030
Y2	1659	1	-0.097	0.030
Zr1	1741	1	0.001	0.030
Nb2	1559	1	-0.013	0.030
Ba1	1455	1	-0.223	0.030
Ba2	1455	2	-0.080	0.028
La2	1578	3	-0.070	0.019
Ce2	1478	3	-0.039	0.016
Nd2	1602	2	0.000	0.027
Sm2	1590	1	0.056	0.030
Eu2	1356	1	-0.245	0.030

Meléndez line list show the importance of the line selection.

Table 4.2: Spearman's ρ and Kendalls' τ rank correlations with the significance of their deviation from zero between the linear fit and the data.

	Spearman's ρ	significance	Kendalls' τ	significance
All elements	0.169	0.348	0.121	0.324
Excluding single lines	0.039	0.862	0.040	0.796
Meléndez line list	0.026	0.885	0.012	0.925

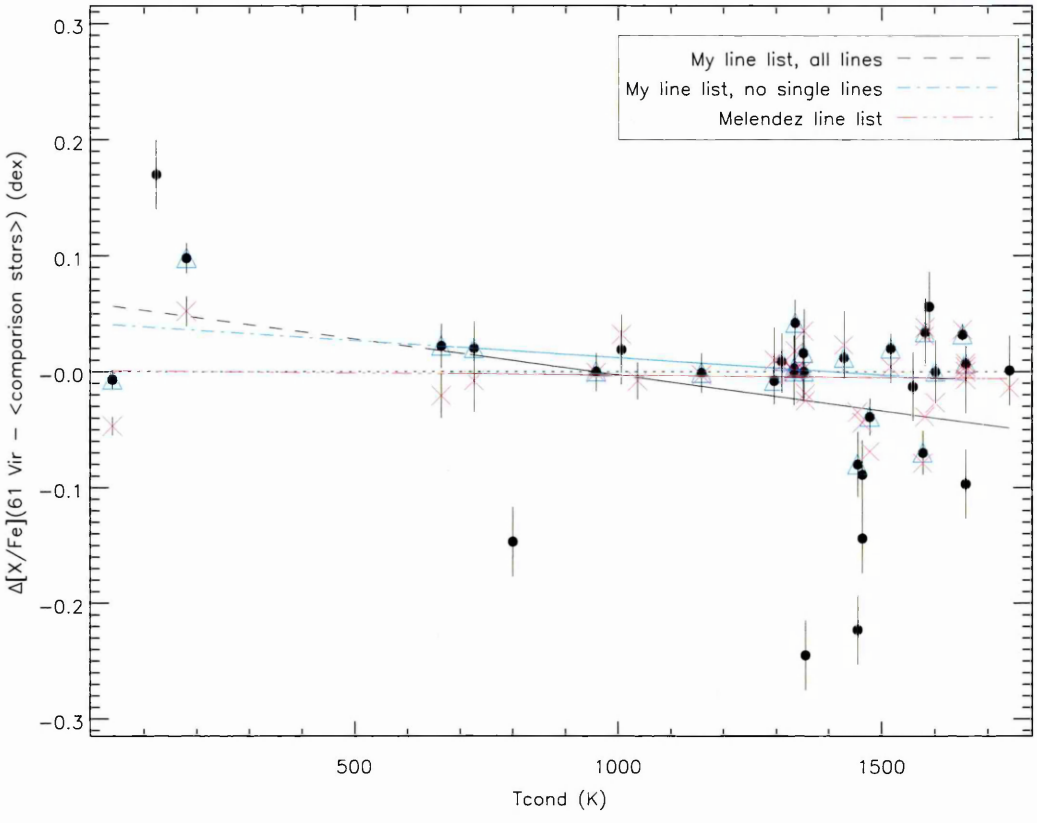

Figure 4.2: Differential abundance ratios of 61 Vir relative to the average of the comparison stars vs. dust condensation temperature with three linear fits. The fit in black is done through all the elements with the differential abundances presented as black filled circles, The fit in blue was performed excluding elements for which only one spectral line was measured with the differential abundances presented as blue triangles. The fit in red used the Meléndez line list with the differential abundances presented as red crosses. Plotted abundances are relative to Fe.

4.1.2 Individual analysis

In Section 4.1.1 I found that there was no significant observable correlation in the differential abundance signature with condensation temperature, although some elements behaved peculiarly. The refractory elements, which were observed in Meléndez et al. [49] to be more depleted with higher condensation temperature, appear to be of similar abundance in 61 Vir and in the comparison stars. Rb is also significantly depleted in 61 Vir compared to other elements with similar condensation temperatures which all behave in a similar manner.

To investigate whether the peculiar behaviours in these elements were due to po-

tential signatures being eliminated through averaging the comparison stars, each star in the sample was individually compared with 61 Vir using a differential abundance analysis. Figures 4.3 to 4.7 shows the abundance differences separated for each comparison star. It can be seen that the abundance pattern varied from star-to-star with no two stars showing the same signature. Further analysis of the trends shown in Figures 4.3 to 4.7 will be shown in Chapter 5.

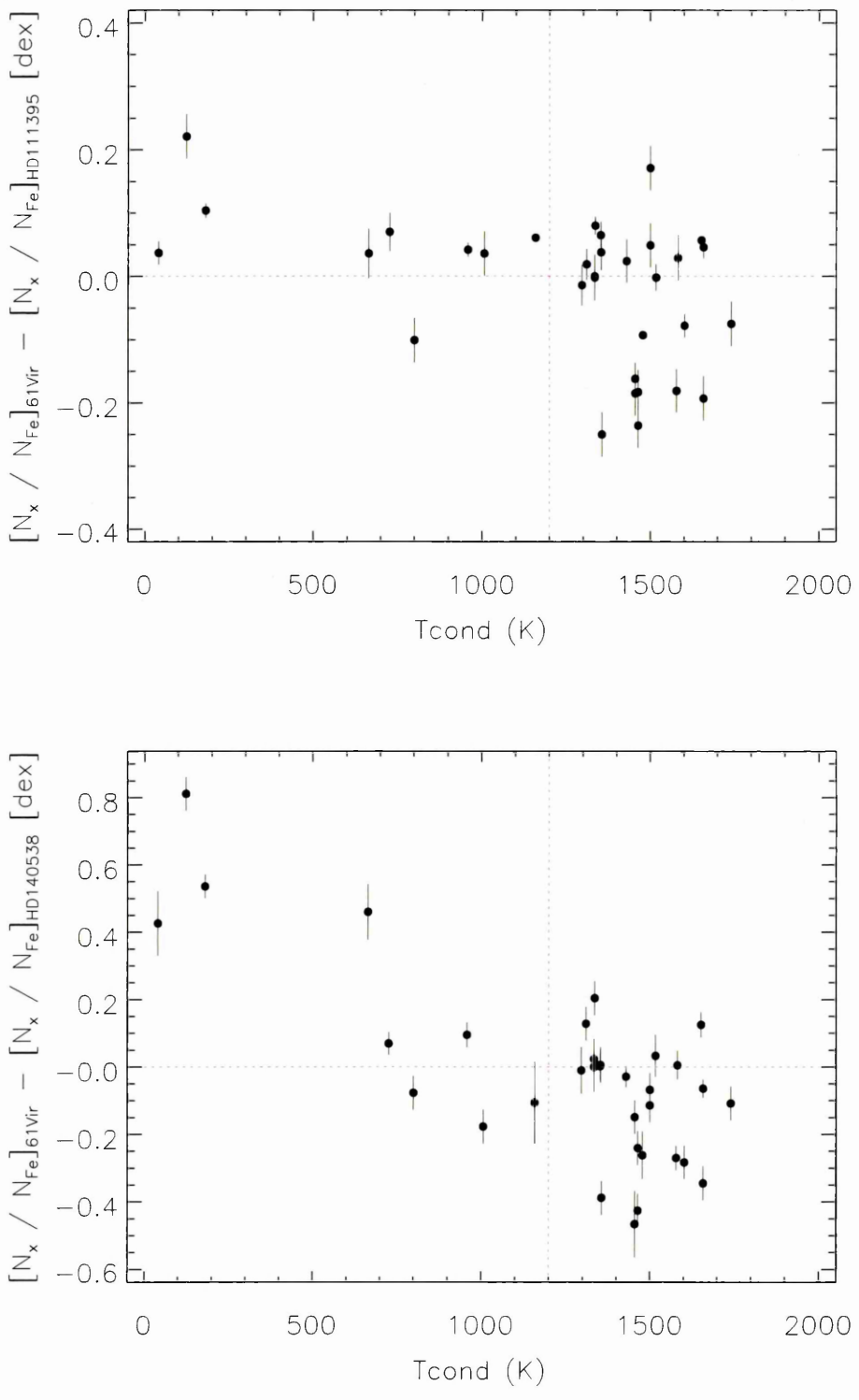

Figure 4.3: Differences between [X/Fe] of 61 Vir and the value for HD 111395 and HD 140538 as a function of condensation temperature $T_{\rm cond}$. For clarity, the break in the trend between volatile and refractory elements found in [49] has been illustrated as a red dotted line at $T_{\rm cond}$=1200 K. For elements where multiple lines were measured, the error was calculated as the standard deviation from the average. Where only 1 line could be measured for the element, the uncertainty was determined through the visual convergence of the standard deviations of multiple lines.

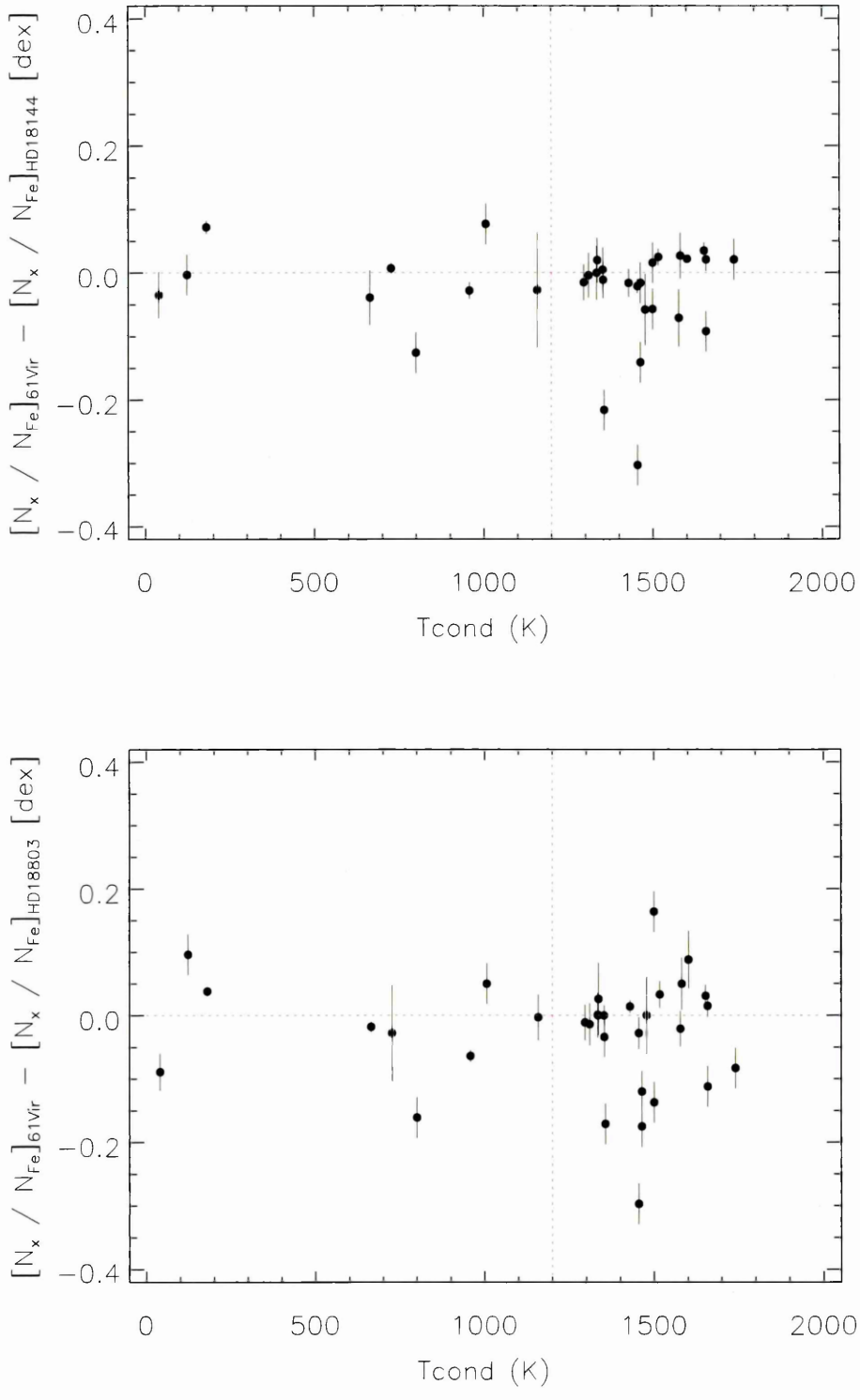

Figure 4.4: Same as Figure 4.3 but for HD 18144 and HD 18803.

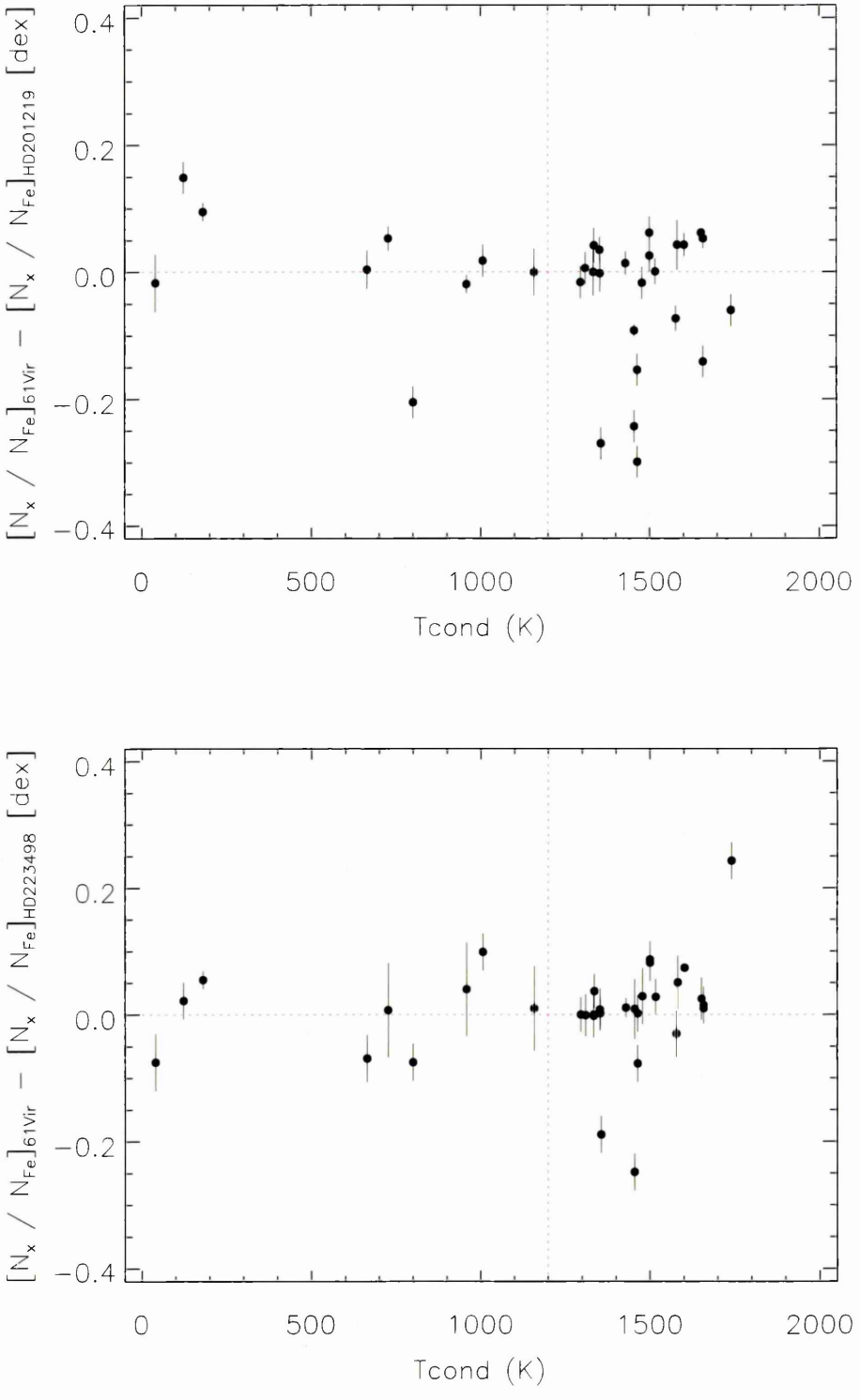

Figure 4.5: Same as Figure 4.3 but for HD 201219 and HD 223498.

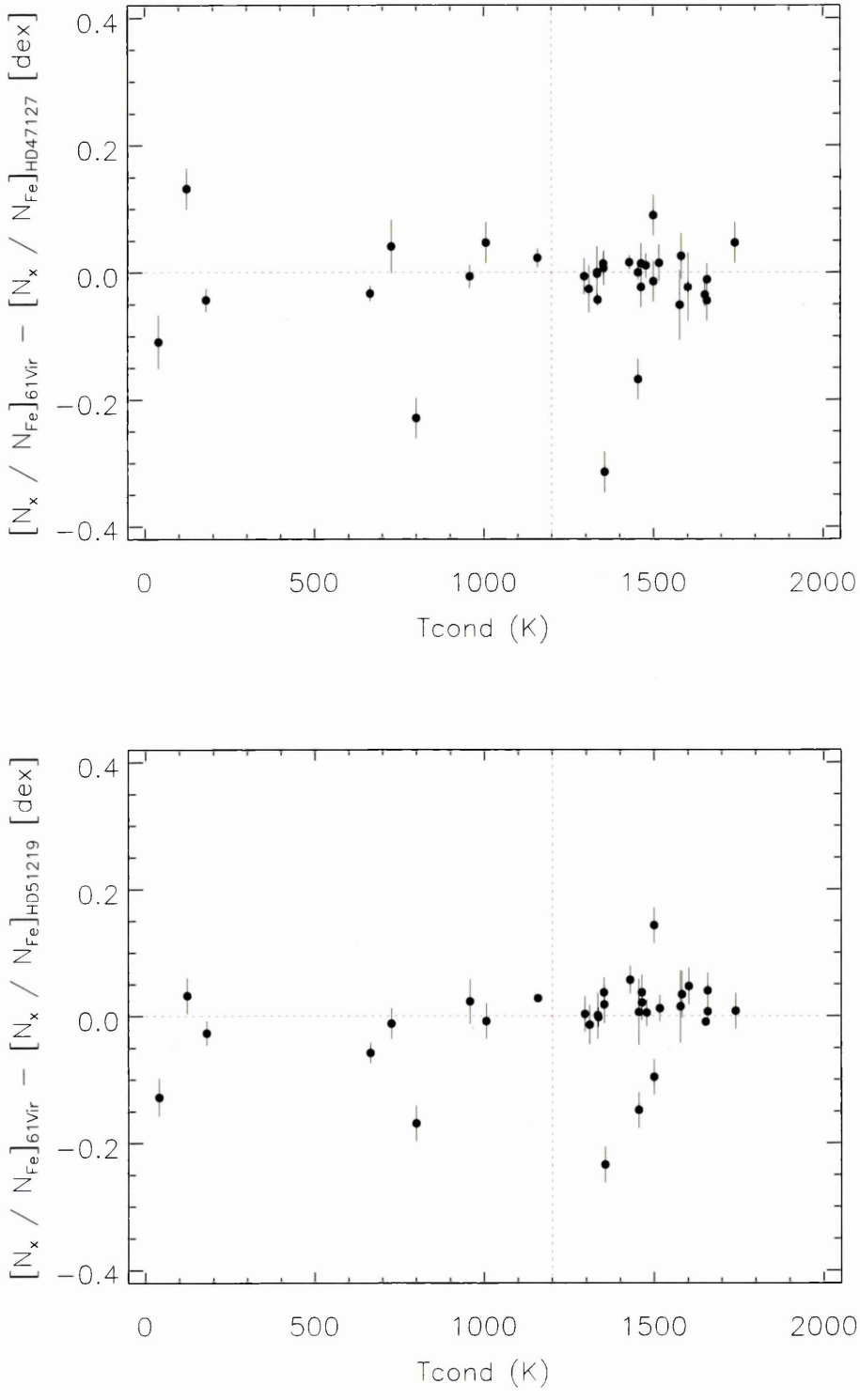

Figure 4.6: Same as Figure 4.3 but for HD 47127 and HD 51219.

From these figures it can be concluded that the "planetary" signature observed in Meléndez et al. [49] is not observable in 61 Vir using my line list.

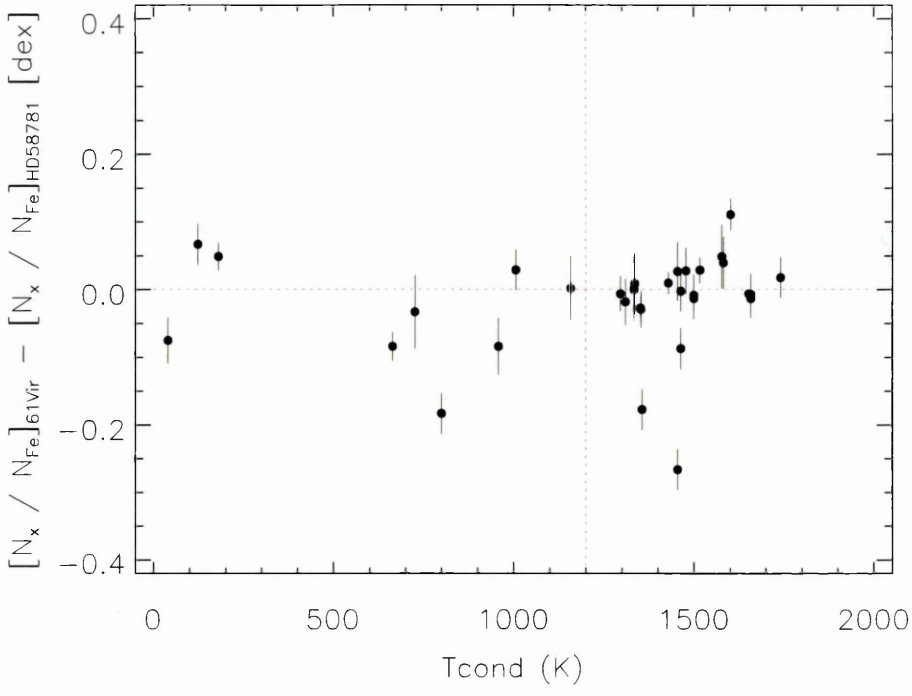

Figure 4.7: Same as Figure 4.3 but for HD 58781.

There are many possible causes for this lack of signature.

1. Comparison stars

   The comparison stars for this sample were selected to be twins and analogs whereas the signature observed in Meléndez et al. [49] is observed when the Sun is compared to solar twins. There was a far greater spread in the differential abundances when the Sun was compared to the solar analogs and the signature was a single linear fit rather than the two linear fits as seen in the solar twins. The solar analogs signature is more similar to the trend observed in the 61 Vir compared to the average of the comparison stars figure (Fig. 4.2) but the trend is not statistically significant. It would have been preferable to perform the analysis using only twins but a catalog with enough twins for 61 Vir so that the parameters are all measured the same way has not been compiled.

2. Line selection

The possibility of the differing signatures being due to the differing line lists will be discussed in Section 4.2.

3. Galactic location and age

If the stars were formed in different regions of the Galaxy they would be subject to different Galactic evolution effects. To investigate this possibility, I plotted a series of figures with position information of the stars obtained from Casagrande et al. [9].

The Galactic radial and vertical positions describe the distances in the Galactocentric coordinate system whilst the perigalactic and apogalactic distances are the distances from the Galactic center to the minimum and maximum distance of the stellar orbit respectively. The orbital eccentricity determines the circularity of the orbit of the star around the galactic centre. A circular orbit will have a value of 0 whilst an elliptical orbit will have a value between 0 and 1. The stars in this sample all have elliptical orbits of varying eccentricity. The maximum distance from the Galactic plane can be used as an indicator of age because it permits the identification of a star as thin (small *zmax*) or thick (large *zmax*) disk. The boundary between thin disk and thick disk is given as $zmax = 0.7\,\mathrm{kpc}$ [87]. The heliocentric space velocities (U,V,W) refer to the Cartesian coordinates along the x, y, and z axes respectively.

As can be seen in Fig. 4.8, the stars are all fairly near to each other with the only potential outliers being HD 51219 and HD 223498 in Fig. 4.8d. The position is indicative of a thick disk star which would imply it was metal poor. However, it can be seen in Table 3.1 that HD 51219 is metal rich and therefore cannot be thick disk. It is very likely that all the stars originate from near to each other, are thin disk and so should be subject to similar Galactic evolution effects.

An analysis of the ages of the stars will be shown in Chapter 5. This will show the importance of knowing the ages of the stars.

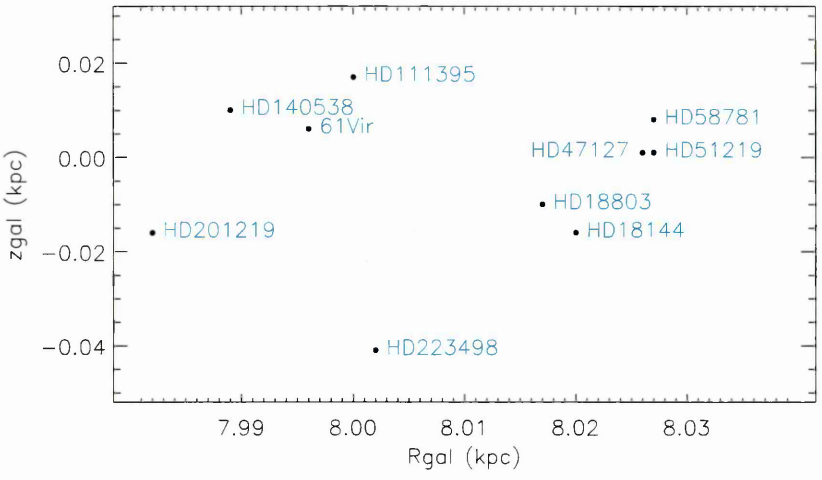

(a) Galactic radial (Rgal) versus Galactic vertical (zgal) locations of the stellar sample.

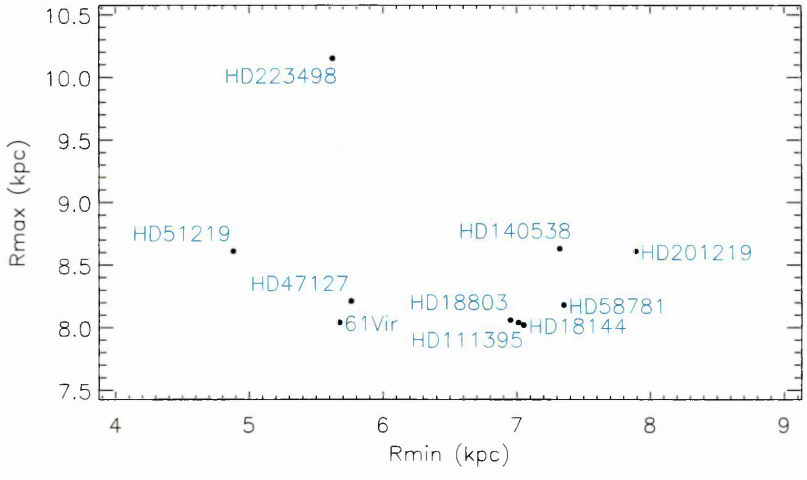

(b) Perigalactic (Rmin) versus apogalactic (Rmax) distances of the stellar sample.

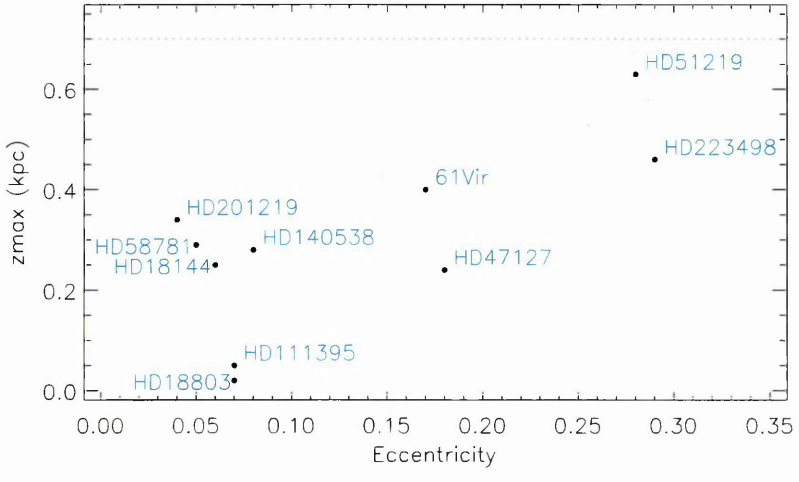

(c) Eccentricity of Galactic orbit versus maximum distance from galactic plane of the stellar sample. The red dashed line represents the boundary between thin and thick disk stars [87].

Figure 4.8: Stellar location plots using data from Casagrande et al. [9].

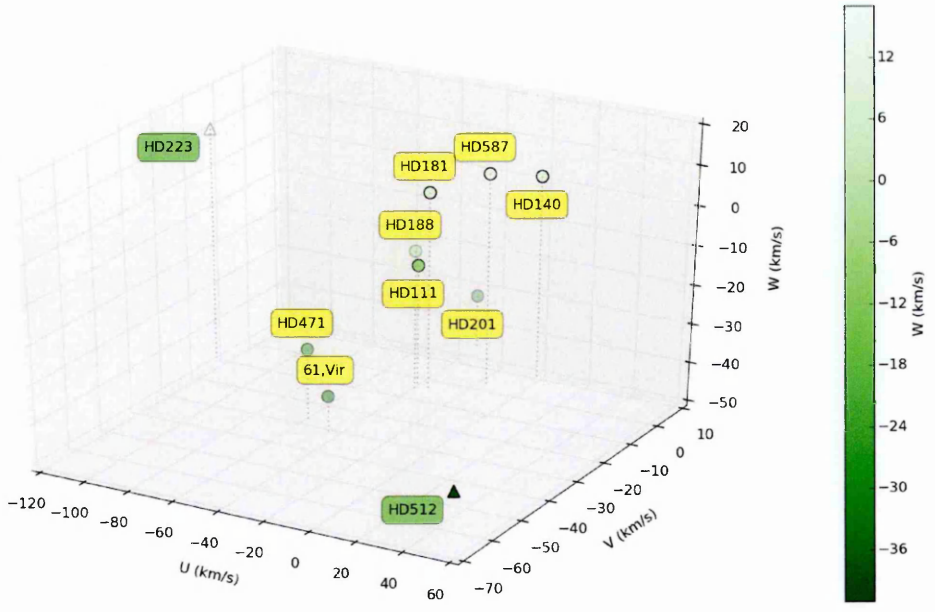

(d) 3-Dimensional visualisation of the heliocentric space velocities U, V, W along the cartesian x, y, and z axes respectively. The W parameter is further depicted using dashed lines to further visualise the height and a colour gradient for the symbols. The stars HD 223498 and HD 51219 have triangular symbols to distinguish them as outliers from the rest of the stellar sample.

Figure 4.8: Stellar location plots using data from Casagrande et al. [9](cont.).

4. No Super-Earth or refractory material

   As mentioned in Section 2.2, the planets around 61 Vir were discovered using the radial velocity method. This only provides a minimum mass, which is given for the Super-Earth orbiting 61 Vir as $5.1 M_{Earth}$. As previously mentioned (Section 2.2), the current accepted upper bound for a Super-Earth is 10 M_{Earth} [78]. The true mass of the planet cannot be known without the inclination angle so the mass estimate of 5.1 M_{Earth} could increase significantly depending on the inclination of the planet orbit, causing the planet to pass the limit of a planet with a rocky core. The planetary radius is also unknown as it has only been detected using radial velocity so the radius of the planet has not been determined. Without knowing the mass or radius, we cannot be sure of the planet being a Super-Earth or the planetary system containing a substantial quantity of refractory material locked in the three planets.

   Meléndez et al. [49] hypothesized that planet formation disrupted the solar proto-

planetary nebula, causing the chemical signature, with the missing $\approx$1.3 M_{Earth} of refractory material being locked in the terrestrial planets. This requires a massive disk during the T Tauri phase (1 $M_{\odot}$ rather than the minimum 0.001 $M_{\odot}$) for enough material to be available to change the photospheric composition [7]. If the T Tauri phase of 61 Vir lacked a massive disk, it may not have contained enough material to change the photospheric composition of 61 Vir when the planets were formed, explaining why a planetary signature cannot be observed in other stars.

5. No planetary signature

   There exists the possibility that the signature observed in Meléndez et al. [49] is not related to the presence of the terrestrial planets but is due to some other unknown effect. No planetary signature is imprinted in the stellar photosphere and so no planetary signature can be observed.

4.2 Comparisons with Meléndez line list

As mentioned in Section 3.3, a line list developed by Meléndez was adopted to perform a study into whether the line selection influenced the planetary signature observed in Meléndez et al. [49]. The same procedure for parameter and abundance determination was performed as with my line list with both the absolute and differential parameters being determined before deriving the abundances. Figure 4.9 depicts the differential abundances between 61 Vir and each star whilst Figures 4.10 to 4.14 highlight the differences in the differential abundance signatures when the Meléndez line list is used and when the elements missing from the Meléndez line list are included.

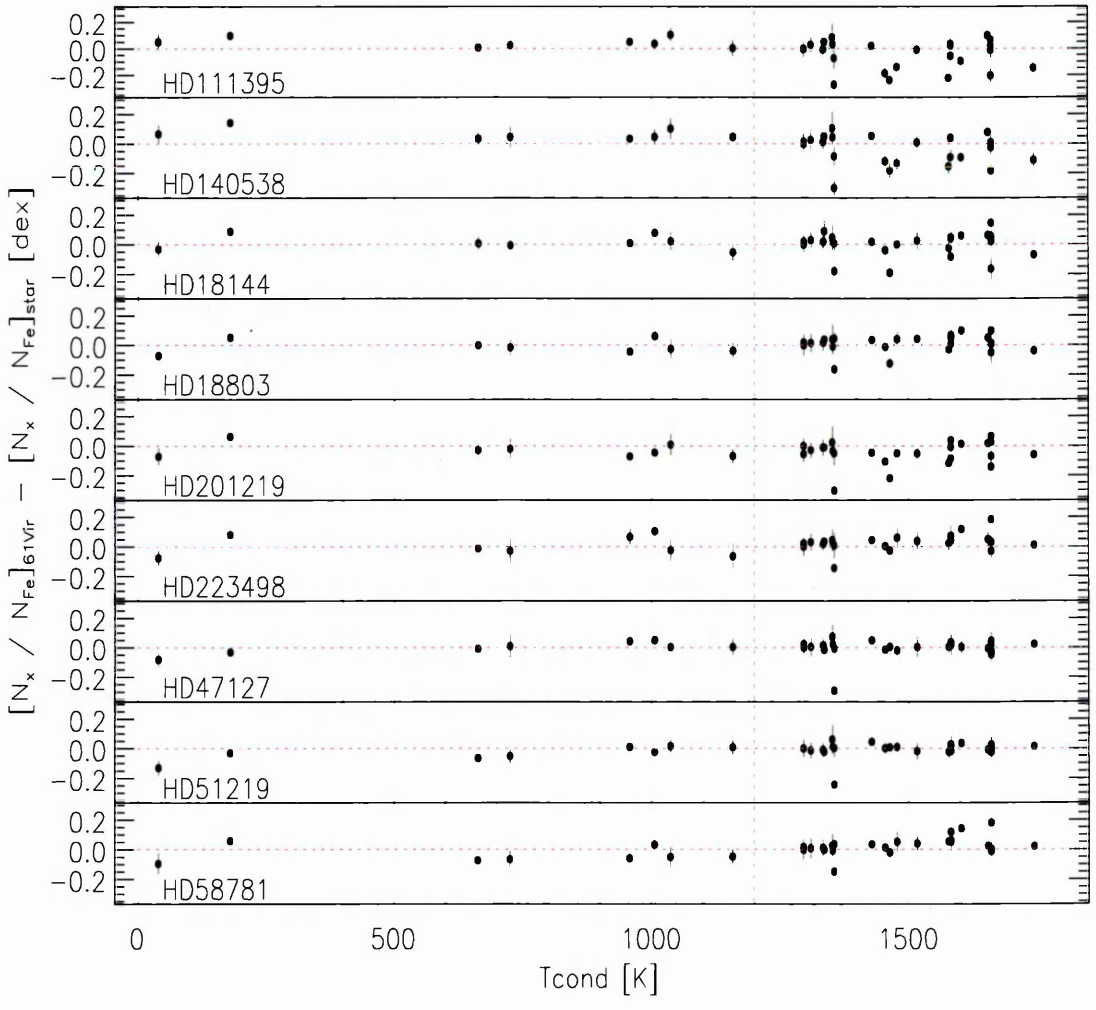

Figure 4.9: Differential abundances between [X/Fe] of 61 Vir and each star as a function of T_{cond} for the Meléndez line list.

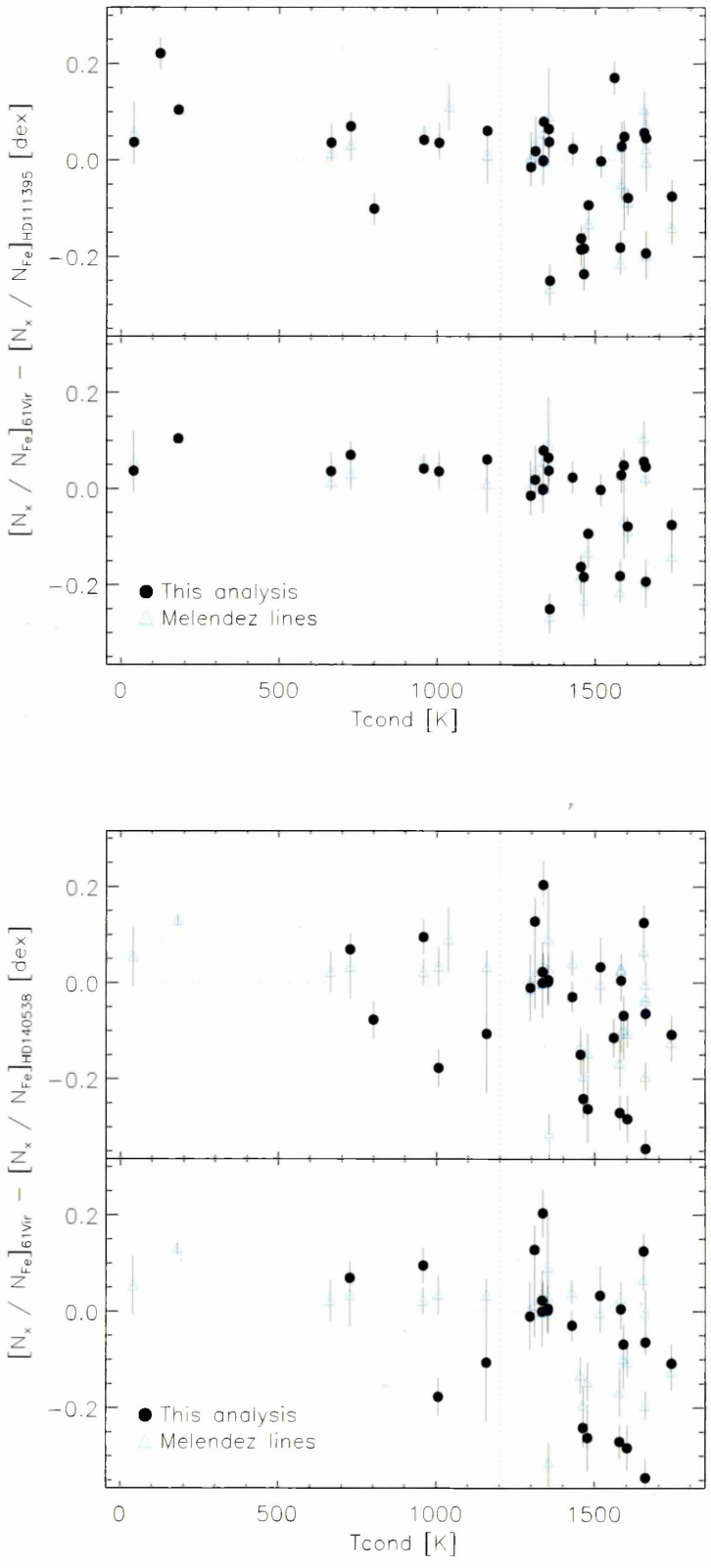

Figure 4.10: Differential abundance ratios of 61 Vir relative to the abundance of HD 111395 and HD 140538 using the Meléndez line list. All abundances are relative to Fe. The top panel shows the abundances obtained from each line list to emphasise what elements differ in each analysis (N, Rb and Nb for my line list; Cu, Pr, Dy for the Meléndez line list). The bottom panel shows the abundances obtained using only the elements found in the Meléndez line list. As previously, the red dotted line at $T_{\rm cond}$=1200 K represents the break in the pattern found in [49].

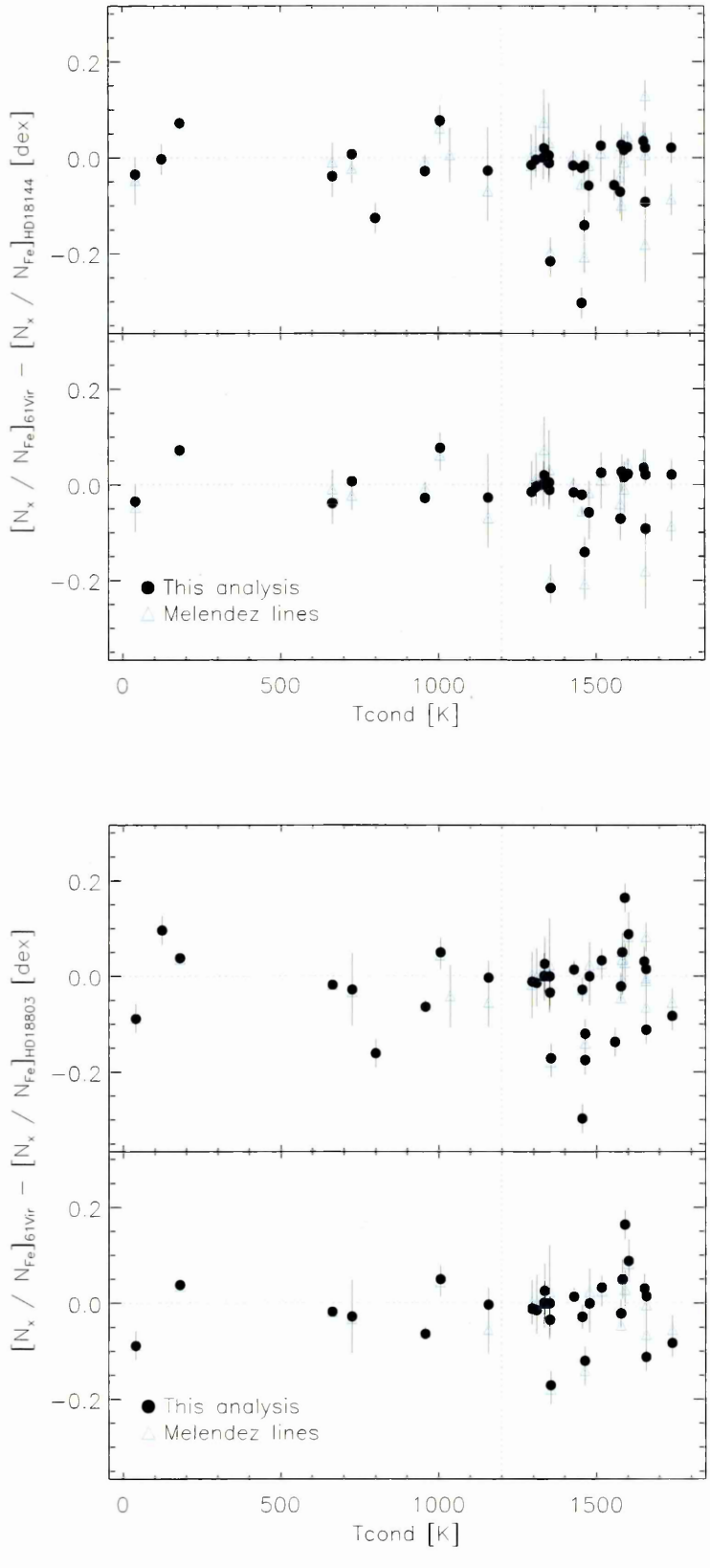

Figure 4.11: Same as Figure 4.10 but for HD 18144 and HD 18803.

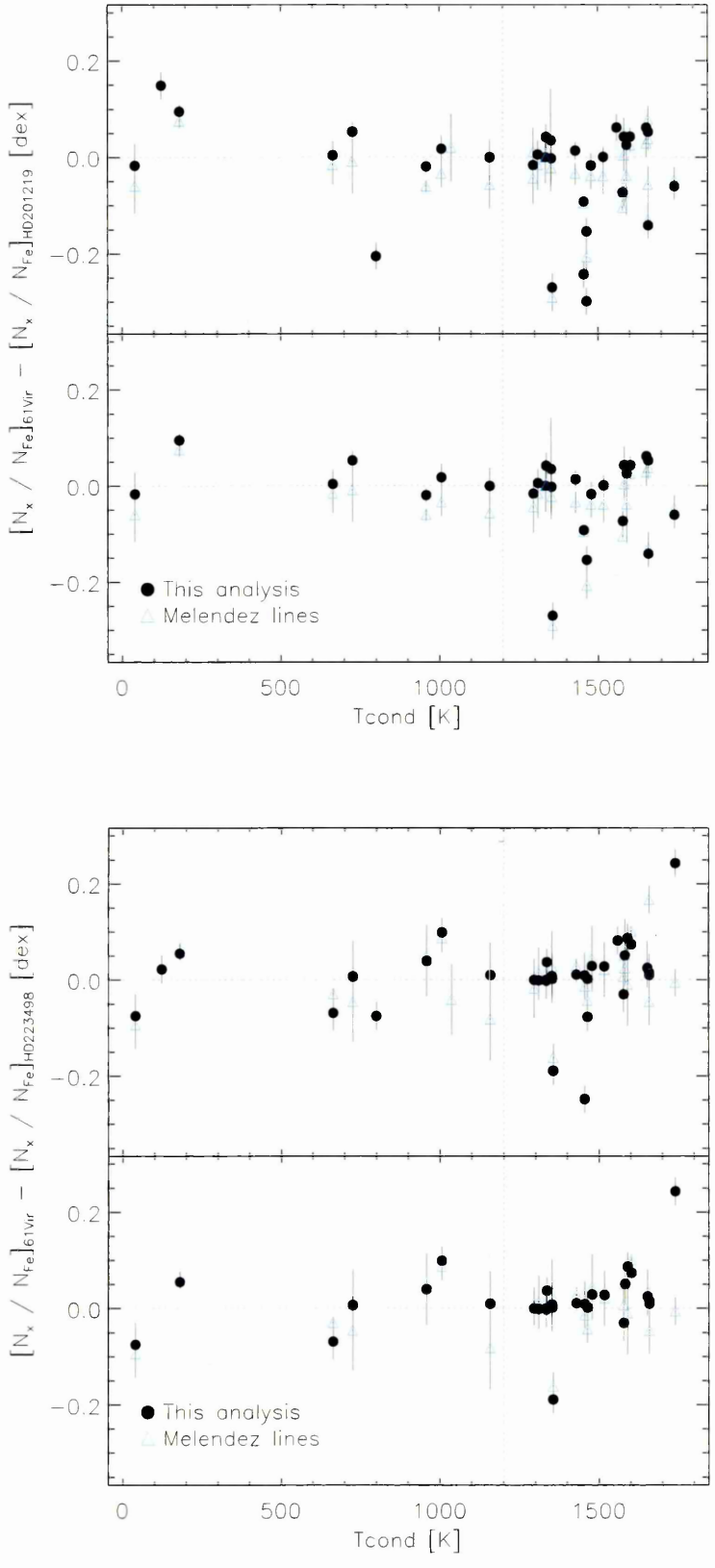

Figure 4.12: Same as Figure 4.10 but for HD 201219 and HD 223498.

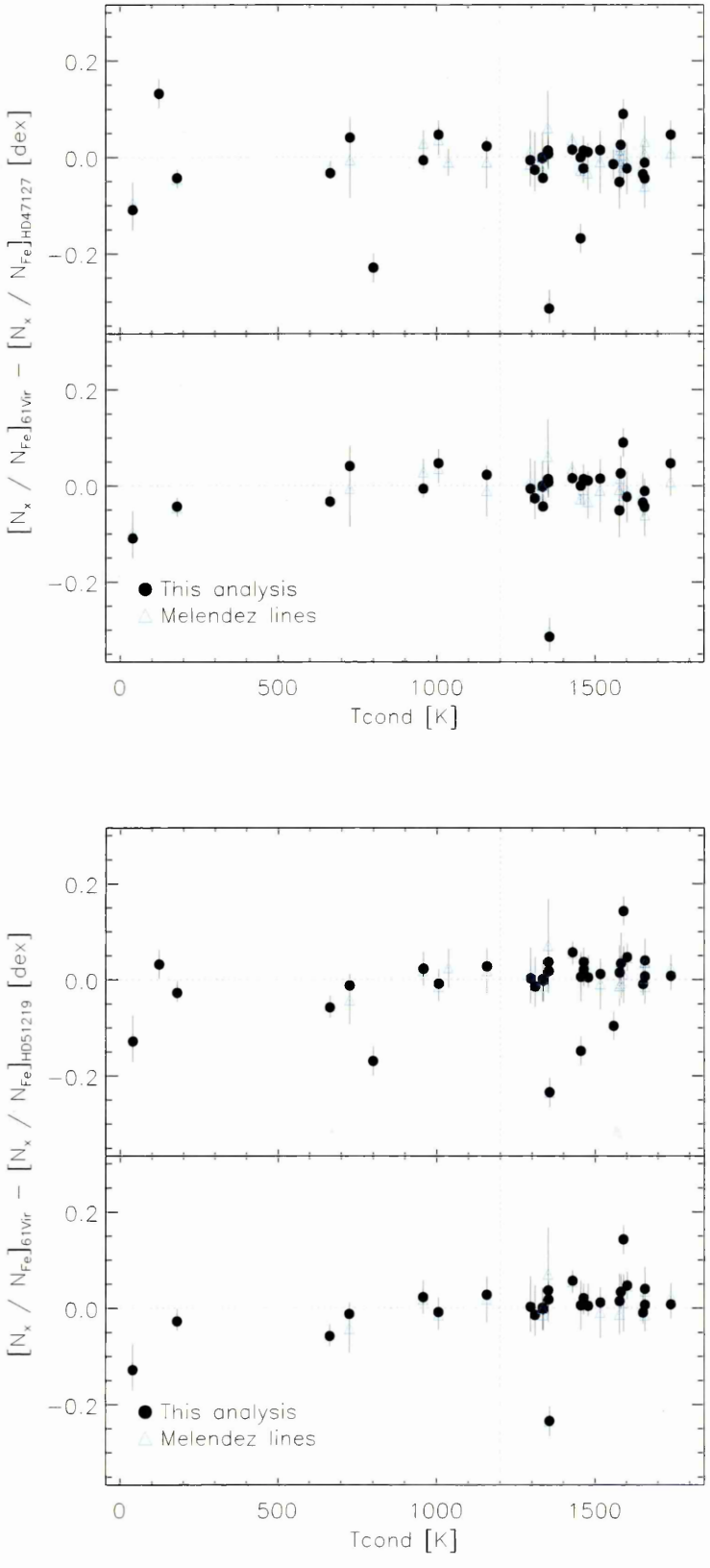

Figure 4.13: Same as Figure 4.10 but for HD 47127 and HD 51219.

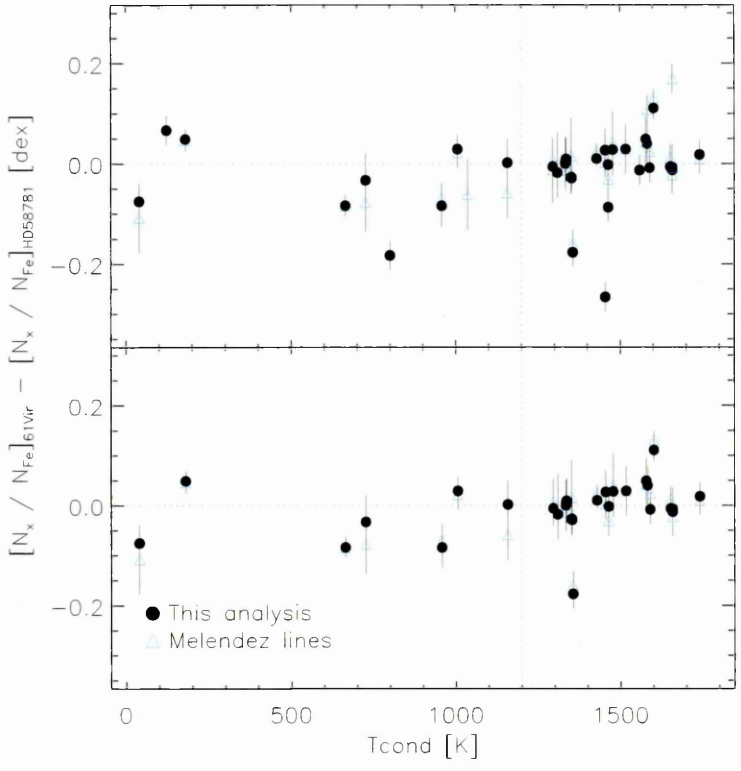

Figure 4.14: Same as Figure 4.10 but for HD 58781.

As can be seen in Figure 4.9 and Figures 4.10 to 4.14, the signatures observed using the Meléndez line list are very similar to those observed in Section 4.1.2. The differences arise from the elements which have been excluded from the Mélendez line list. The Meléndez line list does not include some of the elements which show significant changes from star to star such as Nitrogen and Rubidium. There are three elements in the Meléndez line list which were not measured in my sample - Copper, Praseodymium and Dysprosium. These lines were measured for the Meléndez comparison but excluded from my line list as, in my spectra, they were found in noisy regions, blended by molecules or lacked a nearby well constrained continuum. Overall, the Meléndez line list and my line list produce matching abundance patterns in the low condensation elements but differ with the higher condensation temperature elements.

4.3 Remarks on the analysis

In this analysis, the Meléndez solar planetary signature was not observed and, when the analysis was performed in the same way as Meléndez, there were no visible trends. The analysis was then performed on a star-by-star basis to identify whether there were signatures in individual stars. A small trend in the signature across the stars was observed. The data was reanalysed and sorted according to the stellar parameters and a trend appeared to be in accordance with the surface gravity of the stars. Surface gravity is an indicator of stellar age. This prompted the question to be analysed in Chapter 6 - is the apparent signature dependent on the age of the star and are we observing trends due to stellar age?

Chapter 5

Determining the ages of the stellar sample

The conclusion of the work in Chapter 4 suggested that rather than a planetary signature being observed, a stellar age signature might be observed in the stars in this analysis. To further test this work, an age order for the stars needed to be determined. It is almost impossible to precisely measure the age of these stars but the actual stellar age measurements are not important. The relative age order of the stars is necessary so that further analysis, looking at the differential abundances as a function of age, can be performed.

In this Chapter I aim to discuss the methods used to determine the relative ages of the stellar sample before determining an approximate age order for the stars accounting for all of the factors discussed. For single stars, the star's rotation is a function of age [88] but the stars in this analysis all have very similar and small $\upsilon \sin i$ values so it is not a useful test here for age estimate. The $\upsilon \sin i$ values calculated can be found in Appendix F. The $\log R'_{HK}$ index was not considered for this work as the data was not taken in the correct mode to be able to perform the required analysis.

5.1 log$g$

The values for the surface gravity used in the age determination are those derived when the stellar parameters were obtained (Table 3.1). In general, log$g$ does not give a very precise age determination due to the additional effects of the other parameters.

5.2 HR diagram

The masses and ages of the stars were estimated by fitting evolutionary tracks to their position in the Hertzsprung-Russell (HR) diagram. It was attempted to derive the luminosities using the V magnitudes and Hipparcos parallaxes in van Leeuwen [80] but information on the complete stellar sample was unavailable so luminosities were derived using Casagrande et al. [9] temperatures (see Table 5.1 for values compared to the values obtained using my line list), adopting the bolometric correction by Flower [20].

Table 5.1: Table showing the effective temperature of the stars using my line list and the Casagrande catalogue. Where the uncertainty is not given, it was not supplied in the catalogue.

	$T_{\rm eff}$(K) My line list	$T_{\rm eff}$(K) Casagrande
61 Vir	5684 (35)	5628 (-)
HD 111395	5764 (42)	5614 (80)
HD 140538	5794 (34)	5693 (-)
HD 18144	5672 (43)	5479 (82)
HD 18803	5772 (36)	5621 (80)
HD 201219	5758 (46)	5678 (80)
HD 223498	5670 (43)	5547 (-)
HD 47127	5724 (37)	5641 (-)
HD 51219	5728 (39)	5590 (59)
HD 58781	5726 (39)	5569 (59)

The STARS stellar evolution code [19, 72] was used to construct models for stars of between 0.9 to 1.1 $M_{\odot}$ (with a mass spacing of 0.05 $M_{\odot}$), for metallicities of Z = 0.02 and 0.04. These models have been evolved from the pre-main sequence to the giant branch using 999 meshpoints, a mixing length parameter of 2.0 and without the inclusion of convective overshooting. Figures 5.1 and 5.2 show the position of the

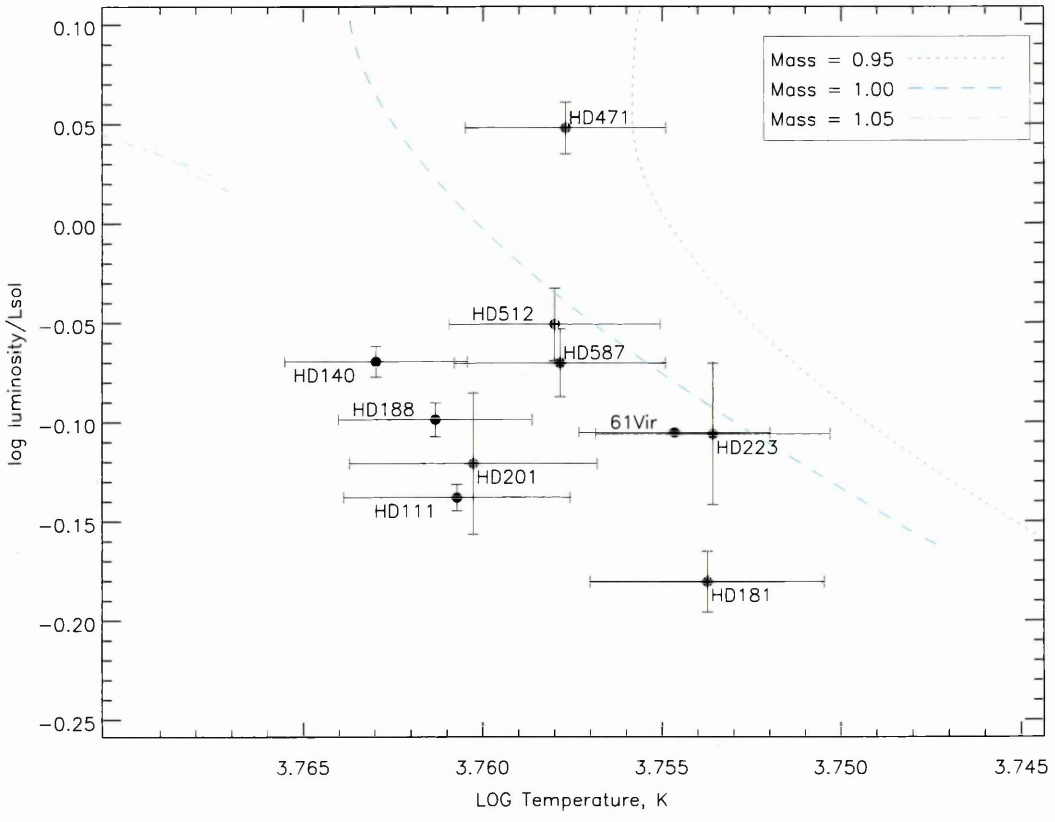

Figure 5.1: Position of the stars in the sample in the HR diagram calculated using the derived temperatures and Casagrande luminosities in comparison with evolutionary tracks calculated with Z = 0.02. The red dotted line is the track for masses of 0.95 $M_{\odot}$; the blue dashed line is the track for masses of 1 $M_{\odot}$; the green dotted and dashed line is the track for masses of 1.05 $M_{\odot}$.

sample stars in the HR diagram compared to the STARS evolutionary tracks. 5.1 shows the stellar positions with the temperature as derived in Section 3.5.1 whilst Figure 5.2 shows the stellar positions with the temperature from Casagrande et al. [9]. The stellar ages and masses were derived by calculating the closest point on the evolutionary track to the star and reading the age and mass of that point. In the case of stars midway between two tracks, such as HD 47127, the age and mass was interpolated between the two tracks. The derived stellar ages, listed in Table 5.2 along with the masses, varied from 0.5 Gyr to 12 Gyr.

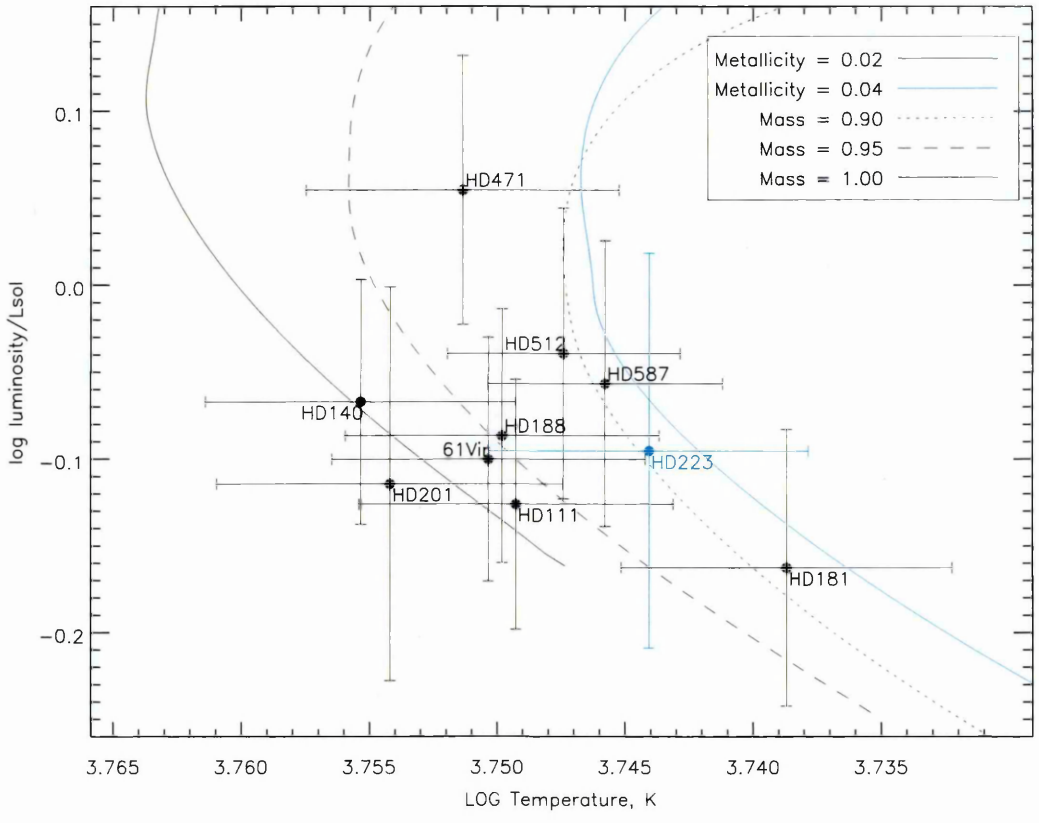

Figure 5.2: Position of the stars in the sample in the HR diagram calculated using the Casagrande temperatures and luminosities in comparison with evolutionary tracks calculated with Z = 0.02 (black) and 0.04 (blue). The dotted line is the track for masses of 0.9 $M_{\odot}$; the dashed line is the track for masses of 0.95 $M_{\odot}$; the solid line is the track for masses of 1 $M_{\odot}$. HD 223498 is blue as the best match was for the higher metallicity track whereas the other stars all fell on the lower metallicity track.

Table 5.2: Ages and masses obtained for each star according to their temperature and luminosity on the HR diagram. The values came directly from the best matching model and did not include uncertainties.

	Age (Gyr)	$\log T_{\rm eff}$ (K)	$\log L/L_{\odot}$	$\log M/M_{\odot}$
HD111395	0.525	3.750	-0.139	1.000
HD201219	1.300	3.752	-0.116	1.000
HD140538	2.980	3.756	-0.066	1.000
HD18803	6.350	3.750	-0.090	0.950
61Vir	6.350	3.750	-0.090	0.950
HD18144	8.580	3.739	-0.178	0.899
HD223498	11.10	3.744	-0.101	0.899
HD58781	12.20	3.746	-0.061	0.899
HD47127	12.60	3.752	0.055	0.924
HD51219	12.90	3.747	-0.035	0.899

5.3 Lithium

It has long been understood that Lithium is an indicator of age [81]. All the stars in this study will have had a pre-main sequence mass greater than $0.06M_{\odot}$ based on their current expected masses. Consequently, they will have reached a high enough core temperature to burn Lithium in proton capture reactions [69]. Lithium is depleted very rapidly due to the steep temperature dependence of the nuclear reactions and the short mixing timescale in fully convective pre-main sequence stars so it would be expected that, upon reaching the zero age main sequence, stars would have very little Lithium remaining. The Lithium that does remain would all burn early on in the star's main sequence lifetime indicating that stars with a measurable Lithium spectral line are the younger stars in this analysis.

Measurements of the Lithium abundance were attempted for all the stars by fitting a synthetic spectrum, calculated adopting the stellar atmospheres previously calculated for each star (Section 3.1), to the observed spectrum at the Li 6707Å line. This Lithium line is a doublet with multiple hyperfine structure components which have to be accounted for when doing this measurement. To do this, I replaced the Lithium doublet used in the initial synthetic spectrum with information on all the hyperfine structure components from Smith et al. [68]. Details of the components are given in Table 5.3.

Table 5.3: Hyperfine structure of the Li 6707 line.

λ (Å)	$\log gf$ (dex)
6707.7561	-0.440
6707.7682	-0.239
6707.9066	-0.965
6707.9080	-1.194
6707.9187	-0.745
6707.9200	-0.965
6707.9196	-1.609
6707.9230	-1.308
6708.0728	-1.434

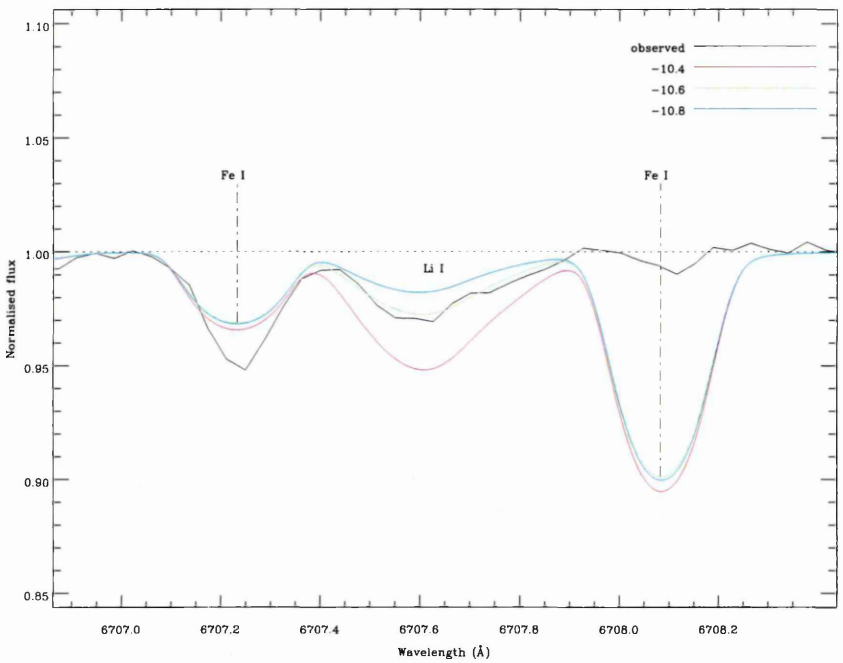

Figure 5.3: Line profile of the observed spectrum of HD 111395 being fitted to 3 synthetic spectra corrected for the Lithium hyperfine structure. The synthetic spectra were produced with Lithium abundances of -10.4 (red), -10.6 (green) and -10.8 (blue) to show that for this star, the best fit is with a Lithium abundance of -10.6.

The Lithium abundance was modified in the synthetic spectrum until there was a match between the synthetic and observed spectra. Of the 10 stars in the sample only 4 of them had a measurable Lithium abundance - 61 Vir, HD 111395, HD 140538, HD 201219 (Table 5.4) so these are defined as the youngest stars.

Table 5.4: Lithium abundances for the stellar sample where the Li 6707 line could be fitted with a synthetic spectrum.

Star	Li abundance (dex)
61 Vir	-10.9
HD 111395	-10.6
HD 140538	-10.5
HD 201219	-11.0

5.4 Wilson-Bappu

The Wilson-Bappu effect is a linear correlation between the logarithm of the full width at half maximum (FWHM), W_0, of the Ca II H or K emission core and the absolute magnitude, M_V, of the star [83]. The latest calculation of this equation from Pace et al. [55] is expressed as

$$M_V = 33.2 - 18.0 \log W_0. \tag{5.1}$$

The absolute stellar magnitude is directly linked to the stellar radius which, for cool stars, evolves over time whilst the mass remains constant. Since $\log g$ is a measure of pressure, the change in radius will cause a change in $\log g$ over time. Park et al. [57] calculated that W_0 should be proportional to $\log g$, hence age, for stars of the same temperature and metallicity.

Of the 10 stars in the sample, only 5 of them exhibited an emission feature in the Ca II H and K lines - HD 111395, HD 140538, HD 18144, HD 18803, HD 201219. To measure W_0, a gaussian was fitted to the feature, ignoring the central absorption as seen in Figure 5.4. The values for W_0 and central wavelength of each star are given in Table 5.5.

Table 5.5: Values obtained for W_0 and the central wavelength from the gaussian fit of the Ca II K line.

Star	W_0 (Å)	Central λ (Å)
HD 18144	0.3911	3933.66
HD 18803	0.3788	3933.65
HD 111395	0.4088	3933.67
HD 140538	0.4002	3933.66
HD 201219	0.4080	3933.67

It can be seen that two of the stars, HD 111395 and HD 201219 - have very similar chromospheric activity, as can also be seen in Figures 5.4a and 5.4e, whilst the least

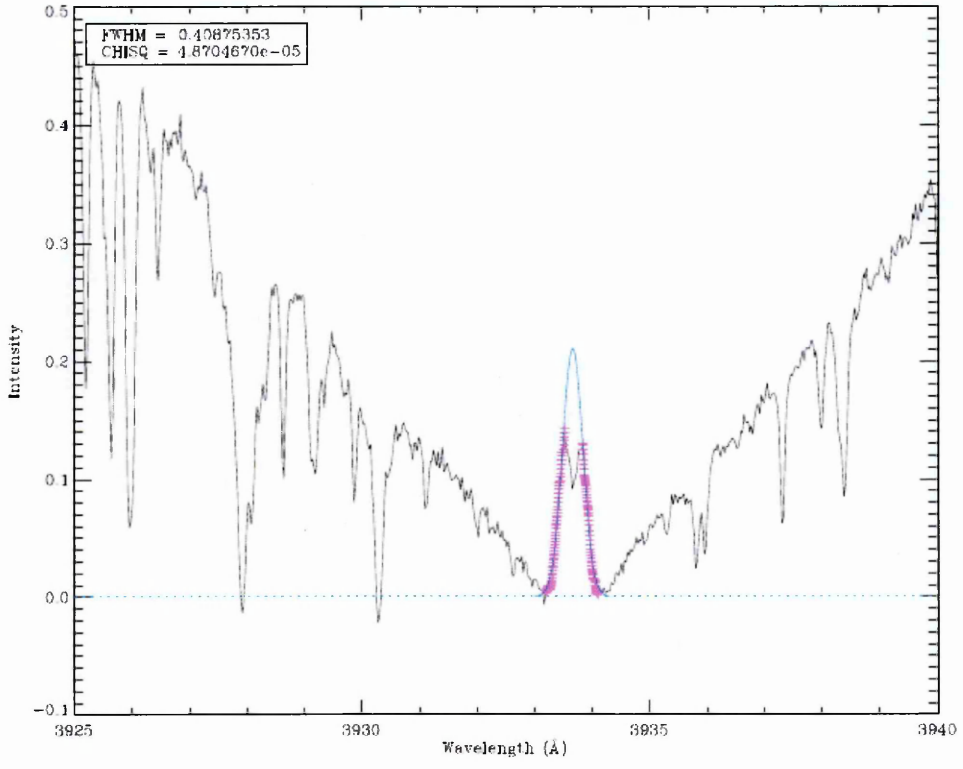

(a) HD 111395

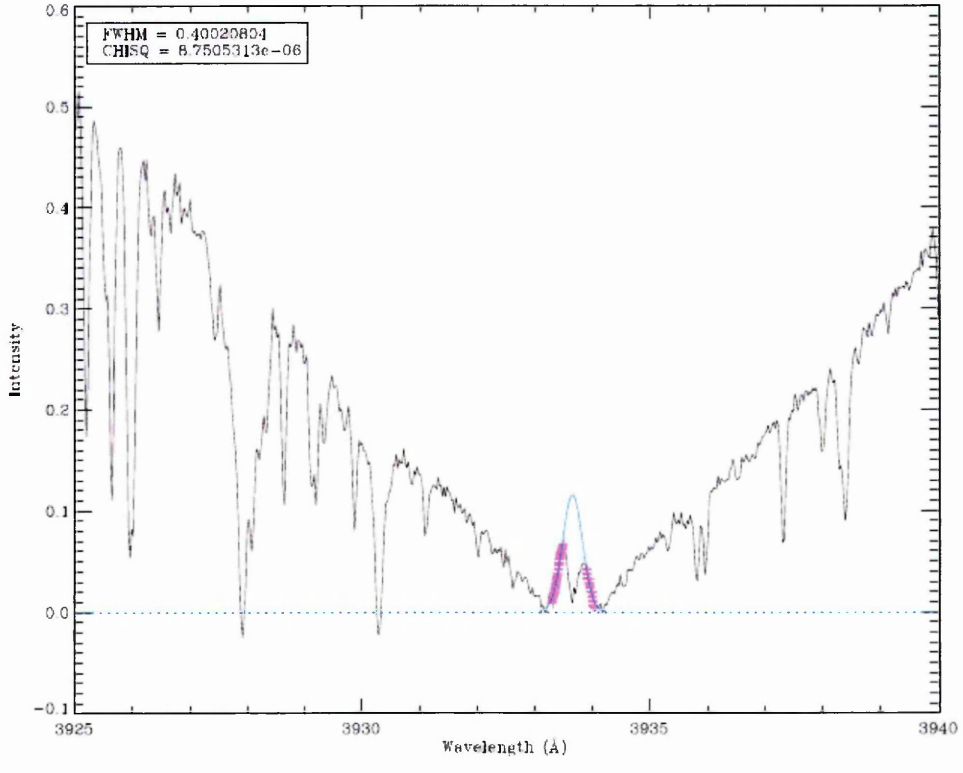

(b) HD 140538

Figure 5.4: Line profile showing the Gaussian fit of the emission from the Ca II H & K lines. The crosses inform the Gaussian fit.

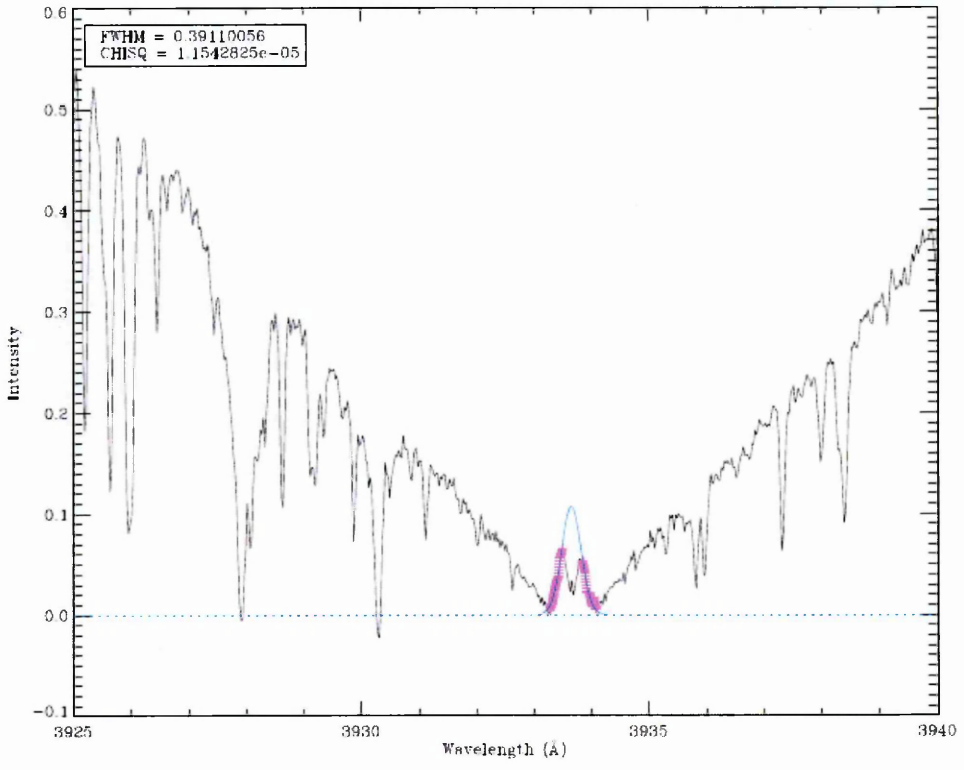

(c) HD 18144

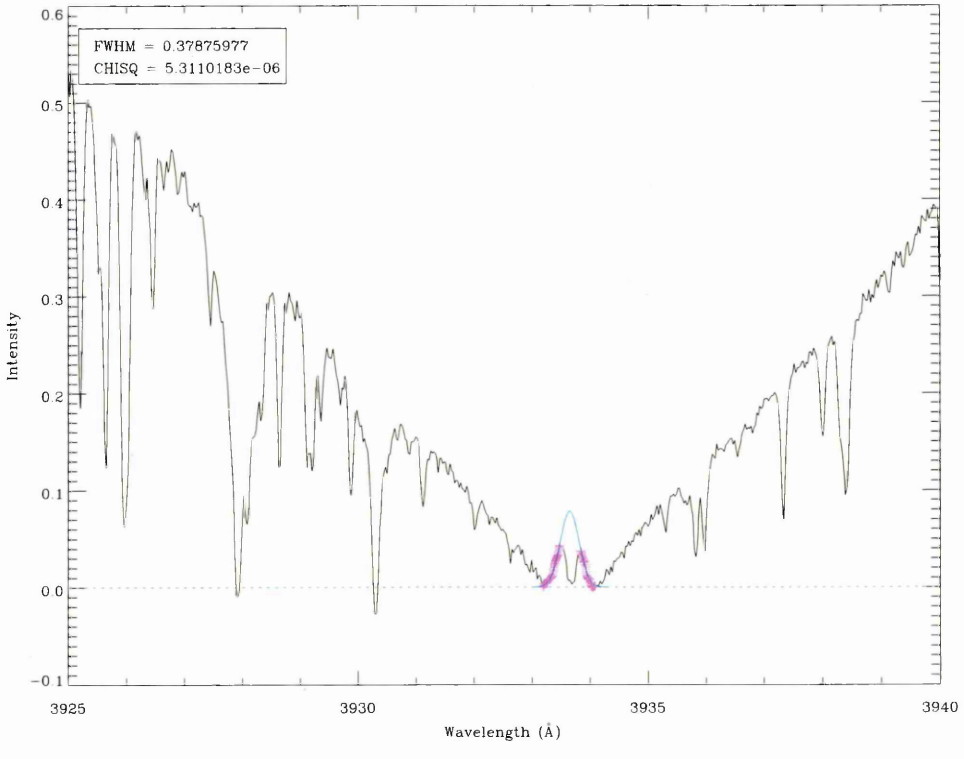

(d) HD 18803

Figure 5.4: Line profile showing the Gaussian fit of the emission from the Ca II H & K lines. The crosses inform the Gaussian fit. (cont.)

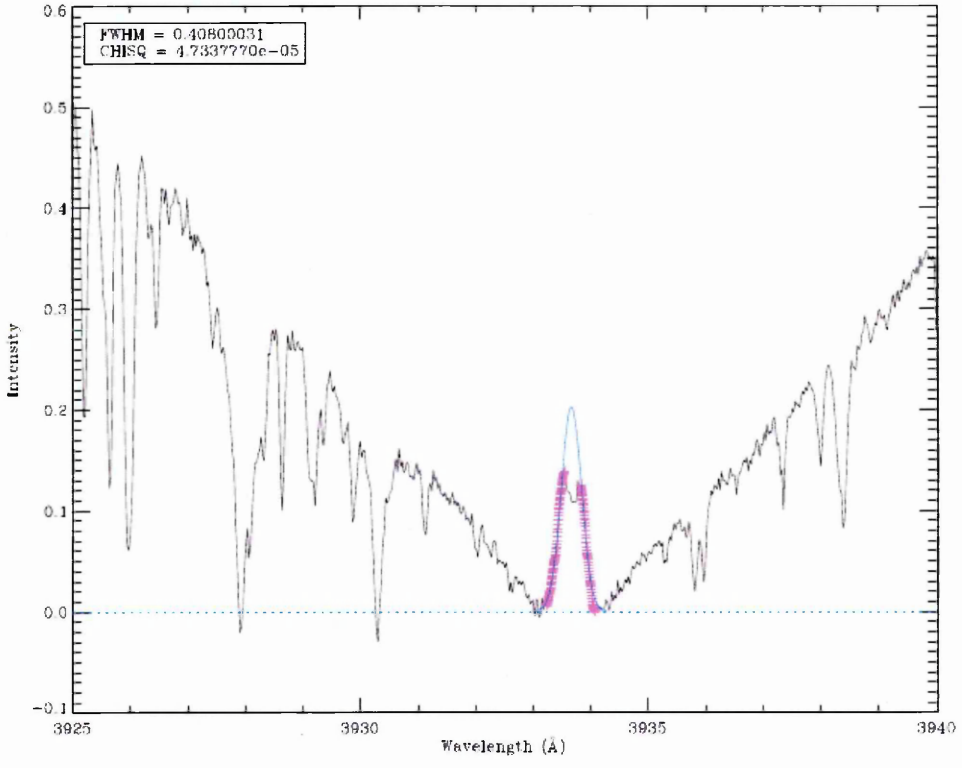

(e) HD 201219

Figure 5.4: Line profile showing the Gaussian fit of the emission from the Ca II H & K lines. The crosses inform the Gaussian fit. (cont.)

active of the stars showing activity is HD 18803.

To check for the linearity, the logarithm of W_0 was plotted against $\log g$ as seen in Fig. 5.5.

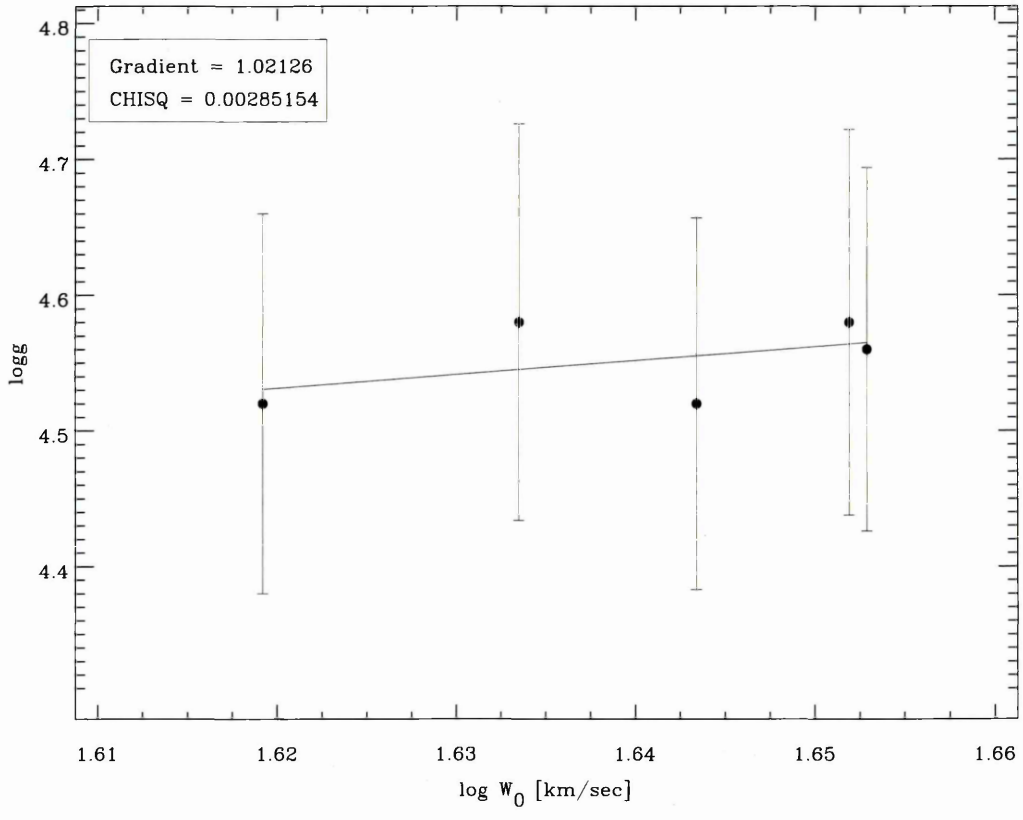

Figure 5.5: The correlation between the logarithm of FWHM and surface gravity. The fit appears flat rather than showing a linearity, which could be due to the small number of stars in the sample.

There is no conclusive linear fit, as indicated by the large chi-squared value of 0.00285. Given the small number of stars in the sample, there could still be linearity between the surface gravity and $\log W_0$ if more stars had been included. Additionally, the $\log g$ range of the stars is very small so there is no large baseline for the fit.

5.5 Measurement of chromospheric activity

Collisional and radiative processes allow the formation of spectral lines. In Sun-like chromospheres, as the stars in this analysis have, collisional terms should dominate

the source functions of ionised metals whilst neutral metals are radiatively dominated [74]. The assumption of LTE breaks down in the cores of Ca II H & K lines which are formed high in the chromosphere. The number of collisional events in the surrounding plasma increases, changing the atmospheric structure and causing the emission reversal at the line cores.

In a similar way to the Wilson-Bappu effect (see Section 5.4), core emission in the Calcium II H and K lines serves as an indicator of stellar chromospheric activity, which is correlated with stellar age [70]. There will be a greater amount of chromospheric emission in younger stars than older stars, allowing an approximate age order for the younger stars to be determined by looking at this emission.

One method of measuring this for all stars rather than just the stars with the chromospheric emission is to measure the integral of the area around the Calcium II H and K lines. The smaller the area, the younger the star.

This integral was performed by first normalising the lines at two fixed regions in the wings: 3931.365 – 3931.822 Å and 3937.519 – 3937.835 Å. These normalisation regions are highlighted in the black boxes in Figure 5.6. Two fixed points within the normalisation regions - 3931.593 Å and 3937.677 Å - were then used as the boundaries of the integration region. The IDL integral function[1] calculates the area between the spectrum and 0 rather than the area between 1 and the spectrum, as required. To counteract this, the integral obtained for below the spectrum is subtracted from the total integration area of $3931.593 \leq x \leq 3937.677$ and $0 \leq y \leq 1$, giving the integration values in Table 5.6.

[1] `http://www.astro.washington.edu/docs/idl/cgi-bin/getpro/library28.html?INTEGRAL`

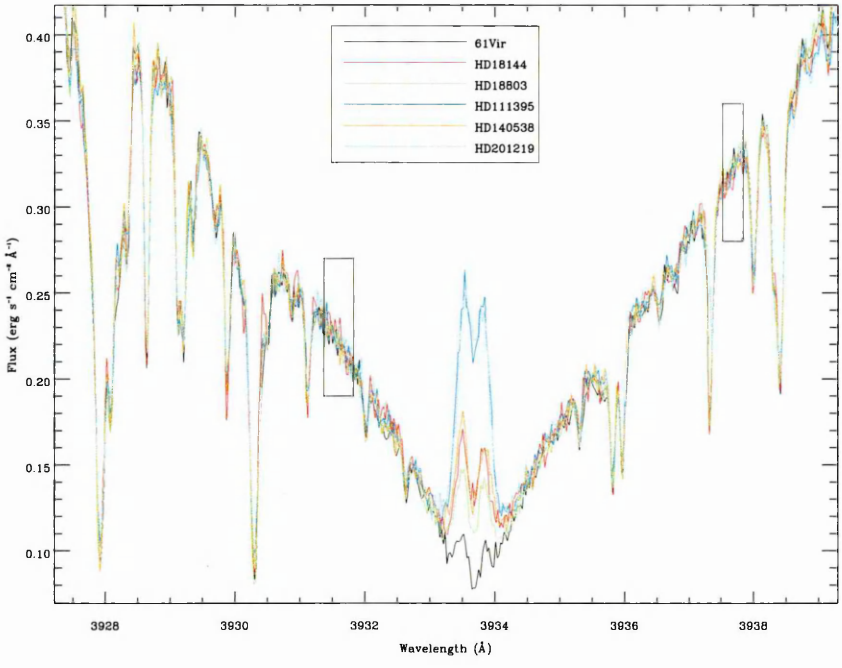

Figure 5.6: Calcium II K line at 3933Å. Showing emission for the stars with emission. Boxes show areas where the normalisation occurred.

Table 5.6: Values of the integral for the Ca II K line taken between 3931.593 and 3937.677 .

Star	Integral (Å)
61Vir	1018.03
HD18144	940.71
HD18803	977.09
HD111395	986.55
HD140538	989.89
HD201219	934.92
HD223498	1021.71
HD47127	1014.53
HD51219	1015.17
HD58781	1019.87

5.6 Determination of age order

After looking at the various age determination methods, an approximate age order was determined. This was done by seeing which star appeared to be the youngest most

often over the various methods, and then the second youngest and so on. Table 5.7 details the age order for each method. All the stars which had a Lithium abundance and for which the Wilson-Bappu effect could be measured were automatically placed in the younger half of the age range.

Table 5.7: Order of stars from youngest to oldest according to each method of age determination.

log g	HR diagram	Lithium	Wilson-Bappu	Chromospheric activity
HD 201219	HD 111395	HD 140538	HD 111395	HD 201219
HD 18144	HD 201219	HD 111395	HD 201219	HD 18144
HD 111395	HD 140538	61 Vir	HD 140538	HD 18803
HD 18803	HD 18803	HD 201219	HD 18144	HD 111395
HD 140538	61 Vir	n/a	HD 18803	HD 140538
61 Vir	HD 18144	n/a	n/a	HD 47127
HD 223498	HD 223498	n/a	n/a	HD 51219
HD 58781	HD 58781	n/a	n/a	61 Vir
HD 51219	HD 47127	n/a	n/a	HD 58781
HD 47127	HD 51219	n/a	n/a	HD 223498

The proposed age order for the stars from youngest to oldest is as follows:

- HD 201219
- HD 111395
- HD 140538
- HD 18144
- HD 18803
- 61 Vir
- HD 58781
- HD 223498
- HD 47127

- HD 51219

This age order was adopted as it was the most representative based on all the information. HD 111395, although potentially younger than HD 201219, is a BY Draconis variable and not a standard star and so it was not selected as the reference star for the further analysis. HD 223498 was shown to be an outlier using heliocentric space velocities (Figure 4.8d) as well as appearing as the oldest star by one of the methods, so was classed as older than HD 58781. In Chapter 6, this age order will be adopted for the analysis.

Chapter 6

The abundance relationship with stellar age

In this Chapter, the potential signature with age will be analysed with the differential abundance analysis being performed using the likely youngest star in the sample, HD 201219, rather than 61 Vir as the reference star. The parameters for the comparison stars had been redetermined relative to HD 201219 using the same technique as for 61 Vir. Table 6.1 shows the differential parameters relative to 61 Vir and relative to HD 201219 for all the stars using the line list from this study. As can be seen, the parameters are very closely matched with a largest effective temperature variation of 8 K, largest microturbulence variation of 0.2 km/s, largest surface gravity variation of 0.3 dex, and largest metallicity variation of 0.02 dex. The uncertainties on the parameters are much greater relative to 61 Vir than HD 201219. All of the stars were normalised relative to 61 Vir except for 61 Vir itself which was normalised relative to a synthetic spectrum. This will have removed some of the systematic effects between the stars and 61 Vir individually and therefore reduced the uncertainties on the parameters. It would be a useful test in the future to perform the normalisation of HD 201219 relative to a synthetic spectrum and normalise the stars relative to HD 201219 to observe any differences in the uncertainties. This wasn't possible during the course of this work.

Table 6.1: Table showing the differential parameters - $T_{\rm eff}$ (K), $\upsilon_{\rm mic}$ (kms^{-1}), log$g$ (ms^{-2}), [Fe/H](dex) - with errors in brackets for the sample of stars using my line list when compared against 61 Vir and HD 201219.

		61 Vir	HD 201219
61 Vir	$T_{\rm eff}$	n/a	5693 (123)
	$\upsilon_{\rm mic}$	n/a	1.04 (0.05)
	log$g$	n/a	4.48 (0.139)
	[Fe/H]	n/a	0.055 (0.159)
HD 111395	$T_{\rm eff}$	5760 (4)	5768 (86)
	$\upsilon_{\rm mic}$	1.15 (0.05)	1.16 (0.06)
	log$g$	4.54 (0.048)	4.57 (0.134)
	[Fe/H]	0.134 (0.084)	0.136 (0.165)
HD 140538	$T_{\rm eff}$	5795 (4)	5801 (53)
	$\upsilon_{\rm mic}$	1.06 (0.06)	1.08 (0.05)
	log$g$	4.53 (0.050)	4.55 (0.137)
	[Fe/H]	0.096 (0.088)	0.097 (0.174)
HD 18144	$T_{\rm eff}$	5674 (15)	5675 (139)
	$\upsilon_{\rm mic}$	1.05 (0.01)	1.07 (0.04)
	log$g$	4.58 (0.056)	4.59 (0.145)
	[Fe/H]	0.144 (0.091)	0.144 (0.151)
HD 18803	$T_{\rm eff}$	5773 (1)	5779 (141)
	$\upsilon_{\rm mic}$	1.07 (0.04)	1.08 (0.05)
	log$g$	4.52 (0.049)	4.55 (0.140)
	[Fe/H]	0.146 (0.088)	0.148 (0.169)
HD 201219	$T_{\rm eff}$	5751 (9)	n/a
	$\upsilon_{\rm mic}$	1.14 (0.07)	n/a
	log$g$	4.55 (0.051)	n/a
	[Fe/H]	0.154 (0.088)	n/a
HD 223498	$T_{\rm eff}$	5665 (1)	5673 (77)
	$\upsilon_{\rm mic}$	1.05 (0.06)	1.06 (0.06)
	log$g$	4.42 (0.045)	4.44 (0.146)
	[Fe/H]	0.222 (0.089)	0.224 (0.154)
HD 47127	$T_{\rm eff}$	5723 (1)	5732 (112)
	$\upsilon_{\rm mic}$	1.08 (0.06)	1.10 (0.07)
	log$g$	4.36 (0.058)	4.39 (0.139)
	[Fe/H]	0.146 (0.093)	0.148 (0.171)
HD 51219	$T_{\rm eff}$	5728 (4)	5735 (89)
	$\upsilon_{\rm mic}$	1.07 (0.07)	1.09 (0.05)
	log$g$	4.41 (0.042)	4.43 (0.139)
	[Fe/H]	0.047 (0.089)	0.048 (0.173)
HD 58781	$T_{\rm eff}$	5726 (4)	5732 (61)
	$\upsilon_{\rm mic}$	1.07 (0.06)	1.09 (0.056)
	log$g$	4.44 (0.061)	4.46 (0.144)
	[Fe/H]	0.150 (0.090)	0.151 (0.166)

6.1 Trend with age

Figures 6.1 to 6.10 show the elemental abundance for all of the stars relative to HD 201219. It can be seen that the relative abundance of the low atomic number elements (C, N, O, Mg, Al, S, Sc hereafter known as light elements) increases with age.

The abundances of the elements around the iron peak remain steady with respect to iron; any fluctuations can be attributed to noise. The elements Y and Sr, and the rare earth elements, are depleted in older stars.

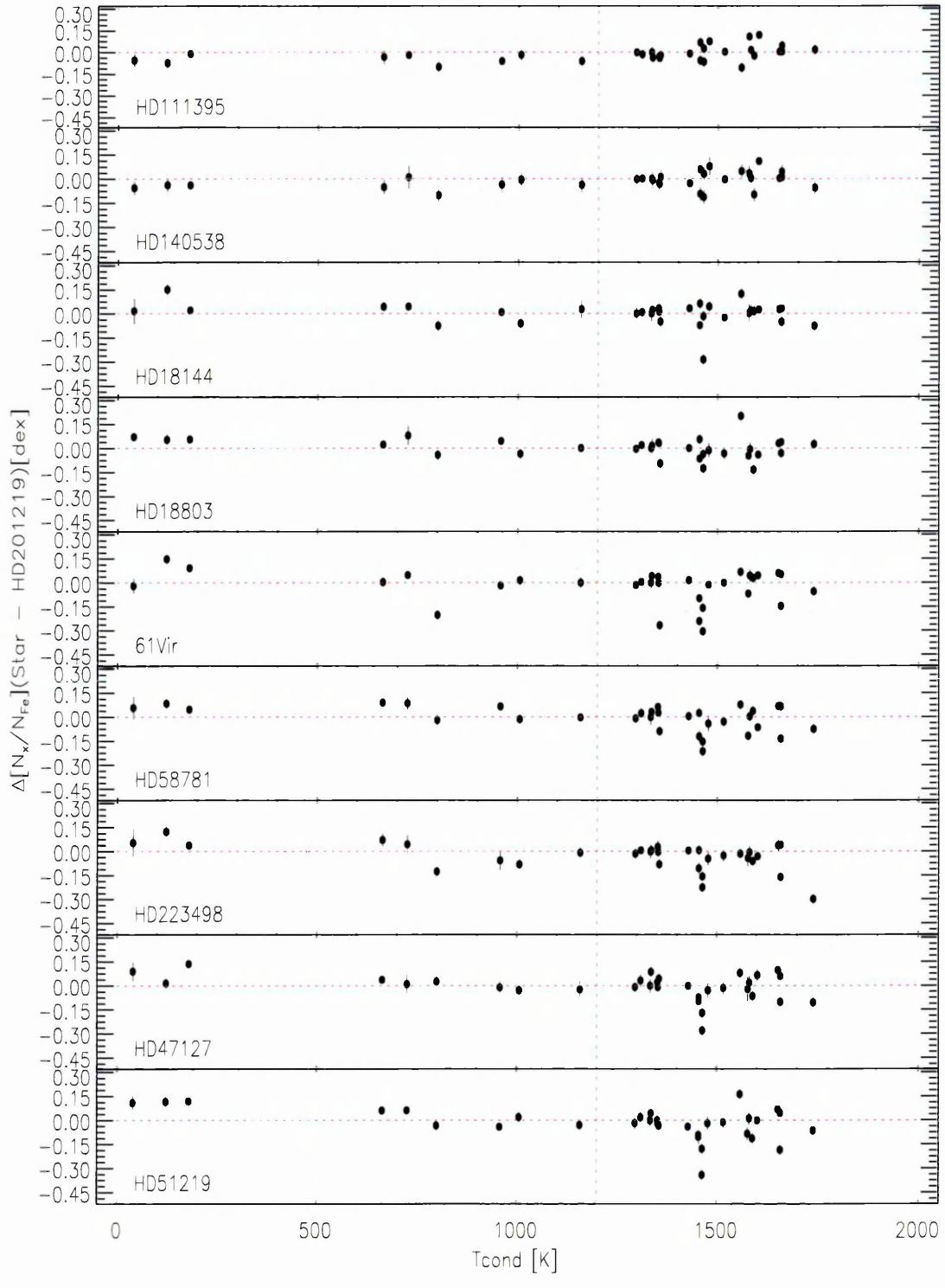

Figure 6.1: Differential abundance ratios for each star relative to HD 201219 vs. dust condensation temperature. All abundances are relative to Fe. The red dotted line at 1200 K represents the break assumed between volatile and refractory elements in [49]. The panels are arranged with the youngest (HD 111395) uppermost, with age increasing downwards.

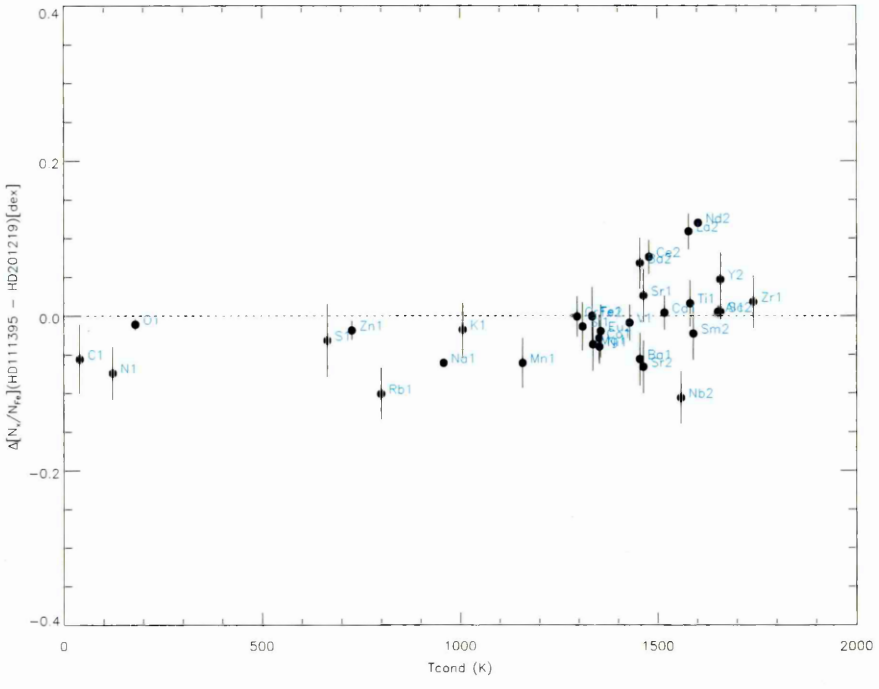

Figure 6.2: Differences between [X/Fe] of HD 111395 and HD 201219 as a function of condensation temperature $T_{\rm cond}$. For elements where multiple lines were measured, the error was calculated as the standard deviation from the average. Where only 1 line could be measured for a certain element, the uncertainty was determined through the visual convergence of the standard deviations of multiple lines (see Section 3.6.1). The dotted line at y=0 represents the abundance being equal between the stars.

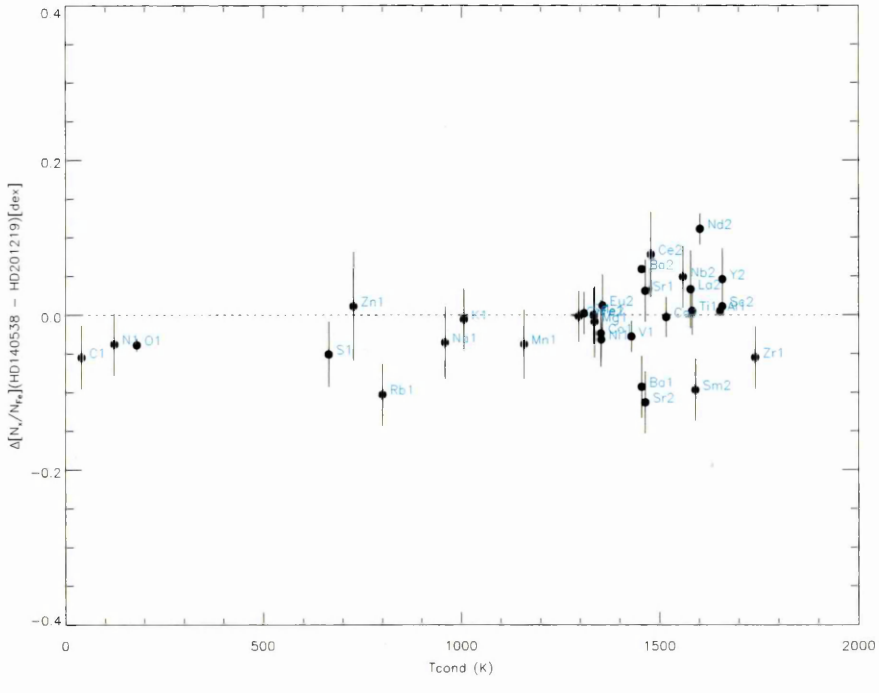

Figure 6.3: Same as Figure 6.2, but for HD 140538 and HD 201219.

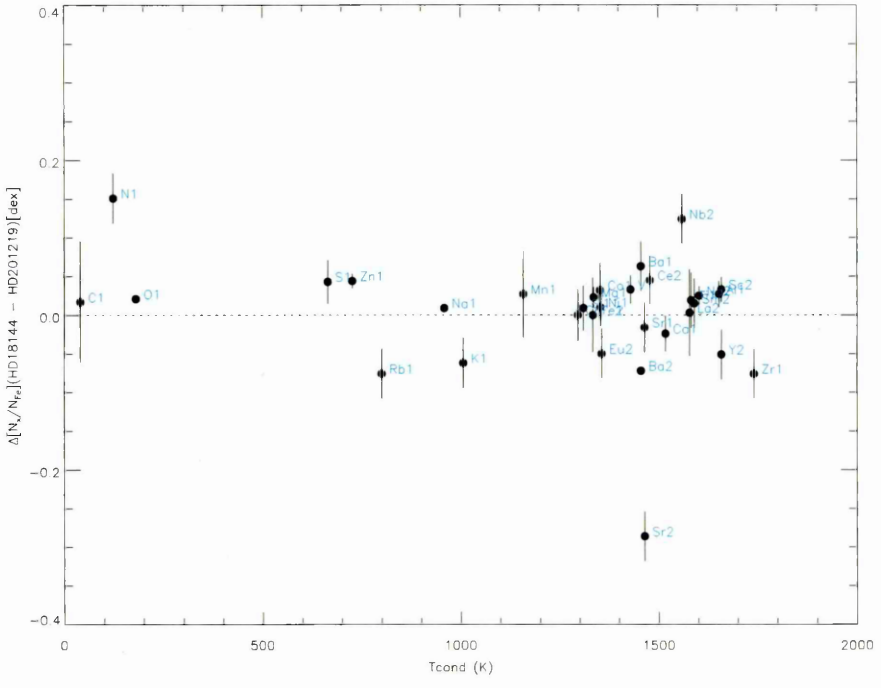

Figure 6.4: Same as Figure 6.2, but for HD 18144 and HD 201219.

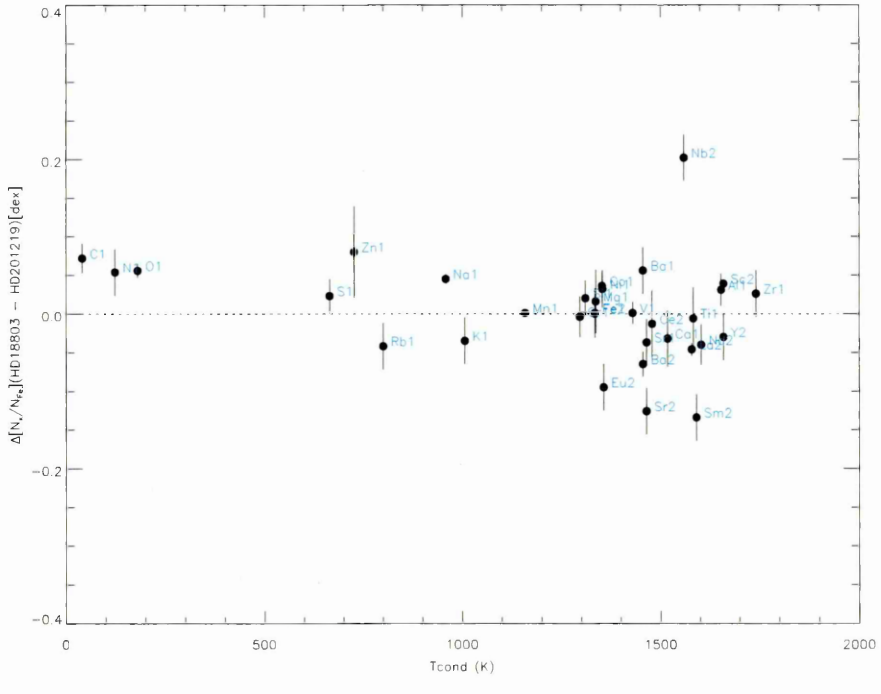

Figure 6.5: Same as Figure 6.2, but for HD 18803 and HD 201219.

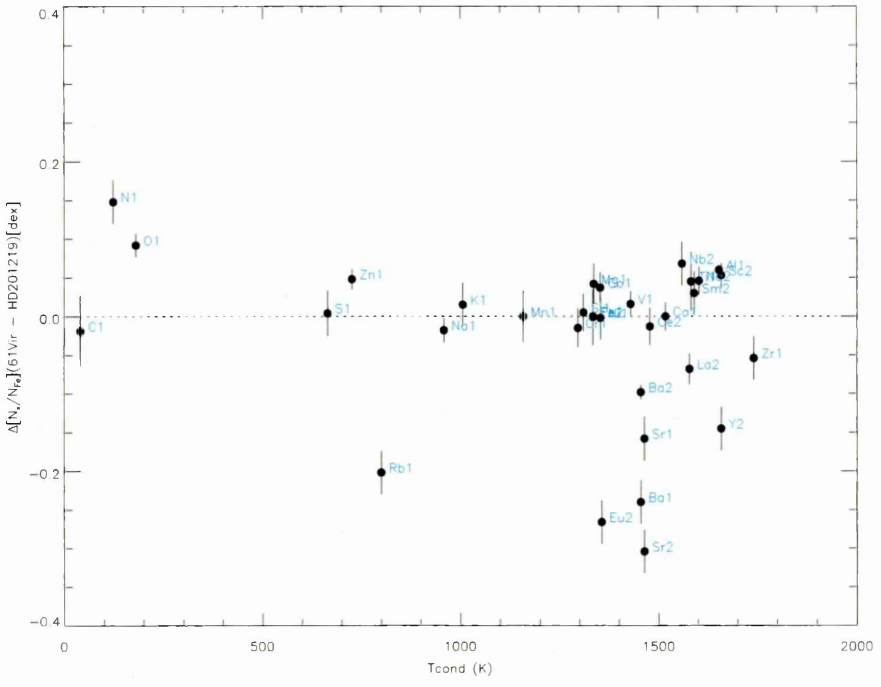

Figure 6.6: Same as Figure 6.2, but for 61 Vir and HD 201219.

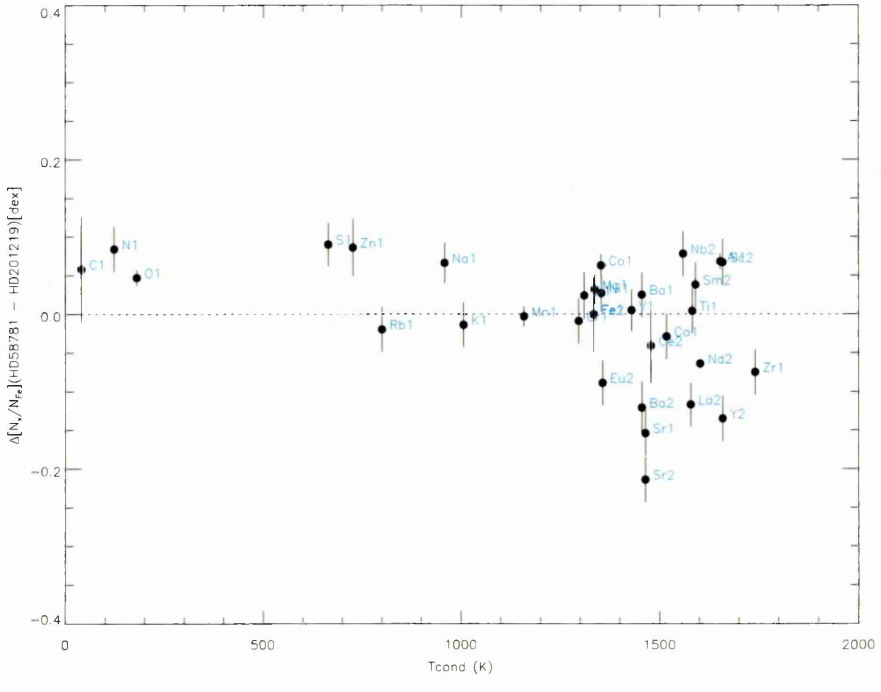

Figure 6.7: Same as Figure 6.2, but for HD 58781 and HD 201219.

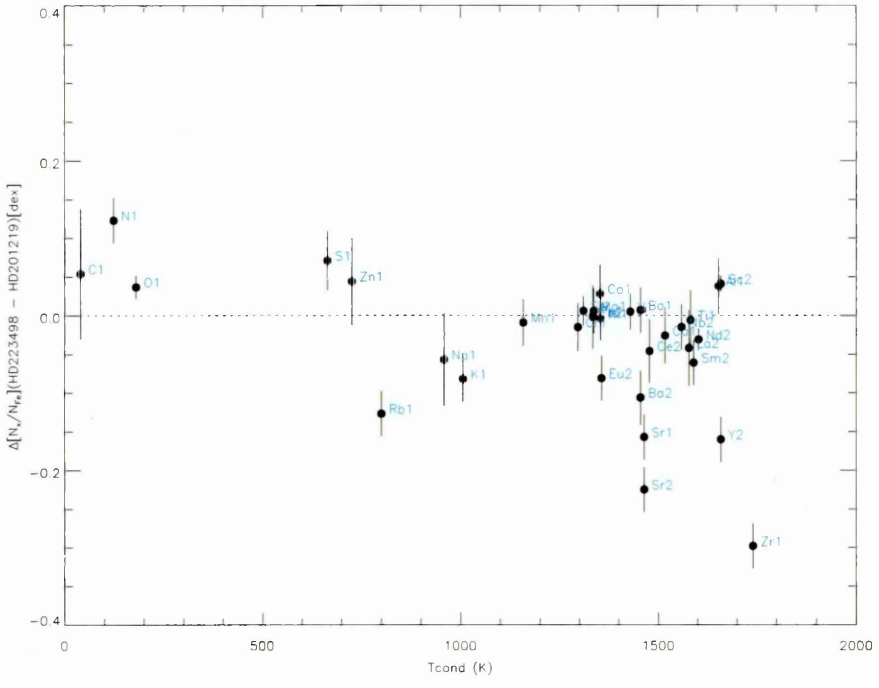

Figure 6.8: Same as Figure 6.2, but for HD 223498 and HD 201219.

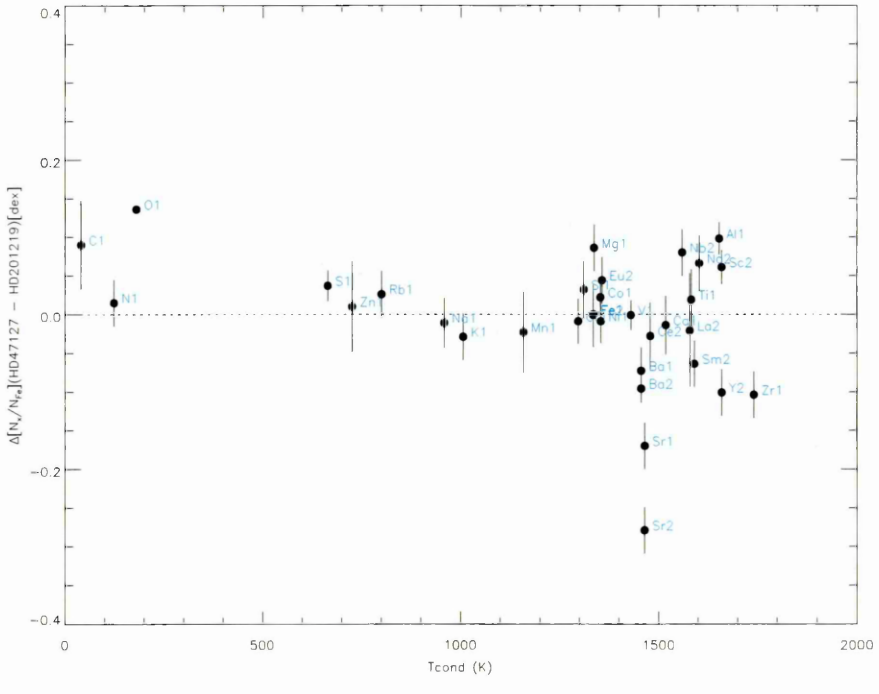

Figure 6.9: Same as Figure 6.2, but for HD 47127 and HD 201219.

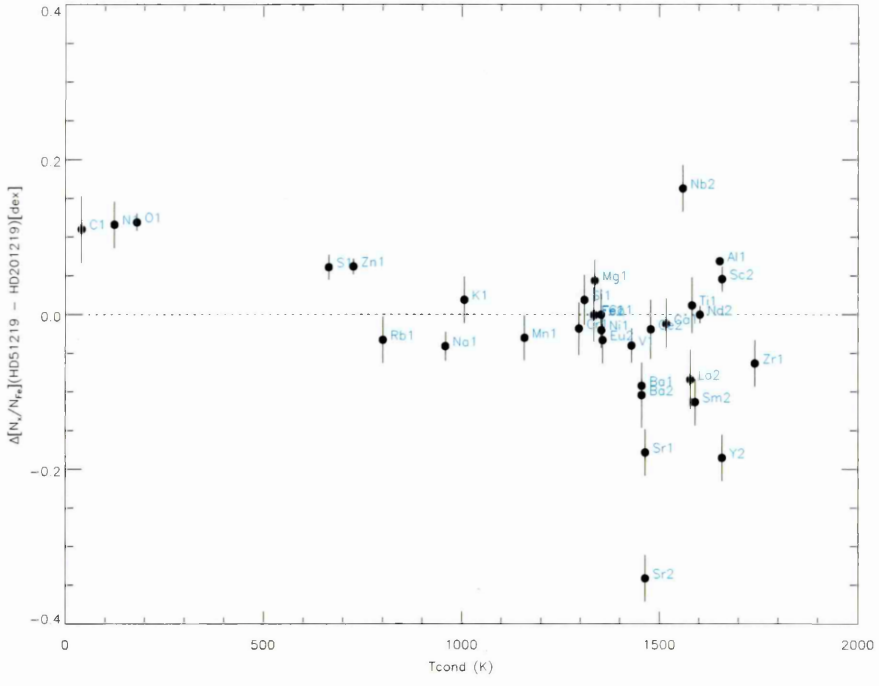

Figure 6.10: Same as Figure 6.2, but for HD 51219 and HD 201219.

6.1.1 Age correlation

The age order of the stars was roughly determined using the methods described in Chapter 5. To test the age order I used the relative abundances of Scandium calculated in the analysis detailed in Section 6.1. Scandium was chosen for 3 reasons: the gradient of the linear fit was high, the gradient is present at more than 4σ, and it had the highest number of lines of all the elements with a high degree of correlation. The test was done with both the ages derived using my temperatures from the HR diagram and the ages from Casagrande et al. [9]. Figure 6.11 shows the fit for Scandium for both the proposed ages and the BaSTI[1] expectation ages determined by Casagrande et al. [9] (see Table 6.2 for ages).

[1] http://basti.oa-teramo.inaf.it/index.html

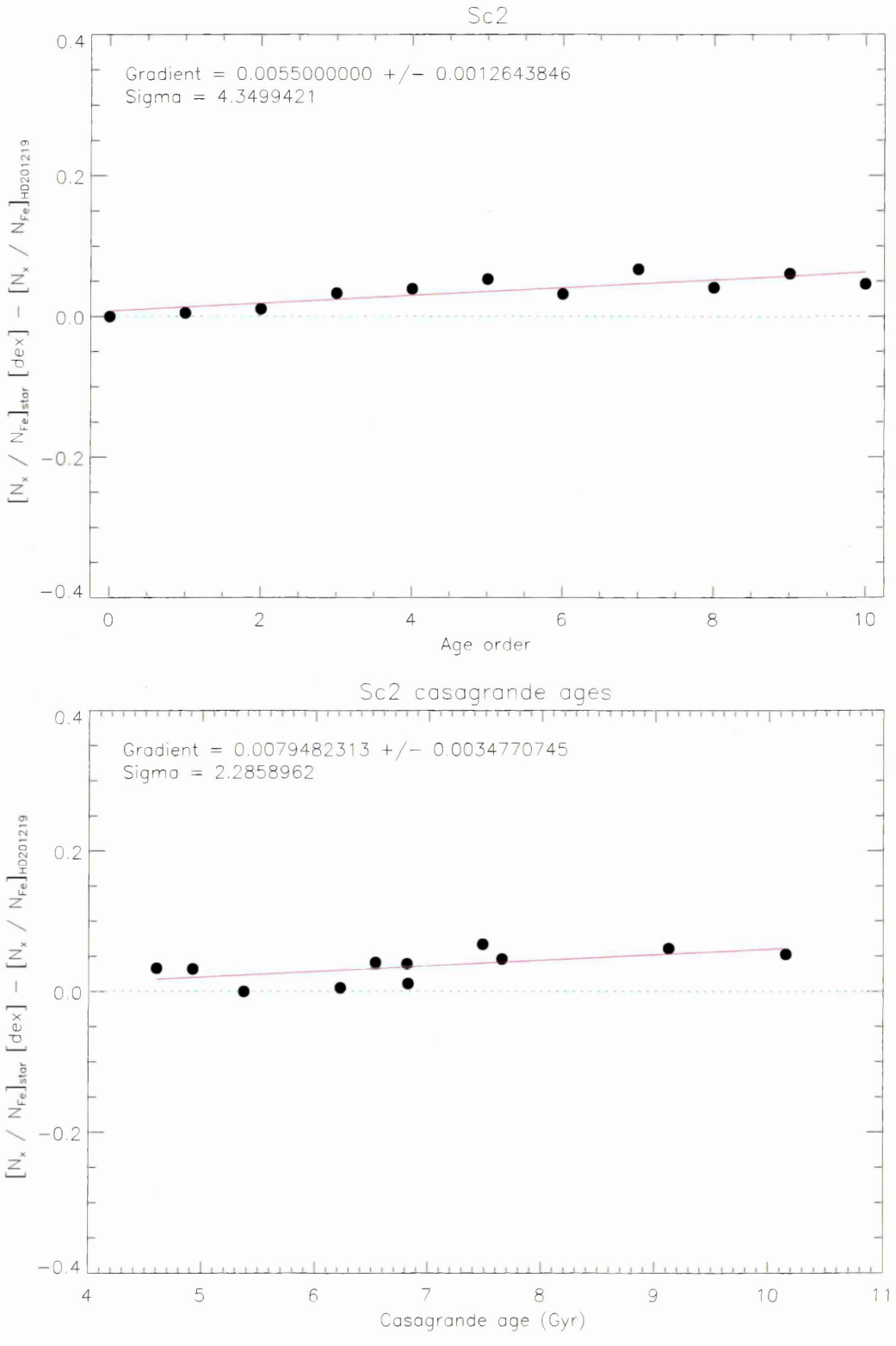

Figure 6.11: Differential abundances against the proposed age order from Chapter 5 (top) and the ages from Casagrande et al. [9] (bottom). In the top figure, the stars have been assigned a number from 0 to 10 based on their age from youngest to oldest and given an equal age separation.

Table 6.2: Table showing the ages of the stars using my line list and the Casagrande catalogue. As can be seen, the derived ages differ by up to 5 Gyr for some stars but the order of age mostly agrees with stars only shifting in one position in the order between the analyses.

	Age (Gyr) My line list	Age (Gyr) Casagrande
61 Vir	6.35	6.53
HD 111395	0.53	4.92
HD 140538	2.98	6.22
HD 18144	8.58	7.48
HD 18803	6.35	6.82
HD 201219	1.30	5.37
HD 223498	11.10	6.81
HD 47127	12.60	7.65
HD 51219	12.90	10.15
HD 58781	12.20	9.12

To test that the correlation for Scandium was not obtained by chance, I resampled the data using the bootstrap method. Each star was once again assigned a number from 0 to 10 using a random number generator and σ was calculated for the trend. This was repeated 40 million times and a histogram showing the fraction of trends at each σ was produced (Fig. 6.12).

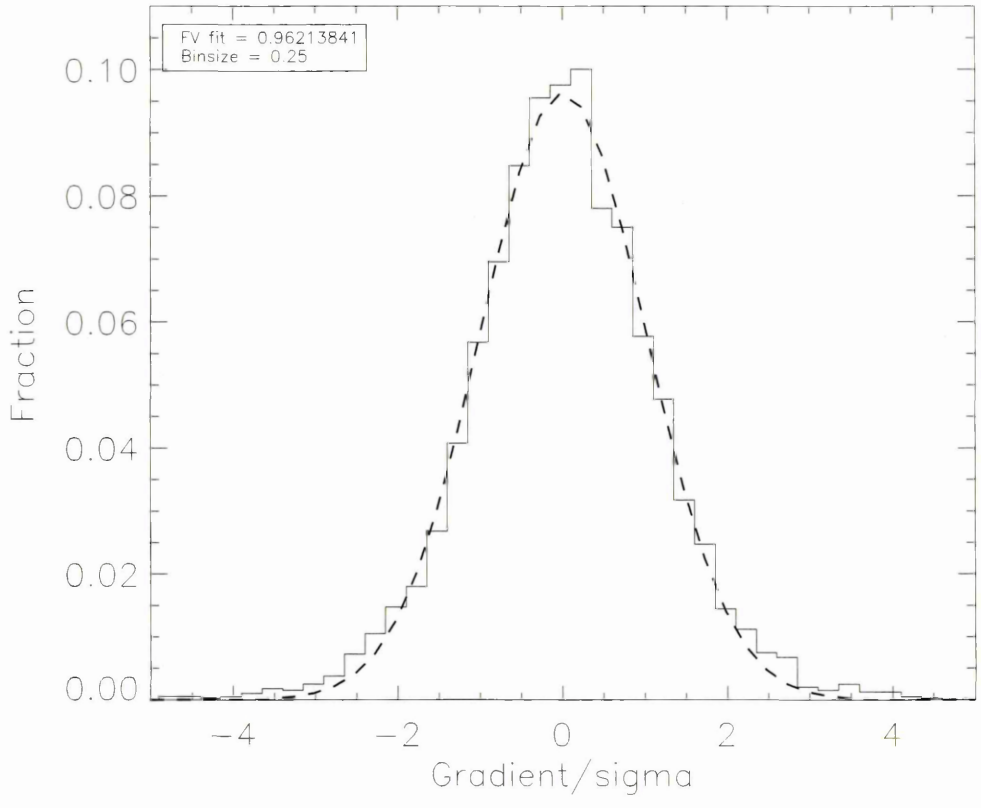

Figure 6.12: Histogram showing the fraction of trends at each sigma using 40 million times.

A gaussian was fitted to the histogram and an F-statistic test was applied to the sample to determine the significance. A significance of 0.97 was achieved showing that the histogram does take the form of a gaussian. The more commonly performed Kolomogrov-Smirnov test was not used due to the large sample size.

A final test on the probability of the proposed age order being achieved by coincidence was performed with the probability of getting 4.35σ being 1.36×10^{-5}. It is therefore highly unlikely that the correlation for Scandium was obtained by chance.

6.2 Age relationship

To explain the abundance differences against stellar age I have separated the elements into categories based on the method through which they are created by stars. The categories adopted were:

- Elements found most commonly in the Universe e.g. Carbon, Nitrogen, Sodium and Aluminium
- Alpha elements produced by type II supernovae
- Iron peak elements
- Elements produced by explosive nucleosynthesis of massive stars
- R-process elements
- S-process elements
- Elements produced through both the R and S-processes.

The relation between elemental abundance and age is directly related to Galactic chemical evolution. These categories were chosen to illustrate this relation as elements within each category should exhibit the same evolutionary trends and characteristics. Figure 6.13 shows the differential abundance for each element against iron abundance.

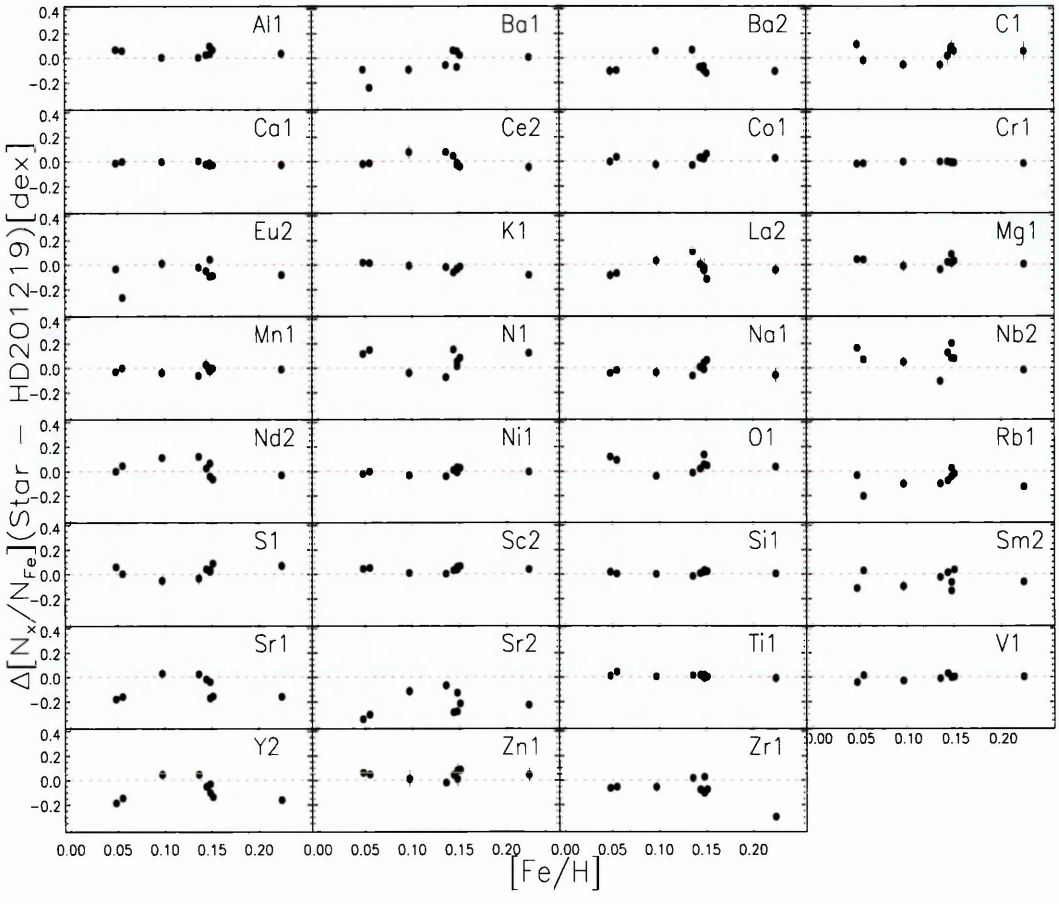

Figure 6.13: Differential abundance ratios against iron abundance for all elements measured relative to HD 201219. The abundances are relative to iron.

6.2.1 Iron

The behaviour of iron across all the stars in age order is depicted in Figure 6.14. There should be a trend showing that the younger the star, the greater the iron abundance but the uncertainty is too large for this to be seen. This means the stars have cosmologically similar ages and therefore are from the same stellar population.

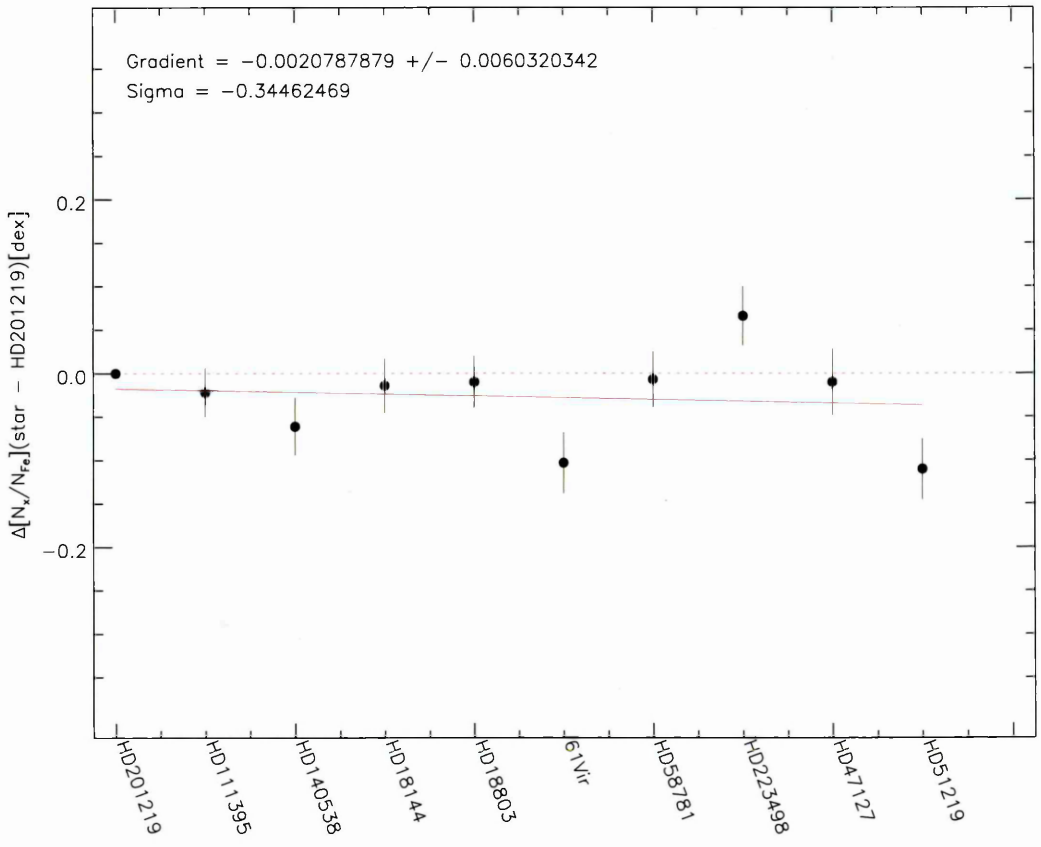

Figure 6.14: Differential abundance ratios of iron for each star relative to HD 201219. The y-axis shows the iron abundance of each star. The red dotted line represents the abundance being equal in the selected star and HD 201219. The red solid line shows the best fit through the stars. Sigma gives the 1 sigma uncertainty on the linear fit.

Iron is produced in type Ia supernovae, which occur when accreting white dwarfs reach their critical mass. As such, they appear late in the evolution of the Galaxy as intermediate-mass stars need to evolve to white dwarfs and their companions have to evolve off the main sequence. Consequently, due to the progressive iron enrichment of the star forming regions of younger stars through Galactic chemical evolution, older stars will be depleted in iron compared to younger stars.

6.2.2 Carbon, Nitrogen, Sodium, Aluminium

Almost all stars in the universe - massive stars, type Ia supernovae, AGB stars - should contribute to the formation of aluminium and sodium. Likewise, carbon is produced by a wide variety of stars including low and intermediate mass stars, and massive stars

according to the Geneva models [17]. Nitrogen is mostly produced by AGB stars of between 4 and 7 $M_{\odot}$ within the CNO cycle. As such, there is an overlap between the stars that produce these elements, enabling a comparison.

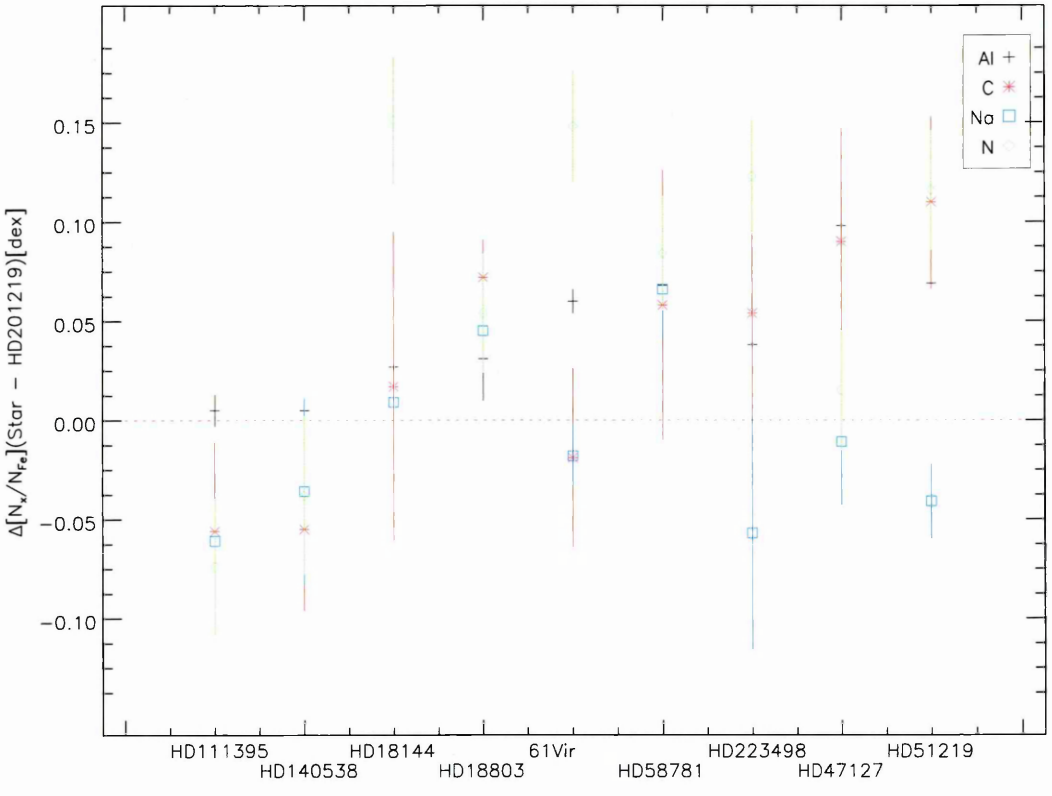

Figure 6.15: Differential abundance ratios for the elements produced in most stars for each star relative to HD 201219. The x-axis shows the age order at equal spacing for each star. The red dotted line represents the abundance being equal in the selected star and HD 201219. The abundances are relative to iron.

In Figure 6.15 it can be seen that the variation of aluminium and sodium relative to Iron is relatively flat whilst nitrogen and carbon fluctuate in a similar manner to oxygen (see Figure 6.18), possibly due to the CNO cycle. However, it must be remembered that there is a single line of nitrogen included in this analysis. The slight fluctuation of carbon and nitrogen can be seen in the Chiappini et al. [12] models (see Figure 6.16) whilst the Kobayashi et al. [40] model (see Figure 6.17) shows aluminium and sodium to be flat, as observed.

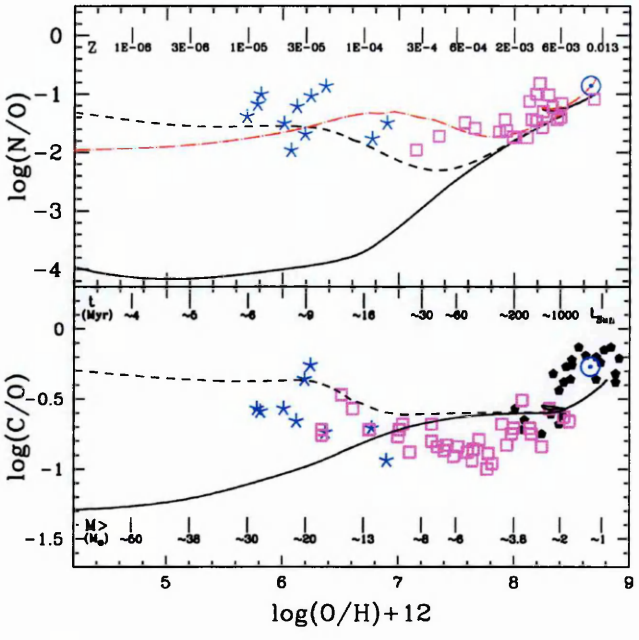

Figure 6.16: Figure 4 taken from Chiappini et al. [12] showing the abundance evolution of Nitrogen and Carbon, reproduced here for clarity. The data points are from Israelian et al. [37] (large squares), Spite et al. [71] (asterisks) and Nissen [52] (pentagons). The solar abundances (circle with dot) are from Asplund et al. [4].

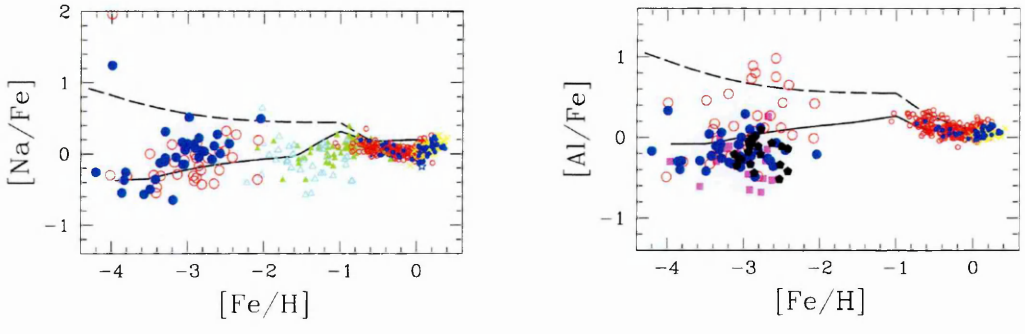

Figure 6.17: Figures 14 and 15 taken from Kobayashi et al. [40] showing the abundance evolution of Sodium and Aluminium, reproduced here for clarity. The data points represent a combination of thin disk (small circles, crosses, stars, triangles) and halo stars (large circles, squares, pentagons).

6.2.3 Type II supernovae alpha elements

Massive stars, greater than 8 $M_{\odot}$, have lifetimes of 15-80 million years. At the end of their life they will have an inner core of iron group elements surrounded by shells of lighter elements. When the iron core contracts, the star will explode, generally producing a type II supernova. The rapid evolution of massive stars means that type II

supernovae are often observed in areas of star formation, where the supernovae explosion has enriched the environment. Alpha elements are produced by the capture of alpha particles in massive stars before they reach the supernova phase. As such, when the star explodes, the alpha elements are released into the interstellar environment. The alpha elements synthesized by type II supernovae measured in this analysis are: Calcium, Magnesium, Oxygen, Sulphur and Silicon. Models from Timmes et al. [75] show that, in general, the abundances of these elements should increase with the age of the star formed from an ISM enriched in alpha elements.

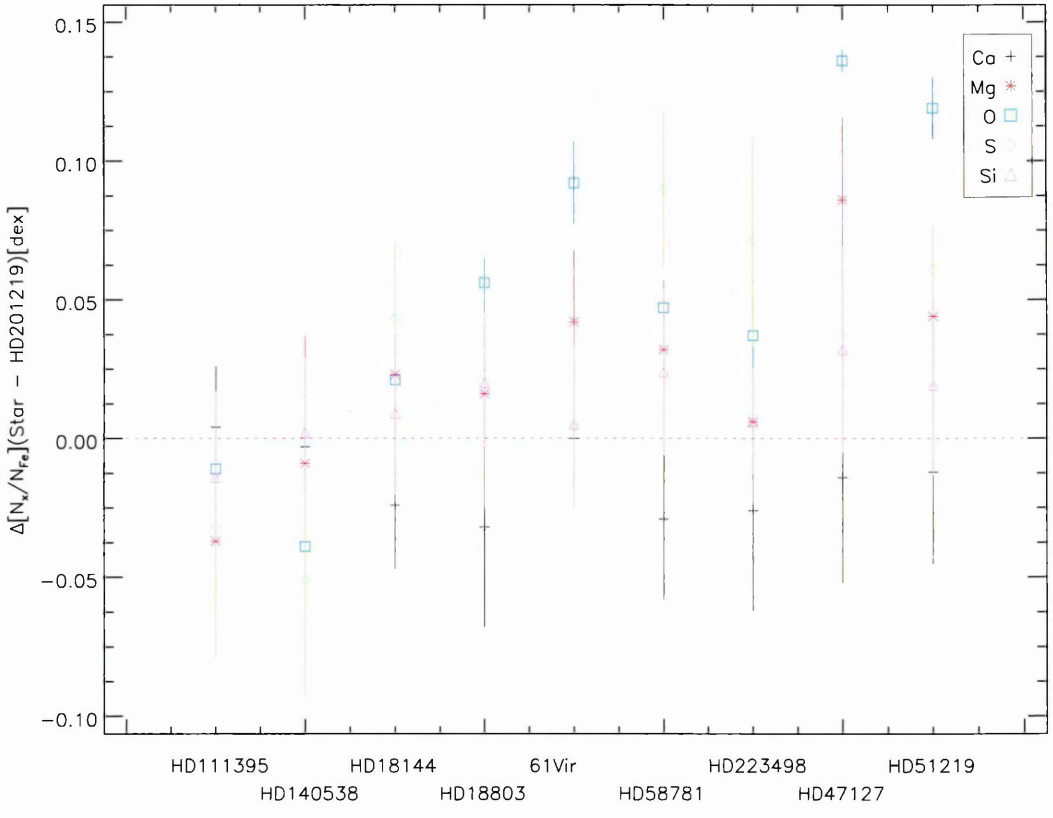

Figure 6.18: Differential abundance ratios for the alpha elements for each star relative to HD 201219. The x-axis shows the age order at equal spacing for each star. The red dotted line represents the abundance being equal in the selected star and HD 201219. The abundances are relative to iron.

Figure 6.18 shows that the older the star (eg. HD 51219) the greater the abundance of each of the alpha elements. There is a clear decrease in almost all of the elements with age. Calcium is the exception as it appears to be almost flat across all the stars

but it is expected to show less of a decrease than the other elements.

6.2.4 Iron peak elements

The iron peak elements are produced by type Ia supernovae. These supernovae make the largest contribution to the iron abundance in the galaxy, producing both iron and elements with similar atomic number. The iron peak elements are expected to behave in the same way as iron.

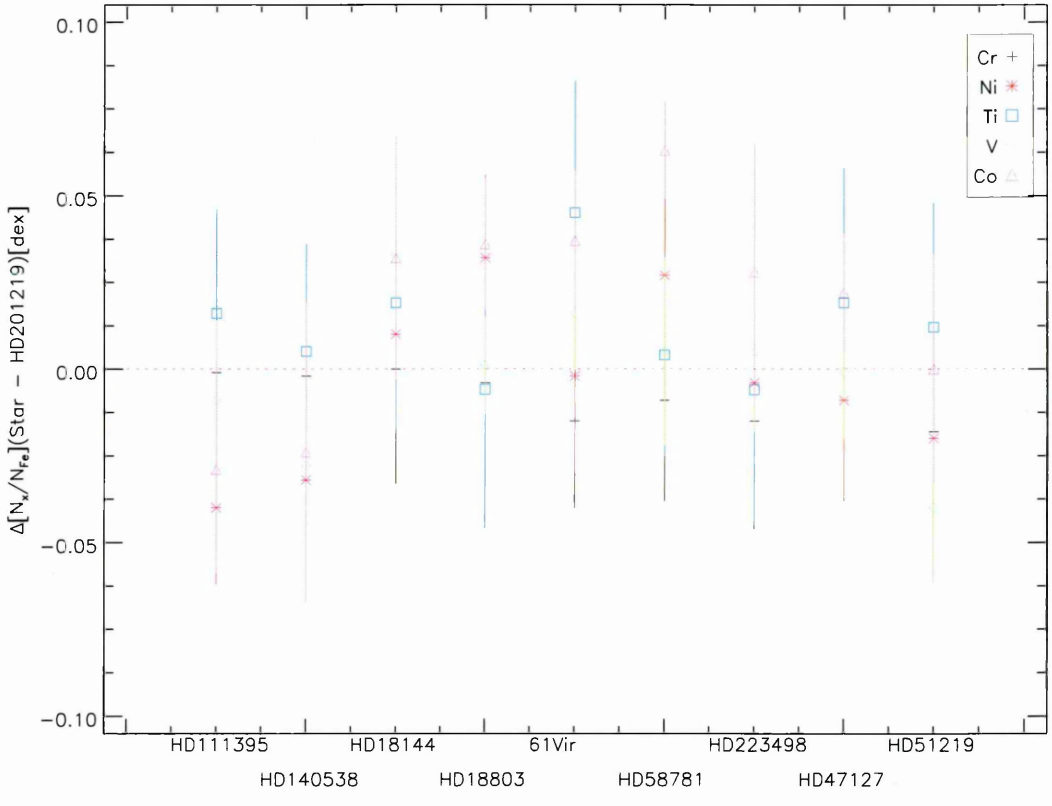

Figure 6.19: Differential abundance ratios for the iron peak elements for each star relative to HD 201219. The x-axis shows the age order at equal spacing for each star. The red dotted line represents the abundance being equal in the selected star and HD 201219. The abundances are relative to iron.

Figure 6.19 shows the iron peak elements. As the abundances for each element are relative to iron in the figure, it was expected that they would remain constant with time. There is no trend with age showing that these elements increase in abundance in the same manner as iron, as expected. This plot agrees with the abundance variations

against iron seen in Edvardsson et al. [16].

6.2.5 Explosive nucleosynthesis of massive stars elements

The expected behaviour of elements produced from explosive nucleosynthesis is not clear from models or observations. Scandium and Zinc are both produced through explosive nucleosynthesis of massive stars. Both elements are around the iron peak - Scandium is lighter whilst Zinc is heavier than Iron - and both are subject to hyperfine structure in solar type stars. They are non-transition elements and only have one stable isotope.

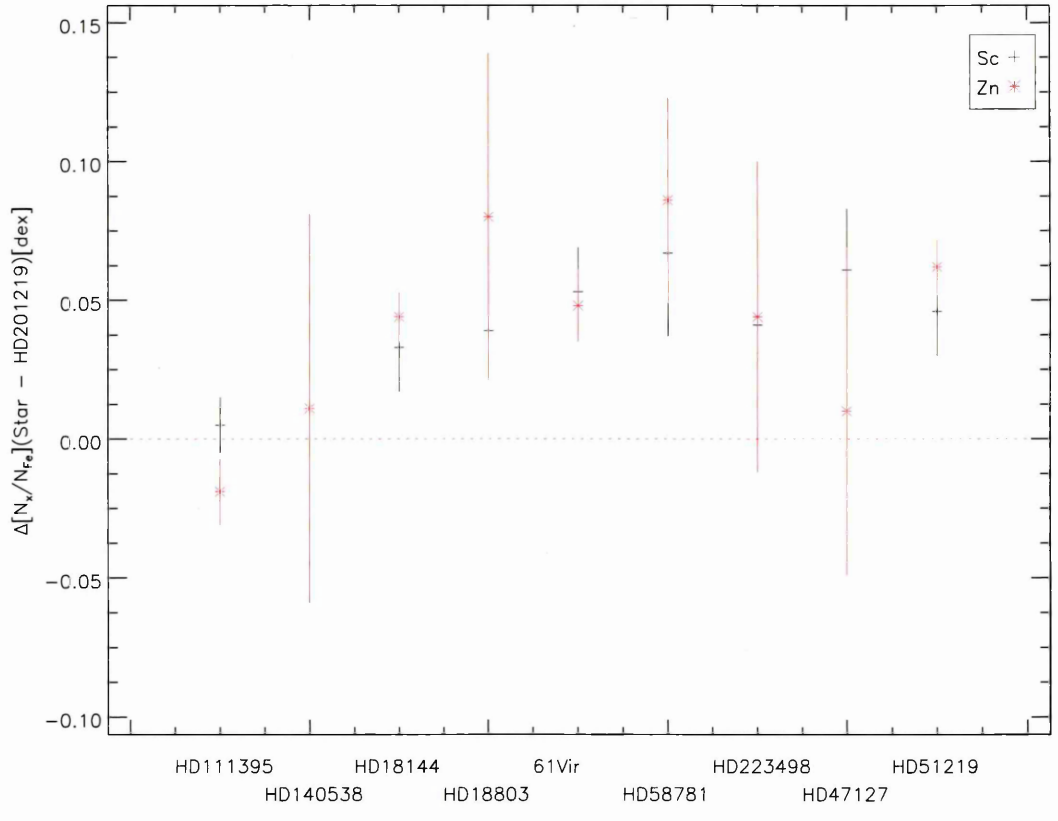

Figure 6.20: Differential abundance ratios for the elements produced by explosive nucleosynthesis of massive stars for each star relative to HD 201219. The x-axis shows the age order at equal spacing for each star. The red dotted line represents the abundance being equal in the selected star and HD 201219. The abundances are relative to iron.

It can be seen in Figure 6.20 that the elements vary in a similar way to some of the

type II supernova alpha elements, although there is no discernible trend with age. The trend for Scandium and Zinc is the same.

6.2.6 R-process elements

The process of a massive star collapsing was discussed in Section 6.2.3. The core collapse of a star will leave a core residue in the form of a neutron star as well as a type II supernova. R-process elements are produced by core-collapse supernovae and neutron star mergers. In both these types of stars, rapid neutron capture occurs due to the high neutron pressure and temperature [29, 84]. Carbon, Silicon and Oxygen burning produce free neutrons. In neutron capture reactions, nuclei capture the free neutrons to create heavier isotopes of the same element. Neutrons continue to be captured until a radioactive and unstable isotope is formed. This isotope will decay, emitting an electron, to create a new element. The nucleus will then resume neutron capture or undergo beta decay until a stable nucleus is produced. These are then ejected into the ISM by neutrino driven winds.

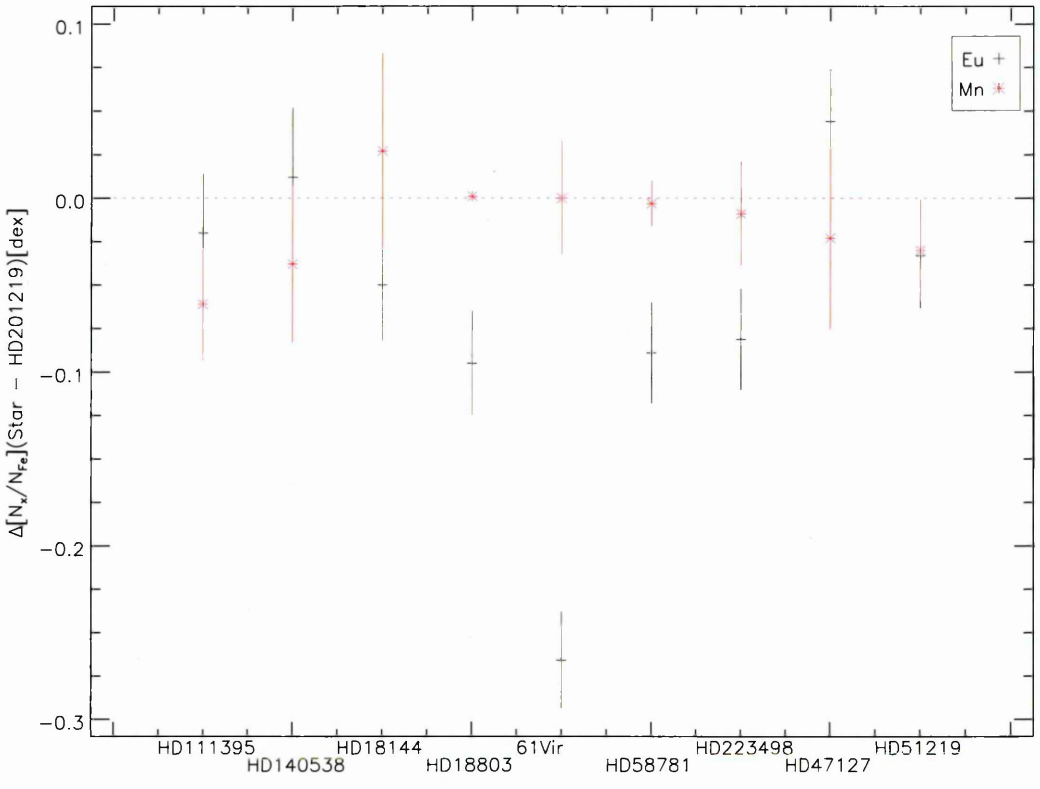

Figure 6.21: Differential abundance ratios for the r-process elements for each star relative to HD 201219. The x-axis shows the age order at equal spacing for each star. The red dotted line represents the abundance being equal in the selected star and HD 201219. The abundances are relative to iron.

Europium and Manganese are seen to behave in different ways in Figure 6.21. Whilst Manganese remains relatively flat with age, Europium fluctuates extensively, showing depletion in 61 Vir. Europium is heavier than Manganese and so is produced later in the stellar lifecycle. If 61 Vir was not formed in a region with much Europium, it may not have as much Europium as the other stars. As with Nitrogen, the abundance has been derived from a single line and so the abundance has to be taken with caution.

6.2.7 S-process elements

Prior to becoming white dwarfs or supernovae, stars evolve to the AGB phase. Many elements are produced in AGB stars through neutron capture reactions. Carbon, Silicon and Oxygen burning produce free neutrons. In neutron capture reactions, nuclei

capture the free neutrons to create heavier isotopes of the same element. Neutrons continue to be captured until a radioactive and unstable isotope is formed. This isotope will decay, emitting an electron, to create a new element. The nucleus will then resume neutron capture or undergo beta decay until a stable nucleus is produced.

S-process elements are produced by AGB stars. In the s-process, the beta decay is on a fast timescale whilst the neutron capture is slow. S-process elements are produced by low and intermediate mass AGB stars. The elements are released into the ISM through winds, as with the r-process elements.

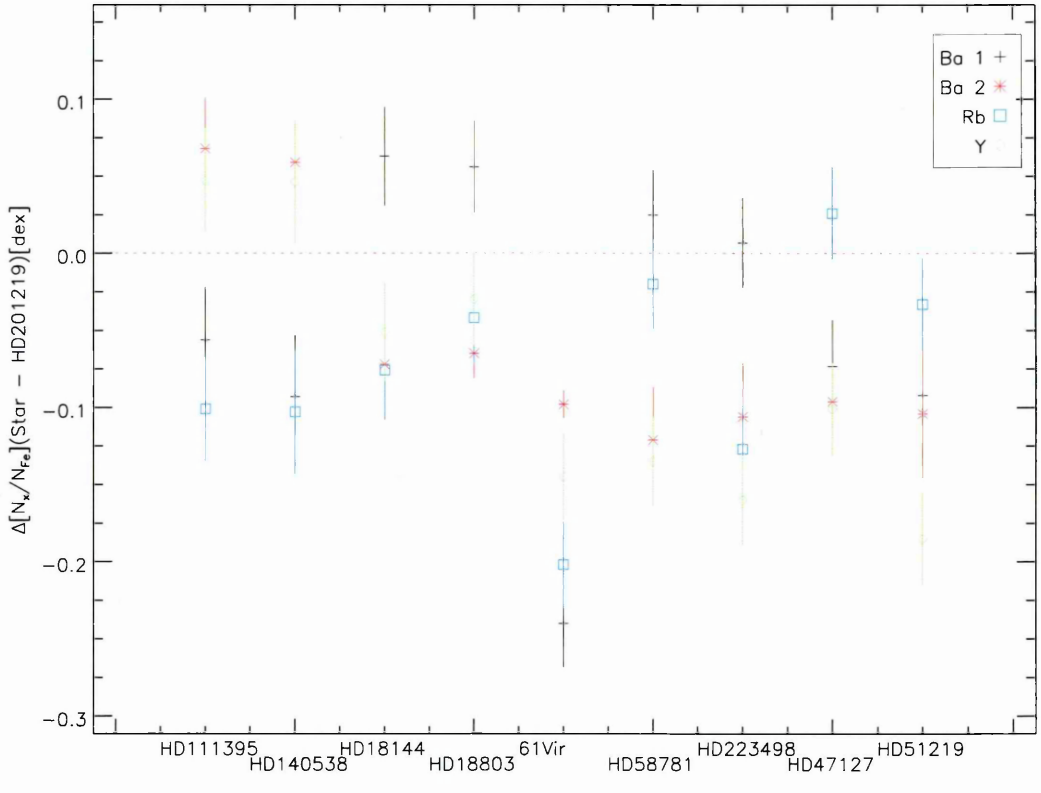

Figure 6.22: Differential abundance ratios for the s-process elements for each star relative to HD 201219. The x-axis shows the age order at equal spacing for each star. The red dotted line represents the abundance being equal in the selected star and HD 201219. The abundances are relative to iron.

As with the Europium, the s-process elements behave differently in 61 Vir than the other stars, showing a significant depletion in comparison. It can be seen in Figure 6.22, although there is a large scatter, the abundances decrease with age.

6.2.8 R and S process elements

There are a set of elements which are produced by both the r and s-process and so these have been grouped together as they show different trends to the separate r and s-process elements. A large scatter is expected in these elements due to the variety of stars producing them.

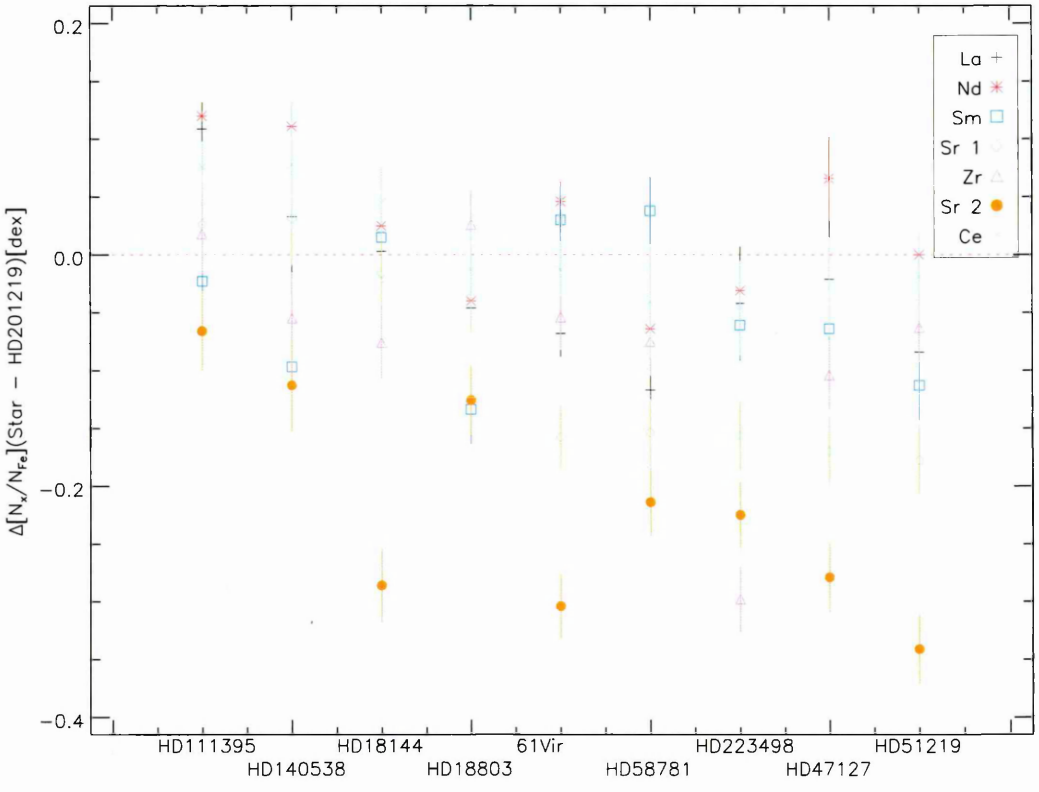

Figure 6.23: Differential abundance ratios for the elements produced by both the r and s process for each star relative to HD 201219. The x-axis shows the age order at equal spacing for each star. The red dotted line represents the abundance being equal in the selected star and HD 201219. The abundances are relative to iron.

The general trend in Figure 6.23 is that the abundance increases with age. However, some elements such as neodymium are almost flat whilst others like samarium show a strong variation. The elements showing the strongest variations are produced by a combination of low-intermediate mass AGB stars as well as stars greater than 12 $M_{\odot}$. The behaviour of these elements agrees with that seen in Cescutti et al. [10] for strontium.

6.2.9 Trend in stars with similar parameters

A sample of the stars showed similar $T_{\rm eff}$, $\upsilon_{\rm mic}$, $\log g$ and metallicity so I decided to see how the behaviour of the elements varied across these stars. I included the differential abundance of HD 201219 against itself to get a clearer view of how the abundances varied from the normalised ones.

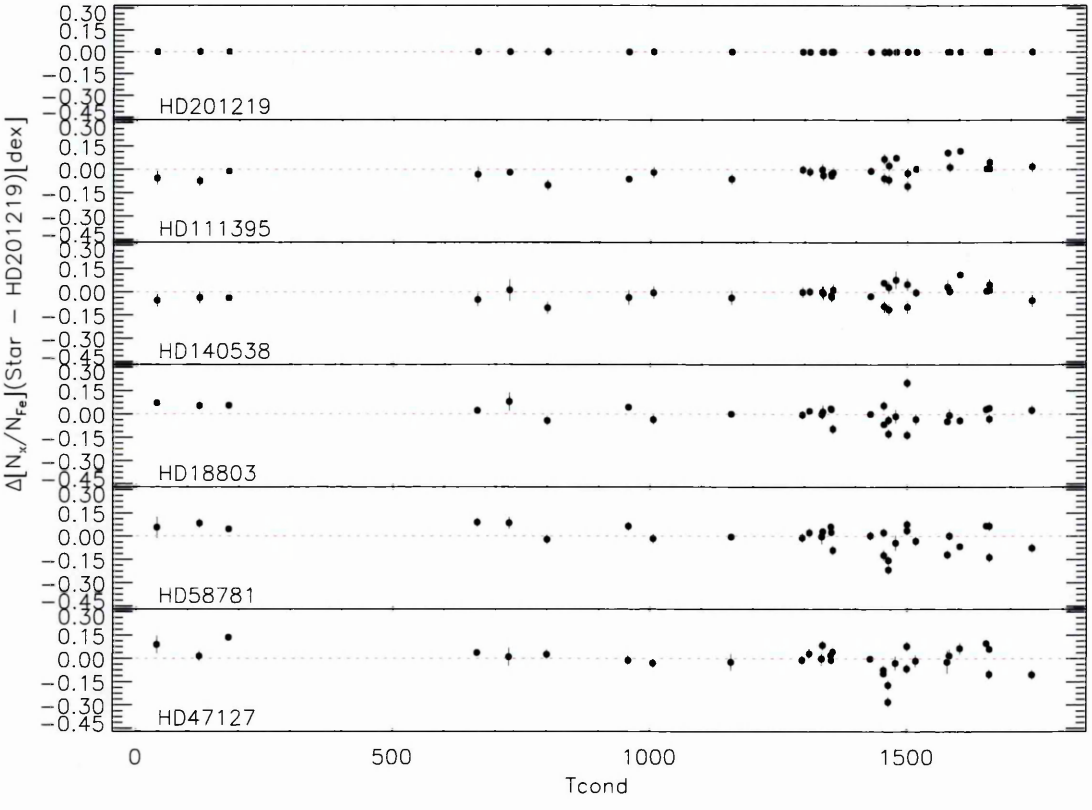

Figure 6.24: Differential abundance ratios for each star relative to HD 201219 vs. dust condensation temperature for stars with similar parameters. All abundances are relative to Fe. HD 201219 has been included in the top panel to show how the abundances vary from zero. The panels are arranged with age increasing downwards.

Figure 6.24 shows the differential abundances of the stars starting from youngest (HD 201219) to oldest star (HD 47127). The elements can be split into approximately 3 groupings based on condensation temperature:

1. elements with $0 < T_{\rm cond} < 500$ K (C, N, O);

2. elements with $500 < T_{\rm cond} < 1200$ K (S, Zn, Rb, Na, K, Mn);

3. elements with 1200 < T_{cond} < 1800 K (Cr, Si, Fe, Mg, Co, Ni, Eu, V, Ba, Sr, Ce, Ca, Nb, La, Ti, Sm, Nd, Al, Sc, Y, Zr).

Whilst the elements in groups 1 and 2 don't vary too much from star to star, there is a clear change in some of the elements in group 3, notably at ~1500 K. There is a set of elements which are more depleted in the oldest star and gradually increase in abundance as the stars reach a similar age to HD 201219.

6.3 Discussion

The original question in this work questioned whether a planetary signature could be identified in a planet-hosting star through a differential abundance analysis. It was seen in Chapter 4 that such a signature could not be observed in this work. An alternative signature was potentially identified with links to the stellar age. It has been seen in this Chapter that there is a likely correlation between differential abundance and the age of stars. Different groups of elements behave in different ways due to the way by which the elements are produced in the Universe. In this section I will discuss possible scenarios for the signatures observed.

6.3.1 Light elements

The elements described as "light" in Section 6.1 - C, N, O, Mg, Al, S, Sc - are elements that would be produced by type Ia supernovae and shell burning in type II supernovae. In Meléndez et al. [51] it is shown how type Ia supernova pollution would affect the abundances of Manganese, Cobalt and Iron. If there were supernova pollution causing an anomalous change in the local environment, it would have been expected that younger stars would be more highly enriched in these light elements than older stars as they would have been formed in areas where the gas was enriched. In this analysis the opposite is seen albeit there is not a strong gradient as there is a small metallicity range. However, the gas in which the younger stars were formed should still be enriched so

this does not explain the opposite signature.

Again in Meléndez et al. [51], the affect of AGB pollution is shown for Nitrogen. If there was AGB pollution, Nitrogen would differ significantly from Carbon and Oxygen. This analysis shows a similar trend between Carbon, Nitrogen and Oxygen and so it is unlikely that there is AGB pollution.

6.3.2 Yttrium, Strontium and the rare earth elements

The changes with Yttrium, Strontium and the rare earth elements are significant with time. The older the star, the more depleted it is in these elements. This is due to the fact that these elements are produced by AGB stars predominately. The changes in these elements are as expected, reflecting Galactic evolution.

6.3.3 The cosmochemical evolution of planets

A plausible explanation for the signature observed in the light elements is based on planets and planetesimals.

If the older stars had exo-asteroids or close-in disrupting planets, under the correct conditions, these would have disintegrated and accreted onto the stellar photosphere, enriching it. These conditions include spin-up caused by fission, deforming the planet and its trajectory towards the central star [64], hydrodynamical forces present in the protoplanetary disk during formation [21] or mass shedding due to rotation [39]. The light elements which are depleted in the younger stars are elements which are known to be found in planets and meteorites within our Solar System. It is therefore likely that any other asteroids or planets would be formed of similar elements. The iron abundance is not enhanced in older stars as the planetary iron abundance would be the same as the stellar iron abundance. At the time when the younger stars formed, the environment would have been more enriched in iron and heavier elements due to Galactic chemical evolution. Any exo-asteroids and exoplanets formed in these stars would have different elemental abundances and so accretion from these would cause

different changes in the elemental signature.

The *Kepler* mission is indicating that at least 50% of all stars have a planet [24]. Additionally, some stars have been observed with disintegrating planets or planetessimals accreting onto the star - WASP-12 and KIC-1255 for example. It could be that any stars which are no longer seen with planets, may have had planets which have since disintegrated. Evidence of disintegrating planets in the stellar photosphere may not have been seen for the following reasons:

1. It is too small to be observed and will never be observable.

2. The uncertainties are too large given current technology. This can be rectified by performing a differential rather than absolute abundance analysis. The benefits of differential abundance analysis are clearly seen in the solar signature observed in Meléndez et al. [49] which had not been visible in absolute abundance analyses. In the future, it may be possible to further decrease the uncertainties given technological advancement.

3. Chemical evolution models have been tuned to mask the signature. If the signature had been observed when some models were first being developed, the signature may have been assumed to be general noise and therefore hidden into other model parameters.

As seen in this analysis, the small uncertainties have yielded information on Galactic evolution that has been previously unobserved outside of models. The possibility that we could be seeing the chemical signatures of the planets and planetessimals that formed early on in the Universe cannot be dismissed.

Chapter 7

Summary

I utilised high resolution and high SNR spectra of 10 stars with similar intrinsic parameters and from similar Galactic locations. In this thesis I presented the results on the differential abundance analysis of the planet-hosting star 61 Vir relative to stars with similar intrinsic parameters.

In Chapter 2, I discussed my method for a more precise continuum placement than used in previous work. The normalisation was manually performed over a range of 6000Å. It is unique in that the normalisation of the comparison stars was performed against the normalised spectrum of the planet host star 61 Vir instead of using a synthetic spectrum.

I then determined the parameters of each of the stars with more lines and robust statistics than seen in any previous work. I selected a large number of lines for measurement which were each checked for hyperfine structure and possible molecular blends, removing those with either characteristic. This resulted in a line list consisting of 584 lines compared to 299 lines in Meléndez et al. [51].

In Chapter 4 61 Vir is investigated through the study of 9 comparison stars with similar stellar parameters. These stars are studied in the context of being examples of similar stars which do not host planets and as such should allow for a planetary signature to be observed, if one exists. The use of high resolution and high SNR spectra from ESPaDOnS has allowed the differential abundances of many elements, including

elements with higher condensation temperatures not measured in Meléndez et al. [49], to be determined. This allows the behaviour of the refractory material to be further constrained. For some elements, I achieved better precision than seen in Meléndez et al. [49] and Meléndez et al. [51]. The differential abundance pattern of 61 Vir relative to the average of the comparison stars was scrutinised with no planetary signature detected. 61 Vir was then analysed relative to each star individually. Performing the differential abundance analysis with reference to each star individually allows for any elemental differences that may have been neutralised upon averaging the stars to become apparent. A variable abundance signature was observed with indications that the variability was due to stellar age. Other reasons were investigated such as the selection of comparison stars, the line list, Galactic location, and the stellar ages. The line list selection was investigated by using the line list from Meléndez et al. [51]. This showed significant differences where elements had been included in my line list but not the Meléndez list, especially for elements with higher condensation temperatures. However, this difference was not related to the signature observed. After the other possibilities had been excluded, the ages of the stars were investigated.

An age order for the stars was determined using a combination of surface gravity measurements, the location of each star on the HR diagram, the lithium abundance, the Wilson-Bappu effect and the chromospheric activity measurement. The star which appeared to be the youngest over the most methods was assigned as the youngest star, and then the second youngest and so on. The age order showed that 61 Vir was in the middle of the stellar sample for age, explaining why the refractory signature was enhanced for some stars and depleted for others. The importance of accurate measuring of stellar ages can be seen clearly in this work. The stars in the sample potentially differ by 10 Gyr which can cause significant stellar evolutionary differences and differences in the Galactic chemistry, which we are observing.

To ascertain whether the signature could be linked to stellar age, the differential abundance analysis was re-performed using the youngest star as the reference star in Chapter 6. By performing the differential abundance analysis against the youngest star

rather than the planet-hosting star, it was hoped that any peculiarities in the planet-hosting star would be eliminated, leaving only the age signatures which showed that older stars were more enhanced in light elements than younger stars. It has proved difficult to draw a definitive conclusion as to the cause of the age variable abundance signature though it seems most plausible that it is caused by the accretion of planets and planetessimals onto the older stars which is linked to Galactic chemical evolution. González Hernández et al. [28] observed that, when subtracting Galactic chemical evolution affects from planet-hosting stars with possible trends, the observed trend became almost negligible, which further suggests that the signatures of Galactic chemical evolution are being observed in these stars. Traditional observations of Galactic chemical evolution require hundreds of stars to show a variation whereas this analysis has shown the same results using 10 stars.

7.1 Future Work

Meléndez et al. [51], Mack et al. [47] and Teske et al. [73] all performed high precision differential abundance analyses on one or two stars other than the Sun and observed abundance differences with condensation temperature. In this analysis, the abundance differences across 10 stars was observed, showing clear differing signatures from star to star, enabling the possible observation of Galactic evolutionary trends.

The small uncertainties and new information found in this analysis shows that all future abundance analysis work should be performed in this way. Most abundance analyses will use automated algorithms to normalise the spectrum whereas a manual normalisation gives far greater control, enabling broad lines to be normalised more accurately than most algorithms. It also prevents any lines from being normalised through the wrong points, modifying the equivalent width and consequently altering the abundances and parameters determined. It would be of value for work to be undertaken to develop a more robust method for automated normalisation that is equivalent to a normalisation performed manually. This could involve a standard automated pro-

cess with an algorithm which flags areas where the continuum match falls below a certain value over a certain spectral range thereby allowing the user to manually normalise that specific area.

To perform a high accuracy differential abundance analysis, the parameters of the comparison stars to be well constrained, including the ages. To search for differences between stars, the stars should ideally be the same age. With unknown stellar ages, potential signatures could be masked by evolutionary effects in the stars of different ages. This in turn means that the masses of stars is important as well. The GAIA observatory will provide high precision distances for many stars which will allow the ages to be better constrained.

There are many extensions to this work which could be performed to further explore the planet accretion theory. The first extension to this work would be to redo the analysis from Meléndez et al. [49] using the line list adopted in this analysis to see if the solar signature is still observable. Given that the main changes in the line list are related to the high condensation temperature elements this could prove significant. As previously stated, this was not possible during the constraints of this work.

The stellar sample analysed in this thesis were selected as stars that were close to each other on the HR diagram and assumed to be very similar. However, they may be on the same bit of the HR diagram but due to metallicity and mass, are actually following different tracks, explaining why the stars in this sample are so different in age. To test the hypothesis, one should analyse another series of stars which are in the same position on the HR diagram which have a wide range of ages. If they show the same signature as seen in this sample, then this could tell us about the cosmochemical evolution of planets and that the planets formed at the beginning of the universe changed with cosmochemistry.

A further extension to the work would be to select a larger sample of stars in a specific region and determine their ages before performing a differential abundance analysis. The ages should be determined by a variety of methods including spectropolarimetry for activity [54] using the $\log R'_{HK}$ values, and photometry for colour indices.

From this, a selection of stars close in age, effective temperature, surface gravity, microturbulence velocity and metallicity could be selected and differential abundance analysis performed to see if any potential planetary signatures, as in Meléndez et al. [49] can be seen.

Appendix A

Previous observations of the stars

This appendix contains information on the number of spectroscopic observations for each of the stars in this analysis. The following information is obtained from the HARPS, HIRES and UVES archives. The table contains the information on the number of spectra, the year the observations were taken and the PI involved. Where more than 100 observations were made, not all the PIs are listed.

Table A.1: Number of previous observations of the targets with HARPS, HIRES and UVES

	HARPS			HIRES			UVES			Combined
Star	Observations	Year	PI	Observations	Year	PI	Observations	Year	PI	
61 Vir	>100	various	Mosser	>100	2005-2008	Butler	10	2001	Paranal	>100
		various	Mayor		1998-99	Cook	14	2004	Silva	
	-	-	-		2004-05	Fischer	18	2006	Melo	
	-	-	-		2010	Howard	1	2012	Sousa	
	-	-	-		2005-2010	Marcy	-	-	-	
	-	-	-		2006	Shkolnik	-	-	-	
	-	-	-		2005-2010	Vogt	-	-	-	
HD 18144	-	-	-	6	1997-1999	Latham	-	-	-	6
HD 18803	-	-	-	>100	2009	Boruchi	-	-	-	>100
	-	-	-		2000-2010	Butler	-	-	-	
	-	-	-		1999-2005	Cochram	-	-	-	
	-	-	-		2005	Fischer	-	-	-	
	-	-	-		1996-2008	Marcy	-	-	-	
	-	-	-		2003-2008	Hillenbrand	-	-	-	
	-	-	-		2001-2007	Laughlin	-	-	-	
	-	-	-		1998	Lissauer	-	-	-	
	-	-	-		2004-2010	Vogt	-	-	-	
HD 47127	-	-	-	27	2005	Cochram	-	-	-	27
	-	-	-		1998	Latham	-	-	-	
HD 51219	-	-	-	16	2002	Butler	-	-	-	16
	-	-	-		1998-99	Latham	-	-	-	
	-	-	-		2001	Laughlin	-	-	-	
	-	-	-		1998-2004	Marcy	-	-	-	
	-	-	-		2005	Vogt	-	-	-	
HD 58781	-	-	-	29	1998-2010	Marcy	-	-	-	29
	-	-	-		1998	Latham	-	-	-	
	-	-	-		2000-2005	Vogt	-	-	-	
	-	-	-		2000-2002	Butler	-	-	-	
	-	-	-		2003-2004	Hillenbrand	-	-	-	
	-	-	-		2012	Howard	-	-	-	
	-	-	-		2014	Boyajian	-	-	-	
HD 111395	-	-	-	15	1997-2012	Marcy	-	-	-	15
	-	-	-		2001-2010	Vogt	-	-	-	
	-	-	-		2009-2012	Fischer	-	-	-	
	-	-	-		2012	Johnson	-	-	-	
	-	-	-		2014	Swift	-	-	-	
	-	-	-		2014	Rogers	-	-	-	
HD 140538	15	2005	Melo	>100	2002-2012	Vogt	2	2004	Carretta	>100

continued.

	HARPS			HIRES			UVES			Combined
Star	Observations	Year	PI	Observations	Year	PI	Observations	Year	PI	
	16	2012	Meléndez		2002-2010	Butler	2	2004	Harries	
					2003-2012	Marcy	6	2011	Cornelisse	
	-	-	-		2006	Meléndez	-	-	-	
	-	-	-		2006-2009	Hillenbrand	-	-	-	
	-	-	-		2006-2012	Fischer	-	-	-	
	-	-	-		2006	Laughlin	-	-	-	
HD 201219	12	various	Melo	25	1997-1998	Latham	-	-	-	37
					2002-2004	Vogt	-	-	-	
	-	-	-		2002-2011	Marcy	-	-	-	
	-	-	-		2003	Butler	-	-	-	
	-	-	-		2006-2011	Hillenbrand	-	-	-	
	-	-	-		2013	Howard	-	-	-	
HD 223498	-	-	-	37	1996-2005	Marcy	-	-	-	37
	-	-	-		1997-2003	Vogt	-	-	-	
	-	-	-		1999	Cochran	-	-	-	
	-	-	-		2001	Butler	-	-	-	
	-	-	-		2003	Hillenbrand	-	-	-	
	-	-	-		2006	Winn	-	-	-	
	-	-	-		2011	Johnson	-	-	-	
	-	-	-		2001	Knutson	-	-	-	

Appendix B

Line list used for my analysis

This appendix contains the line list used for my analysis. It details the element, by atomic number, measured with its wavelength, excitation energy and $\log gf$ alongside the equivalent width measured for each star. The solar lines are included as they were measured for checking $\log gf$.

Table B.1: Details of the element, by atomic number, measured with its wavelength, excitation energy and log gf alongside the equivalent width (Å) measured for each star with my line list. The solar lines are included as they were measured for checking log gf.

Element	λ (Å)	χ(eV)	log(gf)	61 Vir	HD111	HD140	HD181	HD188	HD201	HD223	HD471	HD512	HD587	Sun
'06.00'	5052.1670	7.6850	-1.640	21.81	25.54	25.39	25.75	32.24	28.51	30.82	33.94	29.54	32.78	33.00
'06.00'	5380.3370	7.6850	-1.840	12.60	15.70	15.84	13.21	21.09	18.44	18.97	21.73	18.55	17.74	21.28
'06.00'	6587.6100	8.5370	-1.590	9.41	11.89	11.94	11.45	14.89	11.86	16.42	16.28	13.36	14.76	13.48
'06.00'	9111.8070	7.4880	-0.290	97.62	107.22	109.46	103.82	125.88	116.77	112.57	117.70	112.92	117.09	136.87
'07.00'	8683.4030	10.3300	0.080	7.10	6.72	7.38	7.68	8.96	7.75	9.22	8.11	7.76	8.70	10.99
'08.00'	7771.9413	9.1460	0.360	56.85	61.56	60.85	54.64	67.56	61.86	62.19	70.02	61.90	62.31	69.53
'08.00'	7774.1607	9.1460	0.220	48.83	53.60	53.08	47.48	58.80	54.68	53.52	62.49	55.66	56.15	60.52
'08.00'	7775.3880	9.1460	0.000	38.47	41.40	40.78	36.47	46.22	42.12	41.77	48.56	43.38	43.54	48.84
'11.00'	4751.8220	2.1040	-2.090	17.54	17.60	17.69	21.98	22.00	20.75	20.65	21.06	15.15	22.74	12.61
'11.00'	6154.2260	2.1020	-1.560	41.25	43.02	39.26	50.00	49.63	48.47	52.93	45.56	39.92	53.42	36.48
'12.00'	8923.5690	5.3940	-1.570	64.90	66.81	66.60	70.18	69.74	68.70	76.14	74.46	62.93	68.98	57.94
'12.00'	8997.1530	5.9330	-1.770	23.10	22.47	20.92	25.53	23.46	25.54	28.37	30.60	23.41	26.17	19.89
'12.00'	9986.4740	5.9320	-1.670	29.98	29.85	29.37	36.87	37.35	35.34	39.17	37.63	29.52	38.19	25.34
'13.00'	6696.0230	3.1430	-1.340	45.68	46.69	42.84	50.68	48.97	47.57	56.60	53.57	44.72	51.65	39.22
'13.00'	8773.8960	4.0220	-0.160	98.81	102.18	97.10	107.61	104.32	105.08	111.90	109.31	97.58	108.84	109.27
'14.00'	5684.4840	4.9540	-1.730	62.16	64.76	63.47	65.55	66.88	66.95	71.14	68.57	61.54	68.32	59.69
'14.00'	5690.4250	4.9300	-1.870	52.50	56.74	55.05	56.00	57.24	57.84	59.95	57.16	52.86	58.43	49.12
'14.00'	5772.1460	5.0820	-1.750	51.88	55.57	53.98	56.29	58.56	57.90	61.71	60.70	53.26	59.99	53.09
'14.00'	5948.5410	5.0820	-0.780	90.54	95.83	93.21	102.76	99.36	98.14	100.06	103.13	88.92	101.40	91.08
'14.00'	6125.0210	5.6140	-1.460	34.19	37.43	36.69	38.63	40.56	39.71	43.61	43.33	35.27	41.70	31.42
'14.00'	6131.8520	5.6160	-1.610	25.19	28.10	25.98	27.50	29.96	30.71	32.64	31.14	25.70	30.03	25.01
'14.00'	6142.4830	5.6190	-1.290	37.51	39.83	36.67	38.67	41.67	41.92	44.69	40.91	36.61	43.61	32.03
'14.00'	6145.0160	5.6160	-1.310	39.88	42.97	41.29	41.81	44.49	44.21	47.40	44.69	39.63	44.75	41.16
'14.00'	6583.7070	5.9540	-1.740	17.36	20.51	19.61	20.25	20.97	20.41	23.19	22.19	18.76	20.62	18.58
'14.00'	6800.5960	5.9640	-1.960	11.99	12.94	13.43	15.58	17.50	15.98	18.06	16.57	13.77	17.16	11.79
'14.00'	7005.8800	5.9840	-0.740	73.03	82.35	80.96	86.98	85.77	86.48	92.27	86.67	79.45	88.56	81.66
'14.00'	7375.2460	6.1910	-1.050	35.59	42.92	41.31	42.50	47.08	42.82	51.44	47.69	38.88	46.25	39.65
'14.00'	7557.6910	6.2690	-1.670	10.08	12.25	12.20	10.92	14.25	11.81	14.15	15.62	11.26	13.53	10.84
'14.00'	7680.2660	5.8630	-0.760	77.83	89.11	86.34	87.28	92.69	90.85	93.16	92.10	83.45	92.17	86.48
'14.00'	8728.0100	6.1810	-0.260	95.26	104.93	104.10	103.56	107.06	106.15	105.55	109.20	101.07	103.93	92.38
'14.00'	8883.6840	5.9540	-1.730	14.44	16.78	16.00	15.72	17.64	17.69	18.69	17.88	14.38	17.20	11.90
'14.00'	8899.2310	6.2230	-0.560	41.55	48.91	48.16	46.10	50.13	49.45	52.52	50.01	42.33	50.81	45.33
'14.00'	8925.2950	5.9540	-1.340	31.71	34.00	37.44	35.40	39.41	39.11	41.87	37.54	31.26	35.47	32.20
'16.00'	8693.9310	7.8700	-0.510	11.29	14.12	13.20	11.94	15.80	13.99	16.04	15.93	13.76	17.13	13.87
'16.00'	8694.6260	7.8700	0.080	20.16	25.50	26.06	23.15	27.88	26.91	27.69	27.87	25.30	30.00	29.64
'16.00'	8884.1870	8.4170	-0.770	7.14	8.23	7.99	9.10	10.85	9.93	12.55	11.18	9.09	11.24	8.51
'19.00'	7698.9740	0.0000	-0.170	183.75	188.48	179.35	193.15	183.44	195.25	190.70	180.80	177.57	187.02	178.06
'20.00'	5581.9650	2.5230	-0.550	99.19	105.91	101.03	107.74	103.74	105.02	110.73	104.86	98.83	103.03	104.01
'20.00'	5867.5620	2.9330	-1.570	29.73	33.00	30.31	33.94	30.90	33.57	36.75	33.25	27.97	31.21	24.08
'20.00'	6166.4390	2.5210	-1.140	78.48	83.20	78.40	84.64	80.69	84.45	86.83	81.87	76.12	81.92	71.41
'20.00'	6169.0420	2.5230	-0.790	110.45	116.47	112.67	120.89	113.00	121.88	120.75	112.30	108.85	113.81	98.33
'20.00'	6455.5980	2.5230	-1.340	63.32	66.82	62.64	68.61	65.02	69.50	72.70	68.82	61.42	66.82	56.10
'20.00'	6471.6620	2.5260	-0.680	99.86	105.93	99.30	105.34	101.06	106.92	106.92	102.81	96.64	101.85	90.10
'20.00'	6508.8500	2.5260	-2.160	13.18	15.91	13.40	15.20	12.61	16.06	16.98	14.23	11.31	13.91	10.49
'20.00'	6709.8930	2.9330	-3.160	2.95	3.20	2.59	3.47	3.21	3.44	4.50	2.98	2.70	3.57	2.41
'20.00'	7326.1450	2.9330	-0.200	117.77	126.64	119.10	126.87	122.87	127.61	127.99	121.16	113.78	121.91	102.13
'21.01'	5657.8960	1.5070	-0.600	64.97	67.42	66.42	65.58	68.90	67.58	71.86	73.18	66.61	71.14	66.25
'21.01'	5684.2020	1.5070	-1.070	38.76	37.92	37.53	37.93	40.15	38.42	43.55	45.01	39.10	42.72	36.37
'21.01'	6245.6370	1.5070	-1.030	36.16	36.82	34.88	36.48	38.36	36.21	42.29	41.06	37.93	42.77	35.73
'21.01'	6604.6010	1.3570	-1.300	37.51	37.91	37.43	38.70	40.10	38.24	43.46	43.04	38.65	41.43	37.77
'22.00'	4450.8940	1.8790	0.410	62.16	64.49	58.53	66.55	61.55	63.89	67.11	65.49	57.85	63.78	54.81
'22.00'	4465.8050	1.7390	-0.160	49.71	51.47	48.11	52.35	46.52	51.35	54.87	50.07	46.16	49.86	44.37

continued.

Element	λ (Å)	χ(eV)	log(gf)	61 Vir	HD111	HD140	HD181	HD188	HD201	HD223	HD471	HD512	HD587	Sun
'22.00'	4518.0220	0.8260	-0.320	82.85	84.32	79.25	88.34	80.55	85.64	86.85	84.12	80.89	84.77	77.43
'22.00'	4562.6280	0.0210	-2.650	19.66	18.95	16.36	23.46	17.46	19.09	23.66	20.85	17.65	22.36	11.26
'22.00'	4758.1180	2.2490	0.420	52.24	54.28	50.25	55.61	53.19	54.02	57.50	55.46	49.80	55.94	45.31
'22.00'	4759.2700	2.2560	0.510	55.34	56.83	53.51	59.18	55.64	58.73	59.87	57.16	52.88	58.54	47.65
'22.00'	4778.2550	2.2360	-0.220	20.33	21.06	19.92	23.70	21.32	22.12	27.32	24.21	18.64	23.54	15.73
'22.00'	4820.4110	1.5020	-0.440	55.80	57.01	51.47	59.94	52.85	55.96	60.77	61.06	53.56	55.04	44.79
'22.00'	4913.6140	1.8730	0.160	59.67	58.92	57.25	66.07	60.42	60.03	66.65	63.15	58.58	61.91	53.61
'22.00'	4915.2290	1.8870	-1.010	12.44	13.37	11.09	17.40	12.80	15.08	16.28	13.56	11.46	14.66	8.17
'22.00'	4928.3360	2.1540	0.050	38.98	41.00	37.98	45.18	41.73	42.22	48.50	42.70	37.48	43.42	32.19
'22.00'	4964.7170	1.9690	-0.820	14.03	14.07	13.08	17.14	14.56	13.63	18.34	14.27	13.51	13.73	9.45
'22.00'	4989.1300	1.9810	-0.160	41.98	41.89	39.25	45.23	42.78	43.13	48.39	43.55	38.15	43.58	34.08
'22.00'	4997.0960	0.0000	-2.110	48.12	46.22	39.78	51.20	42.79	44.79	52.86	47.88	42.46	47.68	33.93
'22.00'	5024.8440	0.8180	-0.600	83.69	82.02	77.61	87.98	78.46	83.49	86.49	83.34	80.64	82.28	70.38
'22.00'	5219.7020	0.0210	-2.290	43.04	43.18	38.11	48.13	40.71	41.96	52.52	45.74	39.29	44.92	27.59
'22.00'	5259.9730	2.7380	-0.180	10.20	10.27	9.80	13.32	10.13	11.64	11.79	10.91	9.71	10.98	6.52
'22.00'	5295.7750	1.0670	-1.630	22.41	22.21	20.11	24.23	19.64	21.58	26.00	22.28	18.78	21.47	13.23
'22.00'	5426.2500	0.0210	-3.000	13.82	13.29	9.75	16.06	11.70	11.97	17.63	13.93	10.99	13.19	7.02
'22.00'	5453.6430	1.4430	-1.610	9.04	9.09	7.19	10.67	7.99	9.50	12.03	9.78	8.22	9.02	6.72
'22.00'	5471.1930	1.4430	-1.400	13.76	12.78	9.96	14.82	12.54	12.23	16.95	13.93	10.68	12.53	8.01
'22.00'	5474.2230	1.4600	-1.230	21.52	19.45	15.90	21.81	18.51	19.76	23.75	20.19	17.19	19.97	11.43
'22.00'	5490.1480	1.4600	-0.930	30.90	32.02	29.07	36.69	31.50	33.08	37.63	33.61	28.06	33.15	21.02
'22.00'	5648.5650	2.4950	-0.260	16.82	18.33	13.54	20.49	15.77	18.52	21.27	18.12	14.23	18.67	10.67
'22.00'	5662.1500	2.3180	0.010	32.47	33.12	29.07	36.43	30.81	33.45	39.03	34.58	29.31	33.35	23.06
'22.00'	5679.9160	2.4720	-0.570	8.55	8.08	6.88	9.95	7.36	8.64	10.00	8.37	5.95	7.75	5.43
'22.00'	5689.4600	2.2970	-0.360	19.69	19.04	17.97	23.89	19.99	20.87	25.65	22.33	18.36	21.47	12.09
'22.00'	5702.6560	2.2920	-0.590	12.60	12.91	11.45	13.52	12.47	12.18	17.24	13.39	11.91	12.90	9.23
'22.00'	5716.4450	2.2970	-0.720	9.46	9.74	8.29	10.50	9.38	9.51	11.84	10.44	8.42	9.58	6.46
'22.00'	5739.4690	2.2490	-0.600	14.27	14.41	11.95	14.98	13.26	14.20	16.21	14.17	11.97	13.98	8.41
'22.00'	5766.3590	3.2940	0.380	12.47	14.11	12.39	15.43	13.43	14.96	17.15	13.84	11.23	14.83	9.24
'22.00'	5866.4510	1.0670	-0.840	60.27	60.53	55.22	65.60	59.37	61.73	68.90	62.90	56.68	62.04	47.02
'22.00'	5880.2690	1.0530	-2.040	12.81	12.37	10.67	14.64	12.64	12.01	15.77	12.78	9.72	12.79	7.09
'22.00'	5937.8090	1.0670	-1.890	11.67	11.71	9.28	13.24	10.30	12.28	15.88	12.71	12.07	12.05	7.36
'22.00'	5953.1600	1.8870	-0.320	44.03	46.23	41.08	47.71	45.08	46.17	52.76	48.95	41.62	46.68	36.01
'22.00'	5978.5410	1.8730	-0.490	32.88	33.80	30.10	37.02	32.50	34.89	40.99	36.47	30.38	35.55	23.83
'22.00'	6064.6260	1.0460	-1.940	14.13	13.75	12.86	16.95	14.15	14.52	19.05	15.35	12.90	14.80	8.86
'22.00'	6091.1710	2.2670	-0.420	20.84	21.55	19.49	24.10	21.30	22.87	26.79	24.08	19.19	22.40	16.13
'22.00'	6092.7920	1.8870	-1.370	7.55	6.41	6.00	7.65	7.20	7.97	9.04	7.75	5.81	7.27	4.19
'22.00'	6098.6580	3.0620	-0.010	7.60	8.00	7.03	9.00	7.92	7.84	10.66	9.17	7.12	7.68	6.28
'22.00'	6126.2160	1.0670	-1.420	32.04	32.01	29.48	36.75	31.55	33.19	39.79	34.41	28.61	34.09	23.03
'22.00'	6258.1020	1.4430	-0.350	66.05	63.46	59.48	66.68	61.09	64.55	72.95	64.76	60.82	65.99	52.57
'22.00'	6261.0980	1.4300	-0.470	58.11	60.16	55.77	65.04	58.85	62.26	68.79	63.27	56.47	62.78	47.70
'22.00'	6599.1050	0.9000	-2.080	16.96	16.79	13.99	21.05	16.48	17.08	21.69	18.21	15.68	17.71	9.52
'22.00'	6743.1220	0.9000	-1.630	30.04	28.79	25.17	33.21	28.12	29.04	36.36	31.79	24.85	30.40	18.24
'22.00'	7138.9060	1.4430	-1.590	10.04	11.41	9.09	13.14	10.98	11.99	14.91	11.21	9.17	11.35	7.32
'22.00'	7357.7270	1.4430	-1.120	36.59	33.79	28.30	38.41	31.43	33.58	41.79	34.43	28.65	34.22	22.60
'22.00'	7440.5780	2.2560	-0.700	13.43	11.46	11.07	14.39	12.28	13.46	15.55	13.14	10.11	12.75	8.41
'22.00'	8364.2370	0.8360	-1.750	33.13	33.07	28.94	38.30	32.10	35.53	41.71	35.38	29.47	36.65	22.97
'22.00'	8377.8610	0.8260	-1.610	44.98	43.46	38.24	50.43	41.59	45.25	55.33	46.15	39.49	46.77	28.90
'22.00'	8382.5300	0.8180	-1.630	42.34	40.91	36.31	48.66	39.97	43.62	51.51	44.49	38.38	44.62	28.95
'22.00'	8382.7800	0.8130	-1.780	36.70	38.16	31.44	43.47	36.30	37.49	45.64	41.59	33.19	39.46	23.84
'22.00'	8412.3580	0.8180	-1.480	56.63	57.98	50.46	62.59	56.32	58.49	68.87	59.79	51.71	60.17	41.03
'22.00'	8424.4230	2.1030	-1.600	5.23	4.45	4.42	6.79	5.29	4.71	5.71	5.15	4.12	4.88	3.65
'22.00'	8426.5060	0.8260	-1.250	66.85	66.91	61.65	73.60	64.61	66.76	76.04	69.42	62.44	68.84	51.74
'22.00'	8450.8920	2.2490	-0.900	12.76	13.46	11.38	14.92	13.59	12.11	15.86	13.47	10.84	13.35	8.18
'22.00'	8518.3520	1.8790	-1.080	26.75	30.46	26.55	32.32	30.26	29.36	38.16	30.29	25.96	30.26	22.22
'22.00'	8675.3720	1.0670	-1.660	34.95	38.90	32.46	42.62	34.87	38.14	44.63	39.41	32.12	37.88	23.10

continued.

Element	λ (Å)	χ(eV)	log(gf)	61 Vir	HD111	HD140	HD181	HD188	HD201	HD223	HD471	HD512	HD587	Sun
'22.00'	8682.9800	1.0530	-1.940	21.70	21.53	17.88	25.05	19.86	21.61	28.80	23.36	18.71	22.34	14.28
'22.00'	8692.3310	1.0460	-2.290	12.76	12.02	10.23	13.73	13.44	13.09	15.63	12.73	10.98	13.62	7.11
'22.00'	8766.6760	1.0670	-2.090	8.75	8.56	6.52	10.01	7.60	7.93	10.20	8.65	6.68	9.89	5.51
'22.00'	9705.6640	0.8260	-1.120	79.41	83.97	75.36	84.29	77.48	84.78	89.75	80.54	74.01	81.73	63.04
'22.00'	9718.9600	1.5020	-1.410	24.25	25.88	21.53	25.31	19.69	27.06	30.21	22.53	21.99	27.16	15.55
'23.00'	4827.4580	0.0400	-1.470	26.31	24.58	20.45	32.69	25.56	27.17	35.41	28.31	21.35	27.87	14.64
'23.00'	5727.6520	1.0510	-0.870	14.17	14.58	12.09	18.28	14.30	14.76	19.37	15.24	11.30	15.29	7.75
'23.00'	6039.7220	1.0640	-0.650	19.49	20.04	16.64	23.75	19.80	21.17	25.48	20.73	16.00	21.58	12.25
'23.00'	6090.2140	1.0810	-0.060	47.20	45.00	41.16	52.38	46.94	48.40	56.05	49.00	41.51	50.43	33.65
'23.00'	6111.6450	1.0430	-0.710	18.95	19.54	16.64	24.51	18.81	20.67	25.64	19.98	16.33	19.91	11.51
'23.00'	6119.5230	1.0640	-0.320	31.93	32.02	27.51	37.46	32.35	33.49	40.18	34.44	28.92	35.61	21.86
'24.00'	4491.8500	2.9870	-1.290	16.45	18.48	17.58	20.48	18.37	18.10	21.88	17.30	15.00	19.10	12.12
'24.00'	4492.3050	3.3750	-0.390	34.07	36.09	34.60	39.72	37.59	38.00	41.58	35.89	32.58	38.69	28.51
'24.00'	4575.1070	3.3690	-0.970	13.40	13.47	14.19	17.40	16.11	15.00	18.55	16.89	12.90	15.99	10.62
'24.00'	4755.1400	3.0110	-1.450	10.73	11.36	9.78	11.88	11.42	13.46	13.18	11.88	8.70	11.51	9.08
'24.00'	4764.2930	3.5510	-0.280	30.66	32.46	33.48	34.36	32.98	34.62	36.07	35.80	27.25	34.51	26.33
'24.00'	4767.8560	3.5560	-0.530	20.31	22.39	21.70	23.86	22.26	23.35	26.08	24.14	19.09	23.19	16.94
'24.00'	4790.3330	2.5450	-1.750	20.79	22.45	20.13	24.44	21.99	23.00	26.06	23.43	20.60	22.37	16.25
'24.00'	4801.0250	3.1220	-0.130	50.82	54.21	51.02	55.53	53.65	56.16	59.15	54.47	50.67	55.12	52.93
'24.00'	4936.3360	3.1130	-0.340	52.70	53.98	53.31	60.72	55.63	57.39	60.38	55.75	51.37	57.92	50.71
'24.00'	4964.9270	0.9410	-2.520	49.12	50.55	46.37	55.32	50.39	51.90	58.30	51.28	47.39	51.09	39.67
'24.00'	5220.8920	3.3850	-1.030	14.55	16.60	14.59	18.09	15.53	15.78	19.75	15.91	13.88	16.40	11.01
'24.00'	5238.9610	2.7090	-1.300	22.15	23.20	20.26	27.39	23.88	25.15	29.65	24.88	19.35	24.61	16.36
'24.00'	5243.3540	3.3950	-0.560	26.40	30.16	26.81	30.85	29.42	29.70	33.39	30.05	24.15	29.68	11.03
'24.00'	5287.1780	3.4380	-0.900	13.69	16.31	13.39	16.31	14.62	15.73	19.01	15.50	13.45	15.69	11.18
'24.00'	5296.6910	0.9830	-1.400	100.40	106.80	98.94	108.30	104.22	109.10	112.51	102.96	97.25	105.45	93.26
'24.00'	5304.1800	3.4640	-0.690	18.49	21.36	18.94	22.81	20.87	22.58	26.09	21.33	18.04	22.05	16.10
'24.00'	5312.8560	3.4490	-0.560	23.80	27.38	23.50	28.20	26.33	27.56	30.39	26.99	22.44	26.68	18.99
'24.00'	5318.7710	3.4380	-0.680	21.58	23.96	19.99	26.05	22.09	24.90	27.42	22.50	20.03	23.26	16.10
'24.00'	5329.7850	2.9140	-0.790	41.61	44.27	40.81	48.06	43.65	47.30	50.82	43.90	40.63	45.36	31.71
'24.00'	5345.7960	1.0040	-0.980	122.07	130.76	122.72	134.33	128.72	133.58	136.70	128.57	121.35	127.54	110.82
'24.00'	5442.4070	3.4220	-1.060	11.93	14.70	12.50	15.86	14.48	14.50	17.18	14.47	11.51	13.85	9.02
'24.00'	5628.6430	3.4220	-0.770	17.74	19.93	17.40	21.57	19.09	20.98	24.52	20.56	15.32	20.05	16.17
'24.00'	5664.5790	3.8260	-0.780	6.70	8.83	6.75	9.51	8.57	9.01	9.67	8.50	7.00	9.03	4.82
'24.00'	5694.7400	3.8570	-0.310	22.28	26.01	23.19	28.10	25.74	27.37	31.56	26.19	21.70	27.06	17.86
'24.00'	5781.1800	3.3220	-0.760	20.71	23.23	21.20	27.12	22.81	24.53	29.51	25.66	20.53	23.99	15.42
'24.00'	5783.0630	3.3230	-0.500	38.91	41.72	38.96	45.42	39.57	43.19	49.73	43.69	38.26	42.08	31.91
'24.00'	5783.8500	3.3220	-0.290	51.39	55.20	52.07	58.80	52.94	56.54	63.78	56.72	49.80	55.31	42.85
'24.00'	5787.9180	3.3220	-0.080	54.21	57.74	53.10	59.96	58.22	58.89	63.80	58.57	52.98	58.17	47.07
'24.00'	6630.0110	1.0300	-3.560	10.22	12.17	10.06	14.33	11.36	12.26	15.46	11.99	9.39	12.19	6.68
'24.00'	6661.0750	4.1930	-0.190	14.35	17.42	15.46	18.55	17.64	18.54	21.17	17.54	14.20	17.96	12.27
'24.00'	6926.0870	3.4490	-0.660	27.31	28.32	25.69	32.32	32.27	31.15	36.05	30.54	24.95	35.48	22.13
'24.00'	7400.2490	2.9000	-0.110	91.74	98.01	89.80	101.92	94.96	99.46	103.92	92.71	88.70	95.21	78.90
'25.00'	4754.0420	2.2820	-0.080	157.81	156.69	144.31	169.29	158.51	164.14	167.07	158.10	148.23	158.32	141.03
'25.00'	5388.5440	3.3730	-1.690	6.75	6.44	6.73	9.89	7.80	8.10	10.43	7.27	6.00	8.37	5.98
'26.00'	10167.4690	2.1980	-4.110	31.50	31.83	28.50	34.88	33.64	33.94	35.54	32.38	26.90	32.02	27.19
'26.00'	10216.3130	4.7330	-0.060	142.21	157.87	152.94	168.08	157.15	152.06	161.22	145.46	138.84	158.06	130.77
'26.00'	4478.0170	2.1980	-3.700	27.95	27.96	26.64	31.83	30.15	29.91	36.74	30.67	27.40	31.69	22.84
'26.00'	4485.6750	3.6860	-1.020	23.71	27.30	24.54	29.74	27.45	26.04	32.32	27.28	24.28	28.52	84.73
'26.00'	4502.5909	3.5730	-2.350	32.54	35.05	32.42	35.17	33.69	36.53	39.13	36.19	32.31	34.04	25.01
'26.00'	4508.6850	4.2830	-2.040	19.49	21.80	21.48	22.24	20.14	22.42	26.93	22.41	19.19	21.85	17.57
'26.00'	4509.7350	4.2200	-1.290	47.63	48.62	48.24	52.56	48.20	50.40	57.64	52.73	47.22	51.95	45.82
'26.00'	4510.8205	3.6020	-2.890	15.32	15.89	14.80	18.17	15.93	17.49	20.76	16.08	13.64	18.48	13.96
'26.00'	4514.1839	3.0470	-2.050	63.83	65.61	63.25	68.51	67.25	67.81	71.62	66.24	64.28	65.29	61.73
'26.00'	4517.5240	3.0710	-1.850	78.21	82.04	78.00	86.06	80.26	84.38	85.22	82.68	79.74	84.76	71.88
'26.00'	4546.4690	4.1860	-2.510	9.01	10.38	9.79	11.03	9.63	11.02	11.89	9.80	9.74	9.54	7.35

continued.

Element	λ (Å)	χ(eV)	log(gf)	61 Vir	HD111	HD140	HD181	HD188	HD201	HD223	HD471	HD512	HD587	Sun
'26.00'	4551.6470	3.9430	-2.060	33.06	33.43	32.82	36.62	35.78	36.51	40.34	37.03	32.80	36.93	27.32
'26.00'	4556.9240	3.2510	-2.710	33.24	35.94	32.79	39.15	35.72	35.52	41.13	36.24	32.98	37.23	26.40
'26.00'	4566.5140	3.3010	-2.370	51.19	53.02	49.05	54.47	51.56	53.95	58.35	53.99	49.45	55.62	43.04
'26.00'	4572.8600	3.6540	-2.810	21.41	25.12	21.65	26.23	23.86	23.88	29.10	25.52	22.07	25.41	17.98
'26.00'	4574.2150	3.2110	-2.500	46.52	47.39	45.89	51.72	49.26	49.29	54.61	50.80	45.06	50.28	40.09
'26.00'	4574.7170	2.2790	-2.970	65.03	64.85	63.30	67.43	64.91	65.66	69.69	67.62	62.30	65.88	55.29
'26.00'	4593.5250	3.9430	-2.060	33.37	35.08	33.08	36.56	36.04	35.72	40.39	37.47	34.87	38.40	35.64
'26.00'	4607.6460	3.2660	-1.460	95.47	101.22	95.76	103.57	99.83	103.83	105.00	97.02	93.78	98.23	94.95
'26.00'	4658.2940	3.2670	-3.040	19.08	20.61	18.78	22.50	20.42	21.28	26.59	22.13	17.45	21.69	15.87
'26.00'	4749.9477	4.5580	-1.340	37.73	40.85	39.74	42.31	41.61	42.14	46.45	43.38	37.07	43.04	33.29
'26.00'	4768.6990	4.0760	-2.440	27.47	30.50	28.26	31.94	30.26	30.55	34.84	32.19	26.82	31.18	26.99
'26.00'	4779.4390	3.4150	-2.020	45.43	47.29	43.92	48.81	47.79	48.17	52.24	49.89	44.20	49.81	38.81
'26.00'	4780.8090	4.0760	-2.640	12.03	11.94	11.64	13.26	12.56	12.86	15.43	13.38	10.83	14.35	9.18
'26.00'	4782.0750	4.4350	-1.940	13.05	13.55	13.57	15.17	14.67	15.15	16.43	15.27	11.63	15.22	12.18
'26.00'	4785.9566	4.1430	-1.930	29.85	31.51	30.84	34.84	31.83	35.01	37.42	32.70	28.58	33.40	26.16
'26.00'	4787.8269	2.9980	-2.530	47.71	50.36	48.51	53.78	50.93	51.57	56.50	52.75	46.60	51.01	42.26
'26.00'	4788.7510	3.2370	-1.760	69.01	71.52	70.29	72.52	71.52	73.39	73.97	72.46	68.62	71.55	69.40
'26.00'	4793.9610	3.0470	-3.530	11.12	11.60	9.84	14.65	11.04	10.93	15.55	13.35	10.90	11.56	8.42
'26.00'	4794.3540	2.4240	-4.050	16.81	17.40	14.77	21.49	17.72	17.05	23.80	20.32	16.03	17.92	13.55
'26.00'	4798.7310	1.6080	-4.250	41.77	41.56	39.74	45.42	41.25	42.37	50.58	44.35	39.62	45.95	33.65
'26.00'	4799.4060	3.6400	-2.230	40.05	41.96	41.43	43.83	41.48	42.97	48.35	43.18	38.98	44.03	35.39
'26.00'	4802.5230	4.6070	-1.820	18.66	19.98	18.73	20.39	20.78	20.50	24.68	21.76	17.45	20.03	15.93
'26.00'	4807.7080	3.3680	-2.200	57.12	61.84	58.08	62.96	60.66	64.06	65.78	61.92	55.95	61.00	54.41
'26.00'	4808.1470	3.2510	-2.790	33.64	36.67	34.02	37.39	35.67	36.99	40.91	38.08	33.25	36.51	27.08
'26.00'	4813.1128	3.2740	-2.890	27.84	31.67	28.76	33.47	30.70	30.44	34.14	31.58	27.50	31.94	21.66
'26.00'	4835.8679	4.1030	-1.500	53.75	58.06	54.46	60.91	57.24	60.74	61.45	58.76	52.72	57.92	49.39
'26.00'	4880.5240	4.0760	-2.010	17.92	17.68	18.05	19.89	19.81	19.05	22.86	16.49	14.67	18.84	12.59
'26.00'	4945.6360	4.2090	-1.510	49.33	52.63	47.48	53.36	49.79	54.33	56.70	51.88	48.86	53.96	51.65
'26.00'	4946.3850	3.3680	-1.170	125.82	130.62	118.90	135.71	124.23	132.80	135.21	123.99	120.04	127.25	109.33
'26.00'	4970.4958	3.6350	-1.740	59.96	61.84	60.14	62.99	62.61	62.85	66.87	65.58	58.89	62.75	51.69
'26.00'	4970.6460	3.9600	-1.870	36.58	39.69	36.11	39.29	38.53	40.02	43.22	39.55	35.27	39.81	27.69
'26.00'	4988.9450	4.1540	-0.890	88.27	93.59	89.40	93.93	93.40	96.43	97.08	91.60	86.43	91.03	87.08
'26.00'	4994.1290	0.9150	-3.080	126.46	125.52	123.16	124.76	124.13	128.44	137.45	122.46	121.81	119.61	117.29
'26.00'	4999.1125	4.1860	-1.740	34.47	37.27	35.80	40.81	39.94	40.91	43.82	40.80	35.18	41.33	39.98
'26.00'	5016.4760	4.2560	-1.690	40.17	42.83	39.58	45.68	41.69	39.27	44.94	43.03	37.06	42.71	34.88
'26.00'	5060.0780	0.0000	-5.460	70.15	72.63	66.49	76.38	69.92	72.36	82.09	71.60	69.47	72.38	55.58
'26.00'	5197.9290	4.3010	-1.640	43.20	46.12	42.57	47.60	45.93	44.28	50.30	45.04	41.57	45.93	35.56
'26.00'	5198.7110	2.2230	-2.130	106.83	113.19	105.86	116.81	109.58	113.59	117.53	109.00	104.34	109.53	94.89
'26.00'	5213.8050	3.9430	-2.760	10.62	12.79	11.58	11.71	11.88	11.26	13.74	11.97	9.88	12.52	9.07
'26.00'	5221.0360	4.2940	-1.580	24.70	27.49	24.42	28.12	26.65	27.77	30.67	28.16	23.91	28.08	20.58
'26.00'	5236.2020	4.1860	-1.490	36.52	40.63	39.49	43.46	41.79	42.87	45.06	42.82	39.13	41.22	31.12
'26.00'	5242.4910	3.6340	-0.960	93.49	100.31	98.14	99.03	98.64	103.28	103.90	97.02	91.69	98.59	87.69
'26.00'	5243.7730	4.2560	-1.150	65.58	69.78	67.37	69.45	69.93	69.96	74.02	69.93	65.45	69.68	62.69
'26.00'	5253.0210	2.2790	-3.940	25.21	26.54	24.60	30.42	25.43	27.46	32.91	27.40	24.51	27.93	18.87
'26.00'	5293.9588	4.1430	-1.870	33.93	36.42	35.39	38.53	36.43	38.47	42.31	37.36	33.97	37.47	30.22
'26.00'	5294.5470	3.6400	-2.860	18.72	20.06	20.23	22.83	21.29	22.93	26.39	21.80	18.63	22.07	15.51
'26.00'	5295.2990	4.4150	-1.690	34.98	38.04	36.32	38.02	36.14	38.15	41.79	37.23	33.94	37.45	29.43
'26.00'	5298.7758	3.6420	-2.010	52.03	57.95	53.17	59.30	58.36	57.60	65.01	58.40	53.10	60.16	49.71
'26.00'	5310.4630	5.0860	-1.690	6.91	8.12	6.49	8.97	7.38	7.92	9.97	7.66	6.75	8.10	5.53
'26.00'	5315.0650	4.3710	-1.550	37.08	40.02	38.67	41.74	41.39	41.88	45.02	42.12	36.65	41.19	31.90
'26.00'	5317.5250	4.1430	-2.460	16.45	16.53	14.02	18.66	15.44	17.89	20.31	16.34	15.13	16.84	13.20
'26.00'	5320.0356	3.6420	-2.540	25.11	27.52	24.12	29.35	26.42	27.05	31.95	27.43	23.87	27.83	18.69
'26.00'	5329.9891	4.0760	-1.180	61.50	63.56	60.75	66.00	64.25	64.87	68.76	64.77	60.98	64.51	65.50
'26.00'	5366.4200	5.0670	-2.130	8.08	9.81	8.68	11.27	9.79	10.22	10.70	8.41	8.34	10.43	6.81
'26.00'	5373.6980	4.4730	-0.860	76.87	80.03	73.77	78.96	76.01	75.77	82.60	74.33	71.48	77.48	62.94
'26.00'	5376.8260	4.2940	-2.310	17.26	19.30	18.26	19.65	18.74	19.60	22.17	21.16	19.13	21.94	13.52

continued.

Element	λ (Å)	χ(eV)	log(gf)	61 Vir	HD111	HD140	HD181	HD188	HD201	HD223	HD471	HD512	HD587	Sun
'26.00'	5395.2150	4.4450	-2.170	23.56	27.52	25.39	28.56	28.03	29.54	31.86	28.30	24.36	28.80	20.82
'26.00'	5401.2640	4.3200	-1.920	30.72	35.56	30.38	34.13	32.59	34.37	37.86	33.85	29.67	34.23	27.84
'26.00'	5417.0332	4.4150	-1.680	42.03	43.84	39.84	47.53	44.92	45.96	54.01	46.30	40.79	46.22	38.48
'26.00'	5441.3387	4.3120	-1.730	36.22	40.92	37.86	43.54	41.64	41.51	46.54	42.50	37.12	41.61	31.72
'26.00'	5448.2680	4.1430	-2.020	19.69	23.28	20.77	24.36	23.95	23.51	28.15	24.18	20.62	24.39	16.71
'26.00'	5460.8710	3.0710	-3.580	10.12	12.06	9.24	13.00	11.71	12.11	15.22	12.01	9.80	12.39	8.61
'26.00'	5461.5499	4.4450	-1.900	29.44	34.56	30.27	34.20	33.94	35.39	39.91	33.44	29.22	33.86	25.83
'26.00'	5464.2796	4.1430	-1.400	40.46	45.19	42.51	43.09	44.30	45.66	48.51	46.84	40.04	45.65	38.38
'26.00'	5470.0920	4.4460	-1.810	30.14	32.83	29.86	34.02	32.71	33.56	38.40	34.77	29.63	33.32	25.16
'26.00'	5473.1630	4.1910	-2.140	25.44	25.56	22.46	26.20	26.10	26.74	29.21	26.70	22.85	26.12	20.32
'26.00'	5491.8315	4.1860	-2.180	15.72	15.87	14.73	18.13	18.01	17.67	20.28	17.39	14.36	17.89	11.79
'26.00'	5517.0655	4.2090	-2.370	20.63	23.00	21.59	26.46	23.88	22.92	29.01	23.86	20.71	21.49	17.98
'26.00'	5522.4460	4.2090	-1.550	44.89	50.50	47.49	51.54	49.01	48.73	57.37	52.78	46.86	50.04	44.15
'26.00'	5539.2800	3.6420	-2.660	21.20	22.36	20.36	24.34	21.47	25.31	27.75	24.18	19.75	22.62	15.50
'26.00'	5546.5000	4.3710	-1.310	51.80	58.82	55.92	59.89	57.47	59.05	63.15	57.10	53.90	57.74	50.66
'26.00'	5549.9480	3.6940	-2.910	14.86	14.96	12.65	14.91	13.63	15.35	17.73	15.69	12.52	15.85	11.45
'26.00'	5560.2070	4.4340	-1.190	56.58	58.45	55.68	58.97	57.21	58.75	66.08	59.26	53.64	57.27	53.33
'26.00'	5577.0250	5.0330	-1.550	13.96	14.61	13.50	14.89	14.21	15.25	19.30	14.72	13.83	14.61	10.97
'26.00'	5608.9723	4.2090	-2.400	12.13	14.51	12.72	16.05	14.85	16.08	19.49	15.02	12.11	14.76	10.97
'26.00'	5611.3560	3.6350	-2.990	12.35	12.76	10.98	14.19	12.67	13.34	16.36	13.77	11.13	13.67	9.16
'26.00'	5618.6310	4.2090	-1.270	53.91	58.90	54.97	61.10	57.66	60.85	60.16	60.43	55.41	58.41	52.63
'26.00'	5622.9450	3.6400	-3.090	9.69	11.75	9.88	12.92	11.41	11.93	14.26	12.96	10.44	11.48	8.23
'26.00'	5624.0220	4.3860	-1.480	53.78	59.14	55.23	61.04	58.07	61.05	61.28	59.78	53.85	57.20	44.10
'26.00'	5636.6960	3.6400	-2.610	25.58	26.86	24.92	27.37	24.61	26.76	31.83	25.88	21.69	27.53	19.96
'26.00'	5638.2620	4.2200	-0.870	86.24	92.67	92.44	94.02	89.62	94.15	102.54	90.20	84.61	93.12	78.87
'26.00'	5642.7490	4.6070	-2.120	11.26	13.73	13.62	13.38	13.13	13.59	16.20	14.18	11.33	13.97	11.82
'26.00'	5646.6840	4.2600	-2.500	9.17	9.73	8.60	11.82	11.30	11.73	13.88	11.96	9.31	11.85	7.92
'26.00'	5651.4690	4.4730	-2.000	22.20	25.10	22.42	27.88	24.21	26.57	28.13	24.05	21.90	25.90	18.00
'26.00'	5652.3180	4.2600	-1.950	31.29	33.54	30.92	36.20	33.61	35.13	38.66	33.41	30.23	35.02	27.43
'26.00'	5661.3450	4.2840	-1.730	26.76	30.38	27.68	32.27	29.24	30.60	36.51	31.81	28.26	31.72	23.22
'26.00'	5678.6010	2.4240	-4.670	4.35	4.22	3.89	4.14	4.25	4.69	5.20	3.74	3.05	4.23	2.84
'26.00'	5679.0229	4.6520	-0.920	66.41	71.72	68.79	72.59	71.54	74.46	74.08	69.56	64.11	71.15	62.73
'26.00'	5696.0890	4.5480	-1.720	16.64	18.12	16.32	18.76	18.31	18.85	20.13	18.00	14.74	19.91	12.71
'26.00'	5698.0200	3.6400	-2.680	18.53	20.86	19.12	22.17	21.08	22.03	24.49	23.24	19.79	22.80	14.16
'26.00'	5704.7330	5.0330	-1.400	21.15	25.09	23.76	27.58	24.56	25.80	29.36	26.76	22.57	25.99	19.79
'26.00'	5714.5510	5.0860	-1.700	7.45	9.50	7.44	9.12	9.04	8.20	10.84	8.95	6.84	8.84	7.29
'26.00'	5724.4540	4.2840	-2.640	7.42	7.97	6.85	8.28	7.79	8.84	9.87	7.53	6.39	8.62	5.22
'26.00'	5730.8540	4.9130	-1.440	9.76	9.92	9.10	10.94	10.03	10.99	11.25	10.74	8.22	11.23	7.08
'26.00'	5732.2750	4.9910	-1.560	17.05	19.90	19.29	22.17	20.51	21.69	23.68	21.44	18.18	22.28	14.47
'26.00'	5734.5640	4.9560	-1.570	7.62	9.02	7.89	9.14	8.52	8.23	10.71	8.64	7.34	8.87	6.14
'26.00'	5738.2250	4.2200	-2.340	17.90	17.28	17.17	19.17	19.95	20.66	23.62	19.66	17.48	20.38	14.28
'26.00'	5741.8460	4.2560	-1.850	37.08	39.09	37.94	41.03	39.34	40.81	44.53	40.37	36.47	40.70	32.30
'26.00'	5752.0320	4.5490	-1.170	61.02	67.87	61.77	69.01	64.67	68.43	69.33	64.14	59.99	69.18	56.42
'26.00'	5760.3440	3.6420	-2.490	27.69	29.17	28.21	30.34	29.31	29.62	34.61	30.50	25.53	29.62	23.46
'26.00'	5775.0806	4.2200	-1.290	65.09	69.52	66.20	70.87	69.19	72.46	75.46	70.72	65.54	70.50	61.96
'26.00'	5776.2240	3.6950	-3.360	2.14	2.29	1.96	2.34	2.56	2.42	3.54	2.49	2.18	2.06	2.13
'26.00'	5778.4530	2.5880	-3.430	28.32	30.75	27.13	33.31	29.61	30.11	37.44	31.88	27.44	30.96	22.16
'26.00'	5793.9130	4.2200	-1.700	38.50	41.04	38.87	43.17	40.44	42.45	46.21	42.35	37.39	42.36	35.62
'26.00'	5807.7820	3.2920	-3.410	10.32	12.54	10.65	12.93	11.66	12.41	15.64	12.48	10.25	12.20	9.00
'26.00'	5811.9145	4.1430	-2.430	13.27	14.21	13.75	16.20	14.69	14.95	19.23	15.77	12.84	16.89	11.42
'26.00'	5814.8050	4.2830	-1.970	27.05	29.88	27.06	32.19	29.88	30.59	33.89	30.96	25.65	31.26	23.67
'26.00'	5821.8880	4.9880	-1.610	8.00	8.72	9.40	9.82	9.24	9.82	11.46	10.76	8.88	9.96	7.54
'26.00'	5826.6370	4.2830	-2.940	3.66	3.71	3.03	4.52	4.00	4.52	5.16	4.32	3.59	4.05	3.24
'26.00'	5827.8750	3.2830	-3.410	14.20	16.22	14.32	17.25	16.06	16.97	20.20	16.70	13.74	16.63	11.51
'26.00'	5835.0980	4.2560	-2.370	16.37	18.49	17.15	19.78	19.30	20.94	23.19	20.10	16.50	20.65	14.13
'26.00'	5837.7000	4.2940	-2.340	10.98	13.41	12.14	14.31	12.98	14.64	15.77	13.99	11.74	14.40	9.31

continued.

Element	λ (Å)	χ(eV)	log(gf)	61 Vir	HD111	HD140	HD181	HD188	HD201	HD223	HD471	HD512	HD587	Sun
'26.00'	5844.9170	4.1540	-2.940	5.28	5.65	4.09	6.36	5.47	5.71	7.00	5.47	4.39	6.18	4.49
'26.00'	5845.2660	5.0330	-1.820	7.99	9.66	7.36	9.89	8.25	10.00	11.00	8.43	7.72	9.73	7.05
'26.00'	5849.6820	3.6940	-2.990	9.61	9.87	8.93	10.66	10.00	10.96	13.46	11.47	8.99	10.73	7.41
'26.00'	5851.2050	4.9560	-2.110	5.47	5.37	5.02	6.13	6.42	6.83	7.89	6.27	4.93	5.52	3.03
'26.00'	5852.2170	4.5480	-1.330	47.55	51.21	47.84	52.83	51.92	53.00	57.75	51.75	46.53	51.59	40.41
'26.00'	5853.1483	1.4850	-5.280	11.31	12.84	10.39	14.62	12.79	13.54	16.71	12.73	11.35	13.12	7.23
'26.00'	5855.0760	4.6080	-1.470	25.13	28.05	25.58	28.67	28.25	29.10	32.69	29.28	24.25	28.68	22.38
'26.00'	5856.0830	4.2940	-1.320	37.94	40.77	38.16	41.73	40.62	41.89	46.38	41.78	36.49	41.71	33.63
'26.00'	5858.7780	4.2200	-2.260	16.69	18.56	16.42	19.44	17.65	18.30	22.43	20.48	16.67	19.43	12.53
'26.00'	5861.1070	4.2830	-2.450	10.63	11.86	10.67	13.56	11.84	12.01	14.94	13.19	10.49	12.79	9.27
'26.00'	5871.3040	4.1540	-2.660	4.63	5.25	5.07	5.74	4.58	5.03	6.51	6.28	5.07	5.88	4.88
'26.00'	5879.4870	4.6070	-2.140	12.76	15.07	14.00	15.78	15.56	15.36	17.60	16.34	14.80	15.16	11.03
'26.00'	5880.0272	4.5580	-1.940	15.66	17.26	15.77	17.73	17.04	17.19	19.73	17.07	13.65	16.55	12.36
'26.00'	5883.8130	3.9600	-1.360	77.96	83.20	80.36	87.59	84.12	84.82	90.03	82.15	81.60	84.31	84.13
'26.00'	5902.4730	4.5930	-1.810	17.10	19.13	17.45	20.56	18.84	19.54	23.40	20.14	16.82	19.58	14.62
'26.00'	5909.9700	3.2110	-2.580	41.51	44.15	41.53	46.84	46.10	45.49	51.97	46.31	42.23	47.52	37.86
'26.00'	5927.7860	4.6520	-1.090	46.00	49.65	47.02	50.35	49.69	50.30	54.07	50.92	45.54	51.71	45.13
'26.00'	5929.6670	4.5480	-1.410	45.24	49.58	46.18	49.60	48.15	49.02	53.83	49.79	45.55	51.11	40.98
'26.00'	5943.5780	2.1980	-4.170	14.08	15.20	13.21	17.30	16.17	16.36	21.08	16.40	13.51	17.44	10.35
'26.00'	5956.6920	0.8590	-4.600	61.21	62.28	58.57	65.85	60.19	63.85	69.80	67.00	60.05	64.47	51.14
'26.00'	5963.2390	2.2230	-4.590	4.63	5.36	5.03	5.24	4.40	5.72	7.10	5.96	4.55	5.50	3.02
'26.00'	5969.5590	4.2830	-2.730	5.91	6.00	4.99	7.05	6.29	6.13	7.53	5.16	4.21	7.24	5.17
'26.00'	5976.7770	3.9430	-1.240	73.14	78.24	73.91	80.80	76.74	80.06	82.93	76.79	74.08	77.32	71.15
'26.00'	5978.8920	4.9880	-1.750	6.54	7.43	7.12	6.67	6.73	7.19	8.98	8.92	6.25	8.20	6.31
'26.00'	5987.0650	4.7960	-0.420	78.04	84.57	80.80	83.77	81.78	84.92	88.45	81.17	78.35	81.49	68.78
'26.00'	5999.1710	4.2200	-2.240	8.29	9.46	9.10	9.64	9.83	9.84	11.84	9.30	7.81	10.80	7.42
'26.00'	6003.0100	3.8810	-1.120	101.55	107.74	102.41	110.50	105.12	108.94	110.39	99.17	96.01	106.11	90.28
'26.00'	6005.5420	2.5880	-3.600	27.95	29.71	27.15	33.69	29.60	31.39	36.04	31.25	27.60	31.75	21.62
'26.00'	6008.5560	3.8840	-0.980	103.30	114.03	104.82	115.45	110.24	115.77	119.14	107.64	103.66	112.28	95.92
'26.00'	6012.2060	2.2230	-4.030	29.68	31.68	27.67	33.87	32.31	33.21	38.22	33.04	27.10	34.03	23.42
'26.00'	6015.2430	2.2230	-4.680	6.31	7.15	5.57	8.98	7.66	7.30	9.30	7.38	6.73	8.19	4.80
'26.00'	6019.3640	3.5730	-3.360	7.47	8.23	8.77	9.57	8.72	8.54	10.79	7.88	6.77	9.50	6.15
'26.00'	6024.0490	4.5480	-0.120	131.73	145.26	138.93	150.84	141.45	148.89	149.61	134.96	129.38	140.77	119.94
'26.00'	6027.0509	4.0760	-1.080	70.08	73.61	70.36	74.64	73.79	74.81	78.43	74.94	69.53	74.38	64.15
'26.00'	6034.0330	4.3120	-2.420	9.99	11.84	10.79	13.19	12.04	12.20	14.60	11.79	10.20	12.82	8.36
'26.00'	6035.3340	4.2940	-2.590	7.35	7.94	7.07	8.99	8.17	8.14	9.89	8.01	6.72	8.21	5.50
'26.00'	6055.9920	4.7330	-0.460	75.61	82.71	78.48	81.57	80.48	83.02	85.22	81.92	75.61	80.26	73.19
'26.00'	6065.4820	2.6080	-1.530	137.50	145.73	137.61	151.05	142.38	148.33	153.70	139.29	133.97	140.78	126.79
'26.00'	6078.4910	4.7960	-0.320	89.79	95.97	93.50	100.09	94.61	96.07	100.25	95.97	87.91	96.09	83.04
'26.00'	6078.9990	4.6520	-1.120	49.53	54.70	51.51	55.12	53.09	55.27	57.96	54.07	49.52	54.34	47.33
'26.00'	6082.7080	2.2230	-3.570	41.51	43.68	38.98	46.49	43.39	45.64	49.71	44.35	40.75	45.58	33.83
'26.00'	6093.6430	4.6070	-1.500	35.98	38.29	35.94	39.70	40.41	40.48	43.91	39.95	35.04	39.99	30.83
'26.00'	6094.3640	4.6520	-1.940	21.69	24.95	22.32	25.68	26.30	26.24	29.93	26.69	21.62	26.57	19.84
'26.00'	6096.6620	3.9840	-1.930	44.94	47.81	45.00	49.32	48.00	47.76	53.61	49.19	42.93	48.06	38.33
'26.00'	6100.2710	4.5590	-2.190	11.66	12.82	11.52	12.39	12.48	11.79	14.72	13.86	11.40	12.03	7.96
'26.00'	6105.1280	4.5480	-2.050	14.48	16.44	14.28	16.96	15.93	15.89	20.09	17.27	13.71	16.51	12.65
'26.00'	6120.2460	0.9150	-5.950	8.70	9.54	8.26	10.24	8.72	10.64	11.40	10.36	8.30	10.51	6.32
'26.00'	6127.9060	4.1430	-1.390	52.31	55.09	53.33	57.32	56.19	57.59	61.95	55.58	51.29	57.15	48.33
'26.00'	6151.6170	2.1760	-3.290	57.78	59.37	56.26	62.55	59.39	61.02	64.97	61.68	56.12	61.19	50.71
'26.00'	6159.3680	4.6070	-1.970	15.08	18.05	15.44	17.18	17.66	18.39	20.96	16.95	14.91	17.46	13.05
'26.00'	6165.3600	4.1430	-1.470	50.24	53.78	51.43	54.89	56.22	56.73	57.27	55.76	49.46	56.73	45.99
'26.00'	6173.3340	2.2230	-2.880	73.48	77.61	72.66	79.33	76.17	79.68	81.93	78.15	72.26	77.50	67.33
'26.00'	6187.9870	3.9430	-1.720	55.89	58.72	56.03	61.33	60.27	59.50	63.78	59.44	53.62	58.89	49.07
'26.00'	6200.3129	2.6080	-2.430	77.25	82.88	78.06	84.63	81.59	84.66	88.92	82.27	77.34	83.02	74.64
'26.00'	6213.4290	2.2230	-2.480	93.37	97.75	90.34	99.14	93.77	97.25	102.34	91.68	90.22	95.85	83.44
'26.00'	6226.7300	3.8830	-2.220	33.55	34.89	33.66	38.88	36.05	39.56	40.84	38.92	32.22	36.93	28.51

continued.

Element	λ (Å)	χ(eV)	log(gf)	61 Vir	HD111	HD140	HD181	HD188	HD201	HD223	HD471	HD512	HD587	Sun
'26.00'	6229.2250	2.8450	-2.800	44.89	48.59	42.85	49.35	45.44	48.18	52.95	49.37	42.48	47.35	38.93
'26.00'	6232.6400	3.6540	-1.220	95.13	106.85	97.52	109.56	100.65	106.30	108.98	98.54	95.99	100.89	85.75
'26.00'	6240.6450	2.2230	-3.230	54.86	58.14	54.26	59.68	58.02	59.88	64.55	60.08	54.21	59.24	51.30
'26.00'	6265.1310	2.1760	-2.550	88.81	97.57	91.74	99.36	94.76	99.68	100.86	95.80	89.64	94.92	88.15
'26.00'	6270.2220	2.8580	-2.460	57.92	59.54	57.24	62.45	58.64	60.26	66.83	61.72	56.38	61.38	53.93
'26.00'	6271.2760	3.3320	-2.700	27.76	31.24	28.05	32.44	30.17	31.29	36.75	32.14	27.91	31.71	23.07
'26.00'	6336.8230	3.6860	-0.850	129.64	141.67	129.35	140.63	133.75	139.66	140.97	127.48	123.62	130.14	116.88
'26.00'	6338.8760	4.7950	-1.060	47.32	52.23	48.20	52.18	52.19	52.38	56.27	52.31	45.83	51.69	42.26
'26.00'	6344.1480	2.4330	-2.920	62.83	65.98	64.00	69.41	66.29	67.52	72.61	67.20	61.82	67.98	57.46
'26.00'	6380.7430	4.1860	-1.370	55.74	59.06	55.64	60.28	59.83	60.42	64.16	59.61	55.14	59.95	52.44
'26.00'	6385.7160	4.7330	-1.910	12.91	14.15	12.22	15.25	14.61	14.40	17.52	14.09	12.83	13.79	11.48
'26.00'	6419.6440	3.9430	-2.680	17.58	18.51	16.45	20.57	18.46	20.47	21.64	20.35	16.12	20.20	9.50
'26.00'	6419.9420	4.7330	-0.240	88.60	93.45	89.81	95.66	92.35	95.76	98.72	92.30	86.77	93.30	93.05
'26.00'	6436.4060	4.1860	-2.460	13.19	15.46	13.12	17.47	16.21	15.54	17.78	17.53	13.27	15.97	10.58
'26.00'	6469.1920	4.8350	-0.770	66.78	70.11	66.34	72.79	74.17	72.59	77.85	71.27	69.05	75.14	58.11
'26.00'	6481.8690	2.2790	-2.980	69.36	73.11	68.09	75.51	72.92	74.67	79.41	73.73	67.33	73.60	63.17
'26.00'	6518.3650	2.8310	-2.460	64.37	69.25	62.27	68.24	64.09	69.35	71.65	67.08	61.62	66.60	59.07
'26.00'	6591.3129	4.5930	-2.070	13.82	14.84	13.37	15.33	14.50	16.20	17.71	16.24	12.51	16.44	10.87
'26.00'	6593.8700	2.4330	-2.420	101.85	103.63	99.87	108.32	103.91	107.72	104.80	103.80	98.39	104.59	90.45
'26.00'	6597.5570	4.7950	-1.070	52.79	56.32	52.32	57.26	55.45	56.64	59.06	57.51	49.89	54.43	45.44
'26.00'	6608.0240	2.2790	-4.030	24.61	26.38	23.21	29.57	23.76	25.32	31.03	28.93	22.64	26.90	18.83
'26.00'	6609.1100	2.5590	-2.690	71.87	76.28	71.13	77.81	74.30	75.15	81.30	76.94	72.82	76.96	65.44
'26.00'	6627.5400	4.5480	-1.680	31.97	35.02	32.07	38.14	35.77	36.49	41.17	37.72	31.46	36.75	27.60
'26.00'	6646.9310	2.6080	-3.990	13.41	14.39	13.03	16.35	13.72	14.46	18.65	15.60	12.70	15.14	10.09
'26.00'	6653.8500	4.1540	-2.520	12.96	15.53	13.78	16.20	15.08	16.65	17.57	15.65	12.90	15.88	10.87
'26.00'	6667.7100	4.5840	-2.110	13.48	13.87	12.07	14.36	13.45	14.18	16.25	13.14	11.54	13.96	9.92
'26.00'	6703.5660	2.7580	-3.160	41.70	45.27	41.79	47.62	45.12	46.41	52.40	47.45	42.11	46.77	37.96
'26.00'	6704.4800	4.2170	-2.660	8.66	8.26	7.60	8.52	8.05	8.17	11.14	8.37	7.43	9.04	6.23
'26.00'	6705.1010	4.6070	-1.390	50.03	56.15	53.35	58.92	57.09	58.10	64.00	56.86	52.83	58.80	47.26
'26.00'	6710.3160	1.4850	-4.880	21.74	22.47	19.14	25.64	23.18	23.96	30.06	23.81	20.07	25.10	15.77
'26.00'	6713.7430	4.7950	-1.600	24.87	27.07	25.87	28.94	29.36	27.99	31.47	28.10	23.42	27.66	21.39
'26.00'	6725.3530	4.1030	-2.300	22.48	22.76	20.36	23.99	22.83	23.66	26.66	23.54	20.10	24.21	17.56
'26.00'	6726.6660	4.6070	-1.130	52.70	57.52	52.90	56.85	55.78	58.38	60.88	56.50	51.21	57.31	47.44
'26.00'	6732.0649	4.5840	-2.210	9.06	10.40	8.79	9.86	9.50	9.43	11.43	11.34	8.94	9.70	6.96
'26.00'	6733.1500	4.6380	-1.580	29.75	33.62	30.50	34.59	33.36	33.18	37.76	33.92	30.12	33.26	26.80
'26.00'	6737.9830	4.5580	-1.750	24.39	28.06	24.82	29.98	28.56	29.77	34.15	29.29	24.43	28.86	21.26
'26.00'	6739.5200	1.5570	-4.790	15.36	16.67	14.75	20.02	16.69	17.88	23.18	18.45	14.55	18.29	11.68
'26.00'	6745.0900	4.5800	-2.160	11.51	11.07	10.49	11.22	12.17	11.45	14.54	12.54	9.63	11.57	9.28
'26.00'	6745.9560	4.0760	-2.770	7.87	9.24	8.86	9.38	9.95	9.57	12.34	10.32	7.54	9.33	7.40
'26.00'	6750.1500	2.4240	-2.620	82.90	85.67	80.77	87.24	83.34	86.49	91.68	86.42	81.05	85.01	74.70
'26.00'	6752.7050	4.6380	-1.200	38.99	43.04	39.60	43.44	42.43	44.38	48.33	43.53	38.34	43.47	37.31
'26.00'	6753.4639	4.5580	-2.290	8.11	9.62	7.68	9.29	8.72	9.02	11.20	9.54	7.81	9.15	6.03
'26.00'	6786.8560	4.1910	-2.070	29.61	32.51	28.84	33.34	32.62	34.02	38.72	34.11	28.14	33.44	25.28
'26.00'	6793.2580	4.0760	-2.320	15.55	17.50	14.29	18.26	16.77	18.04	21.27	18.90	15.25	18.06	12.46
'26.00'	6806.8430	2.7270	-3.210	41.43	43.58	39.55	46.57	43.06	44.12	50.23	44.70	39.81	45.92	34.05
'26.00'	6810.2570	4.6070	-0.980	56.39	61.85	58.33	63.39	62.01	63.49	67.80	62.00	56.16	62.14	50.97
'26.00'	6820.3690	4.6380	-1.320	44.11	49.09	46.02	50.29	48.92	51.55	53.08	49.51	44.26	50.12	42.00
'26.00'	6828.5900	4.6380	-0.920	60.68	65.30	61.53	64.89	64.91	66.68	69.59	64.49	59.40	64.02	60.44
'26.00'	6833.2240	4.6380	-2.080	10.70	12.40	10.96	12.95	12.77	12.56	15.71	13.16	10.83	13.03	9.92
'26.00'	6837.0060	4.5930	-1.680	19.30	21.44	19.10	22.84	21.55	22.27	26.18	23.18	18.80	22.49	16.91
'26.00'	6839.8300	2.5590	-3.450	36.01	38.27	33.50	42.80	38.49	40.35	45.26	41.91	35.53	39.68	30.40
'26.00'	6843.6480	4.5480	-0.930	68.77	71.12	67.49	74.79	71.38	73.85	78.01	72.16	66.78	72.67	62.85
'26.00'	6854.8228	4.5930	-1.920	15.14	18.14	17.03	19.04	17.66	19.45	21.02	18.49	15.54	18.47	12.21
'26.00'	6855.1610	4.5580	-0.740	76.75	83.31	79.32	83.87	82.14	85.97	87.42	82.26	75.90	81.99	74.77
'26.00'	6855.7070	4.6070	-1.820	20.26	24.54	22.99	25.47	25.11	26.73	29.59	26.35	21.53	25.56	19.13
'26.00'	6857.2490	4.0760	-2.150	26.25	28.09	26.54	29.45	28.59	30.06	33.94	29.31	25.37	28.82	23.70

continued.

Element	λ (Å)	χ(eV)	log(gf)	61 Vir	HD111	HD140	HD181	HD188	HD201	HD223	HD471	HD512	HD587	Sun
'26.00'	6858.1450	4.6070	-0.930	56.44	62.31	59.40	64.01	62.54	63.82	67.38	62.41	57.56	62.87	55.82
'26.00'	6861.9370	2.4240	-3.890	27.29	27.07	24.01	30.05	29.01	28.67	33.14	26.96	25.00	29.69	20.17
'26.00'	6862.4800	4.5590	-1.570	35.35	38.84	36.33	40.19	40.11	39.95	42.21	38.06	36.92	41.17	31.55
'26.00'	6864.3110	4.5590	-2.320	8.49	8.69	9.15	10.22	8.92	9.76	10.16	9.33	8.15	9.44	7.36
'26.00'	6951.2460	4.5590	-0.880	57.70	60.29	54.52	59.53	57.21	59.87	63.41	59.38	52.51	58.77	49.53
'26.00'	6971.9320	3.0180	-3.340	14.85	17.78	16.26	19.22	16.54	18.41	22.88	18.88	14.96	18.92	11.84
'26.00'	6999.8780	4.1030	-1.560	56.68	65.15	60.63	68.19	63.47	67.09	67.52	64.03	58.43	64.37	55.46
'26.00'	7000.6150	4.1430	-2.380	20.69	22.70	20.85	26.83	23.20	24.22	29.67	25.24	21.53	25.37	18.61
'26.00'	7007.0730	4.9560	-2.020	32.19	34.48	33.44	37.06	34.03	36.41	41.37	36.65	32.75	35.44	5.57
'26.00'	7057.9500	3.6540	-3.380	6.64	6.15	5.62	6.55	5.95	6.65	8.45	6.64	6.88	7.54	4.64
'26.00'	7071.8540	4.6070	-1.700	32.17	34.28	32.04	34.72	36.79	33.41	39.66	36.94	32.40	37.79	31.40
'26.00'	7083.3950	4.9130	-1.200	26.14	30.78	27.62	30.94	29.68	30.92	35.55	30.89	26.21	30.42	24.29
'26.00'	7086.7250	3.6030	-2.380	30.87	31.82	29.28	33.51	31.26	33.06	37.95	34.78	27.53	32.84	24.53
'26.00'	7090.3780	4.2300	-1.210	73.09	75.80	72.95	79.96	77.93	79.03	83.61	75.87	71.15	76.66	72.34
'26.00'	7091.9220	4.9560	-1.290	19.68	21.69	19.54	22.30	23.12	21.85	26.37	21.58	17.52	21.06	16.63
'26.00'	7092.8350	4.5590	-2.030	13.87	13.95	12.24	16.07	16.23	14.90	18.66	14.15	12.43	15.25	10.93
'26.00'	7093.0810	4.5590	-2.020	16.19	16.13	15.45	18.19	18.66	18.05	21.33	17.83	13.77	17.84	13.50
'26.00'	7095.4070	4.2090	-2.020	32.79	34.89	31.30	36.25	34.49	37.09	41.30	35.49	30.46	35.91	28.82
'26.00'	7103.1450	2.4330	-4.510	7.54	7.63	7.17	8.31	7.47	7.45	10.34	7.17	6.45	7.80	4.99
'26.00'	7112.1680	2.9900	-2.990	35.97	39.90	35.40	41.66	40.25	40.96	46.96	41.05	36.39	42.71	30.91
'26.00'	7114.5490	2.6920	-4.010	10.53	10.82	9.41	11.08	10.52	10.23	13.59	10.66	8.89	11.38	7.19
'26.00'	7127.5680	4.9880	-1.040	30.93	33.69	31.19	34.86	34.86	35.67	39.37	33.98	30.26	36.58	30.19
'26.00'	7132.9863	4.0760	-1.620	47.72	50.92	47.80	52.42	52.06	52.57	57.61	51.53	46.00	51.63	43.75
'26.00'	7142.5170	4.9560	-0.820	43.28	46.76	43.53	49.29	49.06	50.04	54.48	47.11	45.06	51.75	38.59
'26.00'	7145.3070	4.6070	-1.160	42.83	47.13	42.73	50.26	48.55	50.24	55.63	49.21	42.39	50.84	40.18
'26.00'	7151.4700	2.4840	-3.730	30.06	34.26	28.31	37.42	32.37	35.53	40.30	34.45	29.51	35.57	26.47
'26.00'	7158.4740	3.6540	-2.890	15.70	18.37	15.63	19.57	18.81	18.82	22.22	20.47	19.60	22.00	13.24
'26.00'	7189.1445	3.0710	-2.770	46.40	50.93	45.23	52.33	47.71	51.06	55.58	51.54	42.72	47.90	40.36
'26.00'	7212.4360	4.9560	-0.850	34.23	39.04	35.35	37.74	40.27	38.72	45.32	39.44	32.22	38.10	34.08
'26.00'	7219.6820	4.0760	-1.690	52.63	54.04	52.81	56.49	55.16	55.91	60.15	55.82	50.98	53.53	47.12
'26.00'	7284.8350	4.1430	-1.750	45.95	48.83	45.84	50.49	49.90	50.58	53.06	49.91	44.45	50.45	42.22
'26.00'	7306.5560	4.1780	-1.740	51.43	52.20	51.77	56.62	55.47	55.20	58.64	53.46	46.86	53.66	44.17
'26.00'	7351.5120	4.9560	-0.630	51.80	53.80	50.39	55.57	54.14	57.48	60.55	55.95	48.20	54.11	46.72
'26.00'	7370.1190	4.7330	-1.720	18.97	23.11	20.61	23.76	20.92	22.71	25.47	22.02	18.60	23.10	16.24
'26.00'	7381.3330	5.3520	-1.130	9.46	11.78	11.44	11.95	13.05	11.43	13.86	11.98	11.22	13.25	8.89
'26.00'	7401.6830	4.1860	-1.590	43.41	48.64	45.61	49.81	48.60	48.86	53.99	49.44	45.39	49.33	42.83
'26.00'	7418.6670	4.1430	-1.370	55.24	58.59	53.68	60.04	57.60	58.51	63.43	58.57	53.43	58.94	48.90
'26.00'	7421.5540	4.6380	-1.800	23.13	25.29	21.87	26.21	23.86	25.44	28.69	24.86	21.29	24.13	16.34
'26.00'	7435.5920	5.3090	-0.710	29.52	33.74	32.21	35.78	33.87	34.65	37.40	33.62	30.29	34.09	27.12
'26.00'	7440.9120	4.9130	-0.570	60.76	64.07	60.25	66.64	64.80	67.22	70.25	64.24	57.76	65.48	55.81
'26.00'	7443.0220	4.1860	-1.820	40.61	42.24	39.94	45.24	43.91	45.22	50.26	45.44	39.15	45.56	35.59
'26.00'	7445.7490	4.2560	-0.100	134.08	144.53	136.57	146.18	140.70	146.88	144.14	138.30	131.27	140.75	150.71
'26.00'	7447.3940	4.9560	-1.200	39.15	42.71	37.74	43.62	43.20	43.12	48.42	43.44	38.60	44.73	34.87
'26.00'	7453.9970	4.1860	-2.410	14.33	16.91	14.88	18.46	17.08	18.33	21.42	16.43	14.43	16.97	12.51
'26.00'	7461.5200	2.5590	-3.580	33.98	35.09	34.02	40.82	37.80	36.82	41.80	38.52	33.61	39.31	28.59
'26.00'	7463.3822	5.0640	-1.720	10.17	10.64	10.52	12.11	12.35	11.47	14.58	12.87	11.41	13.30	9.25
'26.00'	7476.3750	4.7950	-1.680	21.06	23.79	20.50	23.60	23.40	23.68	27.05	24.50	19.84	23.95	18.23
'26.00'	7491.6470	4.3010	-0.890	74.98	80.77	76.96	82.42	80.00	82.54	83.27	79.93	72.26	80.40	68.25
'26.00'	7498.5300	4.1430	-2.250	22.62	23.43	22.17	26.72	23.59	24.97	28.44	26.21	21.73	25.14	18.66
'26.00'	7514.1990	5.3090	-0.860	20.51	21.99	19.88	23.54	24.23	25.06	28.95	22.92	20.13	23.12	16.61
'26.00'	7540.4300	2.7270	-3.850	14.52	14.83	13.78	19.89	16.12	17.40	20.68	16.60	14.69	16.79	12.14
'26.00'	7541.9130	5.1000	-1.860	14.20	15.95	15.34	17.84	15.42	18.19	18.92	16.19	14.20	15.59	12.44
'26.00'	7547.8970	5.1000	-1.350	26.53	29.51	26.15	29.13	27.17	29.86	32.82	31.31	25.55	29.96	21.27
'26.00'	7551.1020	5.0850	-1.630	14.10	14.87	13.56	16.40	15.09	15.84	18.38	14.52	13.35	15.54	10.89
'26.00'	7563.0100	4.8350	-1.960	17.87	21.73	21.54	22.40	21.86	22.97	26.38	22.75	18.86	22.38	16.97
'26.00'	7568.8990	4.2830	-0.770	88.27	94.12	84.42	92.91	92.49	97.78	98.68	91.33	86.99	91.07	82.73

continued.

Element	λ (Å)	χ(eV)	log(gf)	61 Vir	HD111	HD140	HD181	HD188	HD201	HD223	HD471	HD512	HD587	Sun
'26.00'	7582.1210	4.9550	-1.750	12.88	16.58	16.14	17.77	18.70	18.16	19.60	16.37	14.41	16.34	12.22
'26.00'	7583.7870	3.0180	-1.880	95.48	97.52	93.08	98.77	96.90	98.87	103.55	97.25	92.89	98.12	84.98
'26.00'	7710.3630	4.2200	-1.110	75.66	80.30	71.64	79.65	73.35	82.29	80.24	75.71	71.45	79.64	78.41
'26.00'	7719.0490	5.0330	-1.310	34.49	36.39	33.37	39.26	36.67	38.79	43.21	38.75	32.58	38.41	29.78
'26.00'	7733.7240	5.0640	-1.530	13.52	15.13	12.16	14.71	12.76	14.66	16.73	16.85	12.27	14.07	11.06
'26.00'	7737.6620	4.4150	-2.750	4.48	4.37	4.20	4.49	4.02	4.15	6.10	4.14	3.64	4.52	3.74
'26.00'	7746.5960	5.0640	-1.280	22.21	24.25	22.26	24.92	25.03	26.13	29.17	26.90	21.47	26.04	19.04
'26.00'	7751.1090	4.9910	-0.750	54.33	58.48	53.53	57.51	56.86	57.00	65.53	57.41	51.33	57.57	47.03
'26.00'	7802.4730	5.0860	-1.520	18.27	19.85	18.53	20.60	21.07	21.03	24.00	21.60	18.07	20.64	15.90
'26.00'	7807.9090	4.9910	-0.540	68.94	72.05	68.78	74.01	72.91	74.70	78.41	71.68	66.59	73.81	64.16
'26.00'	7820.8030	4.2940	-2.640	8.47	8.56	7.46	9.25	8.28	8.75	9.73	7.94	6.99	8.22	6.28
'26.00'	7844.5550	4.8350	-1.810	14.01	16.50	14.78	15.75	16.32	16.74	19.21	18.49	13.93	15.63	13.40
'26.00'	7855.3990	5.0640	-1.020	33.15	35.60	32.24	35.24	34.47	35.51	40.16	35.82	30.95	35.41	36.81
'26.00'	7879.7480	5.0330	-1.650	13.38	13.99	13.52	14.52	15.33	13.95	16.79	15.94	12.45	12.49	12.06
'26.00'	7955.6920	5.0330	-1.120	27.28	32.74	28.76	32.74	28.91	31.90	35.37	29.71	27.03	33.24	26.03
'26.00'	8028.3130	4.4730	-0.680	79.72	85.54	79.02	87.40	83.02	85.80	88.44	80.18	85.13	82.42	74.53
'26.00'	8075.1500	0.9150	-5.060	48.73	48.77	43.23	53.50	48.87	50.22	60.10	52.48	46.07	52.49	37.93
'26.00'	8096.8750	4.0760	-1.760	41.11	44.65	38.72	47.32	45.64	46.71	52.99	49.49	39.94	47.94	35.75
'26.00'	8207.7420	4.4460	-0.850	71.11	78.53	73.70	77.73	77.97	78.62	81.42	79.42	69.86	73.55	71.07
'26.00'	8248.1290	4.3710	-0.880	69.42	77.69	71.13	77.54	71.76	77.00	81.81	73.05	68.84	76.30	66.64
'26.00'	8284.6030	5.6210	-1.350	3.77	4.21	4.31	4.56	4.35	5.26	5.81	3.67	3.51	4.25	4.17
'26.00'	8365.6320	3.2510	-2.040	75.85	79.66	74.33	83.23	82.12	83.95	87.97	82.31	75.12	84.32	70.90
'26.00'	8401.4000	2.4840	-3.150	38.39	38.20	33.77	43.68	39.63	40.51	48.61	40.49	35.35	41.26	34.14
'26.00'	8424.1410	4.9560	-1.170	37.38	41.70	38.87	43.54	41.83	43.31	46.80	43.10	36.38	41.50	39.59
'26.00'	8453.6570	5.5390	-1.130	8.99	10.44	10.58	10.50	9.49	11.33	14.04	11.69	9.10	11.21	8.18
'26.00'	8471.7430	4.9560	-1.030	43.26	47.29	40.60	49.46	49.49	47.24	56.37	48.39	41.98	48.81	39.78
'26.00'	8481.9810	4.1860	-1.980	27.13	29.41	25.77	32.75	32.23	32.52	34.83	32.40	26.52	33.29	22.26
'26.00'	8515.1084	3.0180	-2.070	91.71	94.78	88.32	98.34	95.01	95.89	101.51	93.96	88.75	96.26	82.81
'26.00'	8526.6690	4.9130	-0.760	67.01	73.58	69.39	71.82	73.31	74.47	78.08	72.54	66.47	72.68	64.53
'26.00'	8527.8520	5.0200	-1.620	18.91	19.94	20.01	18.74	20.91	20.09	25.76	22.65	17.97	20.75	13.25
'26.00'	8571.8040	5.0100	-1.410	34.50	39.91	36.95	40.71	37.38	41.34	44.16	39.40	33.55	39.75	32.53
'26.00'	8611.7950	2.8450	-1.920	119.17	125.95	113.22	134.03	122.81	127.90	130.97	124.77	114.90	128.83	105.55
'26.00'	8613.9400	4.9880	-1.240	32.94	37.30	34.91	37.40	36.90	38.51	42.69	39.07	32.75	37.48	29.43
'26.00'	8616.2800	4.9130	-0.650	53.01	56.91	52.44	57.57	54.22	55.71	60.07	59.21	49.46	55.71	48.40
'26.00'	8621.6007	2.9490	-2.320	76.52	83.00	77.17	83.19	79.76	82.64	88.01	81.61	75.05	80.88	72.86
'26.00'	8632.4140	4.1030	-2.340	17.29	20.95	17.38	23.51	19.76	20.82	25.54	23.21	19.05	23.02	13.64
'26.00'	8763.9660	4.6520	-0.140	124.36	142.42	128.73	151.05	135.91	143.72	145.18	139.54	125.92	142.81	119.43
'26.00'	8793.3420	4.6080	-0.090	134.09	147.31	139.21	150.24	142.87	148.62	154.21	144.82	131.99	141.17	128.07
'26.00'	8796.4840	4.9560	-1.270	32.46	37.01	32.88	40.51	38.92	38.95	45.12	37.69	32.05	38.46	34.22
'26.00'	8846.7400	5.0100	-0.770	60.70	68.59	66.17	70.15	69.39	69.59	71.91	71.59	59.31	69.97	58.65
'26.00'	8876.0240	5.0200	-1.050	37.49	41.98	39.88	43.62	41.32	43.74	47.76	43.19	37.90	43.80	36.10
'26.00'	8920.0130	5.0640	-0.420	62.92	69.48	65.08	70.03	68.04	70.03	73.77	67.66	61.38	69.42	57.40
'26.00'	9146.1280	2.5880	-2.800	59.19	63.09	60.92	65.80	60.13	66.12	69.75	66.21	54.19	65.43	55.40
'26.00'	9861.7340	5.0640	-0.140	80.82	88.31	80.82	89.32	83.45	91.32	92.13	81.72	78.45	85.27	89.76
'26.00'	9951.1580	5.3930	-1.840	11.32	12.67	12.90	10.53	13.75	13.93	13.94	10.79	10.37	12.51	10.37
'26.01'	4491.4050	2.8560	-2.750	77.69	83.19	83.02	80.08	84.06	82.28	85.48	83.19	79.10	83.39	80.05
'26.01'	5256.9380	2.8910	-4.180	17.82	22.59	20.86	20.47	21.10	21.18	23.81	24.18	19.18	24.03	20.76
'26.01'	5425.2570	3.1990	-3.160	42.34	44.59	42.83	42.50	44.56	42.99	47.57	46.74	43.22	45.16	44.20
'26.01'	5534.8470	3.2450	-2.730	52.31	57.59	56.88	51.71	55.90	56.60	55.38	58.15	54.11	55.73	56.60
'26.01'	5991.3760	3.1530	-3.640	27.23	29.96	29.70	27.25	31.82	30.21	32.27	32.48	28.36	32.61	33.45
'26.01'	6084.1110	3.1990	-3.780	18.65	20.06	19.27	19.74	22.40	21.73	22.51	22.68	20.47	22.57	21.41
'26.01'	6113.3220	3.2210	-4.230	10.95	11.89	12.02	10.72	12.58	11.64	13.63	13.05	12.19	12.09	12.44
'26.01'	6149.2580	3.8890	-2.720	31.01	35.78	35.60	31.60	36.20	35.06	35.76	37.68	33.17	35.66	36.07
'26.01'	6247.5570	3.8920	-2.310	46.82	53.05	51.36	46.14	52.00	51.69	51.81	53.14	49.81	51.41	52.90
'26.01'	6369.4620	2.8910	-4.160	14.97	18.37	17.75	16.08	19.08	17.80	19.82	22.18	17.73	20.41	19.09
'26.01'	6432.6800	2.8910	-3.680	38.41	40.79	41.71	37.06	39.18	41.61	42.23	43.50	40.71	42.34	42.82

continued.

Element	λ (Å)	χ(eV)	log(gf)	61 Vir	HD111	HD140	HD181	HD188	HD201	HD223	HD471	HD512	HD587	Sun
'26.01'	6456.3830	3.9030	-2.180	55.66	60.30	62.20	56.88	61.64	63.63	61.80	62.35	58.63	60.94	65.03
'26.01'	7515.8310	3.9030	-3.550	11.62	13.05	12.63	10.10	14.37	14.70	14.90	13.75	12.37	12.26	13.62
'26.01'	7711.7230	3.9030	-2.680	39.75	44.78	44.66	43.19	45.76	46.00	43.69	47.85	41.85	46.11	45.97
'27.00'	4768.0890	3.1910	-0.670	16.27	15.71	15.38	18.71	17.13	16.73	20.64	18.48	14.13	18.80	12.15
'27.00'	4781.4300	1.8830	-2.150	13.84	11.73	11.56	14.48	14.57	14.05	16.38	15.04	11.43	16.92	11.85
'27.00'	4792.8460	3.2520	-0.060	38.53	38.85	36.00	42.28	41.44	40.13	47.03	42.01	37.90	42.63	31.71
'27.00'	5247.9110	1.7850	-2.070	26.02	24.77	21.34	29.90	26.10	26.08	33.84	28.02	23.39	29.64	19.96
'27.00'	5280.6290	3.6290	-0.030	24.81	25.05	22.42	30.37	27.47	25.82	32.30	27.43	23.97	29.54	19.12
'27.00'	5342.6950	4.0210	0.690	36.89	35.91	34.69	38.41	38.72	38.16	43.48	38.48	34.13	40.94	31.70
'27.00'	5352.0450	3.5760	0.060	29.40	28.86	26.53	33.69	32.16	31.33	37.06	32.99	27.33	34.77	24.13
'27.00'	5647.2340	2.2800	-1.560	19.88	18.37	15.39	23.46	21.05	21.93	26.62	22.32	17.45	24.07	13.07
'28.00'	4900.9670	3.4800	-1.670	24.15	23.77	22.95	26.90	27.46	27.34	29.38	26.97	22.14	29.23	21.16
'28.00'	4935.8310	3.9410	-0.350	69.31	68.25	71.06	79.19	74.57	76.11	76.53	69.62	68.69	74.60	63.18
'28.00'	4945.4430	3.7960	-0.820	48.43	49.26	47.13	52.54	51.74	52.00	55.39	51.27	48.34	54.13	44.42
'28.00'	4976.1300	3.6060	-1.250	34.28	35.08	33.81	38.67	38.34	37.49	42.46	37.95	32.83	38.86	30.16
'28.00'	5032.7230	3.8980	-1.270	27.41	28.26	25.65	29.49	29.28	30.36	33.41	28.99	23.42	29.60	23.35
'28.00'	5220.2850	3.7400	-1.310	32.05	33.72	31.00	36.32	35.95	35.98	40.40	35.87	30.92	37.14	28.72
'28.00'	5388.3410	1.9350	-3.560	17.65	16.60	14.55	21.06	18.72	18.49	24.05	18.65	15.71	20.23	13.61
'28.00'	5494.8760	4.1050	-1.160	20.29	22.47	22.11	24.02	25.32	25.05	26.32	23.66	20.42	24.81	17.20
'28.00'	5578.7110	1.6760	-2.640	60.24	59.81	57.18	67.56	64.93	63.97	67.66	63.96	59.43	67.70	56.15
'28.00'	5641.8800	4.1050	-1.070	27.76	28.83	27.82	31.34	30.64	30.82	33.98	30.37	26.31	32.93	22.08
'28.00'	5643.0720	4.1650	-1.240	17.74	17.93	17.92	20.09	19.58	19.60	23.08	19.61	16.72	21.20	16.00
'28.00'	5669.9350	4.2660	-0.960	20.88	22.52	19.60	23.78	23.85	24.34	26.37	24.11	19.25	24.37	17.86
'28.00'	5682.1980	4.1050	-0.470	54.19	56.21	52.56	58.89	60.32	60.20	60.81	55.94	53.56	61.08	50.17
'28.00'	5694.9770	4.0890	-0.610	44.88	47.17	45.06	49.53	49.93	49.60	53.35	49.08	44.23	50.92	43.15
'28.00'	5748.3460	1.6760	-3.260	34.05	35.69	31.84	39.89	37.95	38.70	42.61	37.78	33.07	40.05	31.57
'28.00'	5805.2130	4.1670	-0.640	44.00	47.19	44.69	49.99	51.33	48.47	52.73	49.18	43.65	50.27	43.40
'28.00'	5831.5930	4.1670	-1.070	27.91	28.51	26.28	31.06	31.61	31.46	34.49	30.60	25.09	31.41	24.26
'28.00'	5996.7270	4.2360	-1.060	24.36	24.22	22.85	29.94	29.18	28.10	31.07	26.81	22.55	29.46	21.68
'28.00'	6007.3060	1.6760	-3.330	29.53	30.73	28.45	34.18	32.89	32.54	37.91	33.06	28.27	34.47	25.27
'28.00'	6053.6790	4.2360	-1.070	22.65	23.40	22.46	25.67	26.24	24.72	28.83	26.01	20.99	27.19	20.94
'28.00'	6086.2760	4.2660	-0.530	49.37	49.42	46.78	52.33	53.05	52.31	55.66	52.56	46.72	54.40	43.85
'28.00'	6108.1070	1.6760	-2.450	69.92	70.75	67.13	75.76	73.51	73.43	79.43	74.69	68.44	75.11	64.94
'28.00'	6111.0660	4.0880	-0.870	39.46	40.57	38.60	45.09	44.48	43.95	46.86	42.30	37.76	44.02	35.17
'28.00'	6119.7490	4.2660	-1.350	13.59	13.77	12.90	14.92	15.42	16.37	16.54	15.74	13.01	16.67	11.48
'28.00'	6128.9630	1.6760	-3.330	31.14	30.38	28.24	35.48	33.77	33.78	39.95	32.97	28.27	35.35	26.26
'28.00'	6130.1300	4.2660	-0.960	24.82	24.02	23.03	27.20	27.57	27.43	30.69	26.17	21.60	28.04	22.71
'28.00'	6133.9630	4.0880	-1.830	5.92	5.94	5.54	7.53	7.71	7.58	7.50	7.21	5.94	7.80	5.88
'28.00'	6175.3600	4.0890	-0.550	53.11	56.80	53.32	59.92	62.47	58.03	62.90	60.79	53.75	60.82	48.71
'28.00'	6176.8070	4.0880	-0.260	67.28	70.38	66.05	72.36	74.04	71.93	76.71	72.91	65.99	73.56	66.90
'28.00'	6177.2360	1.8260	-3.500	19.41	19.35	16.02	22.52	21.58	20.02	24.98	21.62	17.54	22.84	15.67
'28.00'	6186.7090	4.1050	-0.960	34.45	35.09	33.26	37.12	38.75	37.39	40.26	37.17	32.52	38.24	30.76
'28.00'	6191.1710	1.6760	-2.350	78.28	79.69	75.25	82.67	80.86	81.91	85.94	81.43	75.92	82.08	70.66
'28.00'	6204.6000	4.0880	-1.100	24.01	26.07	23.43	28.44	29.37	28.33	31.11	27.69	23.64	29.49	23.59
'28.00'	6223.9810	4.1050	-0.910	29.00	31.66	30.33	34.70	35.25	35.92	37.59	33.25	29.83	35.52	28.56
'28.00'	6327.5930	1.6760	-3.150	47.02	46.67	44.70	53.78	50.82	50.71	57.04	51.06	45.71	52.31	39.95
'28.00'	6370.3410	3.5420	-1.940	15.48	15.20	13.46	17.55	18.02	16.98	19.86	17.16	14.28	18.46	10.14
'28.00'	6378.2470	4.1540	-0.830	36.66	36.55	34.71	39.50	40.15	38.99	42.70	39.62	33.47	41.14	31.77
'28.00'	6384.6630	4.1540	-1.130	28.70	29.69	27.68	32.04	32.66	30.84	35.32	31.51	26.83	31.98	24.54
'28.00'	6598.5930	4.2360	-0.980	26.16	29.60	27.75	32.57	34.04	32.25	34.92	32.31	26.94	32.62	28.31
'28.00'	6635.1180	4.4190	-0.820	27.73	30.19	29.13	33.36	33.91	32.96	34.86	30.96	28.03	35.42	25.76
'28.00'	6661.3190	4.2360	-1.770	7.97	9.23	8.91	9.83	11.24	10.25	11.57	9.66	7.87	10.60	7.23
'28.00'	6767.7680	1.8260	-2.170	86.95	89.25	83.77	90.33	92.39	92.53	96.29	92.37	86.21	91.77	80.97
'28.00'	6772.3130	3.6580	-0.980	56.77	57.25	55.23	61.87	60.98	60.72	65.44	60.92	54.45	62.28	50.39
'28.00'	7034.3770	3.5430	-2.010	12.79	14.64	13.51	15.99	15.80	16.29	18.34	16.36	13.14	15.90	12.85
'28.00'	7110.8920	1.9350	-2.980	43.16	43.08	39.22	49.09	48.04	46.77	53.37	47.28	41.94	50.36	39.05

continued.

Element	λ (Å)	χ(eV)	log(gf)	61 Vir	HD111	HD140	HD181	HD188	HD201	HD223	HD471	HD512	HD587	Sun
'28.00'	7385.2360	2.7400	-1.970	50.00	49.03	47.85	52.64	51.15	52.14	56.42	52.56	44.34	54.58	43.91
'28.00'	7525.1110	3.6350	-0.540	73.44	78.04	73.28	80.00	79.97	81.73	83.20	79.36	72.27	81.43	74.44
'28.00'	7555.5980	3.8470	-0.040	100.69	106.72	102.38	110.84	111.74	111.37	115.12	107.79	100.78	110.38	97.62
'28.00'	7574.0430	3.8330	-0.530	67.96	71.92	65.83	73.92	73.06	75.03	79.14	75.57	67.75	77.46	63.92
'28.00'	7727.6130	3.6790	-0.170	105.11	107.45	105.00	111.26	113.46	110.98	116.23	108.66	100.74	108.98	104.11
'28.00'	7797.5860	3.8980	-0.260	84.84	89.85	86.68	94.96	95.98	94.43	96.29	91.72	85.73	94.61	82.36
'28.00'	7855.1250	4.5380	-1.410	9.94	10.90	9.45	11.82	11.72	12.07	13.31	11.97	9.96	12.83	10.43
'30.00'	4810.5280	4.0780	-0.130	72.64	74.17	71.07	75.68	76.54	75.84	76.43	77.58	73.76	77.58	71.01
'30.00'	6362.3380	5.7960	0.150	19.63	21.13	22.93	20.98	26.26	21.81	25.86	21.42	21.59	25.77	19.94
'37.00'	7800.2590	0.0000	0.130	9.84	12.95	11.45	15.27	14.53	16.46	16.01	17.22	12.81	16.00	9.89
'38.00'	4607.3270	0.0000	-0.570	49.19	59.19	55.13	59.65	55.22	59.03	56.44	51.57	47.20	52.36	44.21
'38.01'	10327.3110	1.8390	-0.350	112.57	145.83	136.39	118.57	137.68	154.25	130.29	123.60	111.69	128.83	145.62
'39.01'	4900.1200	1.0330	-0.090	50.36	61.63	59.28	55.70	57.60	59.78	55.26	57.03	50.23	54.68	49.67
'40.00'	6134.5850	0.0000	-1.280	3.68	4.28	3.08	4.47	4.34	4.42	3.27	3.65	3.19	3.94	3.00
'41.00'	4606.7560	0.3480	-0.370	3.53	2.38	2.85	5.02	4.68	3.23	4.41	4.00	3.86	4.03	4.31
'56.00'	6595.3230	1.1200	0.150	1.82	2.94	2.36	4.45	3.79	3.54	4.67	3.04	2.33	3.81	2.95
'56.01'	5853.6680	0.6040	-1.000	61.15	74.10	69.62	64.22	64.54	69.72	65.27	66.58	60.60	62.81	65.84
'56.01'	6496.8970	0.6040	-0.370	104.28	123.04	119.59	111.20	112.63	119.56	114.8	110.26	107.75	110.49	111.57
'57.01'	4662.4980	0.0000	-1.240	6.80	9.98	8.10	7.42	7.83	8.50	8.66	8.12	7.57	7.39	5.14
'57.01'	4748.7260	0.9270	-0.540	3.78	6.28	5.48	4.96	4.46	4.84	5.69	5.30	3.80	4.34	2.78
'57.01'	6390.4770	0.3210	-1.410	3.65	5.19	3.98	4.58	3.83	4.30	5.26	5.60	3.21	3.43	2.97
'58.01'	4562.3590	0.4780	0.230	24.99	29.48	28.11	26.04	23.86	26.19	27.26	29.05	25.29	26.52	25.03
'58.01'	4773.9410	0.9240	-0.290	11.77	14.65	12.50	13.71	13.56	12.95	15.43	13.85	12.57	13.85	8.54
'58.01'	5330.5560	0.8690	-0.460	4.48	5.70	6.27	5.93	5.20	5.21	5.49	5.20	4.40	4.66	3.56
'60.01'	4446.3800	0.2050	-0.350	13.81	16.56	15.84	13.95	13.05	13.61	15.37	18.04	13.46	13.22	12.41
'60.01'	5319.8100	0.5500	-0.140	14.37	16.66	15.20	14.27	12.24	13.67	15.81	16.58	13.07	13.03	11.39
'62.01'	4566.2000	0.3330	-0.590	14.89	14.10	11.68	15.10	11.69	14.99	16.09	15.07	11.78	17.17	10.12
'63.01'	6645.0640	1.3800	0.120	3.61	6.57	6.78	5.95	5.81	6.98	7.07	8.67	6.22	6.27	5.23

Appendix C

Line list used for Meléndez analysis

This appendix contains the line list used for my analysis of the Meléndez lines. It details the element, by atomic number, measured with its wavelength, excitation energy and $\log gf$ alongside the equivalent width measured for each star. The solar lines are included as they were measured for checking $\log gf$.

Table C.1: Details of the element, by atomic number, measured with its wavelength, excitation energy and $\log gf$ alongside the equivalent width (Å) measured for each star with the Meléndez line list. The solar lines are included as they were measured for checking $\log gf$.

Element	λ (Å)	χ(eV)	log(gf)	61 Vir	HD111	HD140	HD181	HD188	HD201	HD223	HD471	HD512	HD587	Sun
'06.00'	5052.167	7.685	-1.64	21.81	25.54	25.39	25.75	32.24	28.51	30.82	33.94	29.54	32.78	33.00
'06.00'	5380.337	7.685	-1.84	12.60	15.70	15.84	13.21	21.09	18.44	18.97	21.73	18.55	17.74	21.28
'06.00'	6587.610	8.537	-1.59	9.41	11.89	11.94	11.45	14.89	11.86	16.42	16.28	13.36	14.76	13.48
'06.00'	7111.469	8.640	-1.08	6.18	7.94	7.18	8.58	10.99	10.57	11.93	11.22	9.96	13.17	11.05
'06.00'	7113.178	8.647	-0.77	19.05	17.50	17.95	22.16	27.30	24.46	29.74	25.21	21.78	28.92	22.76
'08.00'	7771.941	9.146	0.36	56.85	61.56	60.85	54.64	67.56	61.86	62.19	70.02	61.90	62.31	69.53
'08.00'	7774.160	9.146	0.22	48.83	53.60	53.08	47.48	58.80	54.68	53.52	62.49	55.66	56.15	60.52
'08.00'	7775.388	9.146	0.00	38.47	41.40	40.78	36.47	46.22	42.12	41.77	48.56	43.38	43.54	48.84
'11.00'	4751.822	2.104	-2.09	17.54	17.60	17.69	21.98	22.00	20.75	20.65	21.06	15.15	22.74	12.61
'11.00'	5148.839	2.102	-2.06	15.28	14.76	14.19	19.04	18.75	17.83	19.87	16.17	13.79	20.52	11.24
'11.00'	6154.226	2.102	-1.56	41.25	43.02	39.26	50.00	49.63	48.47	52.93	45.56	39.92	53.42	36.48
'11.00'	6160.747	2.104	-1.26	62.83	64.14	60.59	71.64	72.45	70.16	75.23	66.33	60.89	75.39	58.22
'12.00'	4571.096	0.000	-5.69	121.83	118.94	114.57	126.26	120.61	120.81	130.78	126.08	118.58	125.77	118.19
'12.00'	4730.029	4.346	-2.52	79.11	79.56	75.69	76.82	81.99	83.19	91.10	86.44	75.55	86.98	70.55
'12.00'	5711.088	4.346	-1.83	122.46	126.46	121.77	133.33	126.85	128.33	138.01	130.26	122.12	130.11	116.15
'13.00'	6696.023	3.143	-1.34	45.68	46.69	42.84	50.68	48.97	47.57	56.60	53.57	44.72	51.65	39.22
'13.00'	6698.673	3.143	-1.64	30.11	27.78	26.40	34.17	31.77	29.80	38.26	32.42	26.69	33.61	21.59
'13.00'	7835.309	4.022	-0.64	47.54	43.74	46.92	54.65	53.73	52.29	62.58	58.75	48.43	56.28	44.42
'13.00'	7836.134	4.022	-0.49	66.97	63.37	64.88	73.64	72.82	69.63	83.45	80.26	67.42	75.22	60.41
'13.00'	8772.865	4.022	-0.31	87.46	86.65	80.44	89.09	87.99	85.42	93.49	93.47	80.43	91.33	79.35
'13.00'	8773.896	4.022	-0.16	98.81	102.18	97.10	107.61	104.32	105.08	111.90	109.31	97.58	108.84	109.27
'14.00'	5488.983	5.614	-2.29	16.85	25.41	24.39	27.73	29.18	27.68	32.36	31.15	23.38	30.97	21.79
'14.00'	5517.533	5.082	-2.61	12.53	13.63	15.25	14.60	16.54	13.90	20.54	17.00	14.28	11.92	12.94
'14.00'	5645.613	4.930	-1.52	42.69	44.04	43.98	47.75	48.12	46.95	50.45	48.73	44.13	48.56	40.14
'14.00'	5665.555	4.920	-2.04	45.72	47.77	43.51	47.74	47.80	49.04	54.51	52.49	44.94	51.32	42.42
'14.00'	5684.484	4.954	-1.73	62.16	64.76	63.47	65.55	66.88	66.95	71.14	68.57	61.54	68.32	59.69
'14.00'	5690.425	4.930	-1.87	52.50	56.74	55.05	56.00	57.24	57.84	59.95	57.16	52.86	58.43	49.12
'14.00'	5701.104	4.930	-1.58	40.93	43.60	41.12	43.99	44.89	43.40	48.25	46.86	41.73	46.36	37.65
'14.00'	5793.073	4.930	-2.48	42.32	43.99	44.27	46.93	47.90	47.39	52.54	51.10	43.74	50.36	43.15
'14.00'	6125.021	5.614	-1.46	34.19	37.43	36.69	38.63	40.56	39.71	43.61	43.33	35.27	41.70	31.42
'14.00'	6145.016	5.616	-1.31	39.88	42.97	41.29	41.81	44.49	44.21	47.40	44.69	39.63	44.75	41.16
'14.00'	6243.815	5.616	-1.24	45.52	48.61	48.05	49.71	52.22	51.58	53.82	53.35	45.98	55.52	47.01
'14.00'	6244.466	5.616	-1.09	55.73	54.88	51.66	58.25	57.20	60.87	66.67	56.94	53.55	65.77	47.15
'14.00'	6721.848	5.863	-1.51	49.45	52.44	48.87	53.70	55.02	54.69	58.92	59.41	47.78	58.68	40.78
'14.00'	6741.628	5.984	-1.42	17.43	16.62	16.13	17.00	19.75	18.30	20.92	20.29	15.29	19.35	17.32
'16.00'	8693.931	7.870	-0.51	11.29	14.12	13.20	11.94	15.80	13.99	16.04	15.93	13.76	17.13	13.87
'16.00'	8694.626	7.870	0.08	20.16	25.50	26.06	23.15	27.88	26.91	27.69	27.87	25.30	30.00	29.64
'19.00'	7698.974	0.000	-0.17	183.75	188.48	179.35	193.15	183.44	195.25	190.70	180.80	177.57	187.02	178.06
'20.00'	4512.268	2.526	-1.90	31.81	32.06	32.37	33.11	30.33	32.65	34.57	31.39	27.22	30.81	21.11
'20.00'	5260.387	2.521	-1.71	42.70	47.38	46.18	52.25	45.58	50.05	50.48	50.79	44.17	47.40	30.79
'20.00'	5512.980	2.933	-0.46	96.90	111.49	102.76	115.02	106.40	108.13	119.57	113.48	104.68	107.24	91.09
'20.00'	5581.965	2.523	-0.55	99.19	105.91	101.03	107.74	103.74	105.02	110.73	104.86	98.83	103.03	104.01
'20.00'	5590.114	2.521	-0.57	97.68	104.37	99.57	103.80	100.63	105.09	106.66	101.85	96.53	101.32	92.74
'20.00'	5867.562	2.933	-1.57	29.73	33.00	30.31	33.94	30.90	33.57	36.75	33.25	27.97	31.21	24.08
'20.00'	6166.439	2.521	-1.14	78.48	83.20	78.40	84.64	80.69	84.45	86.83	81.87	76.12	81.92	71.41
'20.00'	6169.042	2.523	-0.79	110.45	116.47	112.67	120.89	113.00	121.88	120.75	112.30	108.85	113.81	98.33
'20.00'	6455.598	2.523	-1.34	63.32	66.82	62.64	68.61	65.02	69.50	72.70	68.82	61.42	66.82	56.10
'20.00'	6471.662	2.526	-0.68	99.86	105.93	99.30	105.34	101.06	106.92	106.92	102.81	96.64	101.85	90.10
'20.00'	6499.650	2.523	-0.81	102.23	104.97	99.00	102.56	102.66	105.09	110.63	101.11	97.44	98.86	83.30
'21.00'	4743.830	1.448	0.42	13.61	12.60	11.72	15.86	13.19	14.16	17.75	12.37	10.64	14.47	7.75
'21.00'	5081.574	1.448	0.46	15.05	15.88	14.60	17.76	15.90	15.82	20.93	18.57	14.02	17.90	13.12
'21.00'	5520.497	1.865	0.29	8.94	11.20	9.30	12.65	10.97	11.12	13.88	11.01	8.88	12.09	7.98

continued.

Element	λ (Å)	χ(eV)	log(gf)	61 Vir	HD111	HD140	HD181	HD188	HD201	HD223	HD471	HD512	HD587	Sun
'21.00'	5671.821	1.448	0.49	21.83	22.51	20.48	27.00	22.29	24.51	31.07	26.13	21.03	25.51	14.43
'21.01'	5526.790	1.768	0.02	78.35	80.00	85.55	74.92	82.55	79.21	84.70	87.69	81.85	79.71	81.13
'21.01'	5657.896	1.507	-0.60	64.97	67.42	66.42	65.58	68.90	67.58	71.86	73.18	66.61	71.14	66.25
'21.01'	5684.202	1.507	-1.07	38.76	37.92	37.53	37.93	40.15	38.42	43.55	45.01	39.10	42.72	36.37
'21.01'	6245.637	1.507	-1.03	36.16	36.82	34.88	36.48	38.36	36.21	42.29	41.06	37.93	42.77	35.73
'21.01'	6320.851	1.500	-1.81	7.83	7.79	7.55	7.39	9.18	8.09	10.03	11.83	9.49	10.62	8.42
'21.01'	6604.601	1.357	-1.30	37.51	37.91	37.43	38.70	40.10	38.24	43.46	43.04	38.65	41.43	37.77
'22.00'	4465.805	1.739	-0.16	49.71	51.47	48.11	52.35	46.52	51.35	54.87	50.07	46.16	49.86	44.37
'22.00'	4555.484	0.848	-0.48	75.23	75.90	71.93	79.97	76.26	76.81	80.10	79.10	73.10	76.66	72.36
'22.00'	4758.118	2.249	0.42	52.24	54.28	50.25	55.61	53.19	54.02	57.50	55.46	49.80	55.94	45.31
'22.00'	4759.270	2.256	0.51	55.34	56.83	53.51	59.18	55.64	58.73	59.87	57.16	52.88	58.54	47.65
'22.00'	4820.411	1.502	-0.44	55.80	57.01	51.47	59.94	52.85	55.96	60.77	61.06	53.56	55.04	44.79
'22.00'	4913.614	1.873	0.16	59.67	58.92	57.25	66.07	60.42	60.03	66.65	63.15	58.58	61.91	53.61
'22.00'	5022.868	0.826	-0.43	90.29	91.62	84.70	95.87	86.77	91.28	95.91	92.13	86.04	91.10	76.98
'22.00'	5147.478	0.000	-2.01	48.73	47.41	44.77	53.47	47.04	48.13	56.95	51.90	45.66	51.39	38.07
'22.00'	5219.702	0.021	-2.29	43.04	43.18	38.11	48.13	40.71	41.96	52.52	45.74	39.29	44.92	27.59
'22.00'	5295.775	1.067	-1.63	22.41	22.21	20.11	24.23	19.64	21.58	26.00	22.28	18.78	21.47	13.23
'22.00'	5490.148	1.460	-0.93	30.90	32.02	29.07	36.69	31.50	33.08	37.63	33.61	28.06	33.15	21.02
'22.00'	5739.469	2.249	-0.60	14.27	14.41	11.95	14.98	13.26	14.20	16.21	14.17	11.97	13.98	8.41
'22.00'	5866.451	1.067	-0.84	60.27	60.53	55.22	65.60	59.37	61.73	68.90	62.90	56.68	62.04	47.02
'22.00'	6091.171	2.267	-0.42	20.84	21.55	19.49	24.10	21.30	22.87	26.79	24.08	19.19	22.40	16.13
'22.00'	6126.216	1.067	-1.42	32.04	32.01	29.48	36.75	31.55	33.19	39.79	34.41	28.61	34.09	23.03
'22.00'	6258.102	1.443	-0.35	66.05	63.46	59.48	66.68	61.09	64.55	72.95	64.76	60.82	65.99	52.57
'22.00'	6261.098	1.430	-0.47	58.11	60.16	55.77	65.04	58.85	62.26	68.79	63.27	56.47	62.78	47.70
'22.00'	6743.122	0.900	-1.63	30.04	28.79	25.17	33.21	28.12	29.04	36.36	31.79	24.85	30.40	18.24
'22.01'	4470.853	1.165	-2.02	70.64	69.97	70.05	71.84	69.79	71.43	66.48	67.12	63.34	65.20	80.03
'22.01'	4544.016	1.243	-2.58	42.33	43.82	42.60	43.03	43.56	44.03	48.28	49.63	42.47	45.26	42.19
'22.01'	4583.408	1.165	-2.92	33.69	33.29	32.82	31.97	33.86	34.01	36.82	37.95	33.13	34.19	36.17
'22.01'	4636.320	1.165	-3.02	19.91	21.55	20.22	21.41	20.56	20.33	24.19	24.49	19.93	23.49	19.52
'22.01'	4657.200	1.243	-2.24	50.20	49.91	50.45	48.38	51.86	50.19	51.44	55.21	51.65	52.93	51.46
'22.01'	4779.985	2.048	-1.26	66.37	68.57	67.45	66.39	70.41	69.47	71.02	72.25	66.69	71.27	64.81
'22.01'	4874.009	3.095	-0.80	40.30	40.58	41.05	38.93	41.02	39.29	43.93	46.53	42.49	42.28	44.61
'22.01'	4911.193	3.124	-0.61	57.58	57.02	56.87	59.67	59.53	59.10	63.97	65.48	59.66	61.87	51.11
'22.01'	5211.530	2.590	-1.16	37.00	34.30	35.41	34.22	37.02	35.97	40.40	40.65	35.91	37.09	32.08
'22.01'	5336.771	1.582	-1.59	72.53	73.23	72.67	70.85	73.90	74.58	73.70	77.23	72.90	74.55	70.62
'22.01'	5381.015	1.566	-1.92	61.74	61.61	61.40	61.00	65.52	62.92	67.18	67.63	61.78	63.58	58.09
'22.01'	5418.751	1.582	-2.00	48.61	50.06	49.17	47.91	51.21	49.99	54.54	55.44	50.53	52.91	49.30
'23.00'	5670.853	1.081	-0.42	29.73	28.75	23.86	35.47	28.84	30.49	37.83	31.56	24.26	31.41	18.95
'23.00'	5727.652	1.051	-0.87	14.17	14.58	12.09	18.28	14.30	14.76	19.37	15.24	11.30	15.29	37.78
'23.00'	6039.722	1.064	-0.65	19.49	20.04	16.64	23.75	19.80	21.17	25.48	20.73	16.00	21.58	12.25
'23.00'	6081.441	1.051	-0.57	22.73	22.50	18.95	27.23	22.02	24.39	29.77	23.57	19.62	24.59	15.13
'23.00'	6090.214	1.081	-0.06	47.20	45.00	41.16	52.38	46.94	48.40	56.05	49.00	41.51	50.43	33.65
'23.00'	6119.523	1.064	-0.32	31.93	32.02	27.51	37.46	32.35	33.49	40.18	34.44	28.92	35.61	21.86
'23.00'	6199.197	0.287	-1.30	23.66	22.11	18.66	28.11	22.46	23.52	31.77	23.96	19.42	25.31	13.86
'23.00'	6251.827	0.287	-1.34	26.17	26.22	21.65	32.56	25.96	28.41	35.47	28.18	22.75	28.59	17.06
'24.00'	4801.025	3.122	-0.13	50.82	54.21	51.02	55.53	53.65	56.16	59.15	54.47	50.67	55.12	52.93
'24.00'	4936.336	3.113	-0.34	52.70	53.98	53.31	60.72	55.63	57.39	60.38	55.75	51.37	57.92	50.71
'24.00'	5214.132	3.369	-0.74	24.29	24.95	23.20	25.07	25.02	25.32	28.79	25.37	21.06	25.70	17.94
'24.00'	5220.892	3.385	-1.03	14.55	16.60	14.59	18.09	15.53	15.78	19.75	15.91	13.88	16.40	11.01
'24.00'	5238.961	2.709	-1.30	22.15	23.20	20.26	27.39	23.88	25.15	29.65	24.88	19.35	24.61	16.36
'24.00'	5247.565	0.961	-1.64	91.89	94.41	89.27	98.37	92.39	97.02	100.50	93.64	88.61	94.57	83.54
'24.00'	5272.000	3.449	-0.42	35.09	36.06	33.60	38.86	36.78	38.33	41.32	36.49	32.90	37.92	27.20
'24.00'	5287.178	3.438	-0.90	13.69	16.31	13.39	16.31	14.62	15.73	19.01	15.50	13.45	15.69	11.18
'24.00'	5296.691	0.983	-1.40	100.40	106.80	98.94	108.30	104.22	109.10	112.51	102.96	97.25	105.45	93.26
'24.00'	5300.745	0.983	-2.12	84.21	72.04	67.81	77.73	73.19	74.33	82.03	74.27	67.09	74.48	62.42
'24.00'	5345.796	1.004	-0.98	122.07	130.76	122.72	134.33	128.72	133.58	136.70	128.57	121.35	127.54	110.82

continued.

Element	λ (Å)	χ(eV)	log(gf)	61 Vir	HD111	HD140	HD181	HD188	HD201	HD223	HD471	HD512	HD587	Sun
'24.00'	5348.315	1.004	-1.29	110.87	116.34	110.63	120.18	115.52	118.83	123.26	115.56	110.02	117.25	105.17
'24.00'	5783.063	3.323	-0.50	38.91	41.72	38.96	45.42	39.57	43.19	49.73	43.69	38.26	42.08	31.91
'24.00'	5783.850	3.322	-0.29	51.39	55.20	52.07	58.80	52.94	56.54	63.78	56.72	49.80	55.31	42.85
'24.00'	6661.075	4.193	-0.19	14.35	17.42	15.46	18.55	17.64	18.54	21.17	17.54	14.20	17.96	12.27
'24.01'	4588.199	4.071	-0.62	62.64	68.60	70.25	65.34	68.44	67.43	71.63	68.86	66.93	70.28	68.61
'24.01'	4592.049	4.074	-1.47	45.84	47.90	48.35	45.41	51.51	49.59	51.22	52.22	47.41	49.99	49.36
'24.01'	5237.329	4.073	-1.35	51.01	56.09	55.26	53.66	58.02	57.34	59.40	57.75	54.07	56.68	53.42
'24.01'	5246.768	3.714	-2.56	17.37	16.35	17.90	16.81	16.86	16.72	19.22	19.44	17.07	18.18	19.12
'24.01'	5305.853	3.827	-2.16	22.46	25.86	26.62	23.78	27.61	26.68	28.40	29.32	24.73	28.22	24.39
'24.01'	5308.408	4.071	-2.05	25.53	27.75	27.14	27.47	27.81	28.37	31.04	30.37	25.81	28.48	24.93
'24.01'	5502.067	4.168	-2.11	14.03	15.33	14.17	17.28	19.48	14.08	20.15	19.89	14.10	19.98	17.41
'25.00'	4709.712	2.888	-0.34	75.72	80.25	73.40	80.62	78.83	80.80	85.18	77.42	74.49	80.51	80.38
'25.00'	4739.087	2.941	-0.49	65.73	69.97	66.90	75.50	72.21	71.21	78.03	72.39	66.74	73.35	60.80
'25.00'	5004.892	2.920	-1.63	22.55	19.93	20.11	27.69	24.88	23.03	29.34	23.45	18.21	25.40	15.93
'25.00'	5399.499	3.853	-0.28	46.87	51.93	46.47	57.84	55.34	56.11	63.54	51.65	45.39	55.04	38.88
'25.00'	6013.513	3.072	-0.25	95.69	98.30	92.60	106.37	102.62	104.12	111.13	99.88	92.34	103.99	85.37
'25.00'	6021.819	3.075	0.03	109.53	114.02	105.75	120.95	113.76	118.01	122.41	112.08	103.63	115.11	98.58
'26.00'	4389.244	0.052	-4.58	82.84	86.39	81.71	85.61	84.85	85.86	87.86	84.83	82.38	85.00	73.93
'26.00'	4445.471	0.087	-5.44	50.19	48.97	46.18	53.72	49.00	50.45	57.35	52.77	47.83	52.63	40.16
'26.00'	4602.000	1.608	-3.15	79.70	82.19	81.71	82.04	84.29	83.91	89.72	80.20	78.50	82.29	74.98
'26.00'	4658.294	3.267	-3.04	19.08	20.61	18.78	22.50	20.42	21.28	26.59	22.13	17.45	21.69	15.87
'26.00'	4779.439	3.415	-2.02	45.43	47.29	43.92	48.81	47.79	48.17	52.24	49.89	44.20	49.81	38.81
'26.00'	4788.751	3.237	-1.76	69.01	71.52	70.29	72.52	71.52	73.39	73.97	72.46	68.62	71.55	69.40
'26.00'	4950.104	3.417	-1.67	82.35	88.13	83.72	91.72	85.70	86.95	93.73	87.50	81.23	84.88	78.59
'26.00'	4994.129	0.915	-3.08	126.46	125.52	123.16	124.76	24.13	128.44	137.45	122.46	121.81	119.61	117.29
'26.00'	5016.476	4.256	-1.69	40.17	42.83	39.58	45.68	41.69	39.27	44.94	43.03	37.06	42.71	34.88
'26.00'	5044.210	2.851	-2.03	87.30	89.89	84.03	93.52	85.70	86.54	92.29	87.17	75.71	85.51	77.31
'26.00'	5054.642	3.640	-1.92	45.00	46.00	45.69	49.77	48.99	47.93	56.09	49.11	44.98	50.15	39.98
'26.00'	5127.358	0.915	-3.30	112.81	111.16	111.95	113.97	111.27	112.96	118.42	110.63	107.69	111.03	97.00
'26.00'	5127.679	0.052	-6.12	31.69	28.64	27.12	35.83	31.64	31.73	41.12	34.99	29.92	35.06	19.15
'26.00'	5198.711	2.223	-2.13	106.83	113.19	105.86	116.81	109.58	113.59	117.53	109.00	104.34	109.53	94.89
'26.00'	5225.525	0.110	-4.78	85.89	87.34	82.54	90.74	86.66	89.41	92.07	88.93	83.82	88.18	74.07
'26.00'	5242.491	3.634	-0.96	93.49	100.31	98.14	99.03	98.64	103.28	103.90	97.02	91.69	98.59	87.69
'26.00'	5247.049	0.087	-4.94	76.81	75.79	73.55	79.64	74.67	77.64	83.54	78.85	74.32	79.19	68.34
'26.00'	5250.208	0.121	-4.93	71.23	71.42	67.53	73.12	68.19	73.10	77.78	72.80	67.80	72.09	69.62
'26.00'	5295.299	4.415	-1.69	34.98	38.04	36.32	38.02	36.14	38.15	41.79	37.23	33.94	37.45	29.43
'26.00'	5322.040	2.279	-2.80	78.21	76.19	73.89	86.32	80.76	80.05	83.61	77.11	73.24	79.78	60.30
'26.00'	5373.698	4.473	-0.86	76.87	80.03	73.77	78.96	76.01	75.77	82.60	74.33	71.48	77.48	62.94
'26.00'	5379.574	3.694	-1.51	72.17	70.28	66.16	72.91	71.76	72.18	75.02	71.15	68.50	73.31	65.65
'26.00'	5386.333	4.154	-1.77	37.57	40.81	37.85	41.91	41.23	41.78	49.25	40.62	34.96	42.29	34.93
'26.00'	5466.390	4.371	-0.63	92.28	98.45	93.52	99.46	98.20	99.71	102.81	100.23	84.99	89.12	85.44
'26.00'	5466.987	3.573	-2.23	41.06	42.59	40.79	44.87	42.01	43.62	49.27	44.60	44.36	48.56	35.25
'26.00'	5522.446	4.209	-1.55	44.89	50.50	47.49	51.54	49.01	48.73	57.37	52.78	46.86	50.04	44.15
'26.00'	5546.500	4.371	-1.31	51.80	58.82	55.92	59.89	57.47	59.05	63.15	57.10	53.90	57.74	50.66
'26.00'	5560.207	4.434	-1.19	56.58	58.45	55.68	58.97	57.21	58.75	66.08	59.26	53.64	57.27	53.33
'26.00'	5577.025	5.033	-1.55	13.96	14.61	13.50	14.89	14.21	15.25	19.30	14.72	13.83	14.61	10.97
'26.00'	5618.631	4.209	-1.27	53.91	58.90	54.97	61.10	57.66	60.85	60.16	60.43	55.41	58.41	52.63
'26.00'	5636.696	3.640	-2.61	25.58	26.86	24.92	27.37	24.61	26.76	31.83	25.88	21.69	27.53	19.96
'26.00'	5638.262	4.220	-0.87	86.24	92.67	92.44	94.02	89.62	94.15	102.54	90.20	84.61	93.12	78.87
'26.00'	5649.987	5.099	-0.92	40.85	41.60	39.33	44.26	43.44	43.62	47.44	43.29	38.27	44.23	37.04
'26.00'	5651.469	4.473	-2.00	22.20	25.10	22.42	27.88	24.21	21.90	28.13	24.05	21.90	25.90	18.00
'26.00'	5661.345	4.284	-1.73	26.76	30.38	27.68	32.27	29.24	28.26	36.51	31.81	28.26	31.72	23.22
'26.00'	5679.022	4.652	-0.92	66.41	71.72	68.79	72.59	71.54	64.11	74.08	69.56	64.11	71.15	62.73
'26.00'	5696.089	4.548	-1.72	16.64	18.12	16.32	18.76	18.31	14.74	20.13	18.00	14.74	19.91	12.71
'26.00'	5701.544	2.559	-2.21	93.27	98.66	90.83	103.16	97.22	98.81	106.00	99.46	94.84	100.47	87.52
'26.00'	5705.464	4.301	-1.35	45.80	46.80	44.86	48.01	46.60	48.49	52.77	49.81	43.69	48.34	38.62

continued.

Element	λ (Å)	χ(eV)	log(gf)	61 Vir	HD111	HD140	HD181	HD188	HD201	HD223	HD471	HD512	HD587	Sun
'26.00'	5778.453	2.588	-3.43	28.32	30.75	27.13	33.31	29.61	27.44	37.44	31.88	27.44	30.96	22.16
'26.00'	5784.657	3.396	-2.53	29.23	31.92	28.54	33.59	30.82	32.77	38.33	36.98	32.38	36.58	26.36
'26.00'	5793.913	4.220	-1.70	38.50	41.04	38.87	43.17	40.44	37.39	46.21	42.35	37.39	42.36	35.62
'26.00'	5809.217	3.883	-1.84	59.80	62.53	57.54	65.06	62.02	64.04	69.35	63.54	56.59	63.71	52.89
'26.00'	5852.217	4.548	-1.33	47.55	51.21	47.84	52.83	51.92	53.00	57.75	51.75	46.53	51.59	40.41
'26.00'	5855.076	4.608	-1.47	25.13	28.05	25.58	28.67	28.25	24.25	32.69	29.28	24.25	28.68	22.38
'26.00'	5905.671	4.652	-0.73	67.84	68.92	67.00	71.32	70.99	72.46	74.69	72.32	62.90	71.87	61.53
'26.00'	5916.247	2.453	-2.99	62.19	64.41	61.15	67.79	63.92	68.13	70.39	65.77	61.94	69.99	54.82
'26.00'	5927.786	4.652	-1.09	46.00	49.65	47.02	50.35	49.69	50.30	54.07	50.92	45.54	51.71	45.13
'26.00'	5934.653	3.928	-1.17	91.41	94.49	91.14	97.08	92.83	95.42	101.72	99.41	88.34	95.85	78.78
'26.00'	5956.692	0.859	-4.60	61.21	62.28	58.57	65.85	60.19	60.05	69.80	67.00	60.05	64.47	51.14
'26.00'	5987.065	4.796	-0.42	78.04	84.57	80.80	83.77	81.78	84.92	88.45	81.17	78.35	81.49	68.78
'26.00'	6003.010	3.881	-1.12	101.55	107.74	102.41	110.50	105.12	108.94	110.39	99.17	96.01	106.11	90.28
'26.00'	6005.542	2.588	-3.60	27.95	29.71	27.15	33.69	29.60	31.39	36.04	31.25	27.60	31.75	21.62
'26.00'	6024.049	4.548	-0.12	131.73	145.26	138.93	150.84	141.45	148.89	149.61	134.96	129.38	140.77	119.94
'26.00'	6027.050	4.076	-1.08	70.08	73.61	70.36	74.64	73.79	69.53	78.43	74.94	69.53	74.38	64.15
'26.00'	6055.992	4.733	-0.46	75.61	82.71	78.48	81.57	80.48	83.02	85.22	81.92	75.61	80.26	73.19
'26.00'	6065.482	2.608	-1.53	137.50	145.73	137.61	151.05	142.38	133.97	153.70	139.29	133.97	140.78	126.79
'26.00'	6078.999	4.652	-1.12	49.53	54.70	51.51	55.12	53.09	55.27	57.96	54.07	49.52	54.34	47.33
'26.00'	6082.708	2.223	-3.57	41.51	43.68	38.98	46.49	43.39	45.64	49.71	44.35	40.75	45.58	33.83
'26.00'	6093.643	4.607	-1.50	35.98	38.29	35.94	39.70	40.41	35.04	43.91	39.95	35.04	39.99	30.83
'26.00'	6096.662	3.984	-1.93	44.94	47.81	45.00	49.32	48.00	42.93	53.61	49.19	42.93	48.06	38.33
'26.00'	6151.617	2.176	-3.29	57.78	59.37	56.26	62.55	59.39	56.12	64.97	61.68	56.12	61.19	50.71
'26.00'	6157.728	4.076	-1.26	65.24	69.49	65.42	67.41	67.08	69.49	73.08	69.17	61.83	68.55	59.89
'26.00'	6165.360	4.143	-1.47	50.24	53.78	51.43	54.89	56.22	49.46	57.27	55.76	49.46	56.73	45.99
'26.00'	6173.334	2.223	-2.88	73.48	77.61	72.66	79.33	76.17	72.26	81.93	78.15	72.26	77.50	67.33
'26.00'	6187.987	3.943	-1.72	55.89	58.72	56.03	61.33	60.27	59.50	63.78	59.44	53.62	58.89	49.07
'26.00'	6200.312	2.608	-2.43	77.25	82.88	78.06	84.63	81.59	77.34	88.92	82.27	77.34	83.02	74.64
'26.00'	6213.429	2.223	-2.48	93.37	97.75	90.34	99.14	93.77	90.22	102.34	91.68	90.22	95.85	83.44
'26.00'	6219.279	2.198	-2.43	108.44	112.91	107.20	113.39	108.27	112.13	114.41	106.03	101.91	113.50	90.63
'26.00'	6226.730	3.883	-2.22	33.55	34.89	33.66	38.88	36.05	39.56	40.84	38.92	32.22	36.93	28.51
'26.00'	6240.645	2.223	-3.23	54.86	58.14	54.26	59.68	58.02	54.21	64.55	60.08	54.21	59.24	51.30
'26.00'	6252.554	2.404	-1.68	143.68	152.41	145.19	156.43	148.36	152.00	152.97	148.28	136.17	151.83	135.09
'26.00'	6265.131	2.176	-2.55	88.81	97.57	91.74	99.36	94.76	89.64	100.86	95.80	89.64	94.92	88.15
'26.00'	6270.222	2.858	-2.46	57.92	59.54	57.24	62.45	58.64	56.38	66.83	61.72	56.38	61.38	53.93
'26.00'	6271.276	3.332	-2.70	27.76	31.24	28.05	32.44	30.17	31.29	36.75	32.14	27.91	31.71	23.07
'26.00'	6380.743	4.186	-1.37	55.74	59.06	55.64	60.28	59.83	60.42	64.16	59.61	55.14	59.95	52.44
'26.00'	6392.538	2.279	-4.03	23.14	25.02	21.53	27.51	25.37	24.64	30.08	26.36	21.54	25.58	17.87
'26.00'	6430.844	2.176	-2.00	136.71	140.22	134.04	142.81	136.88	142.46	145.13	133.82	130.65	136.72	119.58
'26.00'	6469.192	4.835	-0.77	66.78	70.11	66.34	72.79	74.17	72.59	77.85	71.27	69.05	75.14	58.11
'26.00'	6498.937	0.958	-4.69	60.89	61.32	54.32	63.29	58.99	60.31	70.62	61.06	54.37	59.83	43.43
'26.00'	6593.870	2.433	-2.42	101.85	103.63	99.87	108.32	103.91	98.39	104.80	103.80	98.39	104.59	90.45
'26.00'	6597.557	4.795	-1.07	52.79	56.32	52.32	57.26	55.45	56.64	59.06	57.51	49.89	54.43	45.44
'26.00'	6625.022	1.011	-5.35	21.60	23.96	20.62	27.36	22.88	24.41	30.07	24.72	21.10	25.80	11.67
'26.00'	6677.985	2.692	-1.41	147.81	157.92	152.32	162.66	154.09	160.17	164.26	152.99	152.21	154.31	144.86
'26.00'	6703.566	2.758	-3.16	41.70	45.27	41.79	47.62	45.12	42.11	52.40	47.45	42.11	46.77	37.96
'26.00'	6705.101	4.607	-1.04	50.03	56.15	53.35	58.92	57.09	52.83	64.00	56.86	52.83	58.80	47.26
'26.00'	6710.316	1.485	-4.88	21.74	22.47	19.14	25.64	23.18	23.96	30.06	23.81	20.07	25.10	15.77
'26.00'	6713.743	4.795	-1.60	24.87	27.07	25.87	28.94	29.36	23.42	31.47	28.10	23.42	27.66	21.39
'26.00'	6725.353	4.103	-2.30	22.48	22.76	20.36	23.99	22.83	23.66	26.66	23.54	20.10	24.21	17.56
'26.00'	6726.666	4.607	-1.13	52.70	57.52	52.90	56.85	55.78	51.21	60.88	56.50	51.21	57.31	47.44
'26.00'	6733.150	4.638	-1.58	29.75	33.62	30.50	34.59	33.36	33.18	37.76	33.92	30.12	33.26	26.80
'26.00'	6739.520	1.557	-4.79	15.36	16.67	14.75	20.02	16.69	17.88	23.18	18.45	14.55	18.29	11.68
'26.00'	6750.150	2.424	-2.62	82.90	85.67	80.77	87.24	83.34	81.05	91.68	86.42	81.05	85.01	74.70
'26.00'	6752.705	4.638	-1.20	38.99	43.04	39.60	43.44	42.43	44.38	48.33	43.53	38.34	43.47	37.31
'26.00'	6793.258	4.076	-2.32	15.55	17.50	14.29	18.26	16.77	18.04	21.27	18.90	15.25	18.06	12.46

continued.

Element	λ (Å)	χ(eV)	log(gf)	61 Vir	HD111	HD140	HD181	HD188	HD201	HD223	HD471	HD512	HD587	Sun
'26.00'	6806.843	2.727	-3.21	41.43	43.58	39.55	46.57	43.06	44.12	50.23	44.70	39.81	45.92	34.05
'26.00'	6810.257	4.607	-0.98	56.39	61.85	58.33	63.39	62.01	56.16	67.80	62.00	56.16	62.14	50.97
'26.00'	6837.006	4.593	-1.68	19.30	21.44	19.10	22.84	21.55	18.80	26.18	23.18	18.80	22.49	16.91
'26.00'	6839.830	2.559	-3.45	36.01	38.27	33.50	42.80	38.49	40.35	45.26	41.91	35.53	39.68	30.40
'26.00'	6843.648	4.548	-0.93	68.77	71.12	67.49	74.79	71.38	73.85	78.01	72.16	66.78	72.67	62.85
'26.00'	6858.145	4.607	-0.93	56.44	62.31	59.40	64.01	62.54	63.82	67.38	62.41	57.56	62.87	55.82
'26.00'	7955.692	5.033	-1.12	27.28	32.74	28.76	32.74	28.91	31.90	35.37	29.71	27.03	33.24	26.03
'26.01'	4508.288	2.856	-2.25	84.10	92.37	92.64	82.88	87.98	91.88	91.97	90.81	88.89	85.35	92.93
'26.01'	4520.224	2.807	-2.61	80.27	79.08	82.21	80.93	84.11	83.73	84.81	83.51	79.87	82.85	84.54
'26.01'	4576.340	2.844	-2.97	63.21	65.06	64.45	63.15	66.76	66.63	68.56	68.53	65.66	67.02	64.06
'26.01'	4620.521	2.828	-3.24	48.03	51.19	50.49	49.58	56.09	54.49	56.50	54.92	51.90	56.15	54.51
'26.01'	4993.358	2.807	-3.68	39.33	37.65	37.76	34.05	39.09	41.78	41.59	40.20	38.02	39.72	42.47
'26.01'	5197.577	3.230	-2.07	88.14	93.46	90.30	91.67	93.43	87.51	92.75	90.87	88.23	93.28	90.41
'26.01'	5325.553	3.221	-3.32	41.54	44.21	44.28	43.41	45.74	44.89	47.37	47.12	45.58	48.10	51.38
'26.01'	5414.073	3.221	-3.64	24.25	26.93	27.39	24.64	29.07	28.69	29.60	31.08	28.49	29.83	34.11
'26.01'	5425.257	3.199	-3.16	42.34	44.59	42.83	42.50	44.56	43.22	47.57	46.74	43.22	45.16	44.20
'26.01'	6084.111	3.199	-3.78	18.65	20.06	19.27	19.74	22.40	21.73	22.51	22.68	20.47	22.57	21.41
'26.01'	6149.258	3.889	-2.72	31.01	35.78	35.60	31.60	36.20	35.06	35.76	37.68	33.17	35.66	36.07
'26.01'	6247.557	3.892	-2.31	46.82	53.05	51.36	46.14	52.00	51.69	51.81	53.14	49.81	51.41	52.90
'26.01'	6369.462	2.891	-4.21	14.97	18.37	17.75	16.08	19.08	17.73	19.82	22.18	17.73	20.41	19.09
'26.01'	6416.919	3.892	-2.65	38.29	40.54	40.82	39.04	42.59	42.50	42.79	44.25	39.03	42.06	40.46
'26.01'	6432.680	2.891	-3.68	38.41	40.79	41.71	37.06	39.18	41.61	42.23	43.50	40.71	42.34	42.82
'26.01'	6456.383	3.903	-2.18	55.66	60.30	62.20	56.88	61.64	63.63	61.80	62.35	58.63	60.94	65.03
'27.00'	5212.691	3.514	-0.11	28.75	27.32	24.36	30.43	29.31	28.85	36.54	28.93	24.41	31.38	25.33
'27.00'	5247.911	1.785	-2.07	26.02	24.77	21.34	29.90	26.10	26.08	33.84	28.02	23.39	29.64	19.96
'27.00'	5280.629	3.629	-0.03	24.81	25.05	22.42	30.37	27.47	25.82	32.30	27.43	23.97	29.54	19.12
'27.00'	5301.039	1.710	-2.00	25.49	27.03	24.09	33.76	30.34	29.64	37.49	31.17	25.61	32.77	21.99
'27.00'	5342.695	4.021	0.69	36.89	35.91	34.69	38.41	38.72	38.16	43.48	38.48	34.13	40.94	31.70
'27.00'	5483.344	1.710	-1.49	74.09	61.87	57.18	71.22	65.50	64.75	76.60	68.59	59.99	70.56	51.13
'27.00'	5530.774	1.710	-2.06	31.35	23.17	21.20	27.88	25.45	24.44	31.43	26.71	22.77	28.81	19.60
'27.00'	5647.234	2.280	-1.56	19.88	18.37	15.39	23.46	21.05	21.93	26.62	22.32	17.45	24.07	13.07
'27.00'	6188.996	1.710	-2.45	15.40	14.24	12.81	18.01	16.73	14.25	20.05	15.80	13.54	16.83	12.28
'27.00'	6454.990	3.632	-0.25	17.83	18.23	16.92	20.57	21.28	19.09	23.73	20.94	17.18	21.59	14.73
'28.00'	4953.200	3.740	-0.58	61.08	62.08	61.04	66.36	63.62	64.35	69.36	64.85	58.46	65.58	60.84
'28.00'	5010.934	3.635	-0.87	57.28	54.80	55.86	57.13	57.16	58.34	58.49	57.41	53.99	57.70	48.54
'28.00'	5589.357	3.898	-1.14	34.51	34.83	31.95	36.39	36.54	36.27	39.78	36.51	31.40	37.53	29.52
'28.00'	5643.072	4.165	-1.24	17.74	17.93	17.92	20.09	19.58	19.60	23.08	19.61	16.72	21.20	16.00
'28.00'	5805.213	4.167	-0.64	44.00	47.19	44.69	49.99	51.33	48.47	52.73	49.18	43.65	50.27	43.40
'28.00'	6086.276	4.266	-0.53	49.37	49.42	46.78	52.33	53.05	52.31	55.66	52.56	46.72	54.40	43.85
'28.00'	6108.107	1.676	-2.45	69.92	70.75	67.13	75.76	73.51	73.43	79.43	74.69	68.44	75.11	64.94
'28.00'	6130.130	4.266	-0.96	24.82	24.02	23.03	27.20	27.57	27.43	30.69	26.17	21.60	28.04	22.71
'28.00'	6176.807	4.088	-0.26	67.28	70.38	66.05	72.36	74.04	71.93	76.71	72.91	65.99	73.56	66.90
'28.00'	6177.236	1.826	-3.50	19.41	19.35	16.02	22.52	21.58	20.02	24.98	21.62	17.54	22.84	15.67
'28.00'	6186.709	4.105	-0.96	34.45	35.09	33.26	37.12	38.75	37.39	40.26	37.17	32.52	38.24	30.76
'28.00'	6204.600	4.088	-1.10	24.01	26.07	23.43	28.44	29.37	28.33	31.11	27.69	23.64	29.49	23.59
'28.00'	6223.981	4.105	-0.91	29.00	31.66	30.33	34.70	35.25	35.92	37.59	33.25	29.83	35.52	28.56
'28.00'	6378.247	4.154	-0.83	36.66	36.55	34.71	39.50	40.15	38.99	42.70	39.62	33.47	41.14	31.77
'28.00'	6643.629	1.676	-2.30	102.61	103.73	100.91	111.25	107.29	109.45	116.41	107.10	101.62	110.72	95.65
'28.00'	6767.768	1.826	-2.17	86.95	89.25	83.77	90.33	92.39	92.53	96.29	92.37	86.21	91.77	80.97
'28.00'	6772.313	3.658	-0.98	56.77	57.25	55.23	61.87	60.98	60.72	65.44	60.92	54.45	62.28	50.39
'28.00'	7797.586	3.898	-0.26	84.84	89.85	86.68	94.96	95.98	94.43	96.29	91.72	85.73	94.61	82.36
'29.00'	5218.197	3.817	0.47	63.80	60.28	58.45	65.11	66.86	62.60	71.35	66.33	59.85	67.29	56.90
'29.00'	5220.066	3.817	-0.44	18.77	18.46	18.00	20.92	21.11	19.82	24.47	22.48	18.60	23.59	16.38
'29.00'	7933.124	3.786	-0.37	35.92	34.38	32.11	43.66	45.68	41.56	50.67	43.27	36.55	48.75	33.91
'30.00'	4722.153	4.030	-0.33	80.35	83.14	74.59	84.27	86.08	83.09	92.54	88.00	79.36	97.00	74.94
'30.00'	4810.528	4.078	-0.13	72.64	74.17	71.07	75.68	76.54	75.84	76.43	77.58	73.76	77.58	71.01

continued.

Element	λ (Å)	χ(eV)	log(gf)	61 Vir	HD111	HD140	HD181	HD188	HD201	HD223	HD471	HD512	HD587	Sun
'30.00'	6362.338	5.796	0.15	19.63	21.13	22.93	20.98	26.26	21.81	25.86	21.42	21.59	25.77	19.94
'38.00'	4607.327	0.000	-0.57	49.19	59.19	55.13	59.65	55.22	59.03	56.44	51.57	47.20	52.36	44.21
'39.01'	4900.120	1.033	-0.09	50.36	61.63	59.28	55.70	57.60	59.78	55.26	57.03	50.23	54.68	49.67
'39.01'	5087.416	1.084	-0.17	44.42	52.40	51.12	46.91	45.96	50.84	45.49	48.74	46.24	49.02	47.53
'39.01'	5200.406	0.992	-0.57	39.65	47.10	48.12	49.88	44.36	47.57	48.07	47.10	37.58	42.12	37.70
'40.01'	4442.992	1.486	-0.42	28.84	34.85	33.35	32.57	32.62	32.35	33.97	32.68	29.05	31.82	21.97
'56.01'	5853.668	0.604	-1.00	61.15	74.10	69.62	64.22	64.54	69.72	65.27	66.58	60.60	62.81	65.84
'56.01'	6141.713	0.704	-0.07	127.05	148.78	138.56	134.68	132.14	142.65	134.70	134.98	124.84	129.65	118.37
'56.01'	6496.897	0.604	-0.37	104.28	123.04	119.59	111.20	112.63	119.56	114.80	110.26	107.75	110.49	111.57
'57.01'	4662.498	0.000	-1.24	8.73	9.98	10.61	7.42	7.83	8.50	7.87	8.12	7.57	7.39	5.14
'57.01'	4748.726	0.927	-0.54	3.78	6.28	6.32	4.96	4.46	4.84	5.69	5.30	3.80	4.34	2.78
'58.01'	4523.075	0.516	-0.03	16.97	20.00	21.71	17.90	16.68	18.71	18.86	20.42	15.90	16.56	16.78
'58.01'	4562.359	0.478	0.23	24.99	29.48	28.11	26.04	23.86	26.19	27.26	29.05	25.29	26.52	25.03
'58.01'	5274.229	1.044	0.15	9.11	12.68	11.00	10.72	10.29	10.61	13.03	12.93	9.54	11.36	8.85
'59.01'	5259.728	0.633	-0.03	3.17	3.49	3.60	4.34	3.37	3.72	4.29	3.84	3.31	3.07	3.38
'60.01'	4446.380	0.205	-0.35	13.81	16.56	15.84	13.95	13.05	13.61	15.37	18.04	13.46	13.22	12.41
'60.01'	5293.160	0.823	0.10	11.47	12.86	13.26	11.12	10.21	11.16	12.58	13.99	10.85	10.60	10.12
'60.01'	5319.810	0.550	-0.14	14.37	16.66	15.20	14.27	12.24	13.67	15.81	16.58	13.07	13.03	11.39
'62.01'	4467.340	0.659	0.15	17.21	17.49	17.51	17.70	16.67	17.36	20.36	20.87	16.04	18.99	4.47
'62.01'	4519.630	0.544	-0.35	6.41	8.55	9.21	8.33	8.30	8.01	10.05	9.61	7.93	8.83	9.26
'62.01'	4676.900	0.040	-0.87	6.02	8.92	8.46	6.35	4.87	8.34	8.79	7.14	6.49	4.61	5.32
'63.01'	6645.064	1.380	0.12	3.61	6.57	6.78	5.95	5.81	6.98	7.07	8.67	6.22	6.27	5.23
'66.01'	4449.700	0.000	-1.03	6.66	5.63	6.46	5.59	5.80	5.65	6.59	7.75	6.30	5.66	9.45

Appendix D

IDL code to interpolate the MARCS model atmospheres

As previously mentioned, the MARCS model atmospheres in the parameter range required are produced in temperature steps of 250 K and surface gravity steps of 0.5. To determine the stellar parameters as accurately as possible, steps of 2 K for $T_{\rm eff}$ and 0.01 for $\log g$ are required. To produce these atmospheres, the following code was written.

The code requires an input directory containing 8 stellar atmosphere files. In this example, temperatures between 5250 and 5750 K, surface gravities between 4.0 and 5.0, and metallicities between -0.25 and 0.5 were required. The input directory contains the minimum and maximum of every combination of these atmospheres to provide a cube from which every atmosphere within these parameters can be linearly interpolated. The interpolation is done by first finding the specified temperature, then finding the specified surface gravity before finding the metallicity.

```
; Name        : marcs_interpolation .pro
; Purpose     : produces a linearly interpolated model atmosphere from
  an initial grid
; Use         : MARCS, temperature, surface_gravity , metallicity
; Inputs      : temperature , surface gravity and metallicity values
```

```
; Outputs        : returns a file named 'star.krz' which is the model
    atmosphere at the inputted temperatures
; Restrictions   : requires directory 'input' with the initial model
    atmospheres

; SPECIFIES THE CODE AS A PROGRAM SO IT CAN BE RUN IN THE
    CODES IN THE PARAMETER DETERMINATION CODES.
PRO MARCS, twant, gwant, zwant

; CHECK FOR UNDEFINED INPUT
IF(N_PARAMS() NE 3)THEN BEGIN
  PRINT, 'SYNTAX: MARCS_INTERPOLATION, TEMP, LOG_G, Z'
  PRINT, '          WHERE TEMP, LOG_G, Z ARE FRACTIONS.'
  GOTO, TERMINATE
ENDIF

; CALCULATION OF THE RATIO FOR EACH PARAMETER BASED ON
    PARAMETERS INPUTTED.

tmin = 5250.0
tmax = 5750.0
t = (twant-tmin)/(tmax-tmin)

gmin = 4.0
gmax = 5.0
g = (gwant-gmin)/(gmax-gmin)

zmin = -0.25
```

```
zmax = 0.5
z = (zwant−zmin)/(zmax−zmin)

print , t, g, z

; SPECIFY THE 8 INPUT FILES (MIN/MAX T/G/Z)

min1min2min3 = 'input/t5250g4.0z−0.25.krz'
max1min2min3 = 'input/t5750g4.0z−0.25.krz'

min1min2max3 = 'input/t5250g4.0z0.50.krz'
max1min2max3 = 'input/t5750g4.0z0.50.krz'

min1max2min3 = 'input/t5250g5.0z−0.25.krz'
max1max2min3 = 'input/t5750g5.0z−0.25.krz'

min1max2max3 = 'input/t5250g5.0z0.50.krz'
max1max2max3 = 'input/t5750g5.0z0.50.krz'

; THE .krz FILES HAVE A HEADER WHICH NEEDS TO BE IN THE NEW
   FILES TO RUN THE .ew FILES CORRECTLY SO THIS HEADER IS
   COPIED FROM AN INPUT FILE TO BE WRITTEN INTO THE OUTPUT
   FILE
HEADER:
; GET HEADER & SAVE
header = STRARR(13)
s=''
OPENR, LUN, min1min2min3, /GET_LUN
```

```
FOR line=0, 12 DO BEGIN
  READF, LUN, s
  header[ line ] = s
ENDFOR
FREE_LUN, LUN


; DUMMY VARIABLES
temp = ''
tempmin = ''
tempmax = ''
chosenmin = DBLARR(56,5)
chosenmax = DBLARR(56,5)


; REDUCES THE GRID TO A GRID FOR THE SPECIFIED TEMPERATURE
FIRST_VARIABLE:
;----------------------------
; CHOSEN 1, MIN 2, MIN 3
OPENR, LUN1MIN, min1min2min3, /GET_LUN
OPENR, LUN1MAX, max1min2min3, /GET_LUN
chosen1min2min3 = DBLARR(56,5)
FOR line=0, 12 DO BEGIN
  READF, LUN1MIN, temp
  READF, LUN1MAX, temp
ENDFOR
FOR line=0, 55 DO BEGIN
  READF, LUN1MIN, tempmin
```

```
  READF, LUN1MAX, tempmax
  min1string = (N_ELEMENTS(STRSPLIT(tempmin, /EXTRACT)) LT 5) ?
     STRSPLIT(tempmin, ',', /EXTRACT) : STRSPLIT(tempmin, /EXTRACT)
  max1string = (N_ELEMENTS(STRSPLIT(tempmax, /EXTRACT)) LT 5) ?
     STRSPLIT(tempmax, ',', /EXTRACT) : STRSPLIT(tempmax, /EXTRACT)
  FOR i=0, N_ELEMENTS(min1string)-1 DO chosenmin[line,i] =
     DOUBLE(ARM_STRTRIM(min1string[i],','))
  FOR i=0, N_ELEMENTS(max1string)-1 DO chosenmax[line,i] =
     DOUBLE(ARM_STRTRIM(max1string[i],','))
  chosen1min2min3[line,*] = chosenmin[line,*] + ((chosenmax[line,*] -
     chosenmin[line,*])*t)
ENDFOR
FREE_LUN, LUN1MIN
FREE_LUN, LUN1MAX
;----------------------------
; CHOSEN 1, MAX 2, MIN 3
OPENR, LUN1MIN, min1max2min3, /GET_LUN
OPENR, LUN1MAX, max1max2min3, /GET_LUN
chosen1max2min3 = DBLARR(56,5)
FOR line=0, 12 DO BEGIN
  READF, LUN1MIN, temp
  READF, LUN1MAX, temp
ENDFOR
FOR line=0, 55 DO BEGIN
  READF, LUN1MIN, tempmin
  READF, LUN1MAX, tempmax
  min1string = (N_ELEMENTS(STRSPLIT(tempmin, /EXTRACT)) LT 5) ?
     STRSPLIT(tempmin, ',', /EXTRACT) : STRSPLIT(tempmin, /EXTRACT)
```

```
  max1string = (N_ELEMENTS(STRSPLIT(tempmax, /EXTRACT)) LT 5) ?
     STRSPLIT(tempmax, ',', /EXTRACT) : STRSPLIT(tempmax, /EXTRACT)
  FOR i=0, N_ELEMENTS(min1string)-1 DO chosenmin[line,i] =
     DOUBLE(ARM_STRTRIM(min1string[i],','))
  FOR i=0, N_ELEMENTS(max1string)-1 DO chosenmax[line,i] =
     DOUBLE(ARM_STRTRIM(max1string[i],','))
  chosen1max2min3[line,*] = chosenmin[line,*] + ((chosenmax[line,*] -
     chosenmin[line,*]) *t)
ENDFOR
FREE_LUN, LUN1MIN
FREE_LUN, LUN1MAX
;----------------------------
; CHOSEN 1, MIN 2, MAX 3
OPENR, LUN1MIN, min1min2max3, /GET_LUN
OPENR, LUN1MAX, max1min2max3, /GET_LUN
chosen1min2max3 = DBLARR(56,5)
FOR line=0, 12 DO BEGIN
  READF, LUN1MIN, temp
  READF, LUN1MAX, temp
ENDFOR
FOR line=0, 55 DO BEGIN
  READF, LUN1MIN, tempmin
  READF, LUN1MAX, tempmax
  min1string = (N_ELEMENTS(STRSPLIT(tempmin, /EXTRACT)) LT 5) ?
     STRSPLIT(tempmin, ',', /EXTRACT) : STRSPLIT(tempmin, /EXTRACT)
  max1string = (N_ELEMENTS(STRSPLIT(tempmax, /EXTRACT)) LT 5) ?
     STRSPLIT(tempmax, ',', /EXTRACT) : STRSPLIT(tempmax, /EXTRACT)
  FOR i=0, N_ELEMENTS(min1string)-1 DO chosenmin[line,i] =
```

```
    DOUBLE(ARM_STRTRIM(min1string[i],','))
  FOR i=0, N_ELEMENTS(max1string)-1 DO chosenmax[line,i] =
    DOUBLE(ARM_STRTRIM(max1string[i],','))
  chosen1min2max3[line,*] = chosenmin[line ,*] + ((chosenmax[line,*] -
    chosenmin[line ,*]) *t)
ENDFOR
FREE_LUN, LUN1MIN
FREE_LUN, LUN1MAX
;----------------------
; CHOSEN 1, MAX 2, MAX 3
OPENR, LUN1MIN, min1max2max3, /GET_LUN
OPENR, LUN1MAX, max1max2max3, /GET_LUN
chosen1max2max3 = DBLARR(56,5)
FOR line=0, 12 DO BEGIN
  READF, LUN1MIN, temp
  READF, LUN1MAX, temp
ENDFOR
FOR line=0, 55 DO BEGIN
  READF, LUN1MIN, tempmin
  READF, LUN1MAX, tempmax
  min1string = (N_ELEMENTS(STRSPLIT(tempmin, /EXTRACT)) LT 5) ?
    STRSPLIT(tempmin, ',', /EXTRACT) : STRSPLIT(tempmin, /EXTRACT)
  max1string = (N_ELEMENTS(STRSPLIT(tempmax, /EXTRACT)) LT 5) ?
    STRSPLIT(tempmax, ',', /EXTRACT) : STRSPLIT(tempmax, /EXTRACT)
  FOR i=0, N_ELEMENTS(min1string)-1 DO chosenmin[line,i] =
    DOUBLE(ARM_STRTRIM(min1string[i],','))
  FOR i=0, N_ELEMENTS(max1string)-1 DO chosenmax[line,i] =
    DOUBLE(ARM_STRTRIM(max1string[i],','))
```

```
  chosen1max2max3[line,*] = chosenmin[line ,*] + ((chosenmax[line ,*] -
      chosenmin[line ,*]) *t)
ENDFOR
FREE_LUN, LUN1MIN
FREE_LUN, LUN1MAX

; REDUCES THE GRID TO THE SPECIFIED TEMPERATURE AND SURFACE
   GRAVITY
SECOND_VARIABLE:
;----------------------------
; CHOSEN 1, CHOSEN 2, MIN 3
chosen1chosen2min3 = DBLARR(56,5)
FOR line=0, 55 DO BEGIN
  chosen1chosen2min3[line,*] = chosen1min2min3[line,*] +
      ((chosen1max2min3[line,*] - chosen1min2min3[line,*])*g)
ENDFOR
;----------------------------
; CHOSEN 1, CHOSEN 2, MAX 3
chosen1chosen2max3 = DBLARR(56,5)
FOR line=0, 55 DO BEGIN
  chosen1chosen2max3[line,*] = chosen1min2max3[line,*] +
      ((chosen1max2max3[line,*] - chosen1min2max3[line,*])*g)
ENDFOR

; REDUCES THE GRID TO A SINGLE FILE AT THE SPECIFIED
   TEMPERATURE, SURFACE GRAVITY AND METALLICITY
;----------------------------
; CHOSEN 1, CHOSEN 2, CHOSEN 3
```

```
chosen1chosen2chosen3 = DBLARR(56,5)
FOR line=0, 55 DO BEGIN
  chosen1chosen2chosen3[line,*] = chosen1chosen2min3[line,*] +
      ((chosen1chosen2max3[line,*] - chosen1chosen2min3[line,*])*z)
ENDFOR

; WRITES THE HEADER AND THE INTERPOLATED ATMOSPHERE
OPENW, LUN, 'star.krz', /GET_LUN
FOR line=0, N_ELEMENTS(header)-1 DO PRINTF, LUN, header[line]
FOR line=0, 55 DO BEGIN
  PRINTF, LUN, chosen1chosen2chosen3[line,0], ' ,' ,
      chosen1chosen2chosen3[line ,1], ' ,' , chosen1chosen2chosen3[line ,2],
      ' ,' , chosen1chosen2chosen3[line ,3], ' ,' ,
      chosen1chosen2chosen3[line ,4], ' ,' ,$
  FORMAT='(E16.9,A1,F10.1,A1,E13.5,A1,E13.5,A1,E13.5,A1)'
ENDFOR
FREE_LUN, LUN

TERMINATE:
END
```

Appendix E

Differential stellar parameter codes

The determination of the differential parameters required the development of four semi-automated codes, requiring human input to start each code with the new parameters. The four codes focus on each of the parameters that need to be known for the MARCS atmospheres ($T_{\rm eff}$, $\log g$, metallicity) and the "microturbulence" velocity. They all require the MARCS interpolation code (outlined in Appendix appendix:marcs) with a fixed name for the stellar atmosphere e.g. *star.krz*, which will be the model atmosphere name used in the comparison star .ew files. Each one is used in order, for example, running the temperature code to get a temperature, then inputting this temperature into the surface gravity code, with the same parameters for metallicity and "microturbulence" velocity as used in the temperature code. The temperature and surface gravity are then carried on into the microturbulence code with the metallicity from the temperature code. Then the metallicity code is run with the temperature, surface gravity and "microturbulence" velocity values that have been calculated. These are then the values used to run the codes again until the parameters do not change. Each code runs with either the Fe I lines for the stars or the Fe I and Fe II lines. The atmosphere of the reference star is made using the parameters obtained from the absolute parameter determination. The value of the "microturbulence" velocity is changed in the tail of the equivalent width files rather than in the code due to the nature of the *width* program.

E.1 Temperature code

The temperature code works by iteratively finding the temperature at which the difference in abundance of the Fe I lines between the reference star and comparison star is zero. This is calculated by subtracting the abundance of the reference star from the abundance of the comparison star on a line by line basis and then averaging this difference. The code calculates this at multiple temperatures causing the difference to vary from positive to negative. The temperature at which $ABN_{star} - ABN_{reference} = 0$ can then be interpolated, as can be seen in the penultimate section of the code. The starting temperature should always be lower than required as the temperature interval is added to it. Changes can be seen in the abundance when temperatures are changed up to 2 K but are negligible at smaller values so the minimum value for the temperature interval should be set to 2 K.

```
close ,/ all

; FILES TO WRITE INTO
out = 'temperature.txt'
figure = 'plot.txt'

; INITIAL STELLAR PARAMETERS FOR COMPARISON STAR
nfe1 = 336        ;number of Fe I lines
logg = 4.60       ; fixed logg used from estimates
z = 0.046         ; fixed metallicity used from estimates
teff = 5700       ; starting temperature - must be lower than needed
t_inc = 2         ;temperature increment

; PRODUCE AND READ THE ABUNDANCE FILE FOR REFERENCE STAR.
```

```
spawn, '~/width/width referencestar_Fe .ew'
readcol, ' referencestar_Fe .abn',lambdaref, exenref, loggfref, landeref,
   eqwref, abnref, devref, unknownref, form = 'F,F,F,F,F,F,F,F'

; THE MAIN CODE
openw, 2, figure
repeat begin
        ; PRODUCE THE MODEL ATMOSPHERE AT THE DESIRED
          PARAMETERS. PRODUCE AND READ THE ABUNDANCE FILE
          FOR THE COMPARISON STAR.
        print, MARCS(teff, logg, z)
        spawn, '~/width/width comparisonstar_Fe.ew'
        readcol, 'comparisonstar_Fe.abn',lambda1, exen1, loggf1, lande1,
          eqw1, abn1, dev1, unknown1, form = 'F,F,F,F,F,F,F,F'

        ; PRINT THE EXCITATION ENERGY, DIFFERENCE IN
          ABUNDANCE, AND DIFFERENCE IN ABUNDANCE AT THE
          EXCITATION ENERGY FOR EACH FE I LINE. IF EXCITATION
          ENERGY IS 0, PRINTS 0 TO REMOVE NaN COMMENT.
        openw, 1, out
        for i = 0, nfe1 - 1 do begin
                if (exen1[i] gt 0) then begin
                        printf, 1, exen1[i], abn1[i] - abnref[i], (abn1[i]
                          - abnref[i])/exen1[i]
                endif else if (exen1[i] eq 0) then begin
                        printf, 1, 0, abn1[i] - abnref[i], 0
                endif
        endfor
```

```
        close, 1

        ; CALCULATE LINEAR FIT THROUGH THE FE I LINES, FINDING
          GRADIENT OF FIT (RESULT[1]). INCREASES TEMPERATURE
          UNTIL GRADIENT REACHES SET VALUE.
        readcol, 'temperature.txt', exen, delabn, grad, form = 'F,F,F'
        result = linfit (exen, delabn, YFIT = yfit)
        printf, 2, teff, result [1]
        print, mean(grad), stddev(grad)
        print, teff, result [1]
        teff = teff + t_inc
endrep until (result [1] lt -0.05)
close,2

; CALCULATES THE TEMPERATURE WHERE GRADIENT = 0
readcol, 'plot.txt', teff, gradplot, form = 'I, F'
t_want = interpol (teff, gradplot,0)
print, t_want

; PLOTS THE GRADIENT AT EACH TEMPERATURE FOR A VISUAL
  CONFIRMATION OF THE TEMPERATURE WANTED.
plot, teff, gradplot, psym = 3
oplot, [5700, 5800], [0.0, 0.0]

end
```

E.2 Surface gravity code

The surface gravity code works in a very similar way to the temperature code but uses both the Fe I and Fe II lines for each star. It calculates the mean abundance difference in the Fe I lines and the mean abundance difference in the Fe II lines at each $\log g$ before calculating the difference between Fe I and Fe II, given in the code as x where $x = newfe1 - newfe2$. The required surface gravity is then found where $x = 0$.

```
close ,/ all

; FILES TO WRITE INTO
out1 = 'fe1.txt'
out2 = 'fe2.txt'
figure1 = 'plot.txt'

; INITIAL STELLAR PARAMETERS FOR COMPARISON STAR
nfe1 = 336          ;number of Fe I lines
nfe2 = 14           ;number of Fe II lines
z = 0.046           ; fixed metallicity from estimates
teff = 5908         ; fixed temperature from estimates
logg = 4.50         ; starting surface gravity - must be lower than needed
logg_inc = 0.01     ; surface gravity increment

; PRODUCE AND READ THE ABUNDANCE FILE FOR REFERENCE STAR.
spawn, '~/width/width referencestar_Fe .ew'
spawn, '~/width/width referencestar_Fe2 .ew'
readcol, ' referencestar_Fe .abn',lambdaref, exenref, loggfref, landeref,
   eqwref, abnref, devref, unknownref, form = 'F,F,F,F,F,F,F,F'
readcol, ' referencestar_Fe2 .abn',lambdaref2, exenref2, loggfref2,
```

```
    landeref2, eqwref2, abnref2, devref2, unknownref2, form =
    'F,F,F,F,F,F,F,F'

openw, 3, figure1

repeat begin
        ; PRODUCE THE MODEL ATMOSPHERE AT THE DESIRED
          PARAMETERS. PRODUCE AND READ THE ABUNDANCE FILE
          FOR THE COMPARISON STAR.
        print, MARCS(teff, logg, z)
        spawn, '~/width/width comparisonstar_Fe.ew'
        spawn, '~/width/width comparisonstar_Fe2.ew'
        readcol, 'comparisonstar_Fe.abn',lambda1, exen1, loggf1, lande1,
          eqw1, abn1, dev1, unknown1, form = 'F,F,F,F,F,F,F,F'
        readcol, 'comparisonstar_Fe2.abn',lambda2, exen2, loggf2, lande2,
          eqw2, abn2, dev2, unknown2, form = 'F,F,F,F,F,F,F,F'

        ; CALCULATES AND WRITES DIFFERENCE IN ABUNDANCE FOR
          EACH FE I LINE
        openw, 1, out1
        for i = 0, nfe1-1 do begin
                printf, 1, abn1[i] - abnref[i]
        endfor
        close, 1

        ; CALCULATES AND WRITES DIFFERENCE IN ABUNDANCE FOR
          EACH FE II LINE
        openw, 2, out2
```

```
        for i = 0, nfe2-1 do begin
                printf , 2, abn2[i] - abnref2[i]
        endfor
        close, 2

        readcol, 'fe1.txt', delabnFe1, form = 'F'
        readcol, 'fe2.txt', delabnFe2, form = 'F'

        ; CALCULATES AND WRITES MEAN FE I AND FE II
          DIFFERENTIAL ABUNDANCE. INCREASES logg UNTIL
          DIFFERENCE SET logg REACHED.
        meanfe1 = mean(delabnFe1)
        meanfe2 = mean(delabnFe2)
        printf , 3, logg, meanfe1, meanfe2
        logg = logg + logg_inc
endrep until (logg gt 4.70)
close,3

; CALCULATES THE logg WHERE DIFFERENCE BETWEEN THE MEAN OF
  FE I AND FE II IS 0.
readcol, 'plot.txt', newlogg, newfe1, newfe2, form = 'F, F, F'
x = newfe1 - newfe2
loggwant = interpol (newlogg, x, 0)
print , loggwant

; PLOTS THE DIFFERENCE IN MEAN ABUNDANCE AT EACH logg FOR A
  VISUAL CONFIRMATION OF THE logg WANTED.
```

```
plot, newlogg, x, psym = 1
oplot, [4.50, 4.70], [0.0, 0.0]

end
```

E.3 "Microturbulence" velocity code

The "microturbulence" velocity code is the most complicated. It requires 3 .ew files for the comparison star labelled a 'a, b, c' each with a differing υ_{mic} value from smallest to largest respectively. The values used are then specified in the code as 'va = 0.90' for example.

```
close ,/ all

; FILES TO WRITE INTO
out1 = 'vmica.txt'
out2 = 'vmicb.txt'
out3 = 'vmicc.txt'
figure = 'plot.txt'

; INITIAL STELLAR PARAMETERS FOR COMPARISON STAR
nfe1 = 336        ;number of Fe I lines
logg = 4.60       ; fixed logg used from estimates
z = 0.046         ; fixed metallicity from estimates
teff = 5908       ; fixed temperature from estimates

; MICROTURBULENCE VELOCITY VALUES USED
va = 0.90
```

```
vb = 1.00
vc = 1.10

; PRODUCE THE MODEL ATMOSPHERE TO BE READ BY THE
   COMPARISON STAR
print , MARCS(teff, logg, z)

; PRODUCE AND READ THE ABUNDANCE FILE FOR REFERENCE STAR.
spawn, '~/width/width referencestar_Fe .ew'
readcol , ' referencestar_Fe .abn',lambdaref, exenref, loggfref , landeref ,
   eqwref, abnref, devref, unknownref, form = 'F,F,F,F,F,F,F,F'


; VMIC A – PRODUCE AND READ THE ABUNDANCE FILE FOR THE
   COMPARISON STAR. WRITE THE EQUIVALENT WIDTH, ABUNDANCE
   DIFFERENCE, AND ABUNDANCE DIFFERENCE AT THE EQUIVALENT
   WIDTH FOR EACH FE I LINE.

spawn, '~/width/width comparisonstar_a .ew'
readcol , 'comparisonstar_a .abn',lambda1a, exen1a, loggf1a, lande1a, eqw1a,
   abn1a, dev1a, unknown1a, form = 'F,F,F,F,F,F,F,F'
openw, 1, out1
for i = 0,nfe1 – 1 do begin
        printf , 1, eqw1a[i], (abn1a[i] – abnref[i]), (abn1a[i] –
           abnref[i])/eqw1a[i]
endfor
close , 1
```

```
; VMIC B – PRODUCE AND READ THE ABUNDANCE FILE FOR THE
   COMPARISON STAR. WRITE THE EQUIVALENT WIDTH, ABUNDANCE
   DIFFERENCE, AND ABUNDANCE DIFFERENCE AT THE EQUIVALENT
   WIDTH FOR EACH FE I LINE.

spawn, '~/width/width comparisonstar_b.ew'
readcol, 'comparisonstar_b.abn',lambda1b, exen1b, loggf1b, lande1b, eqw1b,
   abn1b, dev1b, unknown1b, form = 'F,F,F,F,F,F,F,F'
openw, 1, out2
for i = 0,nfe1 – 1 do begin
        printf, 1, eqw1b[i], (abn1b[i] – abnref[i]), (abn1b[i] –
           abnref[i])/eqw1b[i]
endfor
close, 1

; VMIC C – PRODUCE AND READ THE ABUNDANCE FILE FOR THE
   COMPARISON STAR. WRITE THE EQUIVALENT WIDTH, ABUNDANCE
   DIFFERENCE, AND ABUNDANCE DIFFERENCE AT THE EQUIVALENT
   WIDTH FOR EACH FE I LINE.

spawn, '~/width/width comparisonstar_c.ew'
readcol, 'comparisonstar_c.abn',lambda1c, exen1c, loggf1c, lande1c, eqw1c,
   abn1c, dev1c, unknown1c, form = 'F,F,F,F,F,F,F,F'
openw, 1, out3
for i = 0,nfe1 – 1 do begin
        printf, 1, eqw1c[i], (abn1c[i] – abnref[i]), (abn1c[i] –
           abnref[i])/eqw1c[i]
endfor
```

```
close, 1

; CALCULATES AND WRITES THE GRADIENT AT EACH
   MICROTURBULENCE VELOCITY
openw, 3, figure
readcol, 'vmica.txt', eqwa, delabna, grada, form = 'F,F,F'
readcol, 'vmicb.txt', eqwb, delabnb, gradb, form = 'F,F,F'
readcol, 'vmicc.txt', eqwc, delabnc, gradc, form = 'F,F,F'

result1 = linfit (eqwa, delabna, YFIT = yfita)
result2 = linfit (eqwb, delabnb, YFIT = yfitb)
result3 = linfit (eqwc, delabnc, YFIT = yfitc)

printf, 3, va, result1 [1]
printf, 3, vb, result2 [1]
printf, 3, vc, result3 [1]
close, 3

; CALCULATES THE vmic WHERE THE GRADIENT = 0
readcol, 'plot.txt', vmic, gradplot, form = 'F, F'
vmic_want = interpol (vmic, gradplot ,0)

; PLOTS THE GRADIENT AT EACH vmic FOR A VISUAL CONFIRMATION
   OF THE vmic WANTED.
plot, vmic, gradplot, psym = 1
oplot, [0.0, 2.5], [0.0, 0.0], linestyle = 2

end
```

E.4 Metallicity code

The metallicity code simply requires the mean abundance difference between the two stars. This difference is then added onto the metallicity of the reference star to find the required metallicity for the comparison star.

```
close ,/ all

; FILE TO WRITE INTO
out1 = ' metallicity . txt '

; INITIAL STELLAR PARAMETERS FOR COMPARISON STAR
nfe1 = 336        ;number of Fe I lines
logg = 4.60       ; fixed logg used from estimates
z = 0.046         ; fixed metallicity from estimates
teff = 5908       ; fixed temperature from estimates

; METALLICITY OF REFERENCE STAR
z_ref = 0.056

; PRODUCE AND READ THE ABUNDANCE FILE FOR REFERENCE STAR.
spawn, '~/width/width referencestar_Fe .ew'
readcol, ' referencestar_Fe .abn',lambda1, exen1, loggf1, lande1, eqw1,
   abn1, dev1, unknown1, form = 'F,F,F,F,F,F,F,F'

; PRODUCE THE MODEL ATMOSPHERE AT THE DESIRED PARAMETERS.
   PRODUCE AND READ THE ABUNDANCE FILE FOR THE COMPARISON
   STAR.
print , MARCS(teff, logg, z)
```

```
spawn, '~/width/width comparisonstar_Fe.ew'
readcol, 'comparisonstar_Fe.abn',lambdaref, exenref, loggfref, landeref,
   eqwref, abnref, devref, unknownref, form = 'F,F,F,F,F,F,F,F'

; CALCULATES AND WRITES DIFFERENCE IN ABUNDANCE FOR EACH
   FE I LINE
openw, 1, out1
for i = 0, nfe1-1 do begin
        printf, 1, abnref[i]-abn1[i]
endfor
close, 1

; CALCULATES THE CORRECT METALLICITY USING THE MEAN OF THE
   ABUNDANCE DIFFERENCE AND THE METALLICITY OF THE
   REFERENCE STAR
readcol, ' metallicity .txt', delabnFe1, form = 'F'
print, ' Metallicity = '+strtrim ((mean(delabnFe1) + z_ref),2)

end
```

Appendix F

Rotational velocities

The spectral visualisation tool BINMAG, described in Section 3.3, was used to determine an initial value for the $\upsilon \sin i$. This was done by measuring 238 unblended lines of different sizes over the whole wavelength range for each star and fitting the synthetic spectra to the lines by modifying $\upsilon \sin i$ and υ_r. The average of the values was then calculated to determine the final $\upsilon \sin i$ values which can be seen in Table F.1.

Table F.1: Radial and projected rotational velocities derived by measuring 238 lines in BINMAG and averaging the values obtained.

Star name	v_r (kms^{-1})	$v \sin i$ (kms^{-1})
61 Vir	-7.72 (0.32)	5.42 (1.05)
HD 18144	-0.96 (0.75)	4.89 (1.01)
HD 18803	10.26 (0.50)	5.62 (1.01)
HD 47127	49.88 (1.74)	5.08 (0.86)
HD 51219	-7.80 (1.11)	5.57 (1.87)
HD 58781	5.33 (0.37)	5.17 (0.89)
HD 111395	-8.88 (4.10)	6.02 (0.98)
HD 140538	19.29 (3.38)	5.38 (1.92)
HD 201219	4.96 (1.09)	5.47 (2.69)
HD 223498	-23.81 (3.23)	4.24 (1.96)

Bibliography

[1] Y. Amelin and A. Krot. Pb isotopic age of the Allende chondrules. *Meteoritics and Planetary Science*, 42:1321–1335, August 2007. doi: 10.1111/j.1945-5100.2007.tb00577.x.

[2] E. Anders. Meteorites and the Early Solar System. ARA&A, 9:1, 1971. doi: 10.1146/annurev.aa.09.090171.000245.

[3] E. Anders and N. Grevesse. Abundances of the elements - Meteoritic and solar. Geochim. Cosmochim. Acta, 53:197–214, January 1989. doi: 10.1016/0016-7037(89)90286-X.

[4] M. Asplund, N. Grevesse, and A. J. Sauval. The Solar Chemical Composition. In T. G. Barnes, III and F. N. Bash, editors, *Cosmic Abundances as Records of Stellar Evolution and Nucleosynthesis*, volume 336 of *Astronomical Society of the Pacific Conference Series*, page 25, September 2005.

[5] M. Asplund, N. Grevesse, A. J. Sauval, and P. Scott. The Chemical Composition of the Sun. ARA&A, 47:481–522, September 2009. doi: 10.1146/annurev.astro.46.060407.145222.

[6] P. Baumann, I. Ramírez, J. Meléndez, M. Asplund, and K. Lind. Lithium depletion in solar-like stars: no planet connection. A&A, 519:A87, September 2010. doi: 10.1051/0004-6361/201015137.

[7] S. V. W. Beckwith, A. I. Sargent, R. S. Chini, and R. Guesten. A survey for circumstellar disks around young stellar objects. AJ, 99:924–945, March 1990. doi: 10.1086/115385.

[8] N. Calvet, L. Hartmann, and S. E. Strom. Evolution of Disk Accretion. *Protostars and Planets IV*, page 377, May 2000.

[9] L. Casagrande, R. Schoenrich, M. Asplund, S. Cassisi, I. Ramirez, J. Melendez, T. Bensby, and S. Feltzing. Geneva-Copenhagen survey re-analysis (Casagrande+, 2011). *VizieR Online Data Catalog*, 353:9138, April 2011.

[10] G. Cescutti, C. Chiappini, R. Hirschi, G. Meynet, and U. Frischknecht. The s-process in the Galactic halo: the fifth signature of spinstars in the early Universe? A&A, 553:A51, May 2013. doi: 10.1051/0004-6361/201220809.

[11] Y. Q. Chen and G. Zhao. A Comparative Study on Lithium Abundances in Solar-Type Stars With and Without Planets. AJ, 131:1816–1821, March 2006. doi: 10.1086/499946.

[12] C. Chiappini, R. Hirschi, G. Meynet, S. Ekström, A. Maeder, and F. Matteucci. A strong case for fast stellar rotation at very low metallicities. A&A, 449:L27–L30, April 2006. doi: 10.1051/0004-6361:20064866.

[13] F. D'Antona and I. Mazzitelli. New pre-main-sequence tracks for M less than or equal to 2.5 solar mass as tests of opacities and convection model. ApJS, 90: 467–500, January 1994. doi: 10.1086/191867.

[14] J.-F. Donati, M. Semel, B. D. Carter, D. E. Rees, and A. Collier Cameron. Spectropolarimetric observations of active stars. MNRAS, 291:658, November 1997.

[15] A. Ecuvillon, G. Israelian, N. C. Santos, M. Mayor, and G. Gilli. Abundance ratios of volatile vs. refractory elements in planet-harbouring stars: hints of pollution? A&A, 449:809–816, April 2006. doi: 10.1051/0004-6361:20054534.

[16] B. Edvardsson, J. Andersen, B. Gustafsson, D. L. Lambert, P. E. Nissen, and J. Tomkin. The Chemical Evolution of the Galactic Disk - Part One - Analysis and Results. A&A, 275:101, August 1993.

[17] P. Eggenberger, G. Meynet, A. Maeder, R. Hirschi, C. Charbonnel, S. Talon, and S. Ekström. The Geneva stellar evolution code. Ap&SS, 316:43–54, August 2008.

[18] P. Eggleton. *Evolutionary Processes in Binary and Multiple Stars.*

[19] P. P. Eggleton. The evolution of low mass stars. MNRAS, 151:351, 1971.

[20] P. J. Flower. Transformations from Theoretical Hertzsprung-Russell Diagrams to Color-Magnitude Diagrams: Effective Temperatures, B-V Colors, and Bolometric Corrections. ApJ, 469:355, September 1996. doi: 10.1086/177785.

[21] J. C. Forbes. Curveballs in protoplanetary discs - the effect of the Magnus force on planet formation. MNRAS, 453:1779–1792, October 2015. doi: 10.1093/mnras/stv1712.

[22] L. Fossati, T. Ryabchikova, S. Bagnulo, E. Alecian, J. Grunhut, O. Kochukhov, and G. Wade. The chemical abundance analysis of normal early A- and late B-type stars. A&A, 503:945–962, September 2009. doi: 10.1051/0004-6361/200811561.

[23] L. Fossati, T. Ryabchikova, D. V. Shulyak, C. A. Haswell, A. Elmasli, C. P. Pandey, T. G. Barnes, and K. Zwintz. The accuracy of stellar atmospheric parameter determinations: a case study with HD 32115 and HD 37594. MNRAS, 417:495–507, October 2011. doi: 10.1111/j.1365-2966.2011.19289.x.

[24] F. Fressin, G. Torres, D. Charbonneau, S. T. Bryson, J. Christiansen, C. D. Dressing, J. M. Jenkins, L. M. Walkowicz, and N. M. Batalha. The False Positive Rate of Kepler and the Occurrence of Planets. ApJ, 766:81, April 2013. doi: 10.1088/0004-637X/766/2/81.

[25] G. Gonzalez. The stellar metallicity-giant planet connection. MNRAS, 285:403–412, February 1997.

[26] G. Gonzalez. Parent stars of extrasolar planets - IX. Lithium abundances. MNRAS, 386:928–934, May 2008. doi: 10.1111/j.1365-2966.2008.13067.x.

[27] G. Gonzalez, C. Laws, S. Tyagi, and B. E. Reddy. Parent Stars of Extrasolar Planets. VI. Abundance Analyses of 20 New Systems. AJ, 121:432–452, January 2001. doi: 10.1086/318048.

[28] J. I. González Hernández, E. Delgado-Mena, S. G. Sousa, G. Israelian, C. Santos, N, V. Z. Adibekyan, and S. Udry. Searching for the signatures of terrestrial planets in F-, G-type main-sequence stars. A&A, 552:A6, April 2013.

[29] S. Goriely, A. Bauswein, and H.-T. Janka. r-process Nucleosynthesis in Dynamically Ejected Matter of Neutron Star Mergers. ApJ, 738:L32, September 2011. doi: 10.1088/2041-8205/738/2/L32.

[30] D. F. Gray. *The Observation and Analysis of Stellar Photospheres, 3rd Edition.* Cambridge University Press, September 2005. ISBN 0521851866.

[31] N. Grevesse and A. J. Sauval. Standard Solar Composition. Space Sci. Rev., 85: 161–174, May 1998. doi: 10.1023/A:1005161325181.

[32] N. Grevesse, A. Noels, and A. J. Sauval. Standard Abundances. In S. S. Holt and G. Sonneborn, editors, *Cosmic Abundances*, volume 99 of *Astronomical Society of the Pacific Conference Series*, page 117, 1996.

[33] N. Grevesse, M. Asplund, and A. J. Sauval. The Solar Chemical Composition. Space Sci. Rev., 130:105–114, June 2007. doi: 10.1007/s11214-007-9173-7.

[34] B. Gustafsson. Is the Sun a Sun-Like Star? Space Sci. Rev., 85:419–428, May 1998. doi: 10.1023/A:1005164331058.

[35] B. Gustafsson. Is the Sun unique as a star – and if so, why? *Physica Scripta Volume T*, 130(1):014036, August 2008. doi: 10.1088/0031-8949/2008/T130/014036.

[36] B. Gustafsson, B. Edvardsson, K. Eriksson, U. G. Jørgensen, Å. Nordlund, and B. Plez. A grid of MARCS model atmospheres for late-type stars. I. Methods and general properties. A&A, 486:951–970, August 2008. doi: 10.1051/0004-6361:200809724.

[37] G. Israelian, A. Ecuvillon, R. Rebolo, R. García-López, P. Bonifacio, and P. Molaro. Galactic evolution of nitrogen. A&A, 421:649–658, July 2004. doi: 10.1051/0004-6361:20047132.

[38] G. Israelian, E. Delgado Mena, N. C. Santos, S. G. Sousa, M. Mayor, S. Udry, C. Domínguez Cerde~na, R. Rebolo, and S. Randich. Enhanced lithium depletion in Sun-like stars with orbiting planets. Nature, 462:189–191, November 2009. doi: 10.1038/nature08483.

[39] D. Jewitt, J. Agarwal, H. Weaver, M. Mutchler, and S. Larson. Episodic Ejection from Active Asteroid 311P/PANSTARRS. ApJ, 798:109, January 2015. doi: 10.1088/0004-637X/798/2/109.

[40] C. Kobayashi, H. Umeda, K. Nomoto, N. Tominaga, and T. Ohkubo. Galactic Chemical Evolution: Carbon through Zinc. ApJ, 653:1145–1171, December 2006. doi: 10.1086/508914.

[41] O. P. Kochukhov. Spectrum synthesis for magnetic, chemically stratified stellar atmospheres. In I. I. Romanyuk, D. O. Kudryavtsev, O. M. Neizvestnaya, and V. M. Shapoval, editors, *Physics of Magnetic Stars*, pages 109–118, 2007.

[42] F. G. Kupka, T. A. Ryabchikova, N. E. Piskunov, H. C. Stempels, and W. W. Weiss. VALD-2 – The New Vienna Atomic Line Database. *Baltic Astronomy*, 9: 590–594, 2000.

[43] R. Kurucz. ATLAS9 Stellar Atmosphere Programs and 2 km/s grid. *ATLAS9 Stellar Atmosphere Programs and 2 km/s grid. Kurucz CD-ROM No. 13. Cambridge, Mass.: Smithsonian Astrophysical Observatory, 1993.*, 13, 1993.

[44] R. L. Kurucz, I. Furenlid, J. Brault, and L. Testerman. *Solar flux atlas from 296 to 1300 nm.* 1984.

[45] A. Lobel. SpectroWeb: An Interactive Graphical Database of Digital Stellar Spectral Atlases. In *IAU Joint Discussion*, volume 4 of *IAU Joint Discussion*, page 22, August 2006.

[46] R. E. Luck and U. Heiter. Dwarfs in the Local Region. AJ, 131:3069–3092, June 2006. doi: 10.1086/504080.

[47] C. E. Mack, III, S. C. Schuler, K. G. Stassun, and J. Norris. Detailed Abundances of Planet-hosting Wide Binaries. I. Did Planet Formation Imprint Chemical Signatures in the Atmospheres of HD 20782/81? ApJ, 787:98, June 2014.

[48] M. Mayor and D. Queloz. A Jupiter-mass companion to a solar-type star. Nature, 378:355–359, November 1995. doi: 10.1038/378355a0.

[49] J. Meléndez, M. Asplund, B. Gustafsson, and D. Yong. The Peculiar Solar Composition and Its Possible Relation to Planet Formation. ApJ, 704:L66–L70, October 2009. doi: 10.1088/0004-637X/704/1/L66.

[50] J. Meléndez, I. Ramírez, L. Casagrande, M. Asplund, B. Gustafsson, D. Yong, J. D. Do Nascimento, M. Castro, and M. Bazot. The solar, exoplanet and cosmological lithium problems. Ap&SS, 328:193–200, July 2010. doi: 10.1007/s10509-009-0187-3.

[51] J. Meléndez, M. Bergemann, J. G. Cohen, M. Endl, A. I. Karakas, I. Ramírez, W. D. Cochran, D. Yong, P. J. MacQueen, C. Kobayashi, and M. Asplund. The remarkable solar twin HIP 56948: a prime target in the quest for other Earths. A&A, 543:A29, July 2012. doi: 10.1051/0004-6361/201117222.

[52] P. E. Nissen. CNO at the Surface of Low and Intermediate MS stars (invited review). In C. Charbonnel, D. Schaerer, and G. Meynet, editors, *CNO in the Universe*, volume 304 of *Astronomical Society of the Pacific Conference Series*, page 60, 2003.

[53] A. Nordlund. Solar Twins and Possible Solutions of the Solar and Jupiter Abundance Problems. *ArXiv e-prints*, August 2009.

[54] G. Pace. Chromospheric activity as age indicator. An L-shaped chromospheric-activity versus age diagram. A&A, 551:L8, March 2013. doi: 10.1051/0004-6361/201220364.

[55] G. Pace, L. Pasquini, and S. Ortolani. The Wilson-Bappu effect: A tool to determine stellar distances. A&A, 401:997–1007, April 2003. doi: 10.1051/0004-6361:20030163.

[56] H. Palme. Are There Chemical Gradients in the Inner Solar System? Space Sci. Rev., 92:237–262, April 2000. doi: 10.1023/A:1005247329412.

[57] S. Park, W. Kang, J.-E. Lee, and S.-G. Lee. Wilson-Bappu Effect: Extended to Surface Gravity. AJ, 146:73, October 2013. doi: 10.1088/0004-6256/146/4/73.

[58] J. X. Prochaska and A. McWilliam. On the Perils of Hyperfine Splitting: A Reanalysis of MN and SC Abundance Trends. ApJ, 537:L57–L60, July 2000.

[59] N. Przybilla, K. Butler, S. R. Becker, and R. P. Kudritzki. Quantitative spectroscopy of BA-type supergiants. A&A, 445:1099–1126, January 2006. doi: 10.1051/0004-6361:20053832.

[60] J. A. Robles, C. H. Lineweaver, D. Grether, C. Flynn, C. A. Egan, M. B. Pracy, J. Holmberg, and E. Gardner. A Comprehensive Comparison of the Sun to Other Stars: Searching for Self-Selection Effects. ApJ, 684:691–706, September 2008. doi: 10.1086/589985.

[61] L. A. Rogers. Most 1.6 Earth-radius Planets are Not Rocky. ApJ, 801:41, March 2015. doi: 10.1088/0004-637X/801/1/41.

[62] T. Ryabchikova, L. Fossati, and D. Shulyak. Improved fundamental parameters and LTE abundances of the CoRoT solar-type pulsator HD 49933. A&A, 506: 203–211, October 2009. doi: 10.1051/0004-6361/200911871.

[63] S. G. Ryan and A. J. Norton. *Stellar Evolution and Nucleosynthesis*. January 2010.

[64] P. Sánchez and D. J. Scheeres. Disruption patterns of rotating self-gravitating aggregates: A survey on angle of friction and tensile strength. Icarus, 271:453–471, June 2016. doi: 10.1016/j.icarus.2016.01.016.

[65] N. C. Santos, G. Israelian, and M. Mayor. Spectroscopic [Fe/H] for 98 extra-solar planet-host stars. Exploring the probability of planet formation. A&A, 415: 1153–1166, March 2004. doi: 10.1051/0004-6361:20034469.

[66] S. C. Schuler, D. Flateau, K. Cunha, J. R. King, L. Ghezzi, and V. V. Smith. Abundances of Stars with Planets: Trends with Condensation Temperature. ApJ, 732:55, May 2011. doi: 10.1088/0004-637X/732/1/55.

[67] A. Sicilia-Aguilar, L. W. Hartmann, G. Fürész, T. Henning, C. Dullemond, and W. Brandner. High-Resolution Spectroscopy in Tr 37: Gas Accretion Evolution in Evolved Dusty Disks. AJ, 132:2135–2155, November 2006. doi: 10.1086/508058.

[68] V. V. Smith, D. L. Lambert, and P. E. Nissen. Isotopic Lithium Abundances in Nine Halo Stars. ApJ, 506:405–423, October 1998. doi: 10.1086/306238.

[69] D. R. Soderblom. The Ages of Stars. ARA&A, 48:581–629, September 2010. doi: 10.1146/annurev-astro-081309-130806.

[70] D. R. Soderblom, D. K. Duncan, and D. R. H. Johnson. The chromospheric emission-age relation for stars of the lower main sequence and its implications for the star formation rate. ApJ, 375:722–739, July 1991. doi: 10.1086/170238.

[71] M. Spite, R. Cayrel, B. Plez, V. Hill, F. Spite, E. Depagne, P. François, P. Bonifacio, B. Barbuy, T. Beers, J. Andersen, P. Molaro, B. Nordström, and F. Primas. First stars VI - Abundances of C, N, O, Li, and mixing in extremely metal-poor giants. Galactic evolution of the light elements. A&A, 430:655–668, February 2005. doi: 10.1051/0004-6361:20041274.

[72] R. J. Stancliffe and J. J. Eldridge. Modelling the binary progenitor of Supernova 1993J. MNRAS, 396:1699–1708, July 2009. doi: 10.1111/j.1365-2966.2009.14849.x.

[73] J. K. Teske, L. Ghezzi, K. Cunha, V. V. Smith, S. C. Schuler, and M. Bergemann. Abundance Differences between Exoplanet Binary Host Stars XO-2N and ZO-2S - Dependence on Stellar Parameters. ApJ, 801:L10, March 2015.

[74] N. Thomas, R. The Source Function in a Non-Equilibrium Atmosphere. I. The Resonance Lines. ApJ, 125:260, January 1957. doi: 10.1086/146299.

[75] F. X. Timmes, S. E. Woosley, and T. A. Weaver. Galactic chemical evolution: Hydrogen through zinc. ApJS, 98:617–658, June 1995. doi: 10.1086/192172.

[76] V. Tsymbal. STARSP: A Software System For the Analysis of the Spectra of Normal Stars. In S. J. Adelman, F. Kupka, and W. W. Weiss, editors, *M.A.S.S., Model Atmospheres and Spectrum Synthesis*, volume 108 of *Astronomical Society of the Pacific Conference Series*, page 198, 1996.

[77] S. Udry and N. C. Santos. Statistical Properties of Exoplanets. ARA&A, 45: 397–439, September 2007. doi: 10.1146/annurev.astro.45.051806.110529.

[78] D. Valencia, D. D. Sasselov, and R. J. O'Connell. Radius and Structure Models of the First Super-Earth Planet. ApJ, 656:545–551, February 2007. doi: 10.1086/509800.

[79] J. A. Valenti and D. A. Fischer. Spectroscopic Properties of Cool Stars (SPOCS). I. 1040 F, G, and K Dwarfs from Keck, Lick, and AAT Planet Search Programs. ApJS, 159:141–166, July 2005. doi: 10.1086/430500.

[80] F. van Leeuwen. Validation of the new Hipparcos reduction. A&A, 474:653–664, November 2007. doi: 10.1051/0004-6361:20078357.

[81] S. Vauclair. Lithium as a Stellar Age Indicator. In G. Cayrel de Strobel and A. M. Delplace, editors, *IAU Colloq. 17: Age des Etoiles*, page 38, 1972.

[82] S. S. Vogt, R. A. Wittenmyer, R. P. Butler, S. O'Toole, G. W. Henry, E. J. Rivera, S. Meschiari, G. Laughlin, C. G. Tinney, H. R. A. Jones, J. Bailey, B. D. Carter, and K. Batygin. A Super-Earth and Two Neptunes Orbiting the Nearby Sun-like Star 61 Virginis. ApJ, 708:1366–1375, January 2010. doi: 10.1088/0004-637X/708/2/1366.

[83] O. C. Wilson and M. K. Vainu Bappu. H and K Emission in Late-Type Stars: Dependence of Line Width on Luminosity and Related Topics. ApJ, 125:661, May 1957. doi: 10.1086/146339.

[84] S. E. Woosley, J. R. Wilson, G. J. Mathews, R. D. Hoffman, and B. S. Meyer. The r-process and neutrino-heated supernova ejecta. ApJ, 433:229–246, September 1994. doi: 10.1086/174638.

[85] G. Wuchterl and R. S. Klessen. The First Million Years of the Sun: A Calculation of the Formation and Early Evolution of a Solar Mass Star. ApJ, 560:L185–L188, October 2001. doi: 10.1086/324307.

[86] G. Wuchterl and W. M. Tscharnuter. From clouds to stars. Protostellar collapse and the evolution to the pre-main sequence I. Equations and evolution in the Hertzsprung-Russell diagram. A&A, 398:1081–1090, February 2003. doi: 10.1051/0004-6361:20021707.

[87] Y. Yoshii. *Star Counts and Nature of the Galactic Thick Disk*, page 393. 2013. doi: 10.1007/978-94-007-5612-0_8.

[88] B. Zuckerman and I. Song. Young Stars Near the Sun. ARA&A, 42:685–721, September 2004. doi: 10.1146/annurev.astro.42.053102.134111.